Robust Electrode Displacement Elastography Imaging for Microwave Liver Ablation Using Machine Learning

By

Robert M Pohlman

A dissertation submitted in partial fulfilment of

the requirements for the degree of

Doctor of Philosophy

(Electrical Engineering)

at the University of Wisconsin – Madison

2021

Date of final oral examination:

April 29th, 2021

The dissertation is approved by the following members of the Final Oral Committee:

Tomy Varghese, Professor, Medical Physics.

James L Hinshaw, MD., Professor, Radiology

William A Sethares, Professor, Electrical and Computer Engineering

Varun Jog, Assistant Professor, Electrical and Computer Engineering

Acknowledgments

First, I would like to thank my advisor Dr. Tomy Varghese, for his passion toward our research project and advice toward my professional career. This research work and results would not have been possible without his guidance, technical insight, and mentorship. I am fortunate to have an advisor who allows me to pursue my own interests in the work, while also pushing me toward new goals.

I am grateful for the support of the ablation team, Dr. Timothy Ziemlewicz, Dr. James Hinshaw, Dr. Meghan Lubner, Dr. Shane Wells, Dr. Fred Lee Jr., Marci Alexander, Kelly Wergin, and others who have helped me in passing without learning their name. Additional acknowledgements for Dr. Hinshaw and Dr. Ziemlewicz for the time spent discussing patient treatments and obtaining clinical images as well as acknowledgements for Marci and Kelly who helped me in patient follow-up and *in-vivo* data collection scheduling. I am thankful for Dr. William Sethares and Dr. Varun Jog for their hours spent mentoring and supporting my project. I appreciate Dr. Jingfeng Jiang who helped get my start with elastography and coding support as well as Dr. Carol Mitchell who provided valuable clinical insight and perspectives.

I also share great appreciation to my peers, Rashid Al Mukaddim, Dr. Catherine Steffel, Michael Turney, Dr. Wenjun Yang, Dr. Kayvan Samimi, Yurim Lee, and the countless others who have offered their support.

Finally, I would like to thank my family and friends for their support. Firstly, mother, Holly Pohlman for her unconditional support as well as all my family members, including those not with us anymore. Without their unwavering support and dedication for me, I would not have made it to where I am today. I additionally appreciate all the support from my friends I have had over the years.

Abstract

Hepatocellular carcinoma (HCC) is the 6th most common cancer worldwide with the 3rd highest mortality rate. Although mortality with all other cancers have declined over the last decade, the age-adjusted death-rate for HCC in the United States surged between 2000-2016 by 43% in men and 40% in women, with an estimated 42,000 new liver cancer diagnosis in 2018. A common procedure to increase liver cancer patient survival rates is surgical resection, yet many patients are nonviable candidates due to other liver co-morbidities. Minimally invasive microwave ablation (MWA) is becoming an important alternative, providing similar results to surgical resection with fewer complications. For MWA to provide these excellent results, accurate imaging of tumors before and after ablation is essential to ensure adequate tissue necrosis. Although contrast enhanced computed tomography (CECT) is most often relied upon for this task, ultrasound-based elasticity imaging provides an excellent alternative due to its real-time, cost-effective, and non-ionizing imaging advantage. Conventional B-mode is unfit to provide necessary delineation, but electrode displacement elastography (EDE) has demonstrated high contrast and contrast-to-noise imaging of liver ablations at all depths. However, EDE still retains some limitations from becoming a comparable imaging modality to CECT in the clinical setting. The primary goal of this research is to utilize machine-learning concepts to improve EDE liver ablation delineation and decrease image noise as well as providing clinicians with feedback on ablated region size and location. Results have demonstrated feasibility of this proposed work and verify that our approach has merit. The first aim of this project utilized dictionary representations on displacement estimates demonstrating significant reduction of noise in strain tensor images without negatively influencing boundary delineation. Our second aim tracked ablation dimensions over clinician perturbations during EDE and accounted for physiological motion that can degrade ablation size and contrast consistency. Finally, we utilized the ellipsoidal shape of ablations to autonomously locate and segment strain tensor images with active contour snakes. Together this project is a major stepping-stone to bridging the gap between ultrasound and CECT imaging modalities for monitoring and differential imaging of MWA procedures.

Table of Contents

List of Figures

No table of figures entries found.

List of Tables

Chapter 1: The Research Problem

1.1 Background: Assessment of Liver Tumor Ablation

New liver cancer diagnosis affected approximately 780,000 individuals worldwide in 2012 and claimed nearly 750,000 lives [1-3]. Although mortality with all other cancers have declined over the last decade, the age-adjusted death-rate for liver cancer in the United States surged between 2000-2016 by 43% in men and 40% in women [4]. As of 2018, liver cancer was the fourth leading cause of cancer related deaths worldwide and the seventh most common in incidence [5, 6]. In 2015, the Global Cancer Observatory (GLOBOCAN) reported 854,000 cases of liver cancer with 810,000 deaths globally, a third due to the hepatitis B virus, a third from alcohol use, and the remainder a combination of hepatitis C virus and other factors [7]. In the United States, liver cancer mortality showed an average annual percent increase of 2.17% from 2005 – 2014 with the burden of liver cancer nearly doubling since the mid-1980s [8]. Noone et al. predicted in 2018 that at least 1% of the United States population would be diagnosed with some type of primary liver cancer [9]. Additionally, the Center for Disease Control reported that during the years 2004-2009 only roughly one fourth of liver cancer patients survived even when the cancer had not spread outside the liver [10]. Not only does primary liver cancer depend on chronic viral- and alcohol-related factors, but also as currently shown, factors such as obesity, type 2 diabetes, aflatoxin exposure and nonalcoholic fatty liver disease are significant contributors to liver cancer, specifically hepatocellular carcinoma (HCC) [11, 12]. Due to these contributing factors being widespread in the population and heterogeneity of liver cancers, regimented surveillance and subsequent treatment are difficult to perform before advanced cancer progression occurs and found at initial diagnosis [13, 14].

Surgical resection and transplantation are considered the gold-standard for treatment of malignant liver tumors, however more than 75% of patients remain unsuitable candidates [15, 16]. Criteria for ineligibility include inadequate liver function, advanced disease, multiple metastases, poor anatomic tumor location, or presence of other medical co-morbidities [17-19]. As a result, patients with malignant tumors are often offered minimally invasive, image guided interventional treatments such as thermal ablation or

transcatheter arterial chemoembolization [16]. These minimally invasive treatments are favorable as they avoid large incisions, surgical morbidity and mortality with surgical resection while providing survival benefits like surgical resection [20-22]. Additional benefits of thermal ablation therapies include low cost and ability for repeated treatments if needed in an out-patient clinical setting [23].

Minimally invasive therapies, such as percutaneous thermal ablation, have become an essential alternative to surgical resection and gained popularity for local and minimally invasive treatment of hepatic malignancies [24-29]. Microwave ablation (MWA), a commonly used percutaneous thermal ablation procedure utilizes electromagnetic energy propagation to heat biological tissue resulting in tissue necrosis and thermal coagulation [30-38]. MWA procedures have reported survival rates of up to 10 years after HCC treatment [20], similar in effectiveness as curative surgical resection [24, 39]. Technological advances, including the use of multiple antennas and high-powered MWA devices, is changing treatment paradigms as it enables effective treatment of larger tumors. Recent studies with modern equipment have shown that ablation of primary liver tumors larger than 3 cm have comparable survival rates to tumors smaller than 3 cm [40, 41], expanding the target patient population. Because the placement of multiple antennas used for larger liver tumors requires greater operator skill and improved image guidance, this places a premium on these skills and image guidance optimization to maximize results [42].

Regardless of the underlying tumor being treated, the goal of thermal ablation, including MWA, is to heat malignant tissues to temperatures above 60 ºC resulting in thermal coagulation and necrosis. The treatment is considered complete when the target tumor as well as a 0.5 – 1 cm ablative margin of normal tissue is destroyed while sparing healthy liver parenchyma and vulnerable non-target anatomy [36, 43]. Ultimately, effective ablation is related to appropriate antenna placement, sufficient energy delivery, and the creation of appropriate ablative margins [35]. Thus, an accurate mechanism for assessing the ablative margin is critical to the success of the MWA procedure and unfortunately lacking with current B-mode ultrasound imaging techniques [44]. Successful ablation therefore requires an imaging modality or modalities that accurately depict the target tumor, allow accurate antenna placement, define the surrounding anatomical structures, and appropriately monitor the growing ablation zone [45- 47].

Various imaging features have been used to characterize the ablation zone both during and after an ablation procedure. These include decreased perfusion and changes in signal intensity on magnetic resonance imaging (MRI), increased echogenicity on ultrasound, higher attenuation on CT, and decreased radiotracer uptake on positron emission tomography (PET) [48]. Because of their availability and consistent use by interventionalists, percutaneous MWA are generally performed with ultrasound and/or CT guidance which complement each other in assessing technical success and efficacy at follow-up. Intra-operative CT is well suited for percutaneous ablations as it visualizes tumors in relation to the antenna, ablation zone, and neighboring pathology [49]. Contrast-enhanced computed tomography (CECT) provides a high success rate imaging modality with minimal complications, however it exposes patients to an effective dose of 72 mSv ionizing radiation [50]. It also leaves clinicians with limited target tumor visualization along with the low resolution of intrahepatic vessels [45, 51, 52] .

Conventional B-mode ultrasound is the gold-standard for performing ablative procedures and commonly used to guide percutaneous procedures [36]. This is because ultrasound has advantages of real-time guidance for antenna placement and monitoring of the vaporization created during ablations while being relatively cost-effective and free from radiation exposure [53]. Unfortunately, boundary delineation with ultrasound imaging is limited due to gas bubbles attenuating ultrasound signals, deep location, small tumor size, ablation being obscured by other anatomical and physiological structures, and low echogenicity. Additionally, gas bubbles do not directly correlate with direct tissue coagulation and often overestimates the size of ablated areas [30, 53-56].

Ultrasound elastography, which visualizes the relative stiffness or strain in tissue utilizing measurements of localized deformation and has been used for liver ablation visualization [57-59]. Elastography works well for post-ablation imaging as ablated volumes present with high stiffness contrast in comparison to normal liver parenchyma [60], for both MRI [61] and ultrasound elastography [57, 58]. Post-ablation RF data loops also contain gas bubbles and is collected over a short duration. Echo signals from the bubbles are therefore present in both the pre- and post-deformation RF frames after the ablation procedure and can be used to track deformation. However, there is some loss of boundary delineation distal

to the bubbles, due to increased attenuation causing lower echographic signal-to-noise ratio (SNR) [62]. Pre-ablation tumor imaging on the other hand, has been limited as stiffness contrast varies between patients and cancer types requiring elastographic imaging to be more robust to noise while sensitive enough to detect low stiffness differences. For example, HCC masses are softer than its surrounding generally cirrhotic liver tissue, while liver metastases are generally stiffer than normal liver parenchyma [63]. In this chapter, we report on the use of electrode displacement elastography (EDE) an approach where deformation is induced via manual perturbation of the ablation antenna [57].

Imaging to assess efficacy of MWA procedures most often takes the form of CECT [26] which is costly, time-consuming, and exposes patients to undesirable ionizing radiation and contrast agents. An alternative, real-time, non-ionizing imaging modality that can be used is ultrasound (US). With US, conventional B-mode images show little success for tumor and ablation region visualization [64, 65], however US elastography, which utilizes tissue stiffness as the contrast mechanism, provides higher contrast for both tumor and ablation region delineation [66-68]. We have previously demonstrated that using the microwave antennae for introducing quasi-static deformation required for elastography, subsequently named EDE [69], allows for imaging at all tumor depths when compared to either acoustic radiation force impulse (ARFI) [58] , shear wave elastography imaging (SWEI) [70, 71], or external compression [72]. EDE has since demonstrated high contrast and contrast-to-noise ratios (CNR) for strain imaging in phantoms [73-75], animal models [76, 77], and human patients [58, 78].

1.2 Motivation for this Research

One of the problems associated with treatment of HCC is the risk of tumor recurrence due to metastasis from the original tumor, new tumor formation in a cirrhotic liver, advanced liver disease contributing to higher risk for recurrence or incomplete treatment of the initial tumor. To properly plan treatment for long-term disease-free survival, accurate imaging of mass dimensions and location is needed [24, 97]. CECT is commonly used for accurate tumor portrayal including the spread of tumors and mapping of liver vascular anatomy [26]. CECT is also used for assessment of MWA treatment's efficacy [98].

Unfortunately, CECT is time-consuming, ionizing, and expensive. In search for an efficient imaging modality, ultrasound elastography was evaluated.

Elastography was introduced for imaging tissue stiffness by Ophir et al. [99]. An elastographic approach that has been applied for liver imaging, specifically during and after radiofrequency ablation (RFA) or MWA procedures, is electrode displacement elastography (EDE) [57]. It was shown via simulation that using the antenna to induce quasi-static deformations provided a theoretically higher imaged contrast than external compression elastography [69]. Phantom studies confirm the simulation's findings with the CNR, and strain contrast obtained being significantly higher for EDE due to the local nature of the deformation applied [73-75]. To further validate EDE efficacy, *in-vivo* animal models were utilized showing a high correlation between elastographic imaging and pathologic areas of ablated regions [77, 100]. EDE was then performed on human patients scheduled for a percutaneous minimally invasive ablation procedure to further verify its ability to delineate ablated regions. Yang et al. has shown that image contrast, CNR, and delineation are significantly higher for strain tensor images obtained using EDE than B-mode [78] or ARFI [58] imaging. Furthermore, EDE has shown reliability in visualizing ablations following MWA for a range of tumor types and tumor depths [101, 102]. However, EDE imaging may still result in some ablated regions that are difficult to delineate due to decorrelation noise and out of plane motion. The proposed work will further advance EDE image quality to produce comparable imaging results to CECT to assess treatment efficacy. Success rates and visualization of ablations are improved using dictionary represented displacements to reduce decorrelation noise accompanied by Lagrangian tracking to account for extraneous motion that increase ablation size variability in strain tensor images. Utilizing improved image quality, ablations will be automatically segmented using a novel snake initialization approach and compared to registered CECT virtual slices to evaluate the effectiveness of EDE ablation size and location depiction.

For EDE, RF data was collected and imported into MATLAB for processing following the flow-diagram in Figure 1.1. Note in Figure 1.1 that the pre-deformation frames start on frame 0, while the post-deformation frames start on frame 1. This is to point out that the frames used for displacement estimation

are consecutively sampled RF frames. Within MATLAB, displacement estimates were calculated using a Multilevel 2-D Normalized Cross-Correlation (MNCC) method [79] from consecutive RF frames which will be discussed further in Chapter 3.

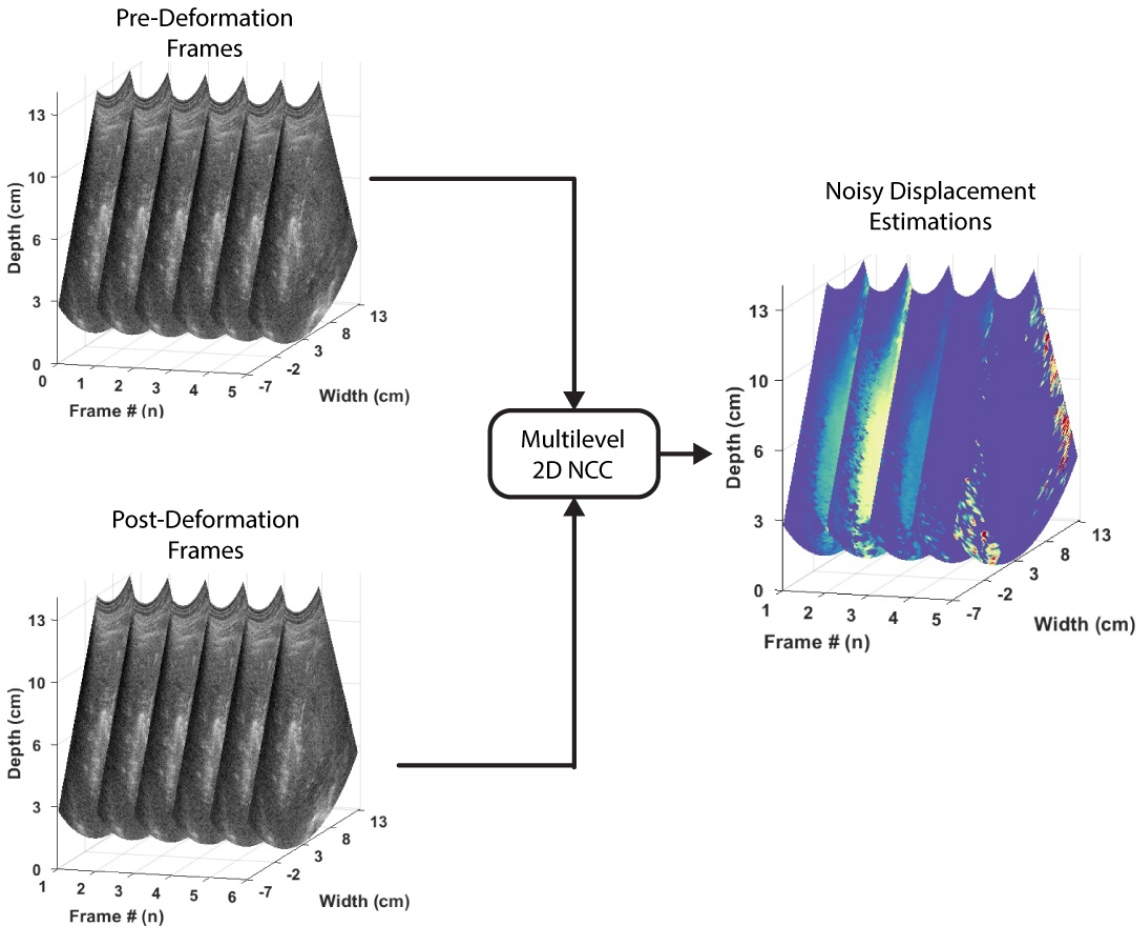

Figure 1.1 - Flowchart describing initial EDE estimation process.

1.3 Scope of this Dissertation

In this dissertation, we will demonstrate improvements in strain image quality for delineating ablated region. Efficacy of EDE for differential imaging of both tumors and ablated regions in human subjects will also be evaluated with a pilot study. Completion of the following Specific Aims formed the basis of the research described in this proposal.

Aim 1: Dictionary learning and representation for enhanced boundary visualization and decorrelation noise reduction of displacement estimations produced with electrode displacement elastography (EDE).

Block-matching based displacement estimation techniques used by EDE are plagued with decorrelation noise and out-of-plane motion. Many approaches have attempted to alleviate this problem via pre-processing [80-83] or regularization approaches [84-89], yet commonly fail to improve ablation boundary visualization. A recent approach regularized cardiac displacement estimation via dictionary representations, showing good denoising results but was limited to a pre-constructed dictionary [90]. We will utilize an adaptively learned global dictionary for representing displacements after the estimation process that can significantly reduce decorrelation noise and increase visualization of masses in corresponding strain tensor images.

Aim 2: Reduction of physiological motion artifacts during electrode displacement elastography using Lagrangian coordinate tracking.

During *in-vivo* EDE data collection, focused displacements are induced to the ablation via clinician perturbations of the microwave antenna, yet other motions may be present due to essential physiological functions. These deformations may result in unintended speckle pattern changes introducing additional displacement estimation variance [91] and inhibiting accurate visualization of the ablation zone degrading ablative margin delineations. We will account for these unintended motions via Lagrangian tracking. When properly tracked, displacements can be accumulated over perturbations to provide consistent strain tensor images and reduce ablation size variance.

Aim 3: Automatic EDE ablation segmentation evaluated against comparable registered CT virtual slices.

Locating the ablation region and segmenting the ablation region is an easy process to perform manually on strain tensor images, yet the process is time-consuming and requires the trained eye of a radiologist for consistent segmentation. We will utilize active contour snakes [92] with the addition of balloon forces [93] and gradient vector flow [94], conforming to strain depiction of ablations including

discontinuous boundaries. In addition, we will utilize random sample consensus [95] (RANSAC) and an ellipsoidal parametric model of ablated masses for snake initialization providing autonomous segmentation. To depict effectiveness of EDE ablation visualization, automatically segmented ablations will be compared to registered CECT virtual slices [96] as a gold-standard of ablation depiction.

Together the aims proposed in this dissertation demonstrate enhanced lesion visualization by increasing boundary delineation and reducing lesion size variability followed by automatic segmentation to provide lesion location and dimensions. These aims show the potential for transforming EDE into and imaging modality for monitoring ablation therapies. EDE imaging performance is compared to the clinical gold standard of CECT. Future computational capability improvements will enable these aims for validating MWA efficacy to be performed in real-time in a clinical setting. These aims incorporate the EDE estimation flow diagram shown in Figure 1.2.

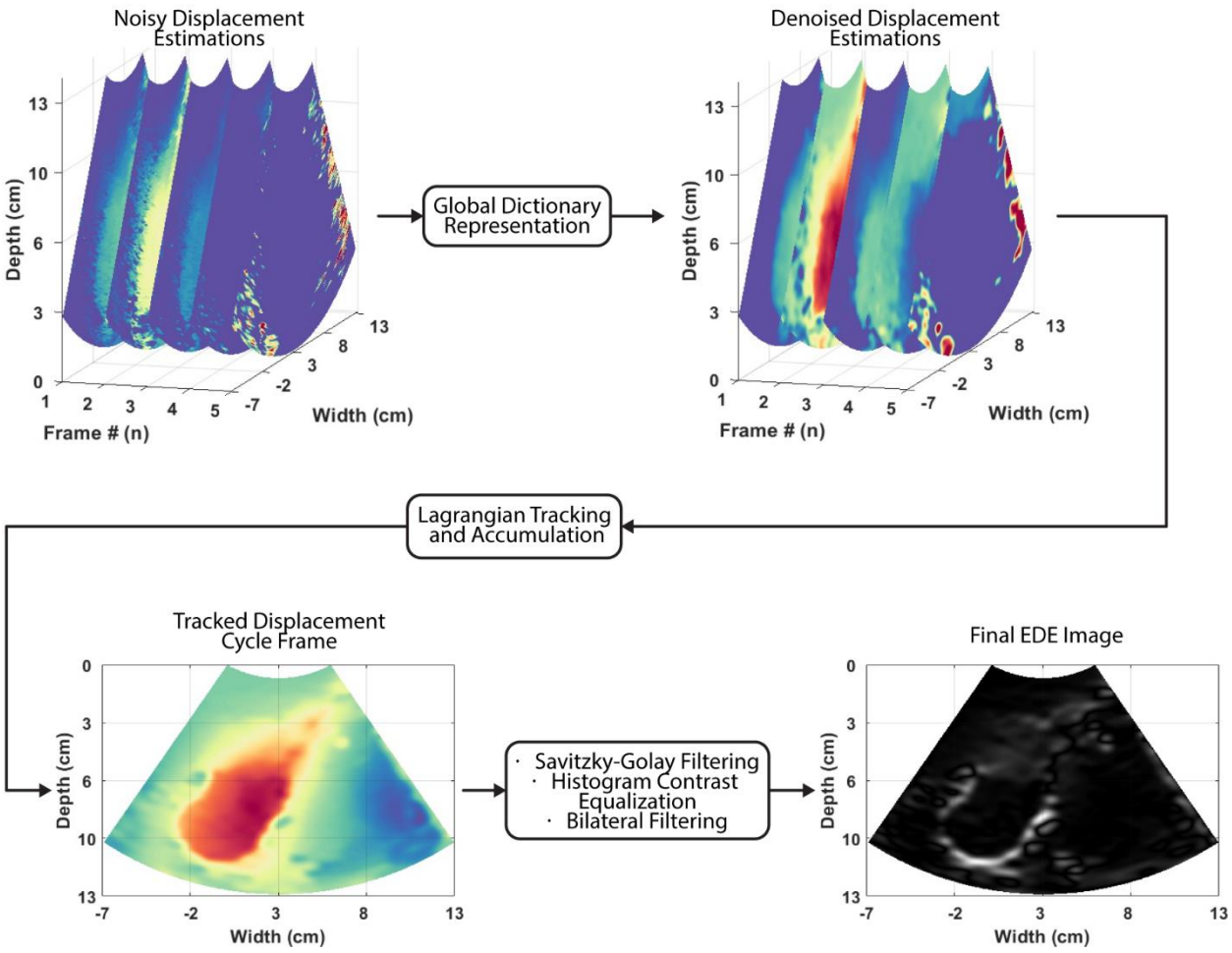

Figure 1.2 – EDE processing for strain images to evaluation pre-ablation tumors and post-ablation regions.

1.4 Summary of Dissertation Chapters

The dissertation to describe the aims described above, is organized as follows.

1.4.1 Chapter 2: Literature Review

This chapter provides an overview of liver cancer burden and various treatment modalities. After treatments are discussed, the importance of medical imaging for microwave liver ablation is presented and the modalities that are commonly used in the clinic are reviewed. Finally, this chapter describes elastographic approaches and how electrode displacement elastography has shown promise for clinical use during MWA.

1.4.2 Chapter 3: Comparison of Displacement Estimation Approaches

Hepatocellular carcinoma and liver metastases are common hepatic malignancies presenting with high mortality rates. Minimally invasive MWA yields high success rates like surgical resection. However, MWA procedures require accurate image guidance during the procedure and for post-procedure assessments. Ultrasound EDE has demonstrated utility for non-ionizing imaging of regions of thermal necrosis created with MWA in the ablation suite. Three strategies for displacement vector tracking and strain tensor estimation, namely Coupled Subsample Displacement Estimation (CSDE), a multilevel 2-D normalized cross-correlation method, and quality-guided displacement tracking (QGDT) have previously shown accurate estimations for EDE. This chapter reports on a qualitative and quantitative comparison of these three algorithms over 79 patients after an MWA procedure.

1.4.3 Chapter 4: Dictionary Learning and Representation for Electrode Displacement Elastography

Block-matching displacement estimation techniques used by EDE are plagued with decorrelation noise and out-of-plane motion. Previous approaches have attempted to alleviate this problem via preprocessing [80-83] or regularization [84-89], yet commonly fail to improve lesion boundary visualization. A recent approach using regularized cardiac displacement estimation via dictionary representations, showing good denoising results but was limited to a pre-constructed dictionary [90]. We utilized an adaptively learned global dictionary for representing displacements after the estimation process that significantly reduces decorrelation noise and increased visualization of masses in strain tensor images.

1.4.4 Chapter 5: Reduction of Physiological Motion Artifacts Using Lagrangian Deformation Tracking

During *in-vivo* EDE data collection, focused displacements are induced to the lesion via freehand clinician perturbations of the microwave antenna, however other motion may be present due to essential physiological functions. These deformations may result in unintended speckle pattern changes introducing additional displacement estimation variance [91], inhibiting accurate visualization of the ablation zone and degrading ablative margin delineations. We will account for these unintended motions via Lagrangian

deformation tracking. When properly tracked, displacements can be accumulated over perturbations to provide consistent strain tensor images and reduce ablation size variance.

1.4.5 Chapter 6: Automatic Segmentation Using Ellipsoid Prior

Locating the ablation region and segmenting the ablation region is an easy process to perform manually on strain images, yet the process is time-consuming and requires the trained eye of a radiologist for consistent segmentation. This chapter presents the utilization of active contour snakes [92] with the addition of balloon forces [93] and gradient vector flow [94], conforming to strain depiction of lesions including discontinuous boundaries. In addition, random sample consensus (RANSAC) and an ellipsoidal parametric model of ablated lesions is utilized for snake initialization providing autonomous segmentation.

1.4.6 Chapter 7: Computed Tomography to Ultrasound Registration

Registration of US and CECT images are essential for quantitative comparison of ablation boundaries and dimensions determined using these modalities. This comparison is essential as stiffness-based imaging using ultrasound has become popular and offers a non-ionizing and cost-effective imaging modality for monitoring minimally invasive ablation procedures. This chapter presents results using a manual image registration method that performs the required CT-US registration.

1.4.7 Chapter 8: Bringing Everything Together: Pre- and Post- Ablation Comparison for Ablative Margin Evaluation

MWA efficacy is correlated with accurate image guidance, specifically validation of appropriate ablative margins. However, conventional methods of B-mode ultrasound and computed tomography (CT) have limitations for accurate visualization. Alternatively, ultrasound elastography has been utilized to demarcate post-ablation zones yet shows some limitations for pre-ablation visualization due to variability in strain contrast between cancer types, requiring more robust elastographic estimation. This chapter utilizes the results from the work in Chapters 3-7 to characterize both pre-ablation tumors and post-ablation zones using electrode displacement elastography for 13 patients with hepatocellular carcinoma or liver metastasis.

1.4.8 Chapter 9: Research Contributions and Future Work

This chapter provides a summary of the research contributions to the field reported in this dissertation and potential avenues for future work.

1.5 References

[1] F. Jacques, S. Isabelle, D. Rajesh, E. Sultan, M. Colin, R. Marise, P. D. Maxwell, F. David, and B. Freddie, "Cancer incidence and mortality worldwide: Sources, methods and major patterns in GLOBOCAN 2012," *International Journal of Cancer*, vol. 136, no. 5, pp. E359-E386, 2015, doi: doi:10.1002/ijc.29210.

[2] M. C. S. Wong, J. Y. Jiang, W. B. Goggins, M. Liang, Y. Fang, F. D. H. Fung, C. Leung, H. H. X. Wang, G. L. H. Wong, V. W. S. Wong, and H. L. Y. Chan, "International incidence and mortality trends of liver cancer: a global profile," *Scientific Reports*, Article vol. 7, p. 45846, 03/31/online 2017, doi: 10.1038/srep45846.

[3] A. C. Society, "Facts & Figures 2018," 2018. [Online]. Available: https://www.cancer.org/cancer/liver-cancer/about/what-is-key-statistics.html.

[4] J. Xu, "Trends in Liver Cancer Mortality Among Adults Aged 25 and Over in the United States, 2000–2016," *NCHS Data Brief, CDC, NCHS*, vol. 314, pp. 1-8, July 2018 2018.

[5] F. Bray, J. Ferlay, I. Soerjomataram, R. L. Siegel, L. A. Torre, and A. Jemal, "Global cancer statistics 2018: GLOBOCAN estimates of incidence and mortality worldwide for 36 cancers in 185 countries," *CA: a cancer journal for clinicians*, vol. 68, no. 6, pp. 394-424, 2018.

[6] M. Mohammadian, K. Allah Bakeshei, and A. Mohammadian-Hafshejani, "International epidemiology of liver cancer: geographical distribution, secular trends and predicting the future," (in eng), *J Prev Med Hyg*, vol. 61, no. 2, pp. E259-e289, Jun 2020, doi: 10.15167/2421-4248/jpmh2020.61.2.1244.

[7] C. Global Burden of Disease Liver Cancer, T. Akinyemiju, S. Abera, M. Ahmed, N. Alam, M. A. Alemayohu, C. Allen, R. Al-Raddadi, N. Alvis-Guzman, Y. Amoako, A. Artaman, T. A. Ayele,

A. Barac, I. Bensenor, A. Berhane, Z. Bhutta, J. Castillo-Rivas, A. Chitheer, J.-Y. Choi, B. Cowie, L. Dandona, R. Dandona, S. Dey, D. Dicker, H. Phuc, D. U. Ekwueme, M. E. S. Zaki, F. Fischer, T. Fürst, J. Hancock, S. I. Hay, P. Hotez, S. H. Jee, A. Kasaeian, Y. Khader, Y.-H. Khang, A. Kumar, M. Kutz, H. Larson, A. Lopez, R. Lunevicius, R. Malekzadeh, C. McAlinden, T. Meier, W. Mendoza, A. Mokdad, M. Moradi-Lakeh, G. Nagel, Q. Nguyen, G. Nguyen, F. Ogbo, G. Patton, D. M. Pereira, F. Pourmalek, M. Qorbani, A. Radfar, G. Roshandel, J. A. Salomon, J. Sanabria, B. Sartorius, M. Satpathy, M. Sawhney, S. Sepanlou, K. Shackelford, H. Shore, J. Sun, D. T. Mengistu, R. Topór-Mądry, B. Tran, K. N. Ukwaja, V. Vlassov, S. E. Vollset, T. Vos, T. Wakayo, E. Weiderpass, A. Werdecker, N. Yonemoto, M. Younis, C. Yu, Z. Zaidi, L. Zhu, C. J. L. Murray, M. Naghavi, and C. Fitzmaurice, "The Burden of Primary Liver Cancer and Underlying Etiologies From 1990 to 2015 at the Global, Regional, and National Level: Results From the Global Burden of Disease Study 2015," (in eng), *JAMA Oncol*, vol. 3, no. 12, pp. 1683-1691, 2017, doi: 10.1001/jamaoncol.2017.3055.

[8] M. Endeshaw, B. D. Hallowell, H. Razzaghi, V. Senkomago, M. T. McKenna, and M. Saraiya, "Trends in liver cancer mortality in the United States: Dual burden among foreign-and US-born persons," *Cancer*, vol. 125, no. 5, pp. 726-734, 2019.

[9] A. M. Noone, N. Howlader, M. Krapcho, D. Miller, A. Brest, M. Yu, J. Ruhl, Z. Tatalovich, A. Mariotto, D. R. Lewis, H. S. Chen, and E. J. Feuer, "SEER Cancer Statistics Review, 1975-2015," National Cancer Institute, Bethesda, MD, September 10, 2018 2018. [Online]. Available: https://seer.cancer.gov/csr/1975_2015/

[10] B. R. Momin, P. S. Pinheiro, H. Carreira, C. Li, and H. K. Weir, "Liver cancer survival in the United States by race and stage (2001-2009): Findings from the CONCORD-2 study," (in eng), *Cancer*, vol. 123 Suppl 24, no. Suppl 24, pp. 5059-5078, 2017, doi: 10.1002/cncr.30820.

[11] A. Marengo, C. Rosso, and E. Bugianesi, "Liver Cancer: Connections with Obesity, Fatty Liver, and Cirrhosis," *Annual Review of Medicine*, vol. 67, no. 1, pp. 103-117, 2016, doi: 10.1146/annurev-med-090514-013832.

[12] R. Sharma, "Descriptive epidemiology of incidence and mortality of primary liver cancer in 185 countries: evidence from GLOBOCAN 2018," (in eng), *Jpn J Clin Oncol,* Jul 28 2020, doi: 10.1093/jjco/hyaa130.

[13] L. Li and H. Wang, "Heterogeneity of liver cancer and personalized therapy," *Cancer letters,* vol. 379, no. 2, pp. 191-197, 2016.

[14] N. N. Massarweh and H. B. El-Serag, "Epidemiology of Hepatocellular Carcinoma and Intrahepatic Cholangiocarcinoma," (in eng), *Cancer Control,* vol. 24, no. 3, p. 1073274817729245, Jul-Sep 2017, doi: 10.1177/1073274817729245.

[15] L.-X. Liu, W.-H. Zhang, and H.-C. Jiang, "Current treatment for liver metastases from colorectal cancer," *World journal of gastroenterology: WJG,* vol. 9, no. 2, p. 193, 2003.

[16] L. S. Poulou, E. Botsa, I. Thanou, P. D. Ziakas, and L. Thanos, "Percutaneous microwave ablation vs radiofrequency ablation in the treatment of hepatocellular carcinoma," *World journal of hepatology,* vol. 7, no. 8, p. 1054, 2015.

[17] J. Bruix and M. Sherman, "Management of hepatocellular carcinoma: an update," *Hepatology,* vol. 53, no. 3, pp. 1020-1022, 2011.

[18] A. J. Bilchik, T. F. Wood, D. Allegra, G. J. Tsioulias, M. Chung, D. M. Rose, K. P. Ramming, and D. L. Morton, "Cryosurgical ablation and radiofrequency ablation for unresectable hepatic malignant neoplasms: a proposed algorithm," *Archives of surgery,* vol. 135, no. 6, pp. 657-664, 2000.

[19] S. Bipat, M. S. van Leeuwen, J. Ijzermans, E. Comans, A. Planting, P. Bossuyt, J.-W. Greve, and J. Stoker, "Evidence-base guideline on management of colorectal liver metastases in the Netherlands," *Neth J Med,* vol. 65, no. 1, pp. 5-14, 2007.

[20] S. Shiina, R. Tateishi, T. Arano, K. Uchino, K. Enooku, H. Nakagawa, Y. Asaoka, T. Sato, R. Masuzaki, Y. Kondo, T. Goto, H. Yoshida, M. Omata, and K. Koike, "Radiofrequency ablation for hepatocellular carcinoma: 10-year outcome and prognostic factors," *Americal Journal of Gastroenterology,* vol. 107, no. 4, pp. 569-77; quiz 578, Apr 2012, doi: 10.1038/ajg.2011.425.

[21] X. Y. Tang, Z. Wang, T. Wang, D. Cui, and B. Zhai, "Efficacy, safety and feasibility of ultrasound-guided percutaneous microwave ablation for large hepatic hemangioma," *Journal of digestive diseases,* vol. 16, no. 9, pp. 525-530, 2015.

[22] Y. R. Huo and G. D. Eslick, "Microwave ablation compared to radiofrequency ablation for hepatic lesions: a meta-analysis," *Journal of Vascular and Interventional Radiology,* vol. 26, no. 8, pp. 1139-1146. e2, 2015.

[23] R. C. Martin, C. R. Scoggins, and K. M. McMasters, "Safety and efficacy of microwave ablation of hepatic tumors: a prospective review of a 5-year experience," *Annals of surgical oncology,* vol. 17, no. 1, pp. 171-178, 2010.

[24] J. Bruix, G. J. Gores, and V. Mazzaferro, "Hepatocellular carcinoma: clinical frontiers and perspectives," *Gut,* vol. 63, no. 5, pp. 844-55, May 2014, doi: 10.1136/gutjnl-2013-306627.

[25] M. Maluccio and A. Covey, "Recent progress in understanding, diagnosing, and treating hepatocellular carcinoma," *A Cancer Journal for Clinicians,* vol. 62, no. 6, pp. 394-9, Nov-Dec 2012, doi: 10.3322/caac.21161.

[26] C. H. Liu, K. R. Avinssh, D. A. Gervais, and D. V. Sahan, "Diagnostic imaging pre- and post-ablation," *Interventional radiological treatment of liver tumors,* A. Adam and P. R. Mueller, Eds., Cambridge ; New York: Cambridge University Press, 2009, pp. 44, 73.

[27] G. Avey, F. T. J. Lee, and J. L. Hinshaw, "Cryotherapy of the liver," *Interventional radiological treatment of liver tumors,* A. Adam and P. R. Mueller, Eds., Cambridge ; New York: Cambridge University Press,, 2009, pp. 181, 202 p.

[28] R. Lencioni and L. Crocetti, "Radiofrequency ablation of liver cancer," *Techniques in Vascular and Interventional Radiology,* vol. 10, no. 1, pp. 38-46, Mar 2007, doi: 10.1053/j.tvir.2007.08.006.

[29] S. Ganguli and S. N. Goldberg, "Radiofrequency equipment and scientific basis for radiofrequency ablation," *Interventional radiological treatment of liver tumors*Cambridge ; New York: Cambridge University Press, 2009, pp. 167, 180.

[30] S. N. Goldberg, G. S. Gazelle, and P. R. Mueller, "Thermal ablation therapy for focal malignancy: a unified approach to underlying principles, techniques, and diagnostic imaging guidance," *American journal of roentgenology,* vol. 174, no. 2, pp. 323-331, 2000.

[31] C. L. Brace, "Microwave tissue ablation: biophysics, technology, and applications," *Critical Reviews™ in Biomedical Engineering,* vol. 38, no. 1, 2010, doi: 10.1615/CritRevBiomedEng.v38.i1.60.

[32] G. D. Dodd III, N. A. Dodd, A. C. Lanctot, and D. A. Glueck, "Effect of variation of portal venous blood flow on radiofrequency and microwave ablations in a blood-perfused bovine liver model," *Radiology,* vol. 267, no. 1, pp. 129-136, 2013.

[33] M. G. Lubner, C. L. Brace, J. L. Hinshaw, and F. T. Lee Jr, "Microwave tumor ablation: mechanism of action, clinical results, and devices," *Journal of Vascular and Interventional Radiology,* vol. 21, no. 8, pp. S192-S203, 2010.

[34] T. J. Vogl, N.-E. A. Nour-Eldin, R. M. Hammerstingl, B. Panahi, and N. N. Naguib, "Microwave ablation (MWA): basics, technique and results in primary and metastatic liver neoplasms–review article," in *RöFo-Fortschritte auf dem Gebiet der Röntgenstrahlen und der bildgebenden Verfahren*, 2017, vol. 189, no. 11: © Georg Thieme Verlag KG, pp. 1055-1066.

[35] M. F. Meloni, J. Chiang, P. F. Laeseke, C. F. Dietrich, A. Sannino, M. Solbiati, E. Nocerino, C. L. Brace, and F. T. Lee Jr, "Microwave ablation in primary and secondary liver tumours: technical and clinical approaches," *International Journal of Hyperthermia,* vol. 33, no. 1, pp. 15-24, 2017.

[36] M. Ahmed, L. Solbiati, C. L. Brace, D. J. Breen, M. R. Callstrom, J. W. Charboneau, M.-H. Chen, B. I. Choi, T. De Baère, and G. D. Dodd III, "Image-guided tumor ablation: standardization of terminology and reporting criteria—a 10-year update," *Radiology,* vol. 273, no. 1, pp. 241-260, 2014.

[37] P. Liang, J. Yu, M.-D. Lu, B.-W. Dong, X.-L. Yu, X.-D. Zhou, B. Hu, M.-X. Xie, W. Cheng, and W. He, "Practice guidelines for ultrasound-guided percutaneous microwave ablation for hepatic malignancy," *World journal of gastroenterology: WJG,* vol. 19, no. 33, p. 5430, 2013.

[38] A. Gillams, N. Goldberg, M. Ahmed, R. Bale, D. Breen, M. Callstrom, M. H. Chen, B. I. Choi, T. de Baere, and D. Dupuy, "Thermal ablation of colorectal liver metastases: a position paper by an international panel of ablation experts, The Interventional Oncology Sans Frontières meeting 2013," *European radiology,* vol. 25, no. 12, pp. 3438-3454, 2015.

[39] D. Palmer and P. Johnson, "The clinical management of hepatic neoplasms," *Interventional radiological treatment of liver tumors*, A. Adam and P. R. Mueller, Eds., Cambridge ; New York: Cambridge University Press,, 2009, pp. 1, 24.

[40] A.-X. Sun, Z.-L. Cheng, P.-P. Wu, Y.-H. Sheng, X.-J. Qu, W. Lu, C.-G. Zhao, and G.-J. Qian, "Clinical outcome of medium-sized hepatocellular carcinoma treated with microwave ablation," *World Journal of Gastroenterology: WJG,* vol. 21, no. 10, p. 2997, 2015.

[41] N. Zhang, W. Lu, X. Cheng, J. Liu, Y. Zhou, and F. Li, "High-powered microwave ablation of larger hepatocellular carcinoma: evaluation of recurrence rate and factors related to recurrence," *Clinical radiology,* vol. 70, no. 11, pp. 1237-1243, 2015.

[42] N. C. Yu, D. S. Lu, S. S. Raman, D. E. Dupuy, C. J. Simon, C. Lassman, B. I. Aswad, D. Ianniti, and R. W. Busuttil, "Hepatocellular carcinoma: microwave ablation with multiple straight and loop antenna clusters—pilot comparison with pathologic findings," *Radiology,* vol. 239, no. 1, pp. 269-275, 2006.

[43] H. W. Huang, "Influence of blood vessel on the thermal lesion formation during radiofrequency ablation for liver tumors," *Medical physics,* vol. 40, no. 7, p. 073303, 2013.

[44] J. Schaible, B. Pregler, W. Bäumler, I. Einspieler, E.-M. Jung, C. Stroszczynski, and L. P. Beyer, "Safety margin assessment after microwave ablation of liver tumors: inter- and intrareader variability," (in eng), *Radiol Oncol,* vol. 54, no. 1, pp. 57-61, 2020, doi: 10.2478/raon-2020-0004.

[45] S. B. Solomon and S. G. Silverman, "Imaging in interventional oncology," *Radiology,* vol. 257, no. 3, pp. 624-640, 2010.

[46] X. Wang, C. T. Sofocleous, J. P. Erinjeri, E. N. Petre, M. Gonen, K. G. Do, K. T. Brown, A. M. Covey, L. A. Brody, and W. Alago, "Margin size is an independent predictor of local tumor

progression after ablation of colon cancer liver metastases," *Cardiovascular and interventional radiology,* vol. 36, no. 1, pp. 166-175, 2013.

[47] M. J. Stone and B. J. Wood, "Emerging local ablation techniques," in *Seminars in interventional radiology,* 2006, vol. 23, no. 01: Published 2006 by Thieme Medical Publishers, Inc., 333 Seventh Avenue, New …, pp. 085-098.

[48] N. I. Sainani, D. A. Gervais, P. R. Mueller, and R. S. Arellano, "Imaging after percutaneous radiofrequency ablation of hepatic tumors: Part 1, Normal findings," *American Journal of Roentgenology,* vol. 200, no. 1, pp. 184-193, 2013.

[49] A. A. van Tilborg, H. J. Scheffer, K. Nielsen, J. H. T. van Waesberghe, E. F. Comans, C. Van Kuijk, P. M. van den Tol, and M. R. Meijerink, "Transcatheter CT arterial portography and CT hepatic arteriography for liver tumor visualization during percutaneous ablation," *Journal of Vascular and Interventional Radiology,* vol. 25, no. 7, pp. 1101-1111. e4, 2014.

[50] B. K. Park, P. R. Morrison, S. Tatli, U. Govindarajulu, K. Tuncali, P. Judy, P. B. Shyn, and S. G. Silverman, "Estimated effective dose of CT-guided percutaneous cryoablation of liver tumors," *European Journal of Radiology,* vol. 81, no. 8, pp. 1702-1706, 2012, doi: 10.1016/j.ejrad.2011.04.067.

[51] H. Takaki, K. Yamakado, A. Nakatsuka, T. Yamada, J. Uraki, M. Kashima, T. Yamanaka, K. Shiraki, Y. Takei, and K. Takeda, "Computed tomography fluoroscopy-guided radiofrequency ablation following intra-arterial iodized-oil injection for hepatocellular carcinomas invisible on ultrasonographic images," *International journal of clinical oncology,* vol. 18, no. 1, pp. 46-53, 2013.

[52] N. H. Asvadi, A. Anvari, R. N. Uppot, A. Thabet, A. X. Zhu, and R. S. Arellano, "CT-guided percutaneous microwave ablation of tumors in the hepatic dome: assessment of efficacy and safety," *Journal of Vascular and Interventional Radiology,* vol. 27, no. 4, pp. 496-502, 2016.

[53] M. W. Lee, Y. J. Kim, H. S. Park, N. C. Yu, S. I. Jung, S. Y. Ko, and H. J. Jeon, "Targeted sonography for small hepatocellular carcinoma discovered by CT or MRI: factors affecting

sonographic detection," *American Journal of Roentgenology,* vol. 194, no. 5, pp. W396-W400, 2010.

[54] T. K. Kim, K. Khalili, and H.-J. Jang, "Local ablation therapy with contrast-enhanced ultrasonography for hepatocellular carcinoma: a practical review," *Ultrasonography,* vol. 34, no. 4, p. 235, 2015.

[55] A. Hakime, S. Yevich, L. Tselikas, F. Deschamps, D. Petrover, and T. De Baere, "Percutaneous thermal ablation with ultrasound guidance. Fusion imaging guidance to improve conspicuity of liver metastasis," *Cardiovascular and interventional radiology,* vol. 40, no. 5, pp. 721-727, 2017.

[56] R. Hoffmann, H. Rempp, D.-E. Keßler, J. Weiß, P. L. Pereira, K. Nikolaou, and S. Clasen, "MR-guided microwave ablation in hepatic tumours: initial results in clinical routine," *European radiology,* vol. 27, no. 4, pp. 1467-1476, 2017.

[57] T. Varghese, J. A. Zagzebski, and F. T. Lee, "Elastographic imaging of thermal lesions in the liver in vivo following radiofrequency ablation: preliminary results," *Ultrasound in Medicine & Biology,* vol. 28, no. 11-12, pp. 1467-1473, 2002/11 2002, doi: 10.1016/s0301-5629(02)00656-7.

[58] W. Yang, T. Varghese, T. Ziemlewicz, M. Alexander, M. Lubner, J. L. Hinshaw, S. Wells, and F. T. Lee, Jr., "Delineation of Post-Procedure Ablation Regions with Electrode Displacement Elastography with a Comparison to Acoustic Radiation Force Impulse Imaging," *Ultrasound in Medicine and Biology,* vol. 43, no. 9, pp. 1953-1962, Sep 2017, doi: 10.1016/j.ultrasmedbio.2017.04.021.

[59] T. Varghese, "Quasi-Static Ultrasound Elastography," *Ultrasound Clin,* vol. 4, no. 3, pp. 323-338, Jul 2009, doi: 10.1016/j.cult.2009.10.009.

[60] M. Z. Kiss, M. J. Daniels, and T. Varghese, "Investigation of temperature-dependent viscoelastic properties of thermal lesions in ex vivo animal liver tissue," (in eng), *Journal of biomechanics,* vol. 42, no. 8, pp. 959-966, 2009, doi: 10.1016/j.jbiomech.2009.03.002.

[61] S. Gordic, J. B. Ayache, P. Kennedy, C. Besa, M. Wagner, O. Bane, R. L. Ehman, E. Kim, and B. Taouli, "Value of tumor stiffness measured with MR elastography for assessment of response of hepatocellular carcinoma to locoregional therapy," *Abdominal Radiology,* vol. 42, no. 6, pp. 1685-1694, 2017.

[62] T. Varghese, U. Techavipoo, J. A. Zagzebski, and F. T. Lee Jr, "Impact of Gas Bubbles Generated During Interstitial Ablation on Elastographic Depiction of In Vitro Thermal Lesions," *Journal of Ultrasound in Medicine,* vol. 23, no. 4, pp. 535-544, 2004, doi: doi:10.7863/jum.2004.23.4.535.

[63] R. J. Dewall, T. Varghese, and C. L. Brace, "Visualizing ex vivo radiofrequency and microwave ablation zones using electrode vibration elastography," *Med Phys,* vol. 39, no. 11, pp. 6692-700, Nov 2012, doi: 10.1118/1.4758061.

[64] J. B. Welch, R. Shukla, N. Igbo, A. K. Singal, J. Kazan-Tannus, and R. D. Soloway, "Use of ultrasound as the initial screening exam for hepatocellular carcinoma in high risk populations," *Open Journal of Gastroenterology,* vol. 3, no. 2, pp. 148-154, 2013, doi: 10.4236/ojgas.2013.32025.

[65] B. J. Fahey, R. C. Nelson, S. J. Hsu, D. P. Bradway, D. M. Dumont, and G. E. Trahey, "In vivo guidance and assessment of liver radio-frequency ablation with acoustic radiation force elastography," *Ultrasound in Medicine and Biology,* vol. 34, no. 10, pp. 1590-603, Oct 2008, doi: 10.1016/j.ultrasmedbio.2008.03.006.

[66] R. Righetti, F. Kallel, R. J. Stafford, R. E. Price, T. A. Krouskop, J. D. Hazle, and J. Ophir, "Elastographic characterization of HIFU-induced lesions in canine livers," *Ultrasound in Medicine and Biology,* vol. 25, no. 7, pp. 1099-113, Sep 1999. [Online]. Available: https://www.ncbi.nlm.nih.gov/pubmed/10574342.

[67] O. Kolokythas, T. Gauthier, A. T. Fernandez, H. Xie, B. A. Timm, C. Cuevas, M. K. Dighe, L. M. Mitsumori, M. F. Bruce, D. A. Herzka, G. K. Goswami, R. T. Andrews, K. M. Oas, T. J. Dubinsky, and B. H. Warren, "Ultrasound-based elastography: a novel approach to assess radio frequency ablation of liver masses performed with expandable ablation probes: a feasibility

study," *Journal of Ultrasound in Medicine,* vol. 27, no. 6, pp. 935-46, Jun 2008. [Online]. Available: https://www.ncbi.nlm.nih.gov/pubmed/18499853.

[68] T. J. Hall, Y. Zhu, and C. S. Spalding, "In vivo real-time freehand palpation imaging," *Ultrasound in Medicine and Biology,* vol. 29, no. 3, pp. 427-35, Mar 2003. [Online]. Available: https://www.ncbi.nlm.nih.gov/pubmed/12706194.

[69] S. Bharat and T. Varghese, "Contrast-transfer improvement for electrode displacement elastography," *Physics in Medicine & Biology,* vol. 51, no. 24, pp. 6403-18, Dec 21 2006, doi: 10.1088/0031-9155/51/24/008.

[70] M. Pernot, M. Couade, P. Mateo, B. Crozatier, R. Fischmeister, and M. Tanter, "Real-time assessment of myocardial contractility using shear wave imaging," *Journal of the American College of Cardiology*, vol. 58, no. 1, pp. 65-72, Jun 28 2011, doi: 10.1016/j.jacc.2011.02.042.

[71] P. J. Hollender, S. J. Rosenzweig, K. R. Nightingale, and G. E. Trahey, "Single- and multiple-track-location shear wave and acoustic radiation force impulse imaging: matched comparison of contrast, contrast-to-noise ratio and resolution," *Ultrasound Med Biol*, vol. 41, no. 4, pp. 1043-57, Apr 2015, doi: 10.1016/j.ultrasmedbio.2014.11.006.

[72] H. Rivaz, I. Fleming, L. Assumpcao, G. Fichtinger, U. M. Hamper, M. A. Choti, G. Hager, and E. Boctor, "Ablation monitoring with elastography: 2D in-vivo and 3D ex-vivo studies," *Med Image Comput Assist Interv,* vol. 11, no. 2, pp. 458-66, 2008.

[73] S. Bharat, T. Varghese, E. L. Madsen, and J. A. Zagzebski, "Radio-frequency ablation electrode displacement elastography: a phantom study," *Medical Physics,* vol. 35, no. 6, pp. 2432-42, Jun 2008, doi: 10.1118/1.2919763.

[74] S. Bharat and T. Varghese, "Radiofrequency electrode vibration-induced shear wave imaging for tissue modulus estimation: a simulation study," *Journal of the Acoustical Society of America,* vol. 128, no. 4, pp. 1582-5, Oct 2010, doi: 10.1121/1.3466880.

[75] J. Jiang, T. Varghese, Q. Chen, T. J. Hall, and J. A. Zagzebski, "Finite element analysis of tissue deformation with a radiofrequency ablation electrode for strain imaging," *IEEE Transactions on*

Ultrasonics, Ferroelectronics, and Frequency Control, vol. 54, no. 2, pp. 281-9, Feb 2007. [Online]. Available: https://www.ncbi.nlm.nih.gov/pubmed/17328325.

[76] N. Rubert, S. Bharat, R. J. DeWall, A. Andreano, C. Brace, J. Jiang, L. Sampson, and T. Varghese, "Electrode displacement strain imaging of thermally-ablated liver tissue in anin vivoanimal model," *Medical Physics*, vol. 37, no. 3, pp. 1075-1082, 2010, doi: 10.1118/1.3301603.

[77] A. T. Fernandez, O. Kolokythas, T. Gauthier, D. A. Herzka, A. V. Patil, and H. Xie, "Comparison of ultrasound strain images with multi-modality imaging techniques in liver RF ablation assessment: Initial ex vivo and clinical results," *Ultrasonics Symposium, 2008.*, pp. 313-316, 2008, doi: 10.1109/ULTSYM.2008.0077.

[78] W. Yang, T. J. Ziemlewicz, T. Varghese, M. L. Alexander, N. Rubert, A. N. Ingle, M. G. Lubner, J. L. Hinshaw, S. A. Wells, F. T. Lee, and J. A. Zagzebski, "Post-Procedure Evaluation of Microwave Ablations of Hepatocellular Carcinomas Using Electrode Displacement Elastography," *Ultrasound in Medicine & Biology*, vol. 42, no. 12, pp. 2893-2902, 2016, doi: 10.1016/j.ultrasmedbio.2016.07.015.

[79] H. Shi and T. Varghese, "Two-dimensional multi-level strain estimation for discontinuous tissue," *Physics in Medicine & Biology*, vol. 52, no. 2, pp. 389-401, Jan 21 2007, doi: 10.1088/0031-9155/52/2/006.

[80] P. Chaturvedi, M. F. Insana, and T. J. Hall, "2-D companding for noise reduction in strain imaging," *IEEE Transactions on Ultrasonics, Ferroelectrics, and Frequency Control*, vol. 45, no. 1, pp. 179-191, 1998, doi: 10.1109/58.646923.

[81] T. Varghese and J. Ophir, "Enhancement of echo-signal correlation in elastography using temporal stretching," *IEEE Transactions on Ultrasonics, Ferroelectrics, and Frequency Control*, vol. 44, no. 1, pp. 173-180, 1997, doi: 10.1109/58.585213.

[82] B. Jing, D. Chuxiong, L. Jianwen, and H. Ping, "Estimation and reduction of decorrelation effect due to tissue lateral displacement in elastography," *IEEE Transactions on Ultrasonics,*

Ferroelectrics, and Frequency Control, vol. 49, no. 5, pp. 541-549, 2002, doi: 10.1109/TUFFC.2002.1002452.

[83] S. K. Alam, J. Ophir, and E. E. Konofagou, "An adaptive strain estimator for elastography," *IEEE Transactions on Ultrasonics, Ferroelectrics, and Frequency Control,* vol. 45, no. 2, pp. 461-472, 1998, doi: 10.1109/58.660156.

[84] P. M. Hayton, M. Brady, S. M. Smith, and N. Moore, "A non-rigid registration algorithm for dynamic breast MR images," *Artificial Intelligence,* vol. 114, no. 1-2, pp. 125-156, 1999.

[85] H. Rivaz, E. Boctor, P. Foroughi, R. Zellars, G. Fichtinger, and G. Hager, "Ultrasound elastography: a dynamic programming approach," *IEEE transactions on medical imaging,* vol. 27, no. 10, pp. 1373-1377, 2008.

[86] C. Pellot-Barakat, F. Frouin, M. F. Insana, and A. Herment, "Ultrasound elastography based on multiscale estimations of regularized displacement fields," *IEEE transactions on medical imaging,* vol. 23, no. 2, pp. 153-163, 2004.

[87] E. Brusseau, J. Kybic, J.-F. Déprez, and O. Basset, "2-D locally regularized tissue strain estimation from radio-frequency ultrasound images: Theoretical developments and results on experimental data," *IEEE Transactions on Medical Imaging,* vol. 27, no. 2, pp. 145-160, 2008.

[88] N. H. Meshram and T. Varghese, "Fast multilevel Lagrangian carotid strain imaging with GPU computing," *Ultrasonics Symposium (IUS), 2017 IEEE International,* pp. 1-4, 2017.

[89] J. Jiang and T. Hall, "A Coupled Subsample Displacement Estimation Method for Ultrasound-based Strain Elastography," *Physics in Medicine & Biology,* vol. 60, pp. 8347-8364, 2015.

[90] N. Ouzir, A. Basarab, H. Liebgott, B. Harbaoui, and J.-Y. Tourneret, "Motion estimation in echocardiography using sparse representation and dictionary learning," *IEEE Transactions on Image Processing,* vol. 27, no. 1, pp. 64-77, 2018.

[91] R. L. Maurice and M. Bertrand, "Lagrangian speckle model and tissue-motion estimation-theory [ultrasonography]," *IEEE transactions on medical imaging,* vol. 18, no. 7, pp. 593-603, 1999.

[92] M. Kass, A. Witkin, and D. Terzopoulos, "Snakes: Active contour models," *International journal of computer vision,* vol. 1, no. 4, pp. 321-331, 1988.

[93] L. D. Cohen, "On active contour models and balloons," *CVGIP: Image understanding,* vol. 53, no. 2, pp. 211-218, 1991.

[94] C. Xu and J. L. Prince, "Gradient vector flow: A new external force for snakes," in *Computer Vision and Pattern Recognition, 1997. Proceedings., 1997 IEEE Computer Society Conference on*, 1997: IEEE, pp. 66-71.

[95] M. A. Fischler and R. C. Bolles, "Random sample consensus: a paradigm for model fitting with applications to image analysis and automated cartography," *Communications of the ACM,* vol. 24, no. 6, pp. 381-395, 1981.

[96] R. M. Pohlman, M. R. Turney, P. H. Wu, C. L. Brace, T. J. Ziemlewicz, and T. Varghese, "2D US-CT Image Registration for Monitoring Percutaneous Hepatic Intervention (under review)," *Medical Physics,* 2019.

[97] D. Palmer and P. Johnson, "The clinical management of hepatic neoplasms," *Interventional radiological treatment of liver tumors,* A. Adam and P. R. Mueller, Eds., Cambridge ; New York: Cambridge University Press,, 2009, pp. 1-24.

[98] R. Lencioni, L. Crocetti, E. Bozzi, and D. Cioni, "Image-guided radiofrequency ablation: techniques and results," *Interventional radiological treatment of liver tumors,* A. Adam and P. R. Mueller, Eds., Cambridge ; New York: Cambridge University Press,, 2009, pp. 148-166.

[99] J. Ophir, I. Cespedes, H. Ponnekanti, Y. Yazdi, and X. Li, "Elastography: A Quantitative Method for Imaging the Elasticity of Biological Tissues," *Ultrasonic Imaging,* vol. 13, no. 2, pp. 111-134, 1991, doi: 10.1177/016173469101300201.

[100] N. Rubert, S. Bharat, R. J. DeWall, A. Andreano, C. Brace, J. Jiang, L. Sampson, and T. Varghese, "Electrode displacement strain imaging of thermally-ablated liver tissue in an *in vivo* animal model," *Medical Physics,* vol. 37, no. 3, pp. 1075-1082, 2010, doi: 10.1118/1.3301603.

[101] R. M. Pohlman, T. Varghese, J. Jiang, T. J. Ziemlewicz, M. L. Alexander, K. L. Wergin, J. L. Hinshaw, M. G. Lubner, S. A. Wells, and F. T. Lee, Jr., "Comparison of Displacement Tracking Algorithms for *in Vivo* Electrode Displacement Elastography," *Ultrasound in Medicine and Biology,* vol. 45, no. 1, pp. 218-232, 2019, doi: 10.1016/j.ultrasmedbio.2018.09.001.

[102] R. M. Pohlman, J. Jiang, W. Yang, T. J. Ziemlewicz, M. L. Alexander, K. L. Wergin, M. G. Lubner, J. L. Hinshaw, F. T. Lee, and T. Varghese, "Comparison study of displacement estimation methods for microwave ablation procedures using electrode displacement elastography," *Ultrasonics Symposium (IUS), 2017 IEEE International,* pp. 1-4, 2017.

Chapter 2: Literature Review

2.1 Liver Cancer Burden

As of 2018, liver cancer is the third leading cause of cancer related deaths worldwide and the seventh most common in incidences [1-3]. In 2015, the Global Cancer Observatory (GLOBOCAN) reported 854,000 cases of liver cancer with 810,000 deaths globally, a third of which was caused by the hepatitis B virus (HBV), a third from alcohol use, and the remainder a combination of hepatitis C virus and other factors [4]. In just the United States (US), liver cancer mortality significantly increased from 2005 – 2014 with the burden of liver cancer nearly doubling since the mid-1980s [5]. Noone et al. predicted in 2018 that at least 1% of the US population would be diagnosed with a form of primary liver cancer [6]. Additionally, the Center for Disease Control (CDC) reported that during the years 2004-2009 only roughly one fourth of liver cancer patients survived even when the cancer had not spread outside the liver [7]. Not only is primary liver cancer caused by viral- and alcohol-related reasons, but it is now shown that factors such as obesity, type 2 diabetes, aflatoxin exposure and nonalcoholic fatty liver disease (NAFLD) are significant contributors to liver cancer, specifically hepatocellular carcinoma (HCC), [8, 9]. Due to these contributing factors being widespread in the population and the heterogeneity of liver cancers, regimented surveillance and subsequent treatment are difficult to perform before advanced cancer progression occurs [10, 11].

2.2 Liver Cancer: Prevalence, Treatment, and Monitoring

Primary liver cancer, i.e., hepatocellular carcinoma, accounts for 75% of new liver tumor diagnosis and remains one of the more difficult cancers to treat with only 20% of patients having a 5-year survival outcome after their initial diagnosis, despite recent advances in treatment approaches [12, 13]. Notably, the earlier liver cancer is detected for respective treatment, the higher the survival rate [14]. Recently, surgical treatments have improved the short-term survival of HCC, but disease recurrence remains a problem for long-term survival of patients [15]. The best options for liver cancer treatment are either surgical resection

[16, 17] or liver transplantation [18, 19] as the best outlook is seen when all cancer is removed from the liver [20], however other options such as chemotherapies [16, 21] and more recently minimally invasive percutaneous treatments [22-26] have been growing as alternative treatment methods [27].

2.2.1 Liver Transplantation

Complete liver transplantation is the most effective method to treat liver cancer and chronic liver disease where HCC typically develop [28]. Patients who have received a liver transplant have shown 5 year survival rates at 72 percent [29]. Unfortunately, liver transplants are hindered largely by the limited number of donors to supply livers for transplantation [30]. For example, in America and Europe the number of patients waiting for liver transplants are dwarfed by the number of performed procedures per year such that less than a third of patients on waiting lists receive a transplant [31]. Therefore, many patients leave waiting lists due to cancer progression thereby weakening the intent to treat via transplantation [32, 33]. As a result, procedures such as surgical resection, transarterial radiation, transarterial embolization, and ablation attempt to slow the progression of liver cancers [12, 16].

2.2.2 Surgical Resection

Over the last decade excluding liver transplantation, resection has been deemed the most effective treatment for early HCC and is the treatment of choice. [16] Liver resection is the standard choice for HCC that develops in a normal liver for patients that qualify for resection, however less than 25% of patients with HCC or colorectal liver metastases can undergo resection [34]. One of the most important factors to ensure safe liver resection is tumor progression and liver function [35], resulting in many resections occurring in regions where hepatitis B is the dominant risk factor for the liver cancer [28]. After surgical liver resection, the recurrence rate is about 50% after 2 years and 75% at 5 years [30]. Recently surgical resection and ablation have shown similar survival outcomes in the range of 60-70% for 5 years for early stages of HCC, single tumor less than 2cm [16]. Improved surgical outcomes in liver resection may also be found using laparoscopic liver resection [36] or specialized post-operative care [37]. Despite high treatment

success using surgical resection, only 9-27% of these patients meet the criteria for surgical liver resection [38, 39].

2.2.3 Chemotherapy

Chemotherapies are also a means of controlling HCC and liver metastasis, especially in conjunction with other surgical methods for pre- [40] and post-operative therapy [41]. The two main methods for chemotherapy are transarterial radioembolization (TARE) and transarterial chemoablation (TACE). TARE is typically well tolerated and provides local radiation treatment, while TACE combines arterial obstruction with chemotherapy [16]. TACE may be more commonly used on patients for whom most of the liver function is still intact and no signs of extrahepatic spread are evident [21]. Unfortunately, chemotherapies may be a high risk factor for patient comorbidities and poor liver function [42, 43] and may result in unforeseen adverse effects when combined [44].

2.2.4 Image Guided Ablation Procedures

Unfortunately, many of the liver cancers treatments proposed above are difficult due to the high risk of morbidity and mortality. Image guided ablations are percutaneous treatments performed under guidance of fluoroscopy, ultrasound, CT, or MRI. These treatments include direct injection of alcohol, temperature manipulations in the form of radiofrequency ablation, microwave ablation, laser ablation, high intensity focused ultrasound (HIFU), and cryoablation, and finally non-thermal energies [45, 46]. Image guided ablations provide a less invasive treatment method than surgical methods, and although surgical resection is the preferred treatment method for liver cancers, ablation is the best suited treatment for patients unable to have surgery due to other comorbidities [47], early stage HCC [48], and those on liver transplant waitlists [21, 49] as they results in less damage to surrounding structures [50, 51]. Ablative procedures result in fewer complications [34], and require accurate pretreatment imaging to detect lesions, their size and location with respect to the surrounding structures. [48]

2.2.4.1 Percutaneous Ethanol Injection

One method for local treatment of HCC is percutaneous ethanol injection (PEI). Ethanol injection functions by inducing dehydration of cells leading to tissue coagulation and finally fibrinous scarring of cancerous cells with clotting of local circulation surrounding the tumor [22, 45, 52]. Ethanol injection has less local control effectiveness than that of thermal ablation but works well when the location of the tumor implies risk of adverse effects [16, 53]. Although PEI has low overall cost and can be performed with only local anesthesia [54], thermal ablations have shown increased survival rates [55].

2.2.4.3 Irreversible Electroporation

Another image guided treatment is irreversible Electroporation (IRE), a nonthermal ablative technique that delivers short electrical pulses between electrodes which creates pores in cell membranes leading to cell necrosis [56]. Although IRE has advantages in theory over thermal ablation methods, it lacks a rigorous comparison to thermal ablation efficacy [27]. Following this, IRE also requires very precise placement, use of more electrodes, and carries risks of cardiac dysrhythmia and muscle spasms to patients [57] hence is not widely used for liver cancer treatments.

2.2.4.2 Cryoablation

Although non-thermal ablation methods are successful treatments for cancerous liver lesions, thermal ablation is the preferred method of treatment for patients where surgical resection is not feasible and tumors less than 2cm where transplantation is not possible [45, 58]. One method for thermal ablation, less commonly used currently, is cryoablation (CA) [59]. CA operates by the Joule-Thomson effect to create freezing temperatures, creating ice formation to cause cell death [60, 61]. For this to be successful, a 1 cm ablative margin 360 degrees surrounding the cancerous tissue should be completely destroyed [62]. One benefit of CA is that it can treat large tumors as multiple probes may be simultaneously used, and shows very similar results to that of other ablation treatments [63]. Unfortunately, cryoablation requires accurate

imaging is required to verify accurate probe placement and has shown limitations in use due to adverse effects such as liver abscess formation, cryoshock, and hemorrhage [59, 62, 64].

2.2.4.3 Radiofrequency Ablation (RFA)

RFA was the most used thermal ablation treatment using elevated temperatures until the more widespread use of Microwave ablation (MWA). A main advantage of RFA as compared to surgical resection is the potential for minimal normal tissue loss and a comparable success rate for tumors less than 3 cm [46] as well as a more cost-effective treatment for early HCC [16]. RFA outcomes for hepatic tumors has improved significantly, achieving necrosis without adverse liver function. RFA is accepted as the best therapeutic choice for non-surgical patients with early-stage HCC and RFA was once established as the primary ablative modality prior to the advent of MWA. [65] Radiofrequency ablation has shown survival rates up to 10 years after HCC treatment, showing RFA is a good first-line treatment for patients with early-stage HCC. [66] For RFA, the entire tumor along with an appropriate ablative margin must reach cytotoxic temperatures in order for adequate eradication of the entire tumor. [46]

The two main goals of RFA are to completely eradicate all viable malignant cells within the targeted region, by attempting to include a 1.0 cm margin of normal tissue around the tumor, and to maintain specificity and accuracy of the therapy. Maintaining an adequate tumor ablation margin lends to the best success rates. [46, 50, 65] RFA utilizes thermal injury to tissue through electromagnetic energy deposited on the tumor tissue. [48, 65] The thermal damage that is done by RFA is dependent on tissue temperature and the duration of heating [65].

Incomplete treatment and tumor recurrence post RFA are still clinical challenges. Residual tumor progression needs to be found at an early stage so therapy can be reperformed [34]. A main downfall of RFA is the inability to eradicate larger tumors and a nonuniform temperature distribution in the ablated region. Target tumor should not be larger than 3-4 cm in its largest axis to ensure that complete ablation can be performed [65]. For tumors between 3cm and 5cm RFA has shown a decrease in success rate, so treatments are often combined with TACE [21]. Current RFA equipment does not provide sufficient

ablation volume to treat tumors larger than 5cm. [21] The only method using RFA for tumors larger than 5 cm is to used overlapping regions which may offer full eradication. [50]

2.2.4.4 Microwave Ablation (MWA)

A similar technique to radiofrequency ablation is that of microwave ablation (MWA) as a procedure growing in popularity as it offers treatment similar in success rates as surgical resection with lower mortality and morbidity [67-70]. Microwave ablation works by using microwave energy to agitate water molecules. This agitation then produces friction and heat thereby causing cell necrosis [21]. Percutaneous microwave coagulation therapy can be used for treatment of neoplasms with results shown using MWA as a method for treating hepatocellular carcinoma, metastatic masses, and adenomas [71-73].

Microwave ablation is shown to produce much larger ablation regions than RFA with similar or improved effects in terms of complete ablation and local tumor progression [74]. Microwave energy has many advantages over other ablation technologies, including larger ablation volumes, faster ablation times, less susceptible to tissue heat sinks, does not require as high cooling needs, use of grounding pads. In addition, due to the manner MWA works, multiple antennae can be used at the same time allowing for larger tumor treatment than with a single RF electrode [21, 69, 75]. These larger, more uniform, and consistent ablation zones were shown to be produced by using up to 3 microwave antennae simultaneously by utilizing constructive interference. The areas of treatment increased by much as 10% when using microwave antenna simultaneously as opposed to sequentially, which is a clear benefit to RFA [76]. By using multiple antennas, the treatment location can be maximized to ensure adequate safety margins [58, 76]. Improved survival rates and lower rates of local tumor progression is due to the MWA's faster heat generation that can overcome vascular perfusion better than RFA [77]. Some problems with using microwave energy are that it is more difficult to generate and deliver to the antenna than RFA. This leads to lower power delivery, shaft heating, and large diameter antenna to accommodate coaxial lines [75].

Many comprehensive studies have shown these positives of using MWA over RFA in a clinical setting. [78-80] A further study showed an effectiveness rate of 91.6% for 107 patients from successful

single session treatments from a multiantenna, high-power, and gas-cooled microwave devices. This was followed with a 76% survival rate at the 14-month follow up appointment [81]. Ablative therapies appear to be as effective as surgery in appropriate cases, especially for HCC less than 3 cm [16, 30].

Due to the growing popularity and utility of MWA at University of Wisconsin Hospitals and Clinics, this dissertation focuses on liver cancer treatment using MWA. As such, one of the primary factors in MWA success is verification of ablative margins, hence accurate and consistent imaging is required to ensure proper procedure execution [24, 76, 82]. In the case of MWA, this is specifically aimed towards proper placement of ablation antennae as well as verification of 0.5 – 1.0 cm margin of normal tissue necrosis surrounding tumor cells to minimize any residual tumor progression [17, 76, 83].

2.3 Clinical Imaging Modalities for Monitoring Liver Cancer Ablation

To achieve proper treatment using MWA, correct energy delivery, proper antenna placement, and most importantly verification of minimal ablative margins are needed, all of which require accurate image representation of pre and post ablation regions [84]. Imaging for MWA treatment planning and post-procedure evaluation takes various forms, with the most used modalities being computed tomography (CT) and magnetic resonance imaging (MRI). B-mode ultrasound (US) has also been used, most commonly for real-time antenna placement. Positron emission tomography (PET) is commonly used for metastatic follow-up [85, 86].

Clinical imaging modalities used can also vary for pre-treatment diagnostics, post-treatment follow-up or for real-time treatment monitoring. Pre-treatment and post-treatment imaging must accurately detect lesion location and size, procedural planning, and location with respect to the surrounding structures [48]. This pre-operative depiction of the hepatic lesion is performed using most commonly CT, MRI, or occasionally US, while post-treatment follow-up utilizes CT, contrast-enhanced CT (CECT), MRI, or PET most often for metastatic lesions based on clinician preference and availability [87]. The ablation procedure is commonly but not universally performed under general anesthesia. General anesthesia is commonly used to immobilize the diaphragm, pain and anxiety management, and to facilitate patient positioning thus aiding

in antenna placement [58]. For use in the operating room or clinical ablation suite, US is most used however contrast-enhanced US (CEUS), CT, CECT, and MRI have also been used for procedure monitoring and efficacy [27, 85, 88].

2.3.1 Ultrasound

There are few studies that claim B-mode US can determine the characteristics of HCC based on echogenicity in B-mode for diagnostic purposes [89]. Unfortunately, conventional B-mode imaging has shown little success in specifically identifying HCC especially for proper delineation [90]. In a study of 160 patients, although a positive prediction rate of 96.3% was obtained, a high negative predictive value of 94% was obtained when using B-mode imaging alone for HCC detection. Hence it is rarely used for actual diagnosis [91] as it is not sensitive enough for detection of smaller tumor regions, especially residual tumor locations after treatment [92].

The primary use of B-mode ultrasound using fundamental and harmonic frequencies in ablation procedures is for real-time guidance and monitoring treatment progress due to ease of use and lack of ionizing radiation [86]. Unfortunately, delineation using B-mode is limited due to gas formation from tissue heating, which results in increased signal attenuation. Despite this factor, a recent study has shown that B-mode US correlates more accurately to in-plane pathology than CT [93]. B-mode ultrasound has also been used for temperature monitoring during ablations and shows promise in real-time visualization, although is not commonly utilized in the clinical setting because temperature estimates are based widely on mean gray scale values, which may result in inaccurate temperature estimations [94, 95]. US Color Doppler flow imaging may be used to assess blood flow to tumors without the use of contrast, although the level of sensitivity and image resolution needed require the use of a technique called superb microvascular imaging [96].

2.3.1.1 Contrast Enhanced Ultrasound (CEUS)

CEUS is another useful modality for visualizing tumor location and ablation efficacy by greatly increasing specificity and sensitivity when compared to B-mode ultrasound so it does offer a more cost-

effective imaging modality than CT and MRI [97-100]. Studies have shown that complete ablation success rate after a single treatment session were higher when using CEUS over B-mode US [101]. In addition to these benefits of CEUS, certain contrast agents allow for better visualization of vasculature in patients presenting with liver cirrhosis [102].

Many first generation contrast agents, such as Levovist (Schering, Berlin, Germany), may only be effective at higher acoustic power with high mechanical index and often only provide a temporary imaging effect, as this effect is based on destruction of the microbubbles [101, 103]. Second generation contrast agents utilize harmonic imaging modes thereby alleviating the need for high mechanical index values by exploiting the nonlinear oscillation of microbubbles in contrast agents using methods such as phase inversion or amplitude modulation [104-106].

Since the contrast agent cannot be continuously injected into patients, one group has shown use of fusing a pre-ablation CEUS image with real time B-mode US for antenna placement and after ablation for efficacy [107]. This allowed for 100% success in visualizing pre- and post-ablated regions and improved workflow of the ablation procedure. Although few drug toxicities to patients have been reported [101], CEUS still requires use of contrast which can be expensive.

2.3.2 Computed Tomography

The most used imaging modality for diagnostic pre-operative depiction of hepatic lesions, contrast enhanced computed tomography (CECT) provides accurate detection of the number of lesions and location, spread of the tumor, and mapping liver vascular anatomy [34, 108]. Treatment planning for microwave ablation uses these CECT or MRI data sets in the manner similar to that used in surgery for tumor resection [109].

Intra-operative CT, typically without the use of contrast is well suited for percutaneous ablations as it visualizes tumors in relation to antenna, ablation zone, and neighboring pathology. Intra-operative CT allows precise visualization of the position of MWA antenna and ablation monitoring for detection of possible complications as well as the vaporization process [110, 111]. More specifically water vapor on CT

appears as a low attenuation area against the background liver parenchyma and can be used to define the potential ablation zone [112, 113].

After the procedure, a diagnostic CECT is often used for follow-up imaging as it shows less artifacts than MRI and allows for visualization of the thorax [27, 114]. After procedure completion, non-contrast enhanced CT does not demonstrate contrast enhancement between residual tumor tissue and the ablation zone due to poor soft-tissue contrast [34] and has shown to be less correlated to pathology than US [93]. Alternatively, CECT shows high sensitivity and specificity for detection of residual tumor tissue so is valuable for post-treatment evaluation [115]. CECT has shown high correlation to pathology after RFA, however did tend to overestimate ablation dimensions [116]. CECT therefore provides a high success rate imaging modality with a low complication rate, however it exposes patients to ionizing radiation and leaves clinicians with limited target tumor visualization and low resolution of intrahepatic vessels [117-119] .

For near real-time monitoring of MWA, variations of conventional CT imaging have been investigated. Use of reconstruction techniques such as highly constrained back-projection (HYPR) allow for CECT reconstruction with lower doses of radiation therefore allowing the potential of real-time visualization and showing higher signal-to-noise (SNR), contrast-to-noise (CNR), and correlation to pathology against conventional low-dose CECT [120]. Despite this potential, utilization of this processing technique has limited results so further investigation should be performed before clinical implementation. Variations in computed tomography have been investigated for improving liver tumor ablation assessments such as cone beam computed tomography [121]. Temperature monitoring using CT attenuation has shown some promise in assessing thermal ablation progress in liver cancer treatments, yet further investigation is needed for consistency due to initial result variability [122]. Despite these studies showing the viability of near real-time imaging using CT, non-contrast CT has been shown to have lower correlation to pathology for RFA and MWA than conventional B-mode US, further discrediting its use for real-time monitoring [93].

2.3.3 Magnetic Resonance Imaging

Magnetic resonance imaging (MRI) is a technique commonly used for pre-treatment planning and patient follow-up, but less commonly used for guiding microwave ablation treatments. MRI is a preferred method for detection and characterization of hepatic tumors as it provides improved anatomic coverage, spatial resolution, and superior soft-tissue contrast compared to other imaging modalities. For example, MRI showed a 97.5% specificity for hepatic mass characterization as compared to 77.3% for CT [34]. Post procedure follow-up contrast enhanced MR imaging has improved soft tissue visualization for viewing tumors and hepatic disease progression [27].

Although MRI is most often used for pre-treatment planning and for post treatment follow-up, real-time images are difficult to use due to MRI time to acquisition time and special considerations need to be taken with regards to the use of metal antennae during the procedure. Interventional magnetic resonance imaging (iMRI) does allow for the real-time use in procedures, providing an open MR system which clinicians can maintain patient contact throughout the procedure [123]. Specifically, iMRI has been utilized with thermal ablations [124, 125], however the use of real-time MRI still requires specially designed applicators, large equipment resulting in small working space for clinicians, and artifact formation from radiofrequency or microwave energy [126].

2.3.4 Positron Emission Tomography

Positron emission tomography (PET) is an imaging modality that utilizes tracers attached to certain molecular compounds the body uses such as glucose where the tracers can then be imaged to see where the body is utilizing this compound [127]. This fact is especially useful for visualizing the enhancement of metabolism in ablation zones [128]. Unfortunately, as PET requires the use of injected tracers, it is unable to be used in real-time monitoring during ablations. Despite this fact, PET is used for improved visualization of tumors and ablated zones and is limited in use due to dosing levels [129]. PET takes an important role in post-procedural follow-up especially for metastatic diseases due to the tumor marker intake [86].

2.3.5 Image Fusion

Image fusion of two or more clinical imaging modalities has shown utility in the clinic where pre-operative CECT or MRI images are registered to the B-mode US to enhance real-time visualization [130]. Intrinsic registration and fusion of pre-operative CT/MR images to US [131-135] has been utilized in some centers [131-133], using common landmarks such as the liver surface and/or vasculature [131-134, 136-144], or electro-magnetic antenna tracking [133]. These approaches require appropriate and careful clinical setup [132]. Data acquisition during breath holds or respiratory gating is essential to improve the accuracy of image fusion [131, 134]. Registration/fusion of the images varies from real-time [131], 15∼20 s [145], 29-74 s [136], to around 5-10 minutes [146]. Recent advancements in computing and automatic image analysis have been able to significantly reduce the extra time required for image registration so that image fusion becomes a feasible option in ablation procedures [147]. This initial rigid registration can be achieved by defining a minimum of three (3) non-collinear common fiducial points in both datasets, or by defining a common plane and single point [148]. Classical methods for implementing multi-modality image registration use mutual information to measure differences and a rigid transformation to warp the previously acquired data with the real time US B-mode images [149, 150]. Although image fusion tools for this purpose have been under development for 20 years, the adoption of these tools has been delayed in the clinic due to the extra time required to achieve satisfactory alignment between the image modalities [151, 152]. Intrinsic registration and fusion of pre-operative CT/MR images to US [131-135] has been utilized in some centers [131-133], using common landmarks such as the liver surface and/or vasculature [131-134, 136-144], or electro-magnetic antenna tracking [133]. These approaches require appropriate and careful clinical setup [132]. Data acquisition during breath holds or respiratory gating is essential to improve the accuracy of image fusion [131, 134]. The registration/fusion of the images varies from real-time [131], 15∼20 s [145], 29-74 s [136], to around 5-10 minutes [146]. Recent advancements in computing and automatic image analysis have been able to significantly reduce the extra time required for the image registration so that image fusion becomes a feasible option in ablation procedures [153-157]. This initial rigid registration can be achieved by defining a minimum of three (3) non-collinear common fiducial points in both datasets, or

by defining a common plane and single point [148]. Classical methods for implementing multi-modality image registration use mutual information to measure differences and a rigid transformation to warp the previously acquired data with the real time US B-mode image [149].

Similar rigid image registration techniques to fuse US with other whole-patient imaging modalities are currently available on several commercial US systems. These systems incorporate CT/MR/PET imaging modalities and fuse them with real time US. Position tracking for these systems uses an electromagnetic system that incorporates a source transmitter along with sensors to track the position of the transducer and/or ablation antenna [151, 158]. One example is the GE Logiq E9 that uses volume navigation (V Nav) where the previously acquired diagnostic volume must first be uploaded in DICOM form onto the US machine [148]. However, manual steps for registration of real-time US with the previously acquired images are required for initial synchronization. The spatial accuracy and clinical efficacy of the V-Nav system from the GE Logiq E9 was evaluated by Hakime et al. [132]. Their experiment specifically compared the choice of landmarks (three anatomical vs. two anatomical and one non-anatomical landmark) and whether anesthesia had any effect on the overall error. The maximum absolute difference between the location of liver nodule in CT and US was used as an accuracy metric. The highest accuracy of 1.9 ± 1.4 mm [132] was achieved with the patient under general anesthesia and both US and CT performed immediately one after the other before registration, which reduced to an accuracy of 7.05 ± 6.95 mm with additional time between the two modalities [132]. The choice of landmarks used also had a significant effect on the registration accuracy. When comparing landmark selection, the maximum absolute difference increased by 5.2 mm when no non-anatomical landmarks were included. This is likely because non-anatomical landmarks are more easily identifiable in both US and CT. There was also an increased registration error of 7.05 ± 6.95 mm when CT was not performed immediately before registration and this is attributed to patient respiration and involuntary distortion of the liver.

In addition, many other manufacturers have their own implementation of image fusion software such as Siemens eSieFusion™, Samsung Sfusion™, and Philips AIUS™. Sfusion™ advertises three different modes for data fusion on the US system: manual landmark-based registration, sweeping auto-

registration, and positioning auto-registration. Positioning auto-registration is the simplest and fastest method on the Samsung system for automatically registering the two datasets. The image fusion system on the Philips system uses two methods for performing automatic registration, both of which use an US sweep to collect data. The sweep provides three-dimensional (3D) information about the liver vessel trees and/or the liver surface. Registration uses this information to automatically find the best fit between the preloaded CT/MRI dataset and the real time US B-mode image.

Outside of commercially available systems, successful reports that automatically register US with other imaging modalities have been discussed in the literature. Wein et al. in [138] presents the foundation for a fully automatic CT to US fusion technique. The method formulates an optimization problem that seeks to maximize the similarity between data from a 3D US sweep and corresponding simulated US data generated from CT images. The experimental setup included a magnetic tracking system, which provided information about the transducer orientation. Experimental results across 25 patients showed a mean fiducial registration error (FRE) and target registration error (TRE) of 9.5 mm and 8.1 mm respectively using an affine transformation. Here FRE represents the error associated with fiducial landmarks while TRE is associated with the targeted tumor region.

MRI has also shown success in slice registration with US [154, 159-161]. Real time US-MRI fusion imaging was evaluated by Kaplan et al. [162] for use in trans-rectal biopsies with the goal of increasing the yield of the biopsy procedure. Image fusion was performed using six common fiducial markers on both the US and MRI images. An affine transformation was used to minimize the distance between the fiducial points and align the 3D MRI image set with US. The authors presented the results only as a proof of concept and evaluated the accuracy of image fusion quantitatively using a split window of US/MRI data. Schlaier et al. [163] assessed the fusion of US/MR using a physical model compatible with both imaging modalities. Authors constructed a plastic box that consisted of water, wooden arrowheads, and plastic reflective spheres. A paired point registration method was used by the navigation system to fuse US with MRI and to automatically determine registration accuracy. Overall, the paired point registration method was highly

accurate and achieved an overall accuracy of 1.08 mm ± 0.61 mm (mean ± standard deviation) for the reflective spheres.

2.4 Research Oriented Imaging for Monitoring Liver Cancer Ablation

2.4.1 Imaging US Attenuation for Ablation Monitoring

Another interesting method for imaging microwave ablation utilizes quantitative US (QUS) approaches specifically using the attenuation coefficient parameter. Several groups have shown the ability of ultrasound attenuation imaging to estimate steatosis or fat content in the liver [164-167]. Ultrasound attenuation has shown promise in estimating osteoporosis in simulation models [168]. With regards to hyperthermia treatments such as MWA, attenuation imaging allows for monitoring as the ultrasound attenuation coefficient increases based on the collagen fiber content in tissue and protein coagulation/denaturation as a response to thermal treatment [169]. In a similar fashion, several groups have reported a correlation between the liver tissue temperature to attenuation coefficient values [170-173]. A-mode ultrasound attenuation shows utility in monitoring hyperthermia with the association of attenuation and temperature [169]. This method, however, only utilizes 1D ultrasound for faster processing and use of a simpler measurement instrument. Most notably, the results of Samimi *et al.* has shown that a local attenuation imaging method using an optimized spectral shift method for monitoring *ex vivo* bovine liver microwave ablation [174]. Additionally, Zhang et al. has shown the feasibility of ultrasonic attenuation coefficient intercept imaging to evaluate MWA zones. Results showed that attenuation imaging provided increased CNR and higher correlation to treatment progress than B-mode images [175].

2.4.2 Ultrasound Temperature Imaging

An additional method used for research in visualizing ablation zones is ultrasound temperature imaging. To estimate temperature, a variety of methods can be utilized using echo- and spectral shifts from changes in speed of sound and thermal expansion, acoustic attenuation coefficient measurements, or changes in backscattered energy arising from tissue inhomogeneities [176]. The most commonly used of

these methods is that of echo- and spectral shift showing results from HIFU ablations [177, 178] and radiofrequency ablations [179, 180].

Although attenuation and temperature imaging show higher correlation to pathology than B-mode ultrasound they do have several limitations. Temperature imaging using ultrasound is still limited to visualizing the relative heating produced during the ablation procedure. Attenuation mapping requires larger regions to accurately compute the power spectra essential for this parametric imaging modality.

2.4.3 Echo Decorrelation Imaging

Another researched approach for monitoring thermal ablations uses echo decorrelation. Echo decorrelation is a real-time method that uses degradations in ultrasound signals, namely signal decorrelation, to map thermal ablation [181]. This method has shown positive results *in vitro*, *ex vivo*, and *in vivo* experiments for focused ultrasound ablations in 2D and 3D imaging planes as well as providing real-time feedback on ablation progress and control [182-185]. Despite successes in monitoring ablation progress, this method still lacks the ability to visualize pre-ablation index tumors against post ablation regions for determining accurate ablative margins in MWA procedures.

2.4.4 Ultrasound Backscatter Imaging

In addition to ultrasound attenuation coefficient changes representing ablation progress, changes in the spatial distribution of scatter in liver tissue provide a visualization method after tissue ablation. This visualization comes from the thermal coagulation produced by ablation disrupting the pseudo-periodic scattering seen in normal liver tissue [186, 187]. Despite progress using this method, limited *in vivo* results have been reported so clinical use is still limited.

2.4.5 Ultrasound Nakagami Imaging

Another ultrasound imaging method that has been researched is Nakagami Imaging [188] which quantifies local scatterer concentrations and distributions in tissue to provide more consistent images as opposed to B-mode imaging over various system settings. Nakagami imaging has been shown to

differentiate between benign and malignant tumors [189, 190], assessing tissue fibrosis [191-193], and to monitor heart tissue regeneration in adult Zebrafish [194]. In addition, Nakagami imaging has shown recent success in visualizing thermal and mechanical ablation for use with high-intensity focused ultrasound (HIFU) [194]. This success is in part due to its ability to highlight the degrading shadowing effects seen in comparable B-mode US during ablative therapies [195] as well as improving visual discrimination of thermograms, an infrared thermal camera image showing radiation dose differences as grayscale intensity image [196].

2.4.6 Elastography Using Ultrasound Radiation Force

Elastography was introduced for imaging tissue stiffness by Ophir et al. (1991). Elastography utilizes a mechanical perturbation with subsequent measurement of displacement and strain from this applied force [197], which can be quasi-static, dynamic, or impulse deformations [198-202]. The mechanical force needed to provide deformation for measurement can be applied externally or internally to the liver [203]. The use of ultrasound radiation force elastography has shown positive results for monitoring tissue stiffness during ablation [204].

Elastography can be used for quantifying the elasticity of tissue using external tissue compression or using the radiation force of ultrasound. By measuring the applied stresses, the calculated strain profile can be transformed into an elastic modulus image of the tissue. Quasi-static elastography was first described as a feasible clinical technique by Ophir [205]. Groups have shown that elastographic approaches are able to visualize the size and position of stiffer lesions, providing an ultrasound imaging method that can overcome some of the limitations of conventional B-mode ultrasound imaging and provide additional new information using a different contrast mechanism [206]. Real-time breast strain imaging has been shown to be reproducible and provides high CNRs as compared to B-mode imaging [207]. These elastograms also provide valuable information on the stiffness of the lesions to aid in characterization of lesion properties [207]. A comparison between imaging thermal lesions was done using B-mode and sonoelastography, with a 100% success rate for complete boundary detection of the thermal lesions using sonoelastography, while

B-mode only showed 37.5% boundary detection [208]. Although studies have shown that strain elastography underestimated ablation zone sizes in human subjects when compared to gold-standard CT imaging, elastographic approaches have demonstrated high correlation in ablation zones in animal models when compared to histopathology [209].

2.4.6.1 Acoustic Radiation Force Imaging

A noninvasive approach for elasticity imaging utilizes acoustic radiation force impulse (ARFI), which applies deformation using focused ultrasound pulses, alleviating the need for manual compression by the operator [210]. Good contrast for pre-ablation and post-ablation malignant tumors has been shown, indicating that ARFI provides superior boundary delineation as compared to conventional B-mode [211]. Despite ARFI showing good results for 2-D imaging, this method provides poor results at depths greater than 8 cm due to the attenuation of the acoustic waves. In addition, ARFI imaging may show large relative measurement bias at different depths when using a curvilinear transducer due to undesired attenuation and A-line lateral spread [212].

In addition, focused ultrasound (FUS) beams have also been used to induce oscillatory deformations for harmonic motion imaging (HMI). HMI has shown good results for tumor detection and ablation monitoring [213, 214]. However when staging liver fibrosis, all approaches using radiation force may fail for individuals with high liver fibrosis/cirrhosis due to high shear wave speeds that the system is unable to track or those with high body mass index (BMI) [215], and for depths greater than 8 cm [216] where attenuation becomes a factor.

2.4.6.2 Shear Wave Imaging

Shear wave elasticity imaging (SWEI) is a similar approach that also utilizes acoustic radiation force but uses several pulse bursts at different focal depths to induce a planar shear wave front [217, 218]. Propagation velocities of shear waves are measured to characterize the elasticity or shear modulus of tissue [219]. Shear wave speed estimation in the liver has been used to monitor RFA showing comparable results

to MRI [220] and monitoring during peri-ablation periods [221]. Despite this result, many liver applications of SWEI are used for staging liver fibrosis since SWEI presents with resolution of 2 mm, too large for the resolution required of ablation monitoring [222]. This method however fails for individuals with high liver fibrosis due to the inability to track high shear wave velocities in these regions, and for individuals with high body-mass-index (BMI) due to the increased attenuation of acoustic waves [219, 223]. Other studies have shown a 2-D sonoelastographic shear velocity estimation approach for characterizing the mechanical properties of tissue [224].

2.4.7 Elastography Using Electrode Perturbation

2.4.7.1 Electrode Vibration Elastography

Electrode vibration elastography (EVE) is a shear wave imaging technique used to monitor RFA and MWA procedures. Contrary to shear wave generation using radiation force or external mechanical vibration, EVE uses transient vibrations to the ablation needle to generate shear waves which are then tracked using high frame rate ultrasound [225]. Early results demonstrated good boundary delineation for phantom and *ex vivo* data [225, 226]. EVE has shown efficacy in imaging thermal ablations, and good correlations in measured areas between elastographic images and gross pathology [226, 227].

2.4.7.2 Electrode Displacement Elastography

Another approach that has been applied for ablation treatment monitoring, specifically during and after RFA or MWA procedures, is electrode displacement elastography (EDE) [228, 229]. EDE comes from the use of the microwave antenna to induce localized deformations in and around the liver tumor being ablated, which due to elasticity contrast between tumors, ablated regions, and normal liver parenchyma, provide real-time, high contrast visualization using ultrasound based methods [230].

It was validated via simulation that using the antenna to induce quasi-static deformations provided a theoretically higher imaged contrast than external compression [231]. Phantom studies confirmed these simulation findings with contrast-to-noise ratio (CNR) and strain contrast obtained being significantly

higher for EDE due to the local nature of the deformation applied [232-234]. To further validate EDE efficacy, *in vivo* animal models were utilized showing a high correlation between EDE strain and pathologic areas of ablated regions [235, 236]. EDE was then performed on human patients scheduled for percutaneous minimally invasive ablation procedures to further verify its ability to delineate ablated regions [216, 237]. Additionally, ablation zones from sonoelastography have been delineated from the nonablated tissue in elastograms showing that the imaged ablated region correlated well with the pathology [238]. Yang et al. has shown that image contrast, CNR, and delineation are significantly higher for strain images obtained using EDE than B-mode [237] or ARFI [216] imaging.

Yang et al. [239] demonstrated for liver ablation procedures, that the image contrast and CNR are much higher for images obtained using EDE than for from the same tumors and ablated region imaged using ARFI. The number of patients that were accurately delineated by independent observers in the study was shown to be 69% for EDE as compared to 12% from ARFI [240]. Additional improvements in computer architecture have permitted accelerated processing of displacement estimation [241, 242] and increased image consistency from advanced denoising [243] and lesion tracking [244]. Due to the extensive utilization of EDE in simulation, *ex vivo*, and *in vivo* imaging for MWA, it is rational choice for further investigation of imaging validation of MWA procedures.

2.4.8 Strain Imaging Algorithms for Elastography

2.4.8.1 Early Strain Estimation Methods

Initial elastography imaging was largely established based on the time shift differences estimated using normalized cross-correlation (NCC) computation between a pair of 1D windowed pre- and post-deformation ultrasound A-line segments which is derived from Fourier theory [197]. The peak of the cross-correlation function between these segments is then the estimated time shift. This is then repeated along each ultrasound A-line segment with an overlap factor to obtain a range of time shift or displacement estimates. The strain profile is determined using Eqn. (1).

$$s_i = \frac{t_{i+1} - t_i}{\Delta T} \quad (1)$$

where s_i is the strain estimate for the segment pair i, t is the time shift between segments for pair i, and ΔT is the spacing between segments.. The spatial resolution of this strain measurement is limited by the dimensions of the A-line segment used for NCC computation and corresponding overlap between A-line segments. The sampling period at which the radiofrequency data is collected also impacts resolution but can be improved using linear interpolation [245-247]. Signal decorrelation between pre- and post-deformation A-line segments also impact the accuracy and precision of the estimated strain. Investigators have attempted to alleviate this problem via companding [248] or temporal stretching before block-matching [249-252].

For estimating local displacements for elastography accurately, tissue motion must satisfy two conditions, namely maximizing signal correlation before and after deformation by ensuring that the out-of-plane motion is minimized as well as ensuring a sufficient amount of deformation that can be tracked with high signal-to-noise ratio [253]. Investigators have utilized the 'strain filter' approach to optimize strain estimation which characterizes the performance of different strain estimation algorithms [254, 255]. The strain filter approach enables optimization of signal processing parameters and applied deformation to improve strain estimation performance. These tradeoffs are described in Varghese et al. 2001 [256].

2.4.8.2 Current Strain Estimation Methods

Many approaches have been proposed over the years that are mainly classified according to the signal-processing method utilized. These are namely frequency domain, maximum likelihood time-domain correlation-based, time and frequency hybrid methods, time-domain maximum a posterior (MAP) Motion-Tracking, Optical Flow-Based, and Mesh based techniques [257].

2.4.8.2.1 Frequency Domain Based Strain Estimation

Tracking in the frequency domain can be performed after calculating the analytic signal from the radiofrequency (RF) data. This can be done by adding an imaginary part to the signal as the signal's Hilbert transform. With the analytic signals, the cross-spectrum function is used to solve for the zero-phase angle

using a root-finding algorithm which then is used to find the time delay [258]. These are reliable for robust estimation in the axial direction, yet tissue deformation is often in 3D. This method cannot be translated to 2D or 3D tracking as there is no lateral phase component between separate A-lines of ultrasound echoes. Frequency domain motion tracking then showed continued use in elastography through strain estimation through power spectral correlation techniques [259, 260], nearest-neighbor weighted least-squares [261], and for high-frame-rate imaging [262].

2.4.8.2.2 Maximum Likelihood Time-Domain Estimation Methods

The maximum likelihood time-domain correlation-based method is one of the most common methods used for displacement estimation [263]. The correlation between two sampled signals which are shifted in time without relying on *a priori* knowledge is estimated at each time shift. The maximum correlation is used as the maximum time shift, which can then be converted to displacement estimates. As this approach utilizes matching signals at different time delays, it can be easily utilized for 2D and 3D estimation. Several algorithm variations have been developed with different pre-processing, correlation functions, and subsampling to improve displacement estimates [248, 264-270]. However, these approaches are often computationally intensive so they are more beneficial for smaller displacements where the computational search range is smaller [257].

2.4.8.2.3 Combining Time-Domain and Frequency Domain methods

Combination of time-domain and frequency domain processing can take the best of both displacement estimation domains yet is not commonly used. The literature has one method combining both time and frequency directly for displacement estimation. This method uses a combination of the zero-phase line in the frequency domain and the correlation map derived from the time-domain [271].

2.4.8.2.4 Time-Domain Maximum *aposteriori* (MAP) Speckle Tracking

As maximum likelihood time-domain methods may result in large errors which arise from cycle jumps due to secondary peaks in correlation functions which occurs often in *in vivo* [272, 273]. To counteract this artifact, motion estimation then utilizes coarse-to-fine displacement estimation with a bias against large displacements [274-276]. This is called maximum *aposteriori* (MAP) speckle tracking as this

method utilizes *apriori* information to reduce the interjected bias. This approach has evolved into motion tracking using regularizers in the form of optimizing a cost-function. As an example, an optimization problem may be posed as the sum of correlation and a measure of motion smoothness [277-285]. Alternatively, MAP estimators can utilize local displacements and iteratively improve their estimations from neighboring displacement information through Bayes theorem [286, 287].

2.4.8.2.5 Optical Flow Tracking

Other methods for speckle tracking take utilize the computer vision formulation of optical flow [288-290]. With estimation using computer vision, two methods are utilized namely region-based [289, 290] and smoothness constraint-based [291] methods. These methods are often used for sub-sample displacement estimations [257].

2.4.8.2.6 Deformable Mesh-Based Tracking

Another method used for estimation is deformable mesh-based motion tracking which operate under the fundamental principles of elasticity [253]. The essence of this method is that a computer mesh is interconnected hence maintains a continuity of motion when displacements are estimated. This may also take forms of a smoothness constraint [292] which is computationally intensive or utilizing the Lame-Navier elasticity equation [293-295].

2.4.9.3 Machine Learning in Elastography

Outside of the conventional methods for displacement estimation, machine learning has seen growing utilization in elastography, namely for classification, displacement/strain estimation and shear wave imaging approaches for elastography. For classification, machine-learning has been used for staging early liver fibrosis [296]. Another classification method utilizes a generative adversarial network (GAN) for anomaly detection in ultrasound images [297]. This constructed computational model then detects anomalous lesions and rates as normal tissue, benign masses, or malignant masses.

For strain estimation, an end-to-end convolutional neural network (CNN) was used for reconstructing ultrasound strain images directly from RF data [298]. Results showed excellent correlation

to ground truth and was also compared to conventional strain estimation [281]. Additionally more recent peer-reviewed publications have shown improvements in computational speed [299] as well as strain estimation using a pyramidal convolutional neural network [300].

In a similar manner, for shear-wave elastography a deep CNN was used to generates a synthetic shear-wave elastography image directly from conventional B-mode ultrasound data [301]. When compared to traditional shear-wave elastography, the synthetic images showed very similar results with very low computational load and without mechanical stimulation that shear wave elastography normally requires. Another machine-learning method allows for shear modulus imaging from a single radiation pulse, which normally requires multiple radiation pulses focused at different depths [302]. This method was able to reconstruct shear wave elastography results accurately but also showed lower noise artifacts against state-of-the-art methods in phantom simulations [303].

Despite the variety of displacement estimation approaches described in the peer-reviewed literature, it would be difficult to fully compare all approaches for the application of visualizing MWA strain distribution. In this dissertation, three displacement estimation methods were chosen for comparison, which lie under the category of MAP estimators. These are namely 2D multilevel-normalized cross correlation [304], quality guided displacement tracking [276], and coupled subsample displacement estimation [305]. The choice to further investigate these methods was their prior utility in EDE. The comparison and detailed description of these methods is presented in Chapter 3.

2.5 References

[1] F. Bray, J. Ferlay, I. Soerjomataram, R. L. Siegel, L. A. Torre, and A. Jemal, "Global cancer statistics 2018: GLOBOCAN estimates of incidence and mortality worldwide for 36 cancers in 185 countries," *CA: a cancer journal for clinicians,* vol. 68, no. 6, pp. 394-424, 2018.

[2] M. Mohammadian, K. Allah Bakeshei, and A. Mohammadian-Hafshejani, "International epidemiology of liver cancer: geographical distribution, secular trends and predicting the future,"

(in eng), *J Prev Med Hyg*, vol. 61, no. 2, pp. E259-e289, Jun 2020, doi: 10.15167/2421-4248/jpmh2020.61.2.1244.

[3] J. M. Llovet, J. Fuster, J. Bruix, and G. Barcelona-Clinic Liver Cancer, "The Barcelona approach: diagnosis, staging, and treatment of hepatocellular carcinoma," *Liver Transpl*, vol. 10, no. 2 Suppl 1, pp. S115-20, Feb 2004, doi: 10.1002/lt.20034.

[4] C. Global Burden of Disease Liver Cancer, T. Akinyemiju, S. Abera, M. Ahmed, N. Alam, M. A. Alemayohu, C. Allen, R. Al-Raddadi, N. Alvis-Guzman, Y. Amoako, A. Artaman, T. A. Ayele, A. Barac, I. Bensenor, A. Berhane, Z. Bhutta, J. Castillo-Rivas, A. Chitheer, J.-Y. Choi, B. Cowie, L. Dandona, R. Dandona, S. Dey, D. Dicker, H. Phuc, D. U. Ekwueme, M. E. S. Zaki, F. Fischer, T. Fürst, J. Hancock, S. I. Hay, P. Hotez, S. H. Jee, A. Kasaeian, Y. Khader, Y.-H. Khang, A. Kumar, M. Kutz, H. Larson, A. Lopez, R. Lunevicius, R. Malekzadeh, C. McAlinden, T. Meier, W. Mendoza, A. Mokdad, M. Moradi-Lakeh, G. Nagel, Q. Nguyen, G. Nguyen, F. Ogbo, G. Patton, D. M. Pereira, F. Pourmalek, M. Qorbani, A. Radfar, G. Roshandel, J. A. Salomon, J. Sanabria, B. Sartorius, M. Satpathy, M. Sawhney, S. Sepanlou, K. Shackelford, H. Shore, J. Sun, D. T. Mengistu, R. Topór-Mądry, B. Tran, K. N. Ukwaja, V. Vlassov, S. E. Vollset, T. Vos, T. Wakayo, E. Weiderpass, A. Werdecker, N. Yonemoto, M. Younis, C. Yu, Z. Zaidi, L. Zhu, C. J. L. Murray, M. Naghavi, and C. Fitzmaurice, "The Burden of Primary Liver Cancer and Underlying Etiologies From 1990 to 2015 at the Global, Regional, and National Level: Results From the Global Burden of Disease Study 2015," (in eng), *JAMA Oncol*, vol. 3, no. 12, pp. 1683-1691, 2017, doi: 10.1001/jamaoncol.2017.3055.

[5] M. Endeshaw, B. D. Hallowell, H. Razzaghi, V. Senkomago, M. T. McKenna, and M. Saraiya, "Trends in liver cancer mortality in the United States: Dual burden among foreign-and US-born persons," *Cancer*, vol. 125, no. 5, pp. 726-734, 2019.

[6] A. M. Noone, N. Howlader, M. Krapcho, D. Miller, A. Brest, M. Yu, J. Ruhl, Z. Tatalovich, A. Mariotto, D. R. Lewis, H. S. Chen, and E. J. Feuer, "SEER Cancer Statistics Review, 1975-2015,"

National Cancer Institute, Bethesda, MD, September 10, 2018 2018. [Online]. Available: https://seer.cancer.gov/csr/1975_2015/

[7] B. R. Momin, P. S. Pinheiro, H. Carreira, C. Li, and H. K. Weir, "Liver cancer survival in the United States by race and stage (2001-2009): Findings from the CONCORD-2 study," (in eng), *Cancer*, vol. 123 Suppl 24, no. Suppl 24, pp. 5059-5078, 2017, doi: 10.1002/cncr.30820.

[8] A. Marengo, C. Rosso, and E. Bugianesi, "Liver Cancer: Connections with Obesity, Fatty Liver, and Cirrhosis," *Annual Review of Medicine*, vol. 67, no. 1, pp. 103-117, 2016, doi: 10.1146/annurev-med-090514-013832.

[9] R. Sharma, "Descriptive epidemiology of incidence and mortality of primary liver cancer in 185 countries: evidence from GLOBOCAN 2018," (in eng), *Jpn J Clin Oncol*, Jul 28 2020, doi: 10.1093/jjco/hyaa130.

[10] L. Li and H. Wang, "Heterogeneity of liver cancer and personalized therapy," *Cancer letters*, vol. 379, no. 2, pp. 191-197, 2016.

[11] !!! INVALID CITATION !!! [11].

[12] C.-Y. Liu, K.-F. Chen, and P.-J. Chen, "Treatment of Liver Cancer," (in eng), *Cold Spring Harb Perspect Med*, vol. 5, no. 9, pp. a021535-a021535, 2015, doi: 10.1101/cshperspect.a021535.

[13] F. Islami, K. D. Miller, R. L. Siegel, S. A. Fedewa, E. M. Ward, and A. Jemal, "Disparities in liver cancer occurrence in the United States by race/ethnicity and state," *CA: A Cancer Journal for Clinicians*, vol. 67, no. 4, pp. 273-289, 2017, doi: 10.3322/caac.21402.

[14] L. Laursen, "A preventable cancer," *Nature*, vol. 516, no. 7529, pp. S2-S3, 2014/12/01 2014, doi: 10.1038/516S2a.

[15] A. Raza and G. K. Sood, "Hepatocellular carcinoma review: current treatment, and evidence-based medicine," (in eng), *World J Gastroenterol*, vol. 20, no. 15, pp. 4115-4127, 2014, doi: 10.3748/wjg.v20.i15.4115.

[16] J. Bruix, G. J. Gores, and V. Mazzaferro, "Hepatocellular carcinoma: clinical frontiers and perspectives," *Gut*, vol. 63, no. 5, pp. 844-55, May 2014, doi: 10.1136/gutjnl-2013-306627.

[17] C. H. Liu, K. R. Avinssh, D. A. Gervais, and D. V. Sahan, "Diagnostic imaging pre- and post-ablation," *Interventional radiological treatment of liver tumors*, A. Adam and P. R. Mueller, Eds., Cambridge ; New York: Cambridge University Press, 2009, pp. 44, 73.

[18] D. Palmer and P. Johnson, "The clinical management of hepatic neoplasms," *Interventional radiological treatment of liver tumors*, A. Adam and P. R. Mueller, Eds., Cambridge ; New York: Cambridge University Press,, 2009, pp. 1-24.

[19] M. Maluccio and A. Covey, "Recent progress in understanding, diagnosing, and treating hepatocellular carcinoma," *A Cancer Journal for Clinicians*, vol. 62, no. 6, pp. 394-9, Nov-Dec 2012, doi: 10.3322/caac.21161.

[20] N. Onaca, G. L. Davis, L. W. Jennings, R. M. Goldstein, and G. B. Klintmalm, "Improved results of transplantation for hepatocellular carcinoma: A report from the international registry of hepatic tumors in liver transplantation," *Liver Transplantation*, vol. 15, no. 6, pp. 574-580, 2009, doi: 10.1002/lt.21738.

[21] R. Lencioni and L. Crocetti, "Local-regional treatment of hepatocellular carcinoma," *Radiology*, vol. 262, no. 1, pp. 43-58, Jan 2012, doi: 10.1148/radiol.11110144.

[22] K. T. Tan and C. S. Ho, "Percutaneous ethanol injection of hepatocellular carcinoma," *Interventional radiological treatment of liver tumors*, A. Adam and P. R. Mueller, Eds., Cambridge ; New York: Cambridge University Press,, 2009, pp. 108, 126 p.

[23] S. Ganguli and S. N. Goldberg, "Radiofrequency equipment and scientific basis for radiofrequency ablation," *Interventional radiological treatment of liver tumors*Cambridge ; New York: Cambridge University Press, 2009, pp. 167-180.

[24] G. D. Dodd, 3rd, M. S. Frank, M. Aribandi, S. Chopra, and K. N. Chintapalli, "Radiofrequency thermal ablation: computer analysis of the size of the thermal injury created by overlapping ablations," *Americal Journal of Roentgenology*, vol. 177, no. 4, pp. 777-82, Oct 2001, doi: 10.2214/ajr.177.4.1770777.

[25] S. N. Goldberg, G. S. Gazelle, and P. R. Mueller, "Thermal ablation therapy for focal malignancy: a unified approach to underlying principles, techniques, and diagnostic imaging guidance," *Americal Journal of Roentgenology,* vol. 174, no. 2, pp. 323-31, Feb 2000, doi: 10.2214/ajr.174.2.1740323.

[26] R. Murakami, S. Yoshimatsu, Y. Yamashita, T. Matsukawa, M. Takahashi, and K. Sagara, "Treatment of hepatocellular carcinoma: value of percutaneous microwave coagulation," *American Journal of Roentgenology,* vol. 164, no. 5, pp. 1159-64, May 1995, doi: 10.2214/ajr.164.5.7717224.

[27] S. A. Wells, J. L. Hinshaw, M. G. Lubner, T. J. Ziemlewicz, C. L. Brace, and F. T. Lee, Jr., "Liver Ablation: Best Practice," (in eng), *Radiol Clin North Am,* vol. 53, no. 5, pp. 933-71, Sep 2015, doi: 10.1016/j.rcl.2015.05.012.

[28] M. Maluccio and A. Covey, "Recent progress in understanding, diagnosing, and treating hepatocellular carcinoma," *CA Cancer J Clin,* vol. 62, no. 6, pp. 394-9, Nov-Dec 2012, doi: 10.3322/caac.21161.

[29] "Organ Procurement and Transplantation Network." Health Resources and Services Administration, U.S. Department of Health and Human Services. https://optn.transplant.hrsa.gov/data/view-data-reports/build-advanced (accessed August 20, 2020).

[30] D. Palmer and P. Johnson, " The clinical management of hepatic neoplasms," *Interventional radiological treatment of liver tumors*, A. Adam and P. R. Mueller, Eds., Cambridge ; New York: Cambridge University Press,, 2009, pp. 1, 24 p. [Online]. Available: http://site.ebrary.com/lib/yale/Doc?id=10279735

[31] P. G. Northup, N. M. Intagliata, N. L. Shah, S. J. Pelletier, C. L. Berg, and C. K. Argo, "Excess mortality on the liver transplant waiting list: Unintended policy consequences and model for End-Stage Liver Disease (MELD) inflation," *Hepatology,* vol. 61, no. 1, pp. 285-291, 2015, doi: 10.1002/hep.27283.

[32] G. Sapisochin and J. Bruix, "Liver transplantation for hepatocellular carcinoma: outcomes and novel surgical approaches," *Nature Reviews Gastroenterology & Hepatology,* vol. 14, no. 4, pp. 203-217, 2017, doi: 10.1038/nrgastro.2016.193.

[33] H. Yeh, E. Smoot, D. A. Schoenfeld, and J. F. Markmann, "Geographic Inequity in Access to Livers for Transplantation," *Transplantation,* p. 1, 2010, doi: 10.1097/tp.0b013e3182066275.

[34] C.-H. Liu, K. R. Avinssh, D. A. Gervais, and D. V. Sahan, "Diagnostic imaging pre- and post-ablation," *Interventional radiological treatment of liver tumors*, A. Adam and P. R. Mueller, Eds., Cambridge ; New York: Cambridge University Press,, 2009, pp. 44, 73 p. [Online]. Available: http://site.ebrary.com/lib/yale/Doc?id=10279735

[35] S. Yamazaki and T. Takayama, "Management strategies to minimize mortality in liver resection for hepatocellular carcinoma," *Japanese Journal of Clinical Oncology*, vol. 47, no. 10, pp. 899-908, 2017, doi: 10.1093/jjco/hyx104.

[36] R. Chanwat, "Useful maneuvers for precise laparoscopic liver resection," *Asian Journal of Endoscopic Surgery,* vol. 11, no. 2, pp. 93-103, 2018, doi: 10.1111/ases.12494.

[37] C. C. Chong, W. Chung, Y. Cheung, A. K. Fung, A. K. Fong, H. Lok, J. Wong, K. Lee, S. K. Chan, and P. B. Lai, "Enhanced recovery after surgery for liver resection," *Hong Kong Medical Journal,* 2019, doi: 10.12809/hkmj187656.

[38] "Primary liver cancers in Japan," *Cancer,* vol. 45, no. 10, pp. 2663-9, May 15 1980. [Online]. Available: https://www.ncbi.nlm.nih.gov/pubmed/6155197.

[39] E. C. Lai, S. T. Fan, C. M. Lo, K. M. Chu, C. L. Liu, and J. Wong, "Hepatic resection for hepatocellular carcinoma. An audit of 343 patients," *Ann Surg*, vol. 221, no. 3, pp. 291-8, Mar 1995. [Online]. Available: https://www.ncbi.nlm.nih.gov/pubmed/7717783.

[40] D. Takeda, H. Nitta, T. Takahara, Y. Hasegawa, N. Itou, and G. Wakabayashi, "Effect of preoperative chemotherapy on postoperative liver regeneration following hepatic resection as estimated by liver volume," *World Journal of Surgical Oncology,* vol. 11, no. 1, p. 65, 2013, doi: 10.1186/1477-7819-11-65.

[41] Y. Inoue, K. Fujii, M. Ishii, S. Kagota, H. Hamamoto, W. Osumi, T. Terasawa, Y. Tsuchimoto, S. Masubuchi, M. Yamamoto, A. Asai, K. Komeda, S. Fukunishi, F. Hirokawa, M. Goto, Y. Narumi, K. Higuchi, and K. Uchiyama, "The Relationship Between Postoperative Chemotherapy and Remnant Liver Regeneration and Outcomes After Hepatectomy for Colorectal Liver Metastasis," *Journal of Gastrointestinal Surgery,* vol. 23, no. 10, pp. 1973-1983, 2019, doi: 10.1007/s11605-018-3952-1.

[42] X. Li, X. W. Fan, W. Liu, L. Guo, Y. Li, X. Hu, X. Liang, X. P. Ma, and S. E. Yang, "Risk factors for damaged liver function after chemotherapy in hepatitis B virus carriers with non-Hodgkin lymphoma," *Genetics and Molecular Research,* vol. 14, no. 1, pp. 2647-2653, 2015, doi: 10.4238/2015.march.30.25.

[43] J. Shindoh, C.-W. D. Tzeng, T. A. Aloia, S. A. Curley, G. Zimmitti, S. H. Wei, S. Y. Huang, A. Mahvash, S. Gupta, M. J. Wallace, and J.-N. Vauthey, "Optimal Future Liver Remnant in Patients Treated with Extensive Preoperative Chemotherapy for Colorectal Liver Metastases," *Annals of Surgical Oncology,* vol. 20, no. 8, pp. 2493-2500, 2013, doi: 10.1245/s10434-012-2864-7.

[44] L. Zarling, H. Emamekhoo, G. Bhutani, T. Ziemlewicz, K. A. Matkowskyj, and C. E. Kyriakopoulos, "Polycystic Liver Disease in a Patient With Metastatic Renal Cell Carcinoma: A Case Report," (in eng), *Anticancer Res,* vol. 40, no. 3, pp. 1527-1534, Mar 2020, doi: 10.21873/anticanres.14098.

[45] C. W. Bailey and M. K. Sydnor, "Current State of Tumor Ablation Therapies," *Digestive Diseases and Sciences,* vol. 64, no. 4, pp. 951-958, 2019, doi: 10.1007/s10620-019-05514-9.

[46] S. Ganguli and S. N. Goldberg, "Radiofrequency equipment and scientific basis for radiofrequency ablation," *Interventional radiological treatment of liver tumors*, A. Adam and P. R. Mueller, Eds., Cambridge ; New York: Cambridge University Press,, 2009, pp. 167, 180 p. [Online]. Available: http://site.ebrary.com/lib/yale/Doc?id=10279735

[47] J. Bruix and M. Sherman, "Management of hepatocellular carcinoma: an update," *Hepatology (Baltimore, Md.),* vol. 53, no. 3, p. 1020, 2011.

[48] R. Lencioni and L. Crocetti, "Radiofrequency ablation of liver cancer," *Tech Vasc Interv Radiol,* vol. 10, no. 1, pp. 38-46, Mar 2007, doi: 10.1053/j.tvir.2007.08.006.

[49] J. K. Heimbach, L. M. Kulik, R. S. Finn, C. B. Sirlin, M. M. Abecassis, L. R. Roberts, A. X. Zhu, M. H. Murad, and J. A. Marrero, "AASLD guidelines for the treatment of hepatocellular carcinoma," *Hepatology,* vol. 67, no. 1, pp. 358-380, 2018.

[50] G. D. Dodd, 3rd, M. S. Frank, M. Aribandi, S. Chopra, and K. N. Chintapalli, "Radiofrequency thermal ablation: computer analysis of the size of the thermal injury created by overlapping ablations," *AJR Am J Roentgenol,* vol. 177, no. 4, pp. 777-82, Oct 2001, doi: 10.2214/ajr.177.4.1770777.

[51] S. N. Goldberg, G. S. Gazelle, and P. R. Mueller, "Thermal ablation therapy for focal malignancy: a unified approach to underlying principles, techniques, and diagnostic imaging guidance," *AJR Am J Roentgenol,* vol. 174, no. 2, pp. 323-31, Feb 2000, doi: 10.2214/ajr.174.2.1740323.

[52] G. D. Dodd, M. C. Soulen, R. A. Kane, T. Livraghi, W. R. Lees, Y. Yamashita, A. R. Gillams, O. I. Karahan, and H. Rhim, "Minimally invasive treatment of malignant hepatic tumors: at the threshold of a major breakthrough," *Radiographics,* vol. 20, no. 1, pp. 9-27, 2000.

[53] M. D. Stasi, L. Buscarini, T. Livraghi, A. Giorgoi, A. Salmi, I. d. Sio, F. Brunello, L. Solmi, E. Caturelli, and F. Magnolfi, "Percutaneous ethanol injection in the treatment of hepatocellular carcinoma: a multicenter survey of evaluation practices and complication rates," *Scandinavian journal of gastroenterology,* vol. 32, no. 11, pp. 1168-1173, 1997.

[54] J. P. McWilliams, S. Yamamoto, S. S. Raman, C. T. Loh, E. W. Lee, D. M. Liu, and S. T. Kee, "Percutaneous ablation of hepatocellular carcinoma: current status," *Journal of Vascular and Interventional Radiology,* vol. 21, no. 8, pp. S204-S213, 2010.

[55] R. A. Lencioni, H.-P. Allgaier, D. Cioni, M. Olschewski, P. Deibert, L. Crocetti, H. Frings, J. Laubenberger, I. Zuber, and H. E. Blum, "Small hepatocellular carcinoma in cirrhosis: randomized comparison of radio-frequency thermal ablation versus percutaneous ethanol injection," *Radiology,* vol. 228, no. 1, pp. 235-240, 2003.

[56] G. Narayanan, P. J. Hosein, G. Arora, K. J. Barbery, T. Froud, A. S. Livingstone, D. Franceschi, C. M. Rocha Lima, and J. Yrizarry, "Percutaneous Irreversible Electroporation for Downstaging and Control of Unresectable Pancreatic Adenocarcinoma," *Journal of Vascular and Interventional Radiology,* vol. 23, no. 12, pp. 1613-1621, 2012/12/01/ 2012, doi: https://doi.org/10.1016/j.jvir.2012.09.012.

[57] A. Golberg and M. L. Yarmush, "Nonthermal Irreversible Electroporation: Fundamentals, Applications, and Challenges," *IEEE Transactions on Biomedical Engineering,* vol. 60, no. 3, pp. 707-714, 2013, doi: 10.1109/TBME.2013.2238672.

[58] T. J. Ziemlewicz, S. A. Wells, M. G. Lubner, C. L. Brace, F. T. Lee, Jr., and J. L. Hinshaw, "Hepatic Tumor Ablation," *Surg Clin North Am,* vol. 96, no. 2, pp. 315-39, Apr 2016, doi: 10.1016/j.suc.2015.12.006.

[59] J. P. Erinjeri and T. W. I. Clark, "Cryoablation: Mechanism of Action and Devices," *Journal of Vascular and Interventional Radiology,* vol. 21, no. 8, pp. S187-S191, 2010, doi: 10.1016/j.jvir.2009.12.403.

[60] M. Ahmed, C. L. Brace, F. T. Lee Jr, and S. N. Goldberg, "Principles of and advances in percutaneous ablation," *Radiology,* vol. 258, no. 2, pp. 351-369, 2011.

[61] A. A. Gage and J. Baust, "Mechanisms of tissue injury in cryosurgery," *Cryobiology,* vol. 37, no. 3, pp. 171-186, 1998.

[62] J. L. Hinshaw and F. T. Lee, "Cryoablation for Liver Cancer," *Techniques in Vascular and Interventional Radiology,* vol. 10, no. 1, pp. 47-57, 2007, doi: 10.1053/j.tvir.2007.08.005.

[63] S. Ei, T. Hibi, M. Tanabe, O. Itano, M. Shinoda, M. Kitago, Y. Abe, H. Yagi, K. Okabayashi, D. Sugiyama, G. Wakabayashi, and Y. Kitagawa, "Cryoablation Provides Superior Local Control of Primary Hepatocellular Carcinomas of >2 cm Compared with Radiofrequency Ablation and Microwave Coagulation Therapy: An Underestimated Tool in the Toolbox," *Annals of Surgical Oncology,* vol. 22, no. 4, pp. 1294-1300, 2015, doi: 10.1245/s10434-014-4114-7.

[64] Y. Yang, C. Wang, Y. Lu, W. Bai, L. An, J. Qu, X. Gao, Y. Chen, L. Zhou, Y. Wu, Y. Feng, M. Zhang, X. Chang, and J. Lv, "Outcomes of ultrasound-guided percutaneous argon-helium cryoablation of hepatocellular carcinoma," (in eng), *J Hepatobiliary Pancreat Sci*, vol. 19, no. 6, pp. 674-84, Nov 2012, doi: 10.1007/s00534-011-0490-6.

[65] R. Lencioni, L. Crocetti, E. Bozzi, and D. Cioni, "Image-guided radiofrequency ablation: techniques and results," *Interventional radiological treatment of liver tumors*, A. Adam and P. R. Mueller, Eds., Cambridge ; New York: Cambridge University Press,, 2009, pp. 148, 166 p. [Online]. Available: http://site.ebrary.com/lib/yale/Doc?id=10279735

[66] S. Shiina, R. Tateishi, T. Arano, K. Uchino, K. Enooku, H. Nakagawa, Y. Asaoka, T. Sato, R. Masuzaki, Y. Kondo, T. Goto, H. Yoshida, M. Omata, and K. Koike, "Radiofrequency ablation for hepatocellular carcinoma: 10-year outcome and prognostic factors," *Am J Gastroenterol,* vol. 107, no. 4, pp. 569-77; quiz 578, Apr 2012, doi: 10.1038/ajg.2011.425.

[67] T. A. Potretzke, T. J. Ziemlewicz, J. L. Hinshaw, M. G. Lubner, S. A. Wells, C. L. Brace, P. Agarwal, and F. T. Lee, Jr., "Microwave versus Radiofrequency Ablation Treatment for Hepatocellular Carcinoma: A Comparison of Efficacy at a Single Center," *Journal of Vascular and Interventional Radiology*, vol. 27, no. 5, pp. 631-8, May 2016, doi: 10.1016/j.jvir.2016.01.136.

[68] C. L. Brace, "Radiofrequency and microwave ablation of the liver, lung, kidney, and bone: what are the differences?," *Current Problems in Diagnostic Radiology,* vol. 38, no. 3, pp. 135-143, 2009/05/01/ 2009, doi: https://doi.org/10.1067/j.cpradiol.2007.10.001.

[69] M. G. Lubner, C. L. Brace, T. J. Ziemlewicz, J. L. Hinshaw, and F. T. Lee, Jr., "Microwave ablation of hepatic malignancy," *Seminars in Interventional Radiology,* vol. 30, no. 1, pp. 56-66, Mar 2013, doi: 10.1055/s-0033-1333654.

[70] G. Avey, F. T. J. Lee, and J. L. Hinshaw, "Cryotherapy of the liver," *Interventional radiological treatment of liver tumors*, A. Adam and P. R. Mueller, Eds., Cambridge; New York: Cambridge University Press,, 2009, pp. 181-202.

[71] R. Murakami, S. Yoshimatsu, Y. Yamashita, T. Matsukawa, M. Takahashi, and K. Sagara, "Treatment of hepatocellular carcinoma: value of percutaneous microwave coagulation," *AJR Am J Roentgenol,* vol. 164, no. 5, pp. 1159-64, May 1995, doi: 10.2214/ajr.164.5.7717224.

[72] K. A. Maciolek, E. J. Abel, S. L. Best, H. Emamekhoo, S. L. Averill, T. J. Ziemlewicz, M. G. Lubner, J. L. Hinshaw, F. T. Lee, and S. A. Wells, "Percutaneous microwave ablation for local control of metastatic renal cell carcinoma," *Abdominal Radiology,* vol. 43, no. 9, pp. 2446-2454, 2018.

[73] A. R. Smolock, M. M. Cristescu, T. A. Potretzke, T. J. Ziemlewicz, M. G. Lubner, J. L. Hinshaw, C. L. Brace, and F. T. Lee Jr, "Microwave ablation for the treatment of hepatic adenomas," *Journal of Vascular and Interventional Radiology,* vol. 27, no. 2, pp. 244-249, 2016.

[74] G. J. Qian, N. Wang, Q. Shen, Y. H. Sheng, J. Q. Zhao, M. Kuang, G. J. Liu, and M. C. Wu, "Efficacy of microwave versus radiofrequency ablation for treatment of small hepatocellular carcinoma: experimental and clinical studies," *Eur Radiol,* vol. 22, no. 9, pp. 1983-90, Sep 2012, doi: 10.1007/s00330-012-2442-1.

[75] M. G. Lubner, C. L. Brace, T. J. Ziemlewicz, J. L. Hinshaw, and F. T. Lee, Jr., "Microwave ablation of hepatic malignancy," *Semin Intervent Radiol,* vol. 30, no. 1, pp. 56-66, Mar 2013, doi: 10.1055/s-0033-1333654.

[76] C. M. Harari, M. Magagna, M. Bedoya, F. T. Lee, Jr., M. G. Lubner, J. L. Hinshaw, T. Ziemlewicz, and C. L. Brace, "Microwave Ablation: Comparison of Simultaneous and Sequential Activation of Multiple Antennas in Liver Model Systems," *Radiology,* vol. 278, no. 1, pp. 95-103, Jan 2016, doi: 10.1148/radiol.2015142151.

[77] T. A. Potretzke, T. J. Ziemlewicz, J. L. Hinshaw, M. G. Lubner, S. A. Wells, C. L. Brace, P. Agarwal, and F. T. Lee, Jr., "Microwave versus Radiofrequency Ablation Treatment for Hepatocellular Carcinoma: A Comparison of Efficacy at a Single Center," *J Vasc Interv Radiol,* vol. 27, no. 5, pp. 631-8, May 2016, doi: 10.1016/j.jvir.2016.01.136.

[78] R. Z. Swan, D. Sindram, J. B. Martinie, and D. A. Iannitti, "Operative microwave ablation for hepatocellular carcinoma: complications, recurrence, and long-term outcomes," *J Gastrointest Surg,* vol. 17, no. 4, pp. 719-29, Apr 2013, doi: 10.1007/s11605-013-2164-y.

[79] E. H. Baker, K. Thompson, I. H. McKillop, A. Cochran, R. Kirks, D. Vrochides, J. B. Martinie, R. Z. Swan, and D. A. Iannitti, "Operative microwave ablation for hepatocellular carcinoma: a single center retrospective review of 219 patients," *J Gastrointest Oncol,* vol. 8, no. 2, pp. 337-346, Apr 2017, doi: 10.21037/jgo.2016.09.06.

[80] M. D. Lu, H. X. Xu, X. Y. Xie, X. Y. Yin, J. W. Chen, M. Kuang, Z. F. Xu, G. J. Liu, and Y. L. Zheng, "Percutaneous microwave and radiofrequency ablation for hepatocellular carcinoma: a retrospective comparative study," *J Gastroenterol,* vol. 40, no. 11, pp. 1054-60, Nov 2005, doi: 10.1007/s00535-005-1671-3.

[81] T. J. Ziemlewicz, J. L. Hinshaw, M. G. Lubner, C. L. Brace, M. L. Alexander, P. Agarwal, and F. T. Lee, Jr., "Percutaneous microwave ablation of hepatocellular carcinoma with a gas-cooled system: initial clinical results with 107 tumors," *J Vasc Interv Radiol,* vol. 26, no. 1, pp. 62-8, Jan 2015, doi: 10.1016/j.jvir.2014.09.012.

[82] M. J. Ryan, J. Willatt, B. S. Majdalany, A. Z. Kielar, S. Chong, J. A. Ruma, and A. Pandya, "Ablation techniques for primary and metastatic liver tumors," *World journal of hepatology,* vol. 8, no. 3, pp. 191-199, 2016, doi: 10.4254/wjh.v8.i3.191.

[83] R. Lencioni and L. Crocetti, "Radiofrequency Ablation of Liver Cancer," *Techniques in Vascular and Interventional Radiology,* vol. 10, no. 1, pp. 38-46, 2007, doi: 10.1053/j.tvir.2007.08.006.

[84] M. F. Meloni, J. Chiang, P. F. Laeseke, C. F. Dietrich, A. Sannino, M. Solbiati, E. Nocerino, C. L. Brace, and F. T. Lee Jr, "Microwave ablation in primary and secondary liver tumours: technical and clinical approaches," *International Journal of Hyperthermia,* vol. 33, no. 1, pp. 15-24, 2017.

[85] H. Rhim, S. N. Goldberg, G. D. Dodd, L. Solbiati, H. K. Lim, M. Tonolini, and O. K. Cho, "Essential techniques for successful radio-frequency thermal ablation of malignant hepatic tumors," *Radiographics,* vol. 21, no. suppl_1, pp. S17-S35, 2001.

[86] T. J. Ziemlewicz, S. A. Wells, M. G. Lubner, C. L. Brace, F. T. Lee, Jr., and J. L. Hinshaw, "Hepatic Tumor Ablation," *Surgical Clinics of North America,* vol. 96, no. 2, pp. 315-39, Apr 2016, doi: 10.1016/j.suc.2015.12.006.

[87] C. H. Cha, F. T. Lee, J. M. Gurney, B. K. Markhardt, T. F. Warner, F. Kelcz, and D. M. Mahvi, "CT Versus Sonography for Monitoring Radiofrequency Ablation in a Porcine Liver," *American Journal of Roentgenology,* vol. 175, no. 3, pp. 705-711, 2000/09 2000, doi: 10.2214/ajr.175.3.1750705.

[88] T. J. Ziemlewicz, J. L. Hinshaw, M. G. Lubner, C. L. Brace, M. L. Alexander, P. Agarwal, and F. T. Lee, "Percutaneous Microwave Ablation of Hepatocellular Carcinoma with a Gas-Cooled System: Initial Clinical Results with 107 Tumors," *Journal of Vascular and Interventional Radiology,* vol. 26, no. 1, pp. 62-68, 2015/01/01/ 2015, doi: https://doi.org/10.1016/j.jvir.2014.09.012.

[89] H. Tanaka, "Current role of ultrasound in the diagnosis of hepatocellular carcinoma," *Journal of Medical Ultrasonics,* vol. 47, no. 2, pp. 239-255, 2020/04/01 2020, doi: 10.1007/s10396-020-01012-y.

[90] D. Cioni, R. Lencioni, and C. Bartolozzi, "Percutaneous ablation of liver malignancies: imaging evaluation of treatment response," (in eng), *Eur J Ultrasound,* vol. 13, no. 2, pp. 73-93, Jun 2001, doi: 10.1016/s0929-8266(01)00122-7.

[91] J. B. Welch, R. Shukla, N. Igbo, A. K. Singal, J. Kazan-Tannus, and R. D. Soloway, "Use of ultrasound as the initial screening exam for hepatocellular carcinoma in high risk populations," *Open Journal of Gastroenterology,* vol. 3, no. 2, pp. 148-154, 2013, doi: 10.4236/ojgas.2013.32025.

[92] B. J. Fahey, R. C. Nelson, S. J. Hsu, D. P. Bradway, D. M. Dumont, and G. E. Trahey, "In vivo guidance and assessment of liver radio-frequency ablation with acoustic radiation force elastography," *Ultrasound Med Biol,* vol. 34, no. 10, pp. 1590-603, Oct 2008, doi: 10.1016/j.ultrasmedbio.2008.03.006.

[93] T. J. Ziemlewicz, J. L. Hinshaw, M. G. Lubner, E. A. Knott, B. J. Willey, F. T. Lee, and C. L. Brace, "Radiofrequency and microwave ablation in a porcine liver model: non-contrast CT and ultrasound radiologic-pathologic correlation," *International Journal of Hyperthermia,* vol. 37, no. 1, pp. 799-807, 2020, doi: 10.1080/02656736.2020.1784471.

[94] C. Yang, H. Zhu, S. Wu, Y. Bai, and H. Gao, "Correlations between B-mode ultrasonic image texture features and tissue temperature in microwave ablation," *Journal of Ultrasound in Medicine,* vol. 29, no. 12, pp. 1787-1799, 2010.

[95] X. Ren, S. Wu, and Y. Zeng, "Experimental study for noninvasive monitoring of hyperthermia based on B-mode ultrasonic tissue characterization," *Journal of Beijing University Technology,* vol. 34, pp. 90-96, 2008.

[96] M. Kudo and H. Tochio, "Intranodular blood supply correlates well with biological malignancy grade determined by tumor growth rate in pathologically proven hepatocellular carcinoma," *Oncology,* vol. 75, no. Suppl. 1, pp. 55-64, 2008.

[97] T. Lorentzen, B. Skjoldbye, and C. Nolsoe, "Microwave ablation of liver metastases guided by contrast-enhanced ultrasound: experience with 125 metastases in 39 patients," *Ultraschall in der Medizin-European Journal of Ultrasound,* vol. 32, no. 05, pp. 492-496, 2011.

[98] R. G. Barr, "Contrast enhanced ultrasound for focal liver lesions: how accurate is it?," *Abdominal Radiology,* vol. 43, no. 5, pp. 1128-1133, 2018, doi: 10.1007/s00261-017-1257-6.

[99] D. O'Neal, T. Cohen, C. Peterson, and R. G. Barr, "Contrast-enhanced ultrasound-guided radiofrequency ablation of renal tumors," *Journal of kidney cancer and VHL,* vol. 5, no. 1, p. 7, 2018.

[100] E. Leen, S. Kumar, S. A. Khan, G. Low, K. O. Ong, P. Tait, and M. Averkiou, "Contrast-enhanced 3D ultrasound in the radiofrequency ablation of liver tumors," *World Journal of Gastroenterology: WJG,* vol. 15, no. 3, p. 289, 2009.

[101] Y. Minami and M. Kudo, "Review of dynamic contrast-enhanced ultrasound guidance in ablation therapy for hepatocellular carcinoma," *World Journal of Gastroenterology: WJG,* vol. 17, no. 45, p. 4952, 2011.

[102] M. Kudo, K. Ueshima, Y. Osaki, M. Hirooka, Y. Imai, K. Aso, K. Numata, M. Kitano, T. Kumada, and N. Izumi, "B-mode ultrasonography versus contrast-enhanced ultrasonography for surveillance of hepatocellular carcinoma: A prospective multicenter randomized controlled trial," *Liver Cancer,* vol. 8, no. 4, pp. 271-280, 2019.

[103] T. Albrecht, C. W. Hoffmann, S. A. Schmitz, S. Schettler, A. Overberg, C. T. Germer, and K.-J. r. Wolf, "Phase-inversion sonography during the liver-specific late phase of contrast enhancement: improved detection of liver metastases," *American journal of roentgenology,* vol. 176, no. 5, pp. 1191-1198, 2001.

[104] P. N. Burns, S. R. Wilson, and D. H. SIMPSON, "Pulse inversion imaging of liver blood flow: improved method for characterizing focal masses with microbubble contrast," *Investigative radiology,* vol. 35, no. 1, p. 58, 2000.

[105] D. Strobel, S. Raeker, P. Martus, E. Hahn, and D. Becker, "Phase inversion harmonic imaging versus contrast-enhanced power Doppler sonography for the characterization of focal liver lesions," *International journal of colorectal disease,* vol. 18, no. 1, pp. 63-72, 2003.

[106] R. Vilana, A. Forner, L. Bianchi, Á. García-Criado, J. Rimola, C. Rodríguez de Lope, M. Reig, C. Ayuso, C. Brú, and J. Bruix, "Intrahepatic peripheral cholangiocarcinoma in cirrhosis patients may display a vascular pattern similar to hepatocellular carcinoma on contrast-enhanced ultrasound," *Hepatology,* vol. 51, no. 6, pp. 2020-2029, 2010.

[107] W. Monsky, C. Keravnou, and M. Averkiou, "Contrast-enhanced ultrasound to ultrasound fusion during microwave ablation: feasibility study in a perfused porcine liver model," *Journal of ultrasound,* vol. 22, no. 3, pp. 323-335, 2019.

[108] A. A. van Tilborg, H. J. Scheffer, K. Nielsen, J. H. T. van Waesberghe, E. F. Comans, C. Van Kuijk, P. M. van den Tol, and M. R. Meijerink, "Transcatheter CT arterial portography and CT

hepatic arteriography for liver tumor visualization during percutaneous ablation," *Journal of Vascular and Interventional Radiology,* vol. 25, no. 7, pp. 1101-1111. e4, 2014.

[109] R. S. Puijk, A. H. Ruarus, H. J. Scheffer, L. G. Vroomen, A. A. van Tilborg, J. J. de Vries, F. H. Berger, P. M. van den Tol, and M. R. Meijerink, "Percutaneous liver tumour ablation: image guidance, endpoint assessment, and quality control," *Canadian Association of Radiologists Journal,* vol. 69, no. 1, pp. 51-62, 2018.

[110] T. J. Vogl, N.-E. A. Nour-Eldin, R. M. Hammerstingl, B. Panahi, and N. N. Naguib, "Microwave ablation (MWA): basics, technique and results in primary and metastatic liver neoplasms–review article," in *RöFo-Fortschritte auf dem Gebiet der Röntgenstrahlen und der bildgebenden Verfahren*, 2017, vol. 189, no. 11: © Georg Thieme Verlag KG, pp. 1055-1066.

[111] P. Liang, J. Yu, M.-D. Lu, B.-W. Dong, X.-L. Yu, X.-D. Zhou, B. Hu, M.-X. Xie, W. Cheng, and W. He, "Practice guidelines for ultrasound-guided percutaneous microwave ablation for hepatic malignancy," *World journal of gastroenterology: WJG,* vol. 19, no. 33, p. 5430, 2013.

[112] J. Chiang, S. Birla, M. Bedoya, D. Jones, J. Subbiah, and C. L. Brace, "Modeling and validation of microwave ablations with internal vaporization," *IEEE Transactions on Biomedical Engineering,* vol. 62, no. 2, pp. 657-663, 2014.

[113] H. Ai, S. Wu, H. Gao, L. Zhao, C. Yang, and Y. Zeng, "Temperature distribution analysis of tissue water vaporization during microwave ablation: Experiments and simulations," *International Journal of Hyperthermia,* vol. 28, no. 7, pp. 674-685, 2012.

[114] V. Vilgrain, M. Esvan, M. Ronot, A. Caumont-Prim, C. Aubé, and G. Chatellier, "A meta-analysis of diffusion-weighted and gadoxetic acid-enhanced MR imaging for the detection of liver metastases," *European radiology,* vol. 26, no. 12, pp. 4595-4615, 2016.

[115] E. Korcakova, H. Mirka, V. Liska, P. Hosek, and K. Bajcurova, "Monitoring after radiofrequency ablation of liver tumors: contrast-enhanced ultrasound vs. contrast-enhanced computer tomography, two days after procedure," *Biomedical Papers,* vol. 162, no. 4, pp. 304-309, 2018, doi: 10.5507/bp.2018.025.

[116] J. L. Vahldiek, C. Erxleben, K. K. Bressem, O. Gemeinhardt, F. Poch, B. Hiebl, K. S. Lehmann, B. Hamm, S. M. Niehues, J. W. Park, A. Krüger, and F. Jung, "Multipolar RFA of the liver: Influence of intrahepatic vessels on ablation zones and appropriateness of CECT in detecting ablation dimensions - Results of an in-vivo porcine liver model," *Clinical Hemorheology & Microcirculation*, Article vol. 70, no. 4, pp. 467-476, 2018, doi: 10.3233/CH-189313.

[117] S. B. Solomon and S. G. Silverman, "Imaging in interventional oncology," *Radiology*, vol. 257, no. 3, pp. 624-640, 2010.

[118] H. Takaki, K. Yamakado, A. Nakatsuka, T. Yamada, J. Uraki, M. Kashima, T. Yamanaka, K. Shiraki, Y. Takei, and K. Takeda, "Computed tomography fluoroscopy-guided radiofrequency ablation following intra-arterial iodized-oil injection for hepatocellular carcinomas invisible on ultrasonographic images," *International journal of clinical oncology*, vol. 18, no. 1, pp. 46-53, 2013.

[119] N. H. Asvadi, A. Anvari, R. N. Uppot, A. Thabet, A. X. Zhu, and R. S. Arellano, "CT-guided percutaneous microwave ablation of tumors in the hepatic dome: assessment of efficacy and safety," *Journal of Vascular and Interventional Radiology*, vol. 27, no. 4, pp. 496-502, 2016.

[120] P.-H. Wu, Z. Borden, and C. L. Brace, "Ablation zone visualization enhancement by periodic contrast-enhancement computed tomography during microwave ablation," *Medical Physics*, vol. 44, no. 6, pp. 2132-2140, 2017, doi: 10.1002/mp.12266.

[121] M. Abdel-Rehim, "Assessment of liver ablation using cone beam computed tomography," *World J Gastroenterol*, vol. 21, no. 2, p. 517, 2015, doi: 10.3748/wjg.v21.i2.517.

[122] J. Pohlan, W. Kress, K.-G. Hermann, J. Mews, M. Kroes, B. Hamm, and T. Diekhoff, "Computed Tomography Thermography for Ablation Zone Prediction in Microwave Ablation and Cryoablation," *Journal of Computer Assisted Tomography*, vol. Publish Ahead of Print, 2020, doi: 10.1097/rct.0000000000001081.

[123] T. Schulz, S. Puccini, J.-P. Schneider, and T. Kahn, "Interventional and intraoperative MR: review and update of techniques and clinical experience," *European Radiology,* vol. 14, no. 12, pp. 2212-2227, 2004, doi: 10.1007/s00330-004-2496-9.

[124] J. Dong, X. Geng, Y. Yang, X. Cai, P. Hu, L. Xia, B. Zhang, and P. Wu, "Dynamic imaging and pathological changes in pig liver after MR-guided microwave ablation," *BMC cancer,* vol. 18, no. 1, pp. 1-11, 2018.

[125] J. Dong, L. Zhang, W. Li, S. Mao, Y. Wang, D. Wang, L. Shen, A. Dong, and P. Wu, "1.0 T open-configuration magnetic resonance-guided microwave ablation of pig livers in real time," *Scientific Reports,* vol. 5, no. 1, p. 13551, 2015, doi: 10.1038/srep13551.

[126] S. Clasen and P. L. Pereira, "Magnetic resonance guidance for radiofrequency ablation of liver tumors," *Journal of Magnetic Resonance Imaging,* vol. 27, no. 2, pp. 421-433, 2008, doi: 10.1002/jmri.21264.

[127] H. A. Ziessman and J. P. O'Malley, *Nuclear medicine: the requisites E-Book*. Elsevier Health Sciences, 2013.

[128] K. Nielsen, H. J. Scheffer, I. C. Pieters, A. A. Van Tilborg, J.-H. T. Van Waesberghe, D. E. Oprea-Lager, M. R. Meijerink, G. Kazemier, O. S. Hoekstra, H. W. Schreurs, C. Sietses, S. Meijer, E. F. Comans, and P. M. Van Den Tol, "The use of PET-MRI in the follow-up after radiofrequency- and microwave ablation of colorectal liver metastases," *BMC Medical Imaging,* vol. 14, no. 1, p. 27, 2014, doi: 10.1186/1471-2342-14-27.

[129] E. R. Ryan, C. T. Sofocleous, H. Schöder, J. A. Carrasquillo, S. Nehmeh, S. M. Larson, R. Thornton, R. H. Siegelbaum, J. P. Erinjeri, and S. B. Solomon, "Split-Dose Technique for FDG PET/CT–guided Percutaneous Ablation: A Method to Facilitate Lesion Targeting and to Provide Immediate Assessment of Treatment Effectiveness," *Radiology,* vol. 268, no. 1, pp. 288-295, 2013, doi: 10.1148/radiol.13121462.

[130] X.-W. Bo, H.-X. Xu, L.-H. Guo, L.-P. Sun, X.-L. Li, C.-K. Zhao, Y.-P. He, B.-J. Liu, D.-D. Li, K. Zhang, and D. Wang, "Ablative safety margin depicted by fusion imaging with post-treatment

contrast-enhanced ultrasound and pre-treatment CECT/CEMRI after radiofrequency ablation for liver cancers," *Br J Radiol,* vol. 90, no. 1078, p. 20170063, 2017, doi: 10.1259/bjr.20170063.

[131] J. Krücker, S. Xu, A. Venkatesan, J. K. Locklin, H. Amalou, N. Glossop, and B. J. Wood, "Clinical utility of real-time fusion guidance for biopsy and ablation," *J Vasc Interv Radiol,* vol. 22, no. 4, pp. 515-24, 2011, doi: 10.1016/j.jvir.2010.10.033.

[132] A. Hakime, F. Deschamps, E. G. De Carvalho, C. Teriitehau, A. Auperin, and T. De Baere, "Clinical evaluation of spatial accuracy of a fusion imaging technique combining previously acquired computed tomography and real-time ultrasound for imaging of liver metastases," *Cardiovasc Intervent Radiol,* vol. 34, no. 2, pp. 338-44, Apr 2011, doi: 10.1007/s00270-010-9979-7.

[133] J. Krücker, S. Xu, N. Glossop, A. Viswanathan, J. Borgert, H. Schulz, and B. J. Wood, "Electromagnetic tracking for thermal ablation and biopsy guidance: clinical evaluation of spatial accuracy," *J Vasc Interv Radiol,* vol. 18, no. 9, pp. 1141-50, 2007.

[134] D. Spinczyk, "Towards the clinical integration of an image-guided navigation system for percutaneous liver tumor ablation using freehand 2D ultrasound images," *Comput Aided Surg,* vol. 20, no. 1, pp. 61-72, 2015, doi: 10.3109/10929088.2015.1076043.

[135] S. J. Ahn, J. M. Lee, D. H. Lee, S. M. Lee, J. H. Yoon, Y. J. Kim, J. H. Lee, S. J. Yu, and J. K. Han, "Real-time US-CT/MR fusion imaging for percutaneous radiofrequency ablation of hepatocellular carcinoma," *J Hepatol,* vol. 66, no. 2, pp. 347-354, 2017, doi: 10.1016/j.jhep.2016.09.003.

[136] A. Y. Kim, M. W. Lee, D. I. Cha, H. K. Lim, Y. T. Oh, J. Y. Jeong, J. W. Chang, J. Ryu, K. J. Lee, J. Kim, W. C. Bang, D. K. Shin, S. J. Choi, D. Koh, B. K. Seo, and K. Kim, "Automatic Registration between Real-Time Ultrasonography and Pre-procedural Magnetic Resonance Images: A Prospective Comparison between Two Registration Methods by Liver Surface and Vessel and by Liver Surface Only (Epub)," *Ultrasound Med Biol,* 2016, doi: 10.1016/j.ultrasmedbio.2016.02.008.

[137] D. H. Lee, W. H. Nam, J. Y. Lee, and J. B. Ra, "Non-rigid registration between 3D ultrasound and CT images of the liver based on intensity and gradient information," *Phys Med Biol,* vol. 56, no. 1, pp. 117-37, 2011, doi: 10.1088/0031-9155/56/1/008.

[138] W. Wein, S. Brunke, A. Khamene, M. R. Callstrom, and N. Navab, "Automatic CT-ultrasound registration for diagnostic imaging and image-guided intervention," *Med Image Anal,* vol. 12, no. 5, pp. 577-85, 2008, doi: 10.1016/j.media.2008.06.006.

[139] T. Lange, N. Papenberg, S. Heldmann, J. Modersitzki, B. Fischer, H. Lamecker, and P. M. Schlag, "3D ultrasound-CT registration of the liver using combined landmark-intensity information," *International journal of computer assisted radiology and surgery,* vol. 4, no. 1, pp. 79-88, 2009.

[140] W. H. Nam, D.-G. Kang, D. Lee, J. Y. Lee, and J. B. Ra, "Automatic registration between 3D intra-operative ultrasound and pre-operative CT images of the liver based on robust edge matching," *Physics in Medicine & Biology,* vol. 57, no. 1, p. 69, 2011.

[141] C. Weon, W. H. Nam, D. Lee, J. Y. Lee, and J. B. Ra, "Position tracking of moving liver lesion based on real-time registration between 2D ultrasound and 3D preoperative images," *Medical physics,* vol. 42, no. 1, pp. 335-347, 2015.

[142] M. Keil, C. Oyarzun Laura, and S. Wesarg, "Ultrasound B-Mode Segmentation for Registration with CT in Percutaneous Hepatic Interventions," in *Clinical Image-Based Procedures. From Planning to Intervention*, Berlin, Heidelberg, K. Drechsler *et al.*, Eds., 2013// 2013: Springer Berlin Heidelberg, pp. 91-97.

[143] J. Banerjee, Y. Sun, C. Klink, R. Gahrmann, W. J. Niessen, A. Moelker, and T. van Walsum, "Multiple-correlation similarity for block-matching based fast CT to ultrasound registration in liver interventions," *Medical Image Analysis,* vol. 53, pp. 132-141, 2019/04/01/ 2019, doi: https://doi.org/10.1016/j.media.2019.02.003.

[144] M. W. Lee, "Fusion imaging of real-time ultrasonography with CT or MRI for hepatic intervention," *Ultrasonography,* vol. 33, no. 4, pp. 227-239, 10 2014, doi: 10.14366/usg.14021.

[145] Z. Su, K. Li, E. Xu, L. Wu, X. Wang, L. Li, J. Wang, P. Lin, Y. Chen, Y. Zhang, J. Li, C. Dufour, B. Mory, and R. Zheng, "A clinical validation study for the feasibility and reliability of three-dimensional ultrasound-ultrasound automatic image registration," *Int J Hyperthermia,* vol. 31, no. 8, pp. 875-82, 2015, doi: 10.3109/02656736.2015.1073370.

[146] D. A. Clevert, P. M. Paprottka, A. Helck, M. Reiser, and C. G. Trumm, "Image fusion in the management of thermal tumor ablation of the liver," *Clin Hemorheol Microcirc,* vol. 52, no. 2-4, pp. 205-16, 2012, doi: 10.3233/CH-2012-1598.

[147] !!! INVALID CITATION !!! [147-151].

[148] E. M. Jung, C. Friedrich, P. Hoffstetter, L. M. Dendl, F. Klebl, A. Agha, P. Wiggermann, C. Stroszcynski, and A. G. Schreyer, "Volume navigation with contrast enhanced ultrasound and image fusion for percutaneous interventions: first results," *PLoS One,* vol. 7, no. 3, p. e33956, 2012, doi: 10.1371/journal.pone.0033956.

[149] S. R. Hertel and G. B. Avinash, "Method and apparatus of multi-modality image fusion," ed: Google Patents, 2010.

[150] D. A. Clevert, P. M. Paprottka, A. Helck, M. Reiser, and C. G. Trumm, "Image fusion in the management of thermal tumor ablation of the liver," *Clinical Hemorheology and Microcirculation,* vol. 52, pp. 205-216, 2012, doi: 10.3233/CH-2012-1598.

[151] J. Stoll, "Ultrasound fusion imaging," *Perspectives in Medicine,* vol. 1, no. 1, pp. 80-81, 2012/09/01/ 2012, doi: https://doi.org/10.1016/j.permed.2012.05.004.

[152] G. Srimathveeravalli, F. Cornelis, J. Mashni, H. Takaki, J. C. Durack, S. B. Solomon, and J. A. Coleman, "Comparison of ablation defect on MR imaging with computer simulation estimated treatment zone following irreversible electroporation of patient prostate," *Springerplus,* vol. 5, p. 219, 2016, doi: 10.1186/s40064-016-1879-0.

[153] E. F. Ferrante, Vivien; Paragios, Nikos, "Slice-to-Volume Deformable Registration: Efficient one shot consensus between plane selection and in-plane deformation," *International Journal of*

Computer Assisted Radiology and Surgery, vol. 10, no. 6, pp. pp.791-800, 2015, doi: 10.1007/s11548-015-1205-2.

[154] E. Ferrante and N. Paragios, "Slice-to-volume medical image registration: A survey," *Medical Image Analysis*, vol. 39, pp. 101-123, 2017/07/01/ 2017, doi: https://doi.org/10.1016/j.media.2017.04.010.

[155] G. Balakrishnan, A. Zhao, M. R. Sabuncu, J. Guttag, and A. V. Dalca, "VoxelMorph: A Learning Framework for Deformable Medical Image Registration," *arXiv preprint arXiv:1809.05231*, 2018.

[156] A. Eklund, P. Dufort, D. Forsberg, and S. M. LaConte, "Medical image processing on the GPU – Past, present and future," *Medical Image Analysis*, vol. 17, no. 8, pp. 1073-1094, 2013/12/01/ 2013, doi: https://doi.org/10.1016/j.media.2013.05.008.

[157] E. Smistad, T. L. Falch, M. Bozorgi, A. C. Elster, and F. Lindseth, "Medical image segmentation on GPUs – A comprehensive review," *Medical Image Analysis*, vol. 20, no. 1, pp. 1-18, 2015/02/01/ 2015, doi: https://doi.org/10.1016/j.media.2014.10.012.

[158] C. Ewertsen, A. Saftoiu, L. G. Gruionu, S. Karstrup, and M. B. Nielsen, "Real-time image fusion involving diagnostic ultrasound," *AJR Am J Roentgenol*, vol. 200, no. 3, pp. W249-55, Mar 2013, doi: 10.2214/AJR.12.8904.

[159] M. P. Heinrich, "Intra-operative Ultrasound to MRI Fusion with a Public Multimodal Discrete Registration Tool," in *Simulation, Image Processing, and Ultrasound Systems for Assisted Diagnosis and Navigation*: Springer, 2018, pp. 159-164.

[160] H. Rivaz, S. J. Chen, and D. L. Collins, "Automatic Deformable MR-Ultrasound Registration for Image-Guided Neurosurgery," *IEEE Transactions on Medical Imaging*, vol. 34, no. 2, pp. 366-380, 2015, doi: 10.1109/TMI.2014.2354352.

[161] D. Drobny, T. Vercauteren, S. Ourselin, and M. Modat, "Registration of MRI and iUS Data to Compensate Brain Shift Using a Symmetric Block-Matching Based Approach," in *Simulation, Image Processing, and Ultrasound Systems for Assisted Diagnosis and Navigation*: Springer, 2018, pp. 172-178.

[162] I. Kaplan, N. E. Oldenburg, P. Meskell, M. Blake, P. Church, and E. J. Holupka, "Real time MRI-ultrasound image guided stereotactic prostate biopsy," *Magn Reson Imaging,* vol. 20, no. 3, pp. 295-9, Apr 2002. [Online]. Available: https://www.ncbi.nlm.nih.gov/pubmed/12117612.

[163] J. R. Schlaier, J. Warnat, U. Dorenbeck, M. Proescholdt, K. M. Schebesch, and A. Brawanski, "Image fusion of MR images and real-time ultrasonography: evaluation of fusion accuracy combining two commercial instruments, a neuronavigation system and a ultrasound system," *Acta Neurochir (Wien),* vol. 146, no. 3, pp. 271-6; discussion 276-7, Mar 2004, doi: 10.1007/s00701-003-0155-6.

[164] P. Gong, C. Zhou, P. Song, C. Huang, U. W. Lok, S. Tang, K. Watt, M. Callstrom, and S. Chen, "Ultrasound Attenuation Estimation in Harmonic Imaging for Robust Fatty Liver Detection," *Ultrasound in Medicine & Biology,* vol. 46, no. 11, pp. 3080-3087, 2020, doi: 10.1016/j.ultrasmedbio.2020.07.006.

[165] T. Tada, T. Kumada, H. Toyoda, S. Nakamura, Y. Shibata, S. Yasuda, Y. Watanuki, K. Tsujii, N. Fukuda, M. Fujioka, K. Takeshima, F. Niwa, S. Ogawa, S. Hashinokuchi, S. Kataoka, H. Ichikawa, and H. Iijima, "Attenuation imaging based on ultrasound technology for assessment of hepatic steatosis: A comparison with magnetic resonance imaging-determined proton density fat fraction," *Hepatology Research,* 2020, doi: 10.1111/hepr.13563.

[166] Y. Kanayama, N. Kamiyama, K. Maruyama, and Y. Sumino, "Real-time ultrasound attenuation imaging of diffuse fatty liver disease," (in eng), *Ultrasound Med Biol,* vol. 39, no. 4, pp. 692-705, Apr 2013, doi: 10.1016/j.ultrasmedbio.2012.10.021.

[167] G. Ferraioli and L. B. Soares Monteiro, "Ultrasound-based techniques for the diagnosis of liver steatosis," (in eng), *World J Gastroenterol,* vol. 25, no. 40, pp. 6053-6062, Oct 28 2019, doi: 10.3748/wjg.v25.i40.6053.

[168] O. Yousefian, Y. Karbalaeisadegh, and M. Muller, "Modeling ultrasound attenuation in porous structures with mono-disperse random pore distributions using the independent scattering

approximation: a 2D simulation study," *Physics in Medicine & Biology,* vol. 64, no. 15, p. 155013, 2019, doi: 10.1088/1361-6560/ab2a32.

[169] N. A. Manaf, M. N. C. Aziz, D. S. Ridzuan, M. I. Mohamad Salim, A. A. Wahab, K. W. Lai, and Y. C. Hum, "Feasibility of A-mode ultrasound attenuation as a monitoring method of local hyperthermia treatment," *Medical & Biological Engineering & Computing,* vol. 54, no. 6, pp. 967-981, 2016/06/01 2016, doi: 10.1007/s11517-016-1480-2.

[170] K. J. Parker, "Ultrasonic attenuation and absorption in liver tissue," *Ultrasound in medicine & biology,* vol. 9, no. 4, pp. 363-369, 1983.

[171] C. A. Damianou, N. T. Sanghvi, F. J. Fry, and R. Maass-Moreno, "Dependence of ultrasonic attenuation and absorption in dog soft tissues on temperature and thermal dose," *The Journal of the Acoustical Society of America,* vol. 102, no. 1, pp. 628-634, 1997.

[172] M. Gertner, B. Wilson, and M. Sherar, "Ultrasound properties of liver tissue during heating," *Ultrasound in Medicine and Biology,* vol. 23, no. 9, pp. 1395-1403, 1997.

[173] U. Techavipoo, T. Varghese, Q. Chen, T. Stiles, J. Zagzebski, and G. Frank, "Temperature dependence of ultrasonic propagation speed and attenuation in excised canine liver tissue measured using transmitted and reflected pulses," *The Journal of the Acoustical Society of America,* vol. 115, no. 6, pp. 2859-2865, 2004.

[174] K. Samimi, J. K. White, C. L. Brace, and T. Varghese, "Monitoring Microwave Ablation of Ex Vivo Bovine Liver Using Ultrasonic Attenuation Imaging," *Ultrasound in Medicine & Biology,* 2017, doi: 10.1016/j.ultrasmedbio.2017.03.010.

[175] S. Zhang, R. Xu, S. Shang, Y. Han, S. Liu, T. Xu, C. Gu, X. Zhu, G. Niu, and M. Wan, "In vivo monitoring of microwave ablation in a porcine model using ultrasonic differential attenuation coefficient intercept imaging," *International Journal of Hyperthermia,* vol. 34, no. 8, pp. 1157-1170, 2018, doi: 10.1080/02656736.2018.1437477.

[176] R. M. Arthur, "Temperature imaging using ultrasound," *Echoes,* vol. 15, no. 20, p. 25, 2012.

[177] D. Liu and E. S. Ebbini, "Real-time 2-D temperature imaging using ultrasound," *IEEE Transactions on Biomedical Engineering,* vol. 57, no. 1, pp. 12-16, 2009.

[178] M. Bayat, J. R. Ballard, and E. S. Ebbini, "Ultrasound thermography: A new temperature reconstruction model and in vivo results," 2017: Author(s), doi: 10.1063/1.4977628. [Online]. Available: https://dx.doi.org/10.1063/1.4977628

[179] M. Daniels, T. Varghese, E. Madsen, and J. Zagzebski, "Non-invasive ultrasound-based temperature imaging for monitoring radiofrequency heating—phantom results," *Physics in Medicine & Biology,* vol. 52, no. 16, p. 4827, 2007.

[180] Y.-D. Liu, Q. Li, Z. Zhou, Y.-W. Yeah, C.-C. Chang, C.-Y. Lee, and P.-H. Tsui, "Adaptive ultrasound temperature imaging for monitoring radiofrequency ablation," *Plos one,* vol. 12, no. 8, p. e0182457, 2017.

[181] T. D. Mast, D. P. Pucke, S. E. Subramanian, W. J. Bowlus, S. M. Rudich, and J. F. Buell, "Ultrasound monitoring of in vitro radio frequency ablation by echo decorrelation imaging," (in eng), *J Ultrasound Med,* vol. 27, no. 12, pp. 1685-97, Dec 2008, doi: 10.7863/jum.2008.27.12.1685.

[182] S. Subramanian, S. M. Rudich, A. Alqadah, C. P. Karunakaran, M. B. Rao, and T. D. Mast, "In Vivo Thermal Ablation Monitoring Using Ultrasound Echo Decorrelation Imaging," *Ultrasound in Medicine & Biology,* vol. 40, no. 1, pp. 102-114, 2014, doi: 10.1016/j.ultrasmedbio.2013.09.007.

[183] T. R. Fosnight, F. M. Hooi, R. D. Keil, A. P. Ross, S. Subramanian, T. G. Akinyi, J. K. Killin, P. G. Barthe, S. M. Rudich, S. A. Ahmad, M. B. Rao, and T. D. Mast, "Echo Decorrelation Imaging of Rabbit Liver and VX2 Tumor during In Vivo Ultrasound Ablation," *Ultrasound in Medicine & Biology,* vol. 43, no. 1, pp. 176-186, 2017, doi: 10.1016/j.ultrasmedbio.2016.08.025.

[184] M. A. Abbass, A.-J. Garbo, N. Mahalingam, J. K. Killin, and T. D. Mast, "Optimized Echo Decorrelation Imaging Feedback for Bulk Ultrasound Ablation Control," *IEEE Transactions on*

Ultrasonics, Ferroelectrics, and Frequency Control, vol. 65, no. 10, pp. 1743-1755, 2018, doi: 10.1109/tuffc.2018.2847599.

[185] M. T. Cox, M. A. Abbass, and T. D. Mast, "Numerical analysis of three-dimensional echo decorrelation imaging," *The Journal of the Acoustical Society of America*, vol. 147, no. 6, pp. EL478-EL483, 2020, doi: 10.1121/10.0001334.

[186] N. Rubert and T. Varghese, "Mean scatterer spacing estimation using multi-taper coherence," (in eng), *IEEE transactions on ultrasonics, ferroelectrics, and frequency control*, vol. 60, no. 6, pp. 1061-1073, 2013, doi: 10.1109/TUFFC.2013.2670.

[187] N. Rubert and T. Varghese, "Mean scatterer spacing estimation in normal and thermally coagulated ex vivo bovine liver," (in eng), *Ultrasonic imaging*, vol. 36, no. 2, pp. 79-97, 2014, doi: 10.1177/0161734613511232.

[188] P.-H. Tsui and C.-C. Chang, "Imaging Local Scatterer Concentrations by the Nakagami Statistical Model," *Ultrasound in Medicine & Biology*, vol. 33, no. 4, pp. 608-619, 2007, doi: 10.1016/j.ultrasmedbio.2006.10.005.

[189] P.-H. Tsui, C.-K. Yeh, Y.-Y. Liao, C.-C. Chang, W.-H. Kuo, K.-J. Chang, and C.-N. Chen, "Ultrasonic Nakagami Imaging: A Strategy to Visualize the Scatterer Properties of Benign and Malignant Breast Tumors," *Ultrasound in Medicine & Biology*, vol. 36, no. 2, pp. 209-217, 2010/02/01/ 2010, doi: https://doi.org/10.1016/j.ultrasmedbio.2009.10.006.

[190] A. Larrue and J. A. Noble, "Modeling of Errors in Nakagami Imaging: Illustration on Breast Mass Characterization," *Ultrasound in Medicine & Biology*, vol. 40, no. 5, pp. 917-930, 2014/05/01/ 2014, doi: https://doi.org/10.1016/j.ultrasmedbio.2013.11.018.

[191] P.-H. Tsui, M.-C. Ho, D.-I. Tai, Y.-H. Lin, C.-Y. Wang, and H.-Y. Ma, "Acoustic structure quantification by using ultrasound Nakagami imaging for assessing liver fibrosis," (in eng), *Scientific reports*, vol. 6, pp. 33075-33075, 2016, doi: 10.1038/srep33075.

[192] M. C. Ho, J. J. Lin, Y. C. Shu, C. N. Chen, K. J. Chang, C. C. Chang, and P. H. Tsui, "Using ultrasound Nakagami imaging to assess liver fibrosis in rats," (in eng), *Ultrasonics,* vol. 52, no. 2, pp. 215-22, Feb 2012, doi: 10.1016/j.ultras.2011.08.005.

[193] X. Yang, P. Rossi, D. W. Bruner, S. Tridandapani, J. Shelton, and T. Liu, "Noninvasive evaluation of vaginal fibrosis following radiotherapy for gynecologic malignancies: a feasibility study with ultrasound B-mode and Nakagami parameter imaging," (in eng), *Medical physics,* vol. 40, no. 2, pp. 022901-022901, 2013, doi: 10.1118/1.4773872.

[194] S. Yeo, C. Yoon, C.-L. Lien, T.-K. Song, and K. K. Shung, "Monitoring of Adult Zebrafish Heart Regeneration Using High-Frequency Ultrasound Spectral Doppler and Nakagami Imaging," (in eng), *Sensors (Basel),* vol. 19, no. 19, p. 4094, 2019, doi: 10.3390/s19194094.

[195] M. Han, N. Wang, S. Guo, N. Chang, S. Lu, and M. Wan, "Nakagami-m parametric imaging for characterization of thermal coagulation and cavitation erosion induced by HIFU," *Ultrasonics Sonochemistry,* vol. 45, pp. 78-85, 2018/07/01/ 2018, doi: https://doi.org/10.1016/j.ultsonch.2018.03.008.

[196] O. Alpar, "Nakagami imaging with related distributions for advanced thermogram pseudocolorization," *Journal of Thermal Biology,* vol. 93, p. 102704, 2020, doi: 10.1016/j.jtherbio.2020.102704.

[197] J. Ophir, I. Cespedes, H. Ponnekanti, Y. Yazdi, and X. Li, "Elastography: A Quantitative Method for Imaging the Elasticity of Biological Tissues," *Ultrasonic Imaging,* vol. 13, no. 2, pp. 111-134, 1991, doi: 10.1177/016173469101300201.

[198] R. G. Barr, G. Ferraioli, M. L. Palmeri, Z. D. Goodman, G. Garcia-Tsao, J. Rubin, B. Garra, R. P. Myers, S. R. Wilson, D. Rubens, and D. Levine, "Elastography Assessment of Liver Fibrosis: Society of Radiologists in Ultrasound Consensus Conference Statement," *Radiology,* vol. 276, no. 3, pp. 845-61, 2015, doi: 10.1148/radiol.2015150619.

[199] K. J. Parker, M. M. Doyley, and D. J. Rubens, "Imaging the elastic properties of tissue: the 20 year perspective," *Phys Med Biol,* vol. 56, no. 1, pp. R1-R29, 2011, doi: 10.1088/0031-9155/56/1/R01.

[200] J. R. Doherty, G. E. Trahey, K. R. Nightingale, and M. L. Palmeri, "Acoustic radiation force elasticity imaging in diagnostic ultrasound," *IEEE Trans Ultrason Ferroelectr Freq Control,* vol. 60, no. 4, pp. 685-701, 2013, doi: 10.1109/TUFFC.2013.2617.

[201] J. Ophir, S. K. Alam, B. Garra, F. Kallel, E. Konofagou, T. Krouskop, and T. Varghese, "Elastography: ultrasonic estimation and imaging of the elastic properties of tissues," (in eng), *Proc Inst Mech Eng H,* vol. 213, no. 3, pp. 203-33, 1999, doi: 10.1243/0954411991534933.

[202] T. Varghese, "Quasi-Static Ultrasound Elastography," *Ultrasound Clin,* vol. 4, no. 3, pp. 323-338, Jul 2009, doi: 10.1016/j.cult.2009.10.009.

[203] H. Rivaz, I. Fleming, L. Assumpcao, G. Fichtinger, U. M. Hamper, M. A. Choti, G. Hager, and E. Boctor, "Ablation monitoring with elastography: 2D in-vivo and 3D ex-vivo studies," *Med Image Comput Assist Interv,* vol. 11, no. 2, pp. 458-66, 2008.

[204] S. A. Eyerly, M. Vejdani-Jahromi, D. M. Dumont, G. E. Trahey, and P. D. Wolf, "The Evolution of Tissue Stiffness at Radiofrequency Ablation Sites During Lesion Formation and in the Peri-Ablation Period," (in eng), *J Cardiovasc Electrophysiol,* vol. 26, no. 9, pp. 1009-1018, 2015, doi: 10.1111/jce.12709.

[205] J. Ophir, I. Cespedes, H. Ponnekanti, Y. Yazdi, and X. Li, "Elastography: a quantitative method for imaging the elasticity of biological tissues," *Ultrason Imaging,* vol. 13, no. 2, pp. 111-34, Apr 1991, doi: 10.1177/016173469101300201.

[206] R. Righetti, F. Kallel, R. J. Stafford, R. E. Price, T. A. Krouskop, J. D. Hazle, and J. Ophir, "Elastographic characterization of HIFU-induced lesions in canine livers," *Ultrasound Med Biol,* vol. 25, no. 7, pp. 1099-113, 1999.

[207] T. J. Hall, Y. Zhu, and C. S. Spalding, "In vivo real-time freehand palpation imaging," *Ultrasound Med Biol,* vol. 29, no. 3, pp. 427-35, Mar 2003. [Online]. Available: https://www.ncbi.nlm.nih.gov/pubmed/12706194.

[208] M. Zhang, B. Castaneda, J. Christensen, W. E. Saad, K. Bylund, K. Hoyt, J. G. Strang, D. J. Rubens, and K. J. Parker, "Real-time sonoelastography of hepatic thermal lesions in a swine model," *Med Phys*, vol. 35, no. 9, pp. 4132-41, Sep 2008, doi: 10.1118/1.2968939.

[209] C. Correa-Gallego, A. M. Karkar, S. Monette, P. C. Ezell, W. R. Jarnagin, and T. P. Kingham, "Intraoperative Ultrasound and Tissue Elastography Measurements Do Not Predict the Size of Hepatic Microwave Ablations," *Academic Radiology*, vol. 21, no. 1, pp. 72-78, 2014, doi: 10.1016/j.acra.2013.09.022.

[210] K. Nightingale, "Acoustic Radiation Force Impulse (ARFI) Imaging: a Review," *Current Medical Imaging Reviews*, vol. 7, no. 4, pp. 328-339, Nov 01 2011, doi: 10.2174/157340511798038657.

[211] B. J. Fahey, R. C. Nelson, S. J. Hsu, D. P. Bradway, D. M. Dumont, and G. E. Trahey, "In vivo guidance and assessment of liver radio-frequency ablation with acoustic radiation force elastography," *Ultrasound in Medicine and Biology*, vol. 34, no. 10, pp. 1590-603, Oct 2008, doi: 10.1016/j.ultrasmedbio.2008.03.006.

[212] H. Zhao, P. Song, M. W. Urban, R. R. Kinnick, M. Yin, J. F. Greenleaf, and S. Chen, "Bias observed in time-of-flight shear wave speed measurements using radiation force of a focused ultrasound beam," *Ultrasound Med Biol*, vol. 37, no. 11, pp. 1884-92, Nov 2011, doi: 10.1016/j.ultrasmedbio.2011.07.012.

[213] E. E Konofagou, C. Maleke, and J. Vappou, "Harmonic motion imaging (HMI) for tumor imaging and treatment monitoring," *Current medical imaging reviews*, vol. 8, no. 1, pp. 16-26, 2012.

[214] H. Chen, T. Payen, Y. Han, C. Palermo, K. Olive, and E. Konofagou, "Harmonic motion imaging for pancreatic tumor detection and high-intensity focused ultrasound ablation monitoring," *Journal of therapeutic ultrasound*, vol. 3, no. S1, p. O81, 2015.

[215] Y. Deng, M. L. Palmeri, N. C. Rouze, S. J. Rosenzweig, M. F. Abdelmalek, and K. R. Nightingale, "Analyzing the Impact of Increasing Mechanical Index and Energy Deposition on Shear Wave Speed Reconstruction in Human Liver," *Ultrasound in Medicine and Biology*, vol. 41, no. 7, pp. 1948-57, Jul 2015, doi: 10.1016/j.ultrasmedbio.2015.02.019.

[216] W. Yang, T. Varghese, T. Ziemlewicz, M. Alexander, M. Lubner, J. L. Hinshaw, S. Wells, and F. T. Lee, Jr., "Delineation of Post-procedure Ablation Regions with Electrode Displacement Elastography with a Comparison to Acoustic Radiation Force Impulse Imaging," *Ultrasound in Medicine & Biology*, Jun 05 2017, doi: 10.1016/j.ultrasmedbio.2017.04.021.

[217] M. Pernot, M. Couade, P. Mateo, B. Crozatier, R. Fischmeister, and M. Tanter, "Real-time assessment of myocardial contractility using shear wave imaging," *Journal of the American College of Cardiology*, vol. 58, no. 1, pp. 65-72, Jun 28 2011, doi: 10.1016/j.jacc.2011.02.042.

[218] P. J. Hollender, S. J. Rosenzweig, K. R. Nightingale, and G. E. Trahey, "Single- and multiple-track-location shear wave and acoustic radiation force impulse imaging: matched comparison of contrast, contrast-to-noise ratio and resolution," *Ultrasound Med Biol*, vol. 41, no. 4, pp. 1043-57, Apr 2015, doi: 10.1016/j.ultrasmedbio.2014.11.006.

[219] A. P. Sarvazyan, O. V. Rudenko, S. D. Swanson, J. B. Fowlkes, and S. Y. Emelianov, "Shear wave elasticity imaging: a new ultrasonic technology of medical diagnostics," *Ultrasound Med Biol*, vol. 24, no. 9, pp. 1419-35, Nov 1998.

[220] W. Shi, A. Anand, S. Sethuraman, S.-W. Huang, H. Xie, H. Agarwal, P. Yan, J. Azevedo, J. Kruecker, and G. Ng, "Monitoring of radiofrequency ablation with shear wave delay mapping," in *Ultrasonics Symposium (IUS), 2015 IEEE International*, 2015: IEEE, pp. 1-4, doi: 10.1109/ULTSYM.2015.0040.

[221] P.-H. Tsui, C.-Y. Wang, Z. Zhou, and Y.-L. Wan, "Monitoring radiofrequency ablation using ultrasound envelope statistics and shear wave elastography in the periablation period: an in vitro feasibility study," *PloS one*, vol. 11, no. 9, p. e0162488, 2016.

[222] K. R. Nightingale, M. L. Palmeri, R. W. Nightingale, and G. E. Trahey, "On the feasibility of remote palpation using acoustic radiation force," *J Acoust Soc Am*, vol. 110, no. 1, pp. 625-34, Jul 2001. [Online]. Available: https://www.ncbi.nlm.nih.gov/pubmed/11508987.

[223] Y. Deng, M. L. Palmeri, N. C. Rouze, S. J. Rosenzweig, M. F. Abdelmalek, and K. R. Nightingale, "Analyzing the Impact of Increasing Mechanical Index and Energy Deposition on Shear Wave

Speed Reconstruction in Human Liver," *Ultrasound Med Biol,* vol. 41, no. 7, pp. 1948-57, Jul 2015, doi: 10.1016/j.ultrasmedbio.2015.02.019.

[224] K. Hoyt, B. Castaneda, and K. J. Parker, "Two-dimensional sonoelastographic shear velocity imaging," *Ultrasound Med Biol,* vol. 34, no. 2, pp. 276-88, Feb 2008, doi: 10.1016/j.ultrasmedbio.2007.07.011.

[225] R. J. DeWall, T. Varghese, and E. L. Madsen, "Shear wave velocity imaging using transient electrode perturbation: phantom and ex vivo validation," (in eng), *IEEE Trans Med Imaging,* vol. 30, no. 3, pp. 666-78, Mar 2011, doi: 10.1109/tmi.2010.2091412.

[226] R. J. Dewall, T. Varghese, and C. L. Brace, "Visualizing ex vivo radiofrequency and microwave ablation zones using electrode vibration elastography," (in eng), *Medical physics,* vol. 39, no. 11, pp. 6692-6700, 2012, doi: 10.1118/1.4758061.

[227] R. J. DeWall and T. Varghese, "Improving thermal ablation delineation with electrode vibration elastography using a bidirectional wave propagation assumption," (in eng), *IEEE Trans Ultrason Ferroelectr Freq Control,* vol. 59, no. 1, pp. 168-73, Jan 2012, doi: 10.1109/tuffc.2012.2169.

[228] T. Varghese, J. A. Zagzebski, and F. T. Lee, Jr., "Elastographic imaging of thermal lesions in the liver in vivo following radiofrequency ablation: preliminary results," *Ultrasound in Medicine & Biology,* vol. 28, no. 11-12, pp. 1467-73, Nov-Dec 2002. [Online]. Available: https://www.ncbi.nlm.nih.gov/pubmed/12498942.

[229] R. M. Pohlman, T. Varghese, J. Jiang, T. J. Ziemlewicz, M. L. Alexander, K. L. Wergin, J. L. Hinshaw, M. G. Lubner, S. A. Wells, and F. T. Lee, Jr., "Comparison of Displacement Tracking Algorithms for *in Vivo* Electrode Displacement Elastography," *Ultrasound in Medicine and Biology,* vol. 45, no. 1, pp. 218-232, 2019, doi: 10.1016/j.ultrasmedbio.2018.09.001.

[230] J. Ophir, S. K. Alam, B. S. Garra, F. Kallel, E. E. Konofagou, T. Krouskop, C. R. B. Merritt, R. Righetti, R. Souchon, S. Srinivasan, and T. Varghese, "Elastography: Imaging the elastic properties of soft tissues with ultrasound," *Journal of Medical Ultrasonics,* vol. 29, no. 4, pp. 155-171, 2002/12 2002, doi: 10.1007/bf02480847.

[231] S. Bharat and T. Varghese, "Contrast-transfer improvement for electrode displacement elastography," *Physics in Medicine & Biology,* vol. 51, no. 24, pp. 6403-18, Dec 21 2006, doi: 10.1088/0031-9155/51/24/008.

[232] S. Bharat, T. Varghese, E. L. Madsen, and J. A. Zagzebski, "Radio-frequency ablation electrode displacement elastography: a phantom study," *Medical Physics,* vol. 35, no. 6, pp. 2432-42, Jun 2008, doi: 10.1118/1.2919763.

[233] S. Bharat and T. Varghese, "Radiofrequency electrode vibration-induced shear wave imaging for tissue modulus estimation: a simulation study," *Journal of the Acoustical Society of America,* vol. 128, no. 4, pp. 1582-5, Oct 2010, doi: 10.1121/1.3466880.

[234] J. Jiang, T. Varghese, Q. Chen, T. J. Hall, and J. A. Zagzebski, "Finite element analysis of tissue deformation with a radiofrequency ablation electrode for strain imaging," *IEEE Transactions on Ultrasonics, Ferroelectrics, and Frequency Control,* vol. 54, no. 2, pp. 281-9, Feb 2007. [Online]. Available: https://www.ncbi.nlm.nih.gov/pubmed/17328325.

[235] N. Rubert, S. Bharat, R. J. DeWall, A. Andreano, C. Brace, J. Jiang, L. Sampson, and T. Varghese, "Electrode displacement strain imaging of thermally-ablated liver tissue in an in vivo animal model," *Medical Physics,* vol. 37, no. 3, pp. 1075-82, Mar 2010, doi: 10.1118/1.3301603.

[236] A. T. Fernandez, O. Kolokythas, T. Gauthier, D. A. Herzka, A. V. Patil, and H. Xie, "Comparison of ultrasound strain images with multi-modality imaging techniques in liver RF ablation assessment: Initial ex vivo and clinical results," in *Ultrasonics Symposium, 2008. IUS 2008. IEEE,* 2008: IEEE, pp. 313-316.

[237] W. Yang, T. J. Ziemlewicz, T. Varghese, M. L. Alexander, N. Rubert, A. N. Ingle, M. G. Lubner, J. L. Hinshaw, S. A. Wells, F. T. Lee, Jr., and J. A. Zagzebski, "Post-Procedure Evaluation of Microwave Ablations of Hepatocellular Carcinomas Using Electrode Displacement Elastography," *Ultrasound Med Biol,* vol. 42, no. 12, pp. 2893-2902, Dec 2016, doi: 10.1016/j.ultrasmedbio.2016.07.015.

[238] O. Kolokythas, T. Gauthier, A. T. Fernandez, H. Xie, B. A. Timm, C. Cuevas, M. K. Dighe, L. M. Mitsumori, M. F. Bruce, D. A. Herzka, G. K. Goswami, R. T. Andrews, K. M. Oas, T. J. Dubinsky, and B. H. Warren, "Ultrasound-based elastography: a novel approach to assess radio frequency ablation of liver masses performed with expandable ablation probes: a feasibility study," *J Ultrasound Med*, vol. 27, no. 6, pp. 935-46, Jun 2008. [Online]. Available: https://www.ncbi.nlm.nih.gov/pubmed/18499853.

[239] W. Yang, T. Varghese, T. Ziemlewicz, M. Alexander, M. Lubner, J. L. Hinshaw, S. Wells, and F. T. Lee, Jr., "Delineation of Post-Procedure Ablation Regions with Electrode Displacement Elastography with a Comparison to Acoustic Radiation Force Impulse Imaging," *Ultrasound in Medicine and Biology*, vol. 43, no. 9, pp. 1953-1962, Sep 2017, doi: 10.1016/j.ultrasmedbio.2017.04.021.

[240] W. Yang, T. Varghese, T. Ziemlewicz, M. Alexander, M. Lubner, J. L. Hinshaw, S. Wells, and F. T. Lee, Jr., "Delineation of Post-Procedure Ablation Regions with Electrode Displacement Elastography with a Comparison to Acoustic Radiation Force Impulse Imaging," *Ultrasound Med Biol*, vol. 43, no. 9, pp. 1953-1962, Sep 2017, doi: 10.1016/j.ultrasmedbio.2017.04.021.

[241] N. H. Meshram and T. Varghese, "GPU accelerated multilevel Lagrangian carotid strain imaging," *IEEE Transactions on Ultrasonics, Ferroelectrics, and Frequency Control*, vol. 65, no. 8, pp. 1370 - 1379, August 2018 2018, doi: 10.1109/TUFFC.2018.2841346.

[242] R. A. Mukaddim, N. H. Meshram, C. C. Mitchell, and T. Varghese, "Hierarchical Motion Estimation With Bayesian Regularization in Cardiac Elastography: Simulation and In Vivo Validation," (in eng), *IEEE Trans Ultrason Ferroelectr Freq Control*, vol. 66, no. 11, pp. 1708-1722, Nov 2019, doi: 10.1109/tuffc.2019.2928546.

[243] R. M. Pohlman and T. Varghese, "Dictionary Representations for Electrode Displacement Elastography," *IEEE Transactions on Ultrasonics, Ferroelectrics, and Frequency Control*, vol. 65, no. 12, pp. 2381-2389, 2018, doi: 10.1109/TUFFC.2018.2874181.

[244] R. M. Pohlman and T. Varghese, "Physiological Motion Reduction Using Lagrangian Tracking for Electrode Displacement Elastography," *Ultrasound in Medicine and Biology,* vol. 46, no. 3, pp. 766-781, March 01, 2020 2019, doi: 10.1016/j.ultrasmedbio.2019.11.001.

[245] P. G. de Jong, T. Arts, A. P. Hoeks, and R. S. Reneman, "Determination of tissue motion velocity by correlation interpolation of pulsed ultrasonic echo signals," (in eng), *Ultrason Imaging,* vol. 12, no. 2, pp. 84-98, Apr 1990, doi: 10.1177/016173469001200202.

[246] R. Boucher and J. Hassab, "Analysis of discrete implementation of generalized cross correlator," *IEEE Transactions on Acoustics, Speech, and Signal Processing,* vol. 29, no. 3, pp. 609-611, 1981, doi: 10.1109/TASSP.1981.1163623.

[247] F. B. Hildebrand, *Introduction to numerical analysis*. Courier Corporation, 1987.

[248] P. Chaturvedi, M. F. Insana, and T. J. Hall, "2-D companding for noise reduction in strain imaging," *IEEE Transactions on Ultrasonics, Ferroelectrics, and Frequency Control,* vol. 45, no. 1, pp. 179-191, 1998, doi: 10.1109/58.646923.

[249] T. Varghese and J. Ophir, "Enhancement of echo-signal correlation in elastography using temporal stretching," *IEEE Transactions on Ultrasonics, Ferroelectrics, and Frequency Control,* vol. 44, no. 1, pp. 173-180, 1997, doi: 10.1109/58.585213.

[250] B. Jing, D. Chuxiong, L. Jianwen, and H. Ping, "Estimation and reduction of decorrelation effect due to tissue lateral displacement in elastography," *IEEE Transactions on Ultrasonics, Ferroelectrics, and Frequency Control,* vol. 49, no. 5, pp. 541-549, 2002, doi: 10.1109/TUFFC.2002.1002452.

[251] S. K. Alam, J. Ophir, and E. E. Konofagou, "An adaptive strain estimator for elastography," *IEEE Transactions on Ultrasonics, Ferroelectrics, and Frequency Control,* vol. 45, no. 2, pp. 461-472, 1998, doi: 10.1109/58.660156.

[252] I. Cespedes and J. Ophir, "Reduction of Image Noise in Elastography," *Ultrasonic Imaging,* vol. 15, no. 2, pp. 89-102, 1993, doi: https://doi.org/10.1006/uimg.1993.1008.

[253] S. Timoshenko and J. Goodier, "Theory of elasticity, 1951," *New York,* vol. 412, p. 108.

[254] T. Varghese and J. Ophir, "A theoretical framework for performance characterization of elastography: the strain filter," *IEEE Transactions on Ultrasonics, Ferroelectrics and Frequency Control*, vol. 44, no. 1, pp. 164-172, 1997/01 1997, doi: 10.1109/58.585212.

[255] T. Varghese, M. Bilgen, and J. Ophir, "Multiresolution imaging in elastography," (in eng), *IEEE Trans Ultrason Ferroelectr Freq Control*, vol. 45, no. 1, pp. 65-75, 1998, doi: 10.1109/58.646912.

[256] T. Varghese, J. Ophir, E. Konofagou, F. Kallel, and R. Righetti, "Tradeoffs in elastographic imaging," *Ultrason Imaging*, vol. 23, no. 4, pp. 216-48, Oct 2001, doi: 10.1177/016173460102300402.

[257] I. Z. Nenadic, M. W. Urban, J. F. Greenleaf, J.-L. Gennisson, M. Bernal, and M. Tanter, *Ultrasound elastography for biomedical applications and medicine*. John Wiley & Sons, 2019.

[258] A. Pesavento, C. Perrey, M. Krueger, and H. Ermert, "A time-efficient and accurate strain estimation concept for ultrasonic elastography using iterative phase zero estimation," *IEEE transactions on ultrasonics, ferroelectrics, and frequency control*, vol. 46, no. 5, pp. 1057-1067, 1999.

[259] E. Konofagou, T. Varghese, J. Ophir, and S. Alam, "Power spectral strain estimators in elastography," *Ultrasound in medicine & biology*, vol. 25, no. 7, pp. 1115-1129, 1999.

[260] T. Varghese, E. Konofagou, J. Ophir, S. Alam, and M. Bilgen, "Direct strain estimation in elastography using spectral cross-correlation," *Ultrasound in medicine & biology*, vol. 26, no. 9, pp. 1525-1537, 2000.

[261] M. K. Hasan, E. M. A. Anas, S. K. Alam, and S. Y. Lee, "Direct mean strain estimation for elastography using nearest-neighbor weighted least-squares approach in the frequency domain," *Ultrasound in medicine & biology*, vol. 38, no. 10, pp. 1759-1777, 2012.

[262] A. Ramalli, O. Basset, C. Cachard, E. Boni, and P. Tortoli, "Frequency-domain-based strain estimation and high-frame-rate imaging for quasi-static elastography," *IEEE transactions on ultrasonics, ferroelectrics, and frequency control*, vol. 59, no. 4, pp. 817-824, 2012.

[263] M. A. Lubinski, S. Y. Emelianov, and M. O'Donnell, "Speckle tracking methods for ultrasonic elasticity imaging using short-time correlation," *IEEE transactions on ultrasonics, ferroelectrics, and frequency control,* vol. 46, no. 1, pp. 82-96, 1999.

[264] T. Varghese, J. Ophir, and I. Cespedes, "Noise reduction in elastograms using temporal stretching with multicompression averaging," *Ultrasound in medicine & biology,* vol. 22, no. 8, pp. 1043-1052, 1996.

[265] L. Huang, Y.-K. Petrank, S.-W. Huang, C. Jia, and M. O'Donnell, "Phase rotation methods in filtering correlation coefficients for ultrasound speckle tracking," *IEEE transactions on ultrasonics, ferroelectrics, and frequency control,* vol. 56, no. 7, pp. 1368-1382, 2009.

[266] P. De Jong, T. Arts, A. Hoeks, and R. Reneman, "Experimental evaluation of the correlation interpolation technique to measure regional tissue velocity," *Ultrasonic imaging,* vol. 13, no. 2, pp. 145-161, 1991.

[267] I. Céspedes, Y. Huang, J. Ophir, and S. Spratt, "Methods for estimation of subsample time delays of digitized echo signals," *Ultrasonic imaging,* vol. 17, no. 2, pp. 142-171, 1995.

[268] B. H. Friemel, L. N. Bohs, K. R. Nightingale, and G. E. Trahey, "Speckle decorrelation due to two-dimensional flow gradients," *IEEE transactions on ultrasonics, ferroelectrics, and frequency control,* vol. 45, no. 2, pp. 317-327, 1998.

[269] B. Geiman, L. Bohs, M. Anderson, S. Breit, and G. Trahey, "A comparison of algorithms for tracking sub-pixel speckle motion," in *1997 IEEE Ultrasonics Symposium Proceedings. An International Symposium (Cat. No. 97CH36118)*, 1997, vol. 2: IEEE, pp. 1239-1242.

[270] F. Viola and W. F. Walker, "A spline-based algorithm for continuous time-delay estimation using sampled data," *IEEE transactions on ultrasonics, ferroelectrics, and frequency control,* vol. 52, no. 1, pp. 80-93, 2005.

[271] E. S. Ebbini, "Phase-coupled two-dimensional speckle tracking algorithm," *IEEE Transactions on Ultrasonics, Ferroelectronics, and Frequency Control,* vol. 53, no. 5, pp. 972-90, May 2006. [Online]. Available: https://www.ncbi.nlm.nih.gov/pubmed/16764451.

[272] E. Weinstein and A. Weiss, "Fundamental limitations in passive time-delay estimation--Part II: Wide-band systems," *IEEE transactions on acoustics, speech, and signal processing*, vol. 32, no. 5, pp. 1064-1078, 1984.

[273] A. Weiss and E. Weinstein, "Fundamental limitations in passive time delay estimation--Part I: Narrow-band systems," *IEEE Transactions on Acoustics, Speech, and Signal Processing*, vol. 31, no. 2, pp. 472-486, 1983.

[274] Y. Zhu and T. J. Hall, "A modified block matching method for real-time freehand strain imaging," *Ultrasonic imaging*, vol. 24, no. 3, pp. 161-176, 2002.

[275] R. Zahiri-Azar and S. E. Salcudean, "Motion estimation in ultrasound images using time domain cross correlation with prior estimates," *IEEE Transactions on Biomedical Engineering*, vol. 53, no. 10, pp. 1990-2000, Oct 2006, doi: 10.1109/TBME.2006.881780.

[276] L. Chen, G. M. Treece, J. E. Lindop, A. H. Gee, and R. W. Prager, "A quality-guided displacement tracking algorithm for ultrasonic elasticity imaging," *Medical Image Analysis*, vol. 13, no. 2, pp. 286-296, 2009/04 2009, doi: 10.1016/j.media.2008.10.007.

[277] J. Jiang and T. J. Hall, "A generalized speckle tracking algorithm for ultrasonic strain imaging using dynamic programming," *Ultrasound in Medicine and Biology*, vol. 35, no. 11, pp. 1863-1879, 2009.

[278] C. Pellot-Barakat, F. Frouin, M. F. Insana, and A. Herment, "Ultrasound elastography based on multiscale estimations of regularized displacement fields," *IEEE transactions on medical imaging*, vol. 23, no. 2, pp. 153-163, 2004.

[279] H. Rivaz, E. Boctor, P. Foroughi, R. Zellars, G. Fichtinger, and G. Hager, "Ultrasound elastography: a dynamic programming approach," *IEEE transactions on medical imaging*, vol. 27, no. 10, pp. 1373-1377, 2008.

[280] Y. Petrank, L. Huang, and M. O'Donnell, "Reduced peak-hopping artifacts in ultrasonic strain estimation using the Viterbi algorithm," *IEEE transactions on ultrasonics, ferroelectrics, and frequency control*, vol. 56, no. 7, pp. 1359-1367, 2009.

[281] H. Rivaz, E. M. Boctor, M. A. Choti, and G. D. Hager, "Real-Time Regularized Ultrasound Elastography," *IEEE Transactions on Medical Imaging,* vol. 30, no. 4, pp. 928-945, 2011, doi: 10.1109/TMI.2010.2091966.

[282] N. Ouzir, A. Basarab, H. Liebgott, B. Harbaoui, and J.-Y. Tourneret, "Motion estimation in echocardiography using sparse representation and dictionary learning," *IEEE Transactions on Image Processing,* vol. 27, no. 1, pp. 64-77, 2018.

[283] J. Luo and E. E. Konofagou, "A fast normalized cross-correlation calculation method for motion estimation," *IEEE Transactions on Ultrasonics, Ferroelectrics, and Frequency Control,* vol. 57, no. 6, pp. 1347-1357, 2010, doi: 10.1109/TUFFC.2010.1554.

[284] H. Chen and T. Varghese, "Multilevel hybrid 2D strain imaging algorithm for ultrasound sector/phased arrays," *Medical Physics,* vol. 36, no. 6Part1, pp. 2098-2106, 2009, doi: 10.1118/1.3121426.

[285] G. Treece, J. Lindop, L. Chen, J. Housden, R. Prager, and A. Gee, "Real-time quasi-static ultrasound elastography," *Interface Focus,* 10.1098/rsfs.2011.0011 vol. 1, no. 4, p. 540, 2011. [Online]. Available: http://rsfs.royalsocietypublishing.org/content/1/4/540.abstract.

[286] M. McCormick, N. Rubert, and T. Varghese, "Bayesian Regularization Applied to Ultrasound Strain Imaging," *IEEE Transactions on Biomedical Engineering,* vol. 58, no. 6, pp. 1612-1620, 2011, doi: 10.1109/TBME.2011.2106500.

[287] P. M. Hayton, M. Brady, S. M. Smith, and N. Moore, "A non-rigid registration algorithm for dynamic breast MR images," *Artificial Intelligence,* vol. 114, no. 1-2, pp. 125-156, 1999.

[288] Y. Zhou and Y.-P. Zheng, "A motion estimation refinement framework for real-time tissue axial strain estimation with freehand ultrasound," *IEEE transactions on ultrasonics, ferroelectrics, and frequency control,* vol. 57, no. 9, pp. 1943-1951, 2010.

[289] T. Zakaria, Z. Qin, and R. L. Maurice, "Optical-flow-based b-mode elastography: Application in the hypertensive rat carotid," *IEEE transactions on medical imaging,* vol. 29, no. 2, pp. 570-578, 2010.

[290] X. Pan, J. Gao, S. Tao, K. Liu, J. Bai, and J. Luo, "A two-step optical flow method for strain estimation in elastography: Simulation and phantom study," *Ultrasonics,* vol. 54, no. 4, pp. 990-996, 2014.

[291] B. K. Horn and B. G. Schunck, "Determining optical flow," *Artificial intelligence,* vol. 17, no. 1-3, pp. 185-203, 1981.

[292] Y. Zhu, P. Chaturvedi, and M. F. Insana, "Strain imaging with a deformable mesh," *Ultrasonic imaging,* vol. 21, no. 2, pp. 127-146, 1999.

[293] F. Yeung, S. F. Levinson, D. Fu, and K. J. Parker, "Feature-adaptive motion tracking of ultrasound image sequences using a deformable mesh," *IEEE transactions on medical imaging,* vol. 17, no. 6, pp. 945-956, 1998.

[294] N. Gokhale, M. Richards, A. Oberai, P. Barbone, and M. Doyley, "Simultaneous elastic image registration and elastic modulus reconstruction," in *2004 2nd IEEE International Symposium on Biomedical Imaging: Nano to Macro (IEEE Cat No. 04EX821)*, 2004: IEEE, pp. 543-546.

[295] J. Kybic and D. Smutek, "Computational elastography from standard ultrasound image sequences by global trust region optimization," in *Biennial International Conference on Information Processing in Medical Imaging*, 2005: Springer, pp. 299-310.

[296] Y. Chen, Y. Luo, W. Huang, D. Hu, R.-q. Zheng, S.-z. Cong, F.-k. Meng, H. Yang, H.-j. Lin, and Y. Sun, "Machine-learning-based classification of real-time tissue elastography for hepatic fibrosis in patients with chronic hepatitis B," *Computers in biology and medicine,* vol. 89, pp. 18-23, 2017.

[297] T. Fujioka, K. Kubota, M. Mori, Y. Kikuchi, L. Katsuta, M. Kimura, E. Yamaga, M. Adachi, G. Oda, and T. Nakagawa, "Efficient anomaly detection with generative adversarial network for breast ultrasound imaging," *Diagnostics,* vol. 10, no. 7, p. 456, 2020.

[298] S. Wu, Z. Gao, Z. Liu, J. Luo, H. Zhang, and S. Li, "Direct Reconstruction of Ultrasound Elastography Using an End-to-End Deep Neural Network," in *International Conference on Medical Image Computing and Computer-Assisted Intervention*, 2018: Springer, pp. 374-382.

[299] A. Zayed and H. Rivaz, "Fast Strain Estimation and Frame Selection in Ultrasound Elastography using Machine Learning," *IEEE transactions on ultrasonics, ferroelectrics, and frequency Control,* 2020.

[300] A. K. Tehrani and H. Rivaz, "Displacement estimation in ultrasound elastography using pyramidal convolutional neural network," *IEEE transactions on ultrasonics, ferroelectrics, and frequency control,* vol. 67, no. 12, pp. 2629-2639, 2020.

[301] R. R. Wildeboer, R. J. Van Sloun, C. K. Mannaerts, P. Moraes, G. Salomon, M. Chammas, H. Wijkstra, and M. Mischi, "Synthetic Elastography using B-mode Ultrasound through a Deep Fully-Convolutional Neural Network," *IEEE Transactions on Ultrasonics, Ferroelectrics, and Frequency Control,* 2020.

[302] T. Ahmed and M. Hasan, "SHEAR-net: An End-to-End Deep Learning Approach for Single Push Ultrasound Shear Wave Elasticity Imaging," *arXiv preprint arXiv:1902.04845,* 2019.

[303] P. Kijanka and M. W. Urban, "Local phase velocity based imaging: A new technique used for ultrasound shear wave elastography," *IEEE transactions on medical imaging,* vol. 38, no. 4, pp. 894-908, 2018.

[304] H. Shi and T. Varghese, "Two-dimensional multi-level strain estimation for discontinuous tissue," *Physics in Medicine & Biology,* vol. 52, no. 2, pp. 389-401, Jan 21 2007, doi: 10.1088/0031-9155/52/2/006.

[305] J. Jiang, T. Varghese, C. L. Brace, E. L. Madsen, T. J. Hall, S. Bharat, M. A. Hobson, J. A. Zagzebski, and F. T. Lee, "Young's modulus reconstruction for radio-frequency ablation electrode-induced displacement fields: a feasibility study," *IEEE Transactions on Medical Imaging,* vol. 28, no. 8, pp. 1325-34, Aug 2009, doi: 10.1109/TMI.2009.2015355.

Chapter 3: Comparison of Displacement Estimation Approaches

Three strategies for displacement vector tracking and strain tensor estimation, namely Coupled Subsample Displacement Estimation (CSDE), a multilevel 2-D normalized cross-correlation method, and quality-guided displacement tracking (QGDT) have previously shown accurate estimations for EDE. This chapters reports on a qualitative and quantitative comparison of these three algorithms over 79 patients after an MWA procedure and was adapted from my peer-review journal publication [1].

3.1 Background for Displacement Estimation Methods

Electrode displacement elastography (EDE) utilizes a displacement estimation algorithm to estimate antenna induced quasi-static deformations. Many of these algorithms employ time-delay estimation (TDE) and have been implemented using one-dimensional (1-D) or two-dimensional (2-D) algorithms utilizing sum squared differences (SSD), sum absolute differences (SAD), and normalized cross-correlation (NCC) based methods [2, 3]. Most of these approaches estimate only the axial component of the displacement vector and strain tensor, while both axial and lateral displacement vectors and strain tensor estimations are essential for EDE due to angle of ablation needle insertion. Many algorithms have incorporated 2-D tracking kernels for axial and lateral estimations [4, 5], however lateral estimation accuracy and resolution is low due to conventional ultrasound imaging constraints [6]. 2-D algorithms have incorporated interpolation [6, 7], scaling factors [8], pitch and beamwidth parameters [9], lateral phase [10, 11], regularization [12], and beam steering/ compounding [13-15] to increase lateral displacement accuracy and resolution. In previous work, three NCC-based algorithms have shown accurate axial and lateral displacement and strain tensor estimations for EDE, namely, quality-guided displacement tracking (QGDT) [16], coupled subsample displacement estimation (CSDE) [17], and a Multilevel 2-D NCC method [18].

R. M. Pohlman, T. Varghese, J. Jiang, T. J. Ziemlewicz, M. L. Alexander, K. L. Wergin, J. L. Hinshaw, M. G. Lubner, S. A. Wells, and F. T. Lee, Jr., "Comparison of Displacement Tracking Algorithms for *in Vivo* Electrode Displacement Elastography," *Ultrasound in Medicine and Biology*, vol. 45, no. 1, pp. 218-232, 2019, doi: 10.1016/j.ultrasmedbio.2018.09.001.

Now that EDE based strain imaging has been shown to be feasible for imaging thermally coagulated regions within the liver in a clinic, in this chapter we compare the performance of these three algorithms.

3.2 Comparison of Displacement Estimation Algorithms for EDE

3.2.1 *In Vivo* Data for Comparing Algorithms

Patients scheduled for a minimally invasive liver ablation procedure at the University of Wisconsin Hospital and Clinics (UWHC) were approached to be part of this study. The study population mirrors the patient population serviced by UWHC. Patients who could not provide informed consent or institutionalized patients were excluded from the study. There was no upper limit on age. Patient data collection followed a protocol approved by the health sciences institutional review board at UW – Madison after obtaining informed consent from the patient. MWA procedures were performed under general anesthesia. After placing the 17-gauge antenna under B-mode ultrasound guidance and fixation to the tumor with an ice ball using CO_2 cooling at the probe tip, followed by location verification using intra-operative computed tomography, 80 frames of pre-ablation radiofrequency (RF) data were collected utilizing a Siemens S2000 system (Siemens Medical Solutions USA, Inc., Malvern, PA, USA) system. A single focal zone with a 6C1HD curvilinear transducer was used, centered at the depth of the target tumor, with a center frequency of 6 MHz enabling an approximately 20 Hz frame rate. Radiofrequency signals were sampled at 40 MHz During data collection, the clinician(s) performing the procedure perturbed the antenna by approximately 3 mm to provide localized deformations to liver tissue. Motion of approximately 1 mm is desirable as it provides sufficient deformations for EDE strain estimation without disrupting antenna location. After MWA was performed and technical success confirmed using intra-operative CECT, an additional 80 frames of post-ablation RF data were collected. After the procedure, signal and image processing was performed offline using corresponding software packages in MATLAB 2019a (The Math Works, Inc., Natick, Massachusetts). RF data acquired from 79 patients were analyzed in this chapter. Patient demographics are described in Table 3.1.

Table 3.1 -Patient Demographics. Values represent the mean (standard deviation).

Variable	Hepatocellular Carcinoma (n = 51)	Metastasis (n = 21)	Benign Masses (n = 7)	Total (n = 79)
Weight (lb)	191 (56)	185 (32)	182 (107)	191 (41)
Age (years)	64 (8.7)	63 (14)	36 (6.0)	61 (13)
Depth: < 5cm	14%	5%	0%	11%
5 cm < & < 8cm	51%	52%	43%	52%
8cm<	35%	43%	57%	39%
Diameter: < 2cm	37%	30%	29%	35%
2cm< & <3cm	43%	43%	14%	40%
3cm<	20%	27%	57%	25%

3.2.2 Quality-Guided Displacement Tracking (QGDT) Search Strategy

The first method evaluated was a QGDT search strategy described by Chen et al. [19]. This displacement tracking algorithm utilizes a seed-based search strategy quantified by a data quality metric. The quality metric used can be either the correlation coefficient, phase gradient variance, or other user defined metrics. The algorithm begins by creating a grid of N seeds. The seed with the highest valued quality is then processed to estimate its displacement and correlation, along with its nearest neighbors. If the displacement quality of the neighbor is higher than that of the current seed, the current seed is discarded, and the new seed processed. This is continued until all pixels in the RF frame are processed. The QGDT method has been previously applied to EDE using a kernel size of 3.5 wavelengths × 7 A-lines using normalized correlation coefficient values greater than 0.75 as the quality metric [20, 21]. A kernel size of 1 wavelength × 3 A-lines is used for the displacement estimation for this study.

3.2.3 Fast Hybrid Algorithm with Coupled Subsample Displacement Estimation

The second method used is a fast hybrid algorithm [22] with Coupled Subsample Displacement Estimation (CSDE) [23], which incorporates regularized motion tracking and a predictive search approach, similar to QGDT. The method begins by estimating integer local displacements with a regularized search strategy using large 2-D kernels. A variant of the classic, block matching algorithm is then used to compute

displacements on a 6-point diamond stencil grid with a cost associated with each possible solution. The Viterbi algorithm is used to identify trusted displacement seeds and its path. If the first and last displacement vectors of the diamond stencil are different and the correlation value of the displacement vector at the center of the stencil is 0.7 or higher, then that center of the stencil is marked as a trusted seed. These seeds are then used in a modified predictive search strategy described in [24]. Initialized seeds from the regularized search and all displacements estimated with correlation coefficients less than 0.4 are then discarded. Any holes that the latter produces are interpolated or extrapolated from immediate neighbors. Once this process is completed, the search kernel on the post-deformation RF frame is shifted by the integer displacements just found. Next the correlation functions around the vicinity of the correlation peak from the integer displacements are solved to obtain subsample displacement estimates. Subsample displacement vectors then found by fitting the coordinates of a selected iso-contour to an ellipse. The final displacement vector is the sum of the integer and subsample displacements. CSDE was utilized to process EDE data sets on human subjects that were reported in [25] where an initial kernel size of 7.5 wavelengths × 29 A-lines was used. The algorithm resulted in a final density of 1 wavelength × 2 axial lines.

3.2.4 Multilevel Method

The third algorithm evaluated in this study is a 2D multilevel algorithm [26]. The multilevel algorithm operates as a pyramid, where initial displacements are computed starting on a coarse grid using large kernels, followed by computations on finer and finer spatial grids to obtain high SNR estimates with high spatial resolution. This method first transforms the RF data into envelope signals for fast and coarse displacement estimation. 2D normalized cross-correlation is then used on down-sampled envelope data to track displacements using a large 2D kernel. The displacements who do not meet a correlation coefficient threshold are either replaced with the nearest neighbors or interpolated. This coarse displacement map is then used as an initial displacement estimate for the next level of displacement calculations. The next level displacements are calculated on envelope data with more samples, with 2D cross correlation and correlation coefficient thresholding performed again using a smaller kernel size and a higher correlation coefficient

threshold. This is repeated for all levels until the final level is reached. Here 2D normalized cross correlation is used on RF data to achieve the highest resolution displacement estimates using the smallest kernel size [26]. For this study, 4 levels of the 2D multilevel algorithm were used, utilizing kernel sizes of [8, 4, 2, 1] wavelengths × [7, 5, 3, 3] axial lines.

A normalized correlation coefficient metric of 0.75 was maintained for all methods in this study. In addition, the final kernel size was reduced to 1 wavelength × 3 A-lines to be consistent across all displacement estimation methods allowing for a fair comparison. Although, the estimation performance of each of the methods compared was not optimized in this study, we compare the performance of these methods using the exact same processing parameters for a fair comparison.

3.2.5 Data Gridding

In addition to displacement vector tracking and estimation, an important step for all these methods is the approach used to transform displacement data from a sector format to a rectilinear grid. Trigonometric identities using both x and y displacement vectors were used [27] to generate axial and lateral displacement vectors for the sector array data. An additional post-displacement task was to localize a rectangular region of interest containing the ablated tumor region and regions of normal liver surrounding it from all the displacement tracking methods for comparison. Because the displacement tracking methods described above provide different displacement mapping spatial resolutions, all data sets were up-sampled to a grid size of 0.1 mm × 0.1 mm. This is done to ensure that all filtering and additional processing done to displacement data is consistent among the three methods. Once all data from the methods are on consistent data maps, further filtering can be done to remove any displacement errors. The first filtering stage applied a 2 mm × 2 mm median filter to data sets to remove false-peak displacement errors, while retaining edge information related to ablated regions. The final filtering stage used 1-D cubic spline smoothing to produce a smoother displacement map by minimization of the expression in Eqn. (2).

$$\sum_{i=1}^{n}\{Y_i - \hat{f}(x_i)\}^2 + \lambda \int \hat{f}''(x)^2\,dx \tag{2}$$

where $Y_i = f(x_i)$ for $\{x_i : i = 1,...,n\}$, $\hat{f}(x_i)$ is the cubic spline estimate, and λ is the smoothing factor. Spline smoothing used a smoothing factor of 1,000 in the axial direction and 10,000 in the lateral direction. After filtering of displacement data, a 9-point least squares method for strain calculation was performed on all data sets [28].

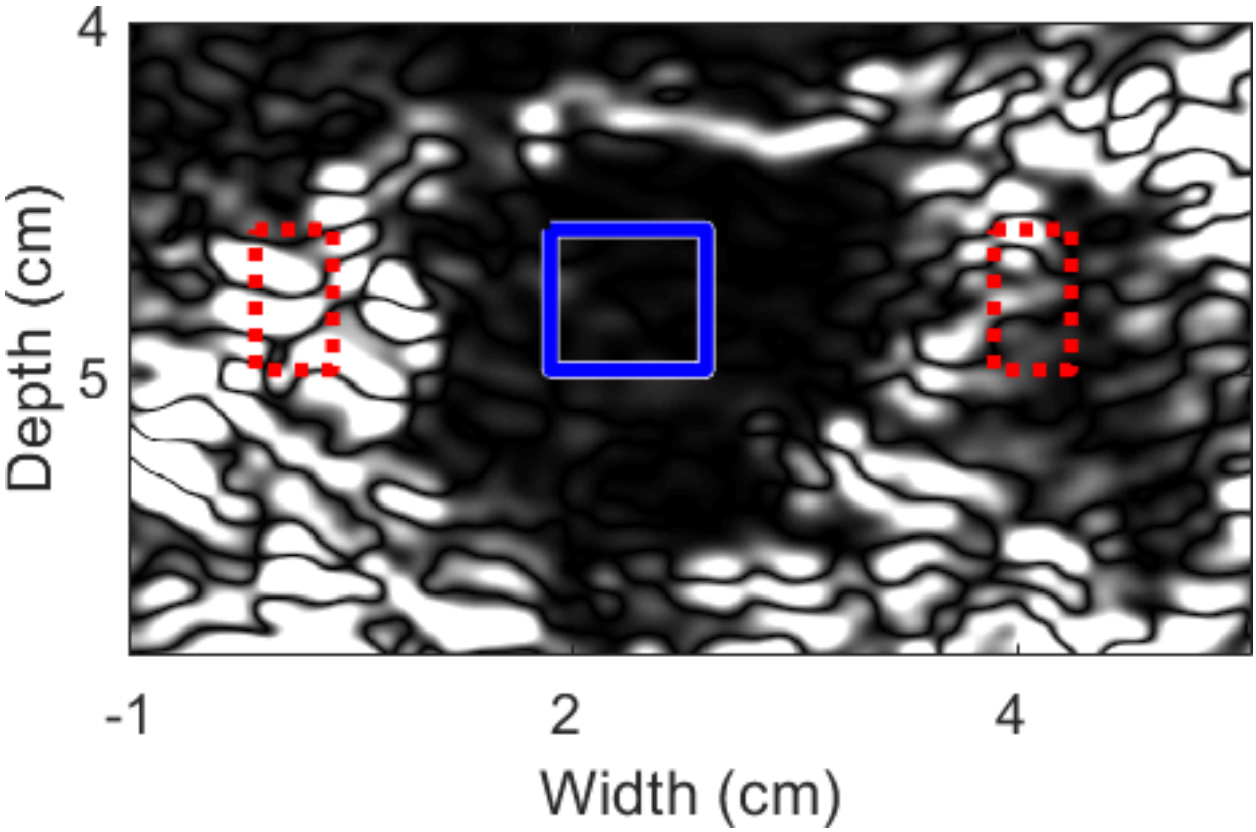

Figure 3.1 - An example of the region-of-interest (ROIs) selected for comparison on axial strain tensor image produced using CSDE. The solid blue ROI denotes the ROI inside the ablation zone and the dotted red ROIs are the halo regions outside the ablation zone at the same depth as the blue ROI. The area enclosed within the blue ROI and both red ROIs combined were equal.

3.2.6 Region-of-Interest (ROI) Placement

To quantitatively compare all three methods, a rectangular ROI was used with an example shown in Figure 3.1. ROI locations were maintained the same for all three displacement estimation methods and strain tensors computed. Measurements taken were the mean, standard deviation of estimates in the inner ROI, the contrast between the inner ROI against the outer ROI, and the CNR of the inner ROI compared to the outer ROI.

Once all masses were processed using CSDE, Multilevel, and QGDT strategies, axial and lateral strain tensors obtained were compared to each other. Displacement tracking and strain tensor estimation was performed on the exact same RF frame pairs to ensure accurate comparisons of results. The frame pair was selected based on whether an ablation zone was visualized for at least 2 of the displacement tracking strategies. If a RF frame pair exists where all three methods provided delineation of the ablated region, that frame pair was preferred.

3.2.7 Contrast and Contrast-to-Noise Ratio Comparison

The ratio of mean strain outside to inside of the ROI's placed in the ablated region and background, where both are at the same depth, is computed to obtain the contrast using Eqn. (2). Contrast obtained using EDE utilizes the halo region as the outside ROI for comparison [29, 30]. Contrast-to-noise ratio (CNR) is calculated using Eqn. (4), as shown in [47].

$$Contrast = \frac{\mu_{s_2}}{\mu_{s_1}} \tag{3}$$

$$CNR = \frac{2(\mu_{s_1} - \mu_{s_2})^2}{(\sigma_{s_1}^2 + \sigma_{s_2}^2)} \tag{4}$$

where μ and σ are the mean and standard deviation, and subscripts s_1 and s_2 strain magnitudes inside and outside the ablation zone, respectively.

3.3 Results of Algorithm Comparison

Displacement and strain results were computed for all 79 patients in this study using all three methods. Displacement vector estimates were median filtered and smoothened using spline interpolation, with strain tensor images constructed at all stages: with no filtering, median filtering, and median filtering combined with spline interpolation. An example of axial and lateral strain tensor images that incorporate median filtering and spline interpolation for all displacement tracking methods are illustrated in Figure 3.2. Note that consistent delineations of ablated regions with axial and lateral strain imaging are observed for all methods in Figure 3.2. Over the 79 data sets investigated, computation with CSDE tends to estimate larger ablated regions containing less noise artifacts in both axial and lateral strain tensor images as compared to both Multilevel and QGDT approaches. Since lesion size is not a focus of this study, it is a subjective measure noted by the authors. On the other hand, visualized noise artifacts are quantified by the standard deviation metric on strain tensor images.

Quantitative comparison results over the 79 patients in our study were grouped based on the type of liver mass diagnosed: HCC (n=51), metastases (n=21), and all masses (n=79) which also includes benign masses (n=7). Distributions of mean, standard deviation, contrast, and CNR across all patients and all three displacement estimation methods are shown in Figure 3.3 - Figure 3.6.

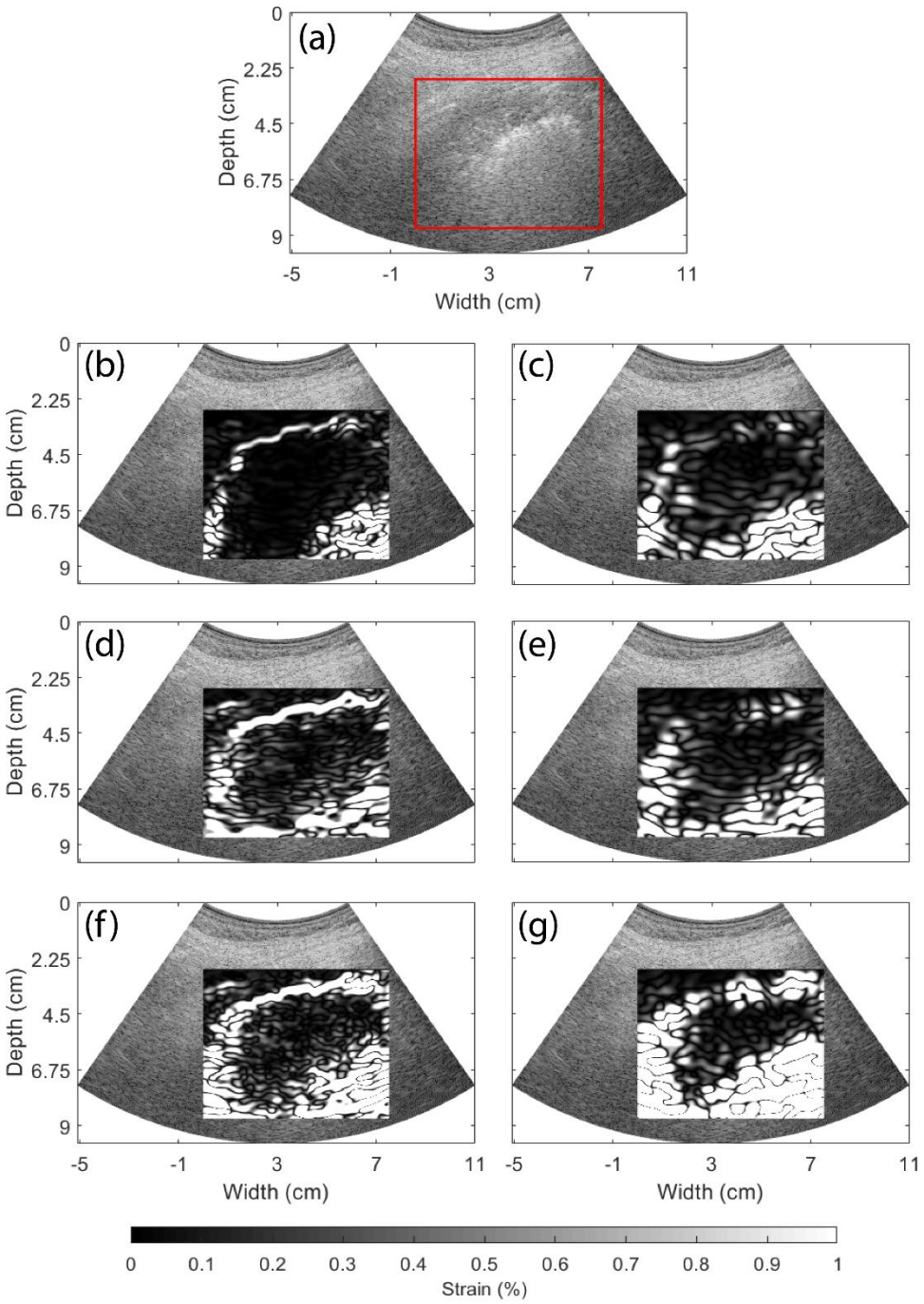

Figure 3.2 - Illustration of axial and lateral strain tensor images produced using CSDE, Multilevel, and QGDT approaches for a patient with colon metastasis at a depth of 6 cm. (a) B-mode image with ROI, (b) CSDE axial strain tensor image, (c) CSDE lateral strain tensor image, (d) Multilevel axial strain tensor image, (e) Multilevel lateral strain tensor image, (f) QGDT axial strain tensor image, and (g) QGDT lateral strain tensor image.

3.3.1 Mean Strain parameter

Figure 3.3 displays mean strain distributions across all masses (a), HCC (b), and metastatic masses (c), respectively. For both CSDE and Multilevel methods, lateral strains have wider distributions than axial strains which are reversed for QGDT as shown in Figure 3.3 (a). In most *in-vivo* human ablations the antenna is inserted at a 30° - 45° angle with respect to the transducer, therefore strain distribution incurred in the localized region around the antenna is expected in both axial and lateral directions. In addition, in Figure 3.3 (a), CSDE appears to estimate lower values of axial and lateral strains with very narrow upper and lower quartiles meaning very low variation between patients.

Axial and lateral strain estimation with all three approaches shows similar distributions near the median strain for all masses in Figure 3.3 (a) and HCC masses in (b), except for the tighter distribution with axial QGDT. Of all three estimation approaches, QGDT shows the highest variation in the axial strain distribution and appears skewed toward larger strain magnitudes shown in Figure 3.3 (a) and (c). Metastatic masses in Figure 3.3 (c) have similar distributions, except for the wider axial QGDT distribution. Another important aspect is that all distributions are strongly skewed toward larger magnitude strains for metastatic masses.

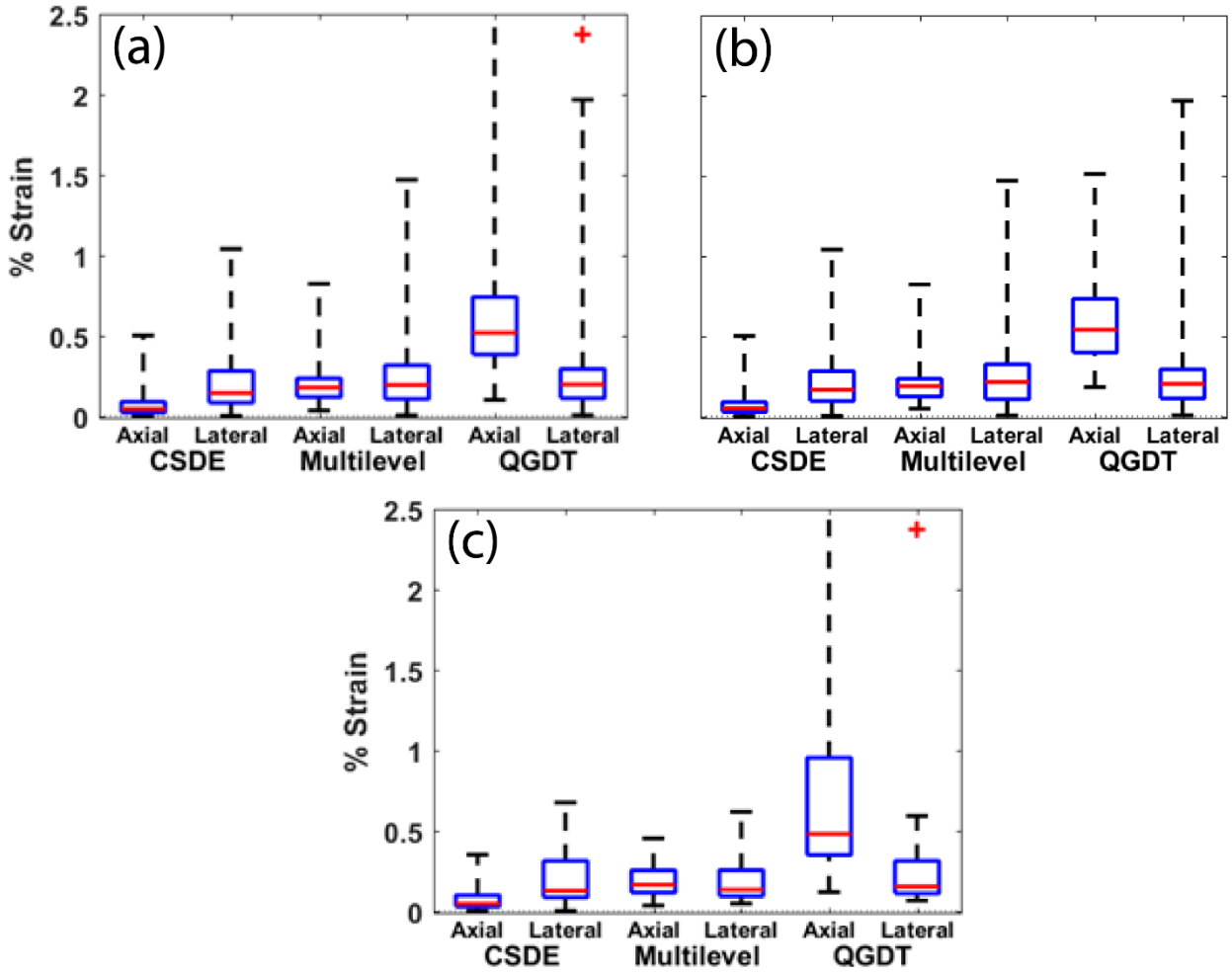

Figure 3.3 - Mean strain magnitude distributions inside the ablation zone. Distributions are shown for (a) all masses, (b) HCC masses, and (c) metastatic masses using CSDE, Multilevel, and QGDT methods.

3.3.2 Standard Deviation of the Strain Distribution

Standard deviation distributions of strain magnitudes illustrated in Figure 3.4 represent all masses (a), HCC (b), and metastatic masses (c). Standard deviation values relate to the amount of variability and noise seen within ablated zones. For all masses represented by Figure 3.4 (a), CSDE has the lowest standard deviation median and range. Multilevel shows low median standard deviation and tight quartiles, but a larger range than CSDE. QGDT on the other hand has the largest median standard deviation and largest range. Both QGDT distributions are skewed toward larger standard deviations. Similar results are seen for HCC masses in Figure 3.4 (b). Note that the metastatic masses in Fig. 4 (c), show similar standard deviation

medians as the masses in Figure 3.4 (a) and (b), but CSDE and Multilevel present with tighter quartiles and ranges. QGDT shows large standard deviation values inside ablated zones of metastatic masses.

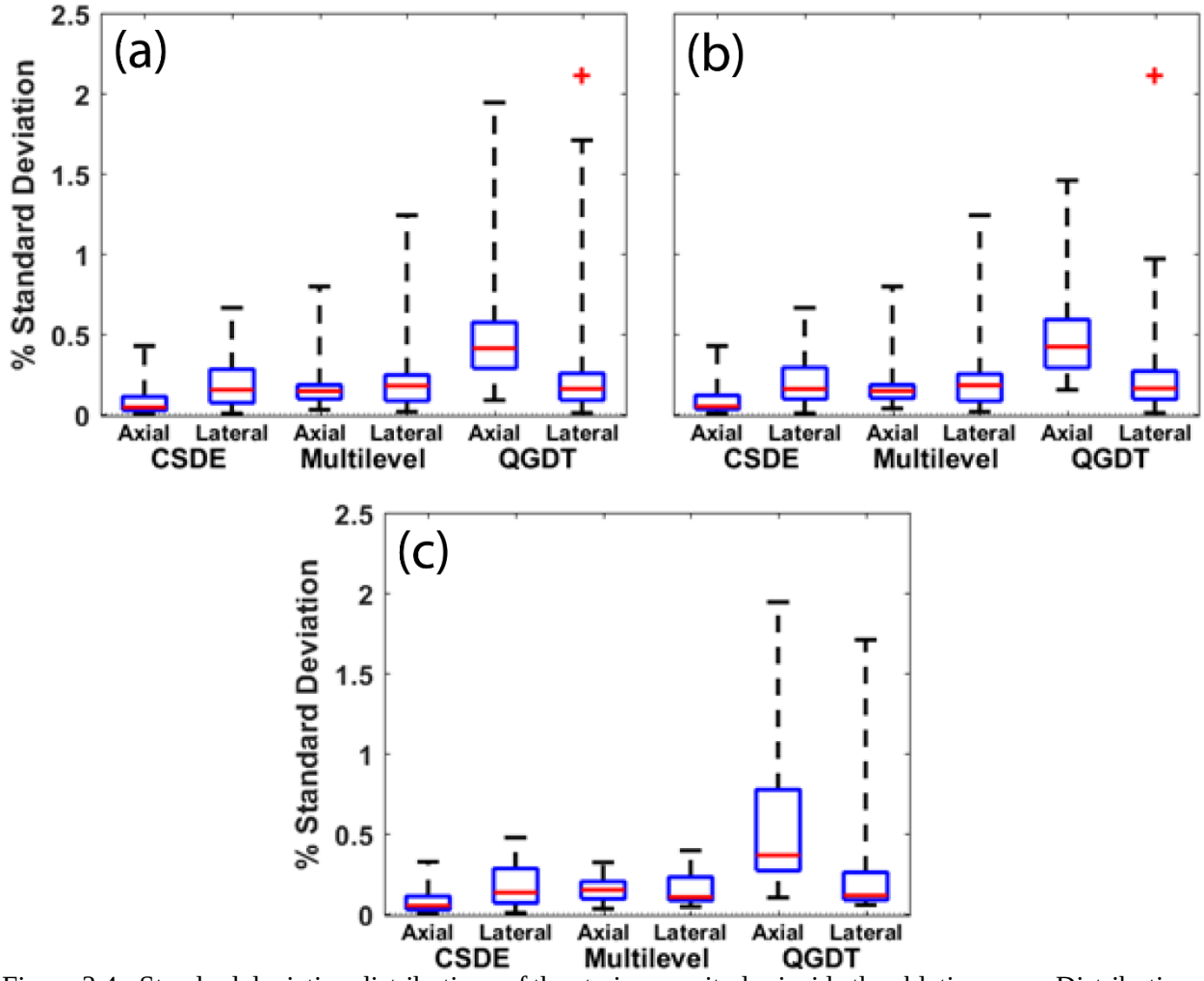

Figure 3.4 - Standard deviation distributions of the strain magnitudes inside the ablation zone. Distributions are shown for (a) all masses, (b) HCC masses, and (c) metastatic masses using CSDE, Multilevel, and QGDT methods.

3.3.3 Ablation Contrast in Strain Tensor Images

Strain magnitude contrast for each mass was calculated using Eqn. (3), and the distribution shown in Figure 3.5. Contrast is indicated as negative since ablated regions present with low strain due to their increased stiffness, while the halo around ablated regions has relatively high strain values. Therefore, lower contrast values, i.e., large negative numbers, indicate increased contrast between ablated region and

surrounding tissue. When all masses are considered in Figure 3.5 (a), axial strain estimated with CSDE shows the largest contrast (median value), and other methods show relatively similar median contrast values. CSDE also indicates larger quartile ranges than the Multilevel and QGDT methods and is skewed toward lower contrasts. Main differences between the strain contrast metric for HCC masses shown in Fig. 3.5 (b), versus that for metastases in Figure 3.5 (c), is the smaller contrast range for metastatic masses when compared to HCC. Axial strain tensors estimated with the Multilevel method provides a consistent contrast range visualized by the tightest distribution for all methods and masses. In general, we anticipate that the stiffness of the ablated region should only vary in a small range when the thermal dose distribution utilized is similar [31, 32].

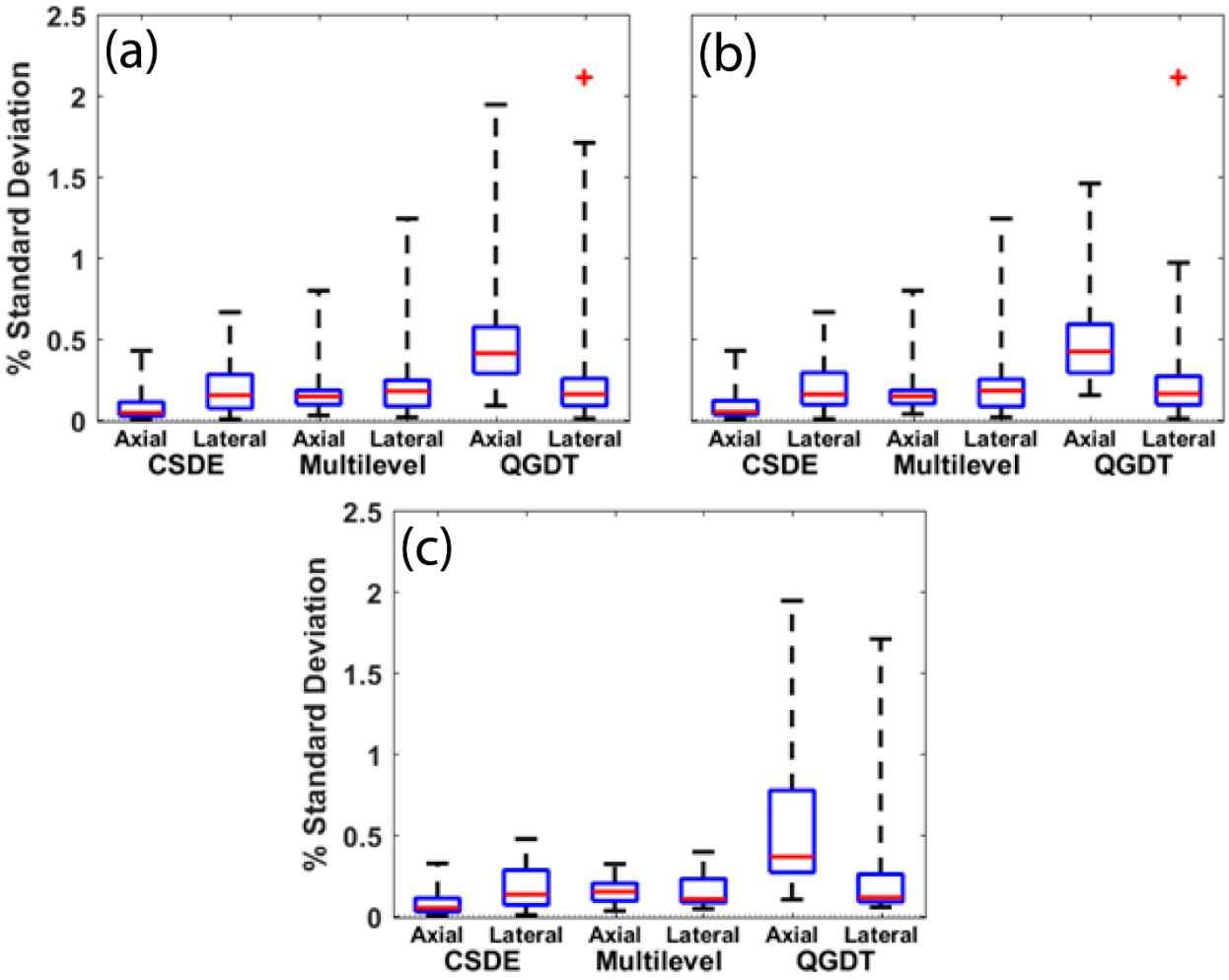

Figure 3.5 - Contrast distributions of the strain magnitudes inside and outside the ablation zone. Distributions are shown for (a) all masses, (b) HCC and (c) metastatic masses using CSDE, Multilevel, and QGDT methods.

3.3.4 Ablation Contrast-to-Noise Ratio in Axial and Lateral Strain Tensor Images

CNR values are calculated using Eqn. (4), and distributions obtained across patients are shown in Figure 3.6. Higher CNR values indicate improved mass detectability [25]. In Figure 3.6 (a), Multilevel and QGDT methods both show the highest median CNR values with tight, similar quartile ranges for all masses. Axial strain estimated with CSDE shows the lowest CNR. In addition, both axial and lateral strains estimated with CSDE have the largest ranges. The CNR for HCC masses in Fig. 3.6 (b) do not vary when compared to the distribution for all masses in Figure 3.6 (a). On the other hand, metastatic masses in Figure

3.6 (c) present with very tight distributions for CNR estimated using QGDT and Multilevel, respectively. Both strain tensors estimated using Multilevel present with positive CNRs for metastatic masses. Axial and lateral strain tensors estimated using CSDE show the largest ranges in CNR, with CSDE axial strain tensors having the lowest CNR.

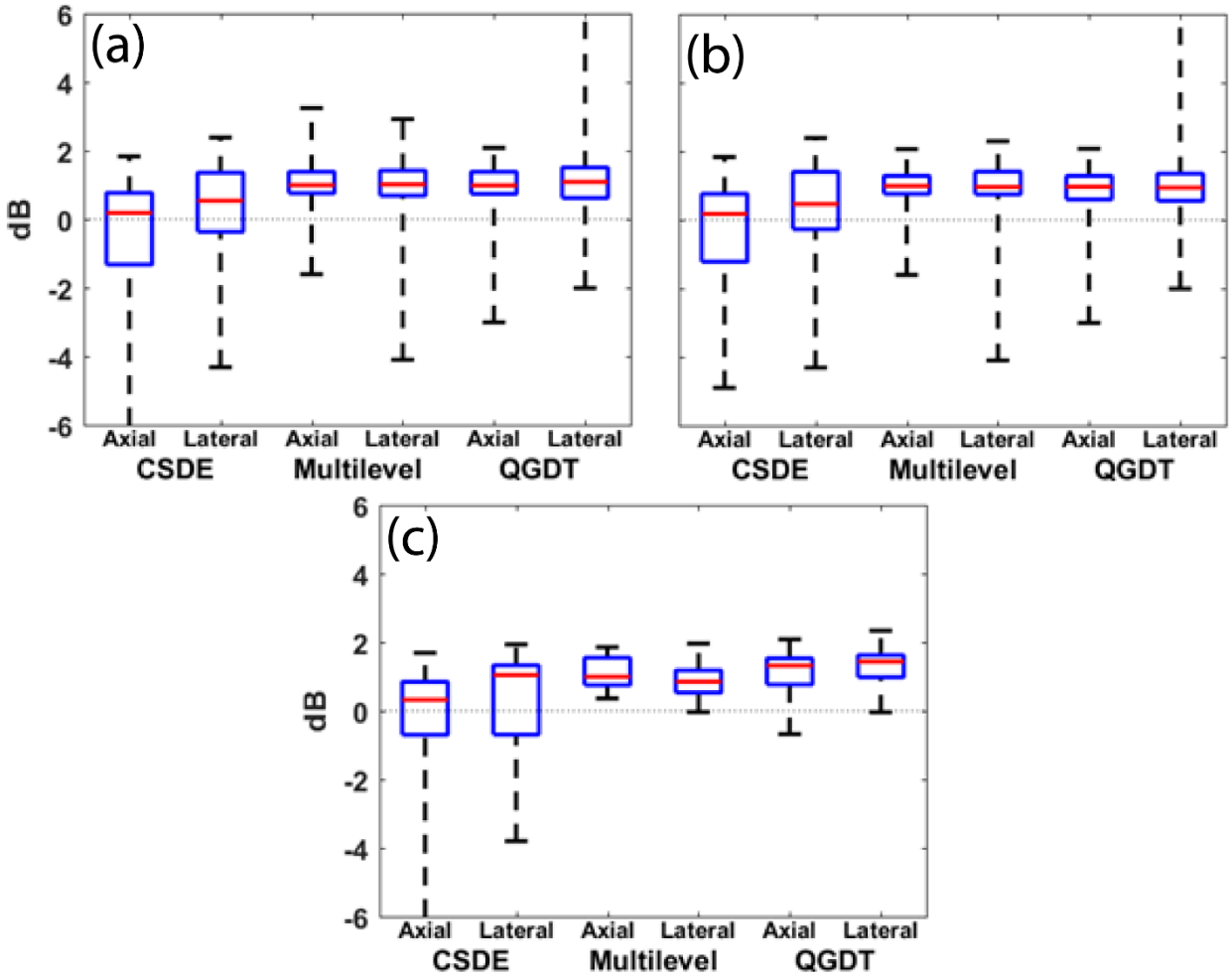

Figure 3.6 - Contrast-to-noise ratio distributions of the strain magnitudes inside and outside the ablation zone. Distributions are shown for (a) all masses, (b) HCC and (c) metastatic masses using CSDE, Multilevel, and QGDT methods.

3.3.5 Ablation Success Rates Based on Ablation Region Visualization

A final important aspect to consider with these displacements tracking methods is how successful and consistent these methods are in visualizing ablation regions. Success rates were calculated using the

same frame pairs that were used in the distributions previously reported in this study by a single observer.

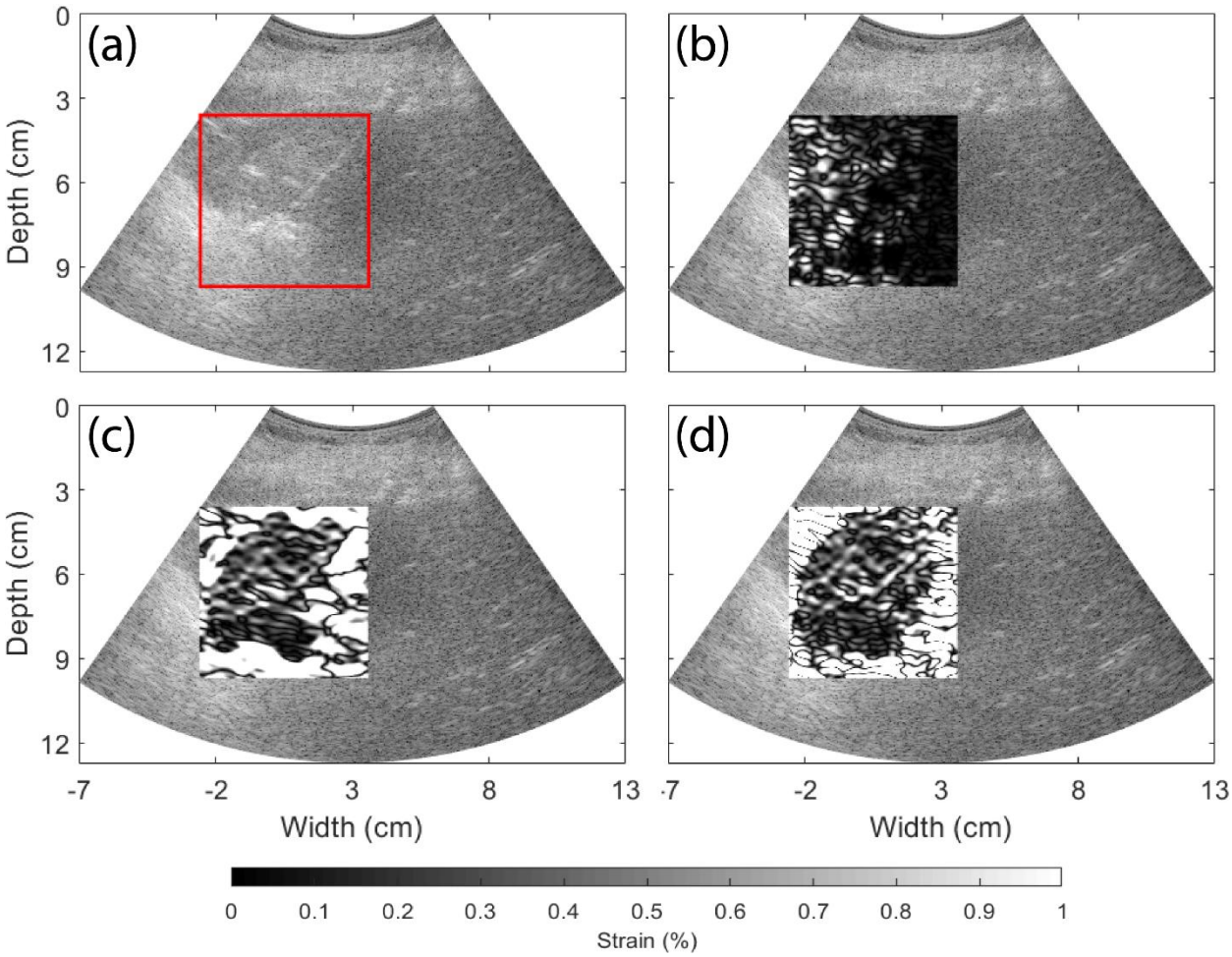

Figure 3.7 - An example of axial strain tensor images of the same frame pair across the three methods. (a) B-mode image with ROI, (b) CSDE axial strain tensor, (c) Multilevel axial strain tensor, and (d) QGDT axial strain tensor. In this example, Multilevel and QGDT axial strain tensors would be deemed successful since ablation region can be visualized, while CSDE is unsuccessful.

Table 3.2 - Success rates for visualizing the ablation region with CSDE, Multilevel, and QGDT for all masses.

	CSDE	**Multilevel**	**QGDT**
Axial	63%	89%	83%
Lateral	69%	79%	68%

The same strain dynamic range (0-1%) was used for all the strain tensor images computed from the three methods. Examples of successful and unsuccessful results are shown in Figure 3.7. Success rates for the three methods are reported in Table 3.2, and noted as a qualitative assessment of the strain tensor images.

3.4 Discussion of Performance of Displacement Estimation Methods

Patient demographics in Table 3.1 are also correlated to the distributions plotted in Figure 3.3 - Figure 3.6, specifically for differences seen relative to mass type. For distributions of the mean strain metric computed in an ROI within the ablated region of each mass type, the distribution for all masses shown in Figure 3.3 (a), closely match that shown for HCC (n = 51) alone in Figure 3.3 (b). This is true for all methods other than for the axial strain tensors generated using QGDT. A similar trend is seen in the distributions of the standard deviation metric in Figure 3.4. These results demonstrate that metastatic masses (n = 21) (see Figure 3.3 (c) and Figure 3.4 (c)), do not contribute significantly to the distributions plotted for all masses for the CSDE and Multilevel methods. Furthermore, the tighter distribution also implies that these methods provide lower noise artifacts for metastatic masses when compared to HCC.

On the other hand, the distribution obtained for the contrast metric estimated from the strain tensor images in Figure 3.5, differ from the distributions seen for the other metrics. Here, the distributions obtained with all three methods do not significantly differ for HCC (Figure 3.5 (b)), versus metastatic masses (Figure 3.5 (c)). On the other hand, CNR distributions in Figure 3.6 show significant differences among mass type. Like Figure 3.3 and Figure 3.4, metastatic masses in Figure 3.6 (c) are represented by tight distributions for the Multilevel and QGDT methods. These results indicate that the local EDE deformations for metastatic masses are tracked with lower standard deviations when compared to HCC masses. These increased standard deviations are also reflected in the CNR distributions.

Based on the distributions of the mean, standard deviation, contrast and CNR metrics shown in Figure 3.3-Figure 3.6, we evaluated the statistical significance of the results for the different metrics and methods. We found that the estimated mean, standard deviation, and CNR metrics computed from the strain tensors demonstrate statistically significant differences between estimation methods with $p <<< 0.001$,

while the contrast metric was not significantly different. Therefore, mean, standard deviation, and CNR are valid metrics for the comparison of estimation methods against each another. In addition, within each estimation method, we did not obtain any statistically significant differences between mass types, indicating that each estimation method produces consistent results regardless of mass type.

Table 3.3 - Mean and standard deviation (std) of the contrast and CNR metric for the three methods.

Method		**Contrast (dB)** mean (std)	**CNR (dB)** mean (std)
CSDE	**Axial**	-15.1 (13.9)	-0.571 (1.98)
	Lateral	-8.94 (12.4)	0.215 (1.59)
Multilevel	**Axial**	-8.42 (4.61)	1.06 (0.633)
	Lateral	-8.93 (6.96)	0.953 (0.918)
QGDT	**Axial**	-8.87 (6.44)	0.924 (0.790)
	Lateral	-9.12 (7.31)	1.13 (0.998)

A comparison of contrast and CNR in axial and lateral strain tensor images for all patients is presented in Table 3.3. CSDE presents with the largest contrast in the axial direction, while the lateral direction for CSDE and both directions for other methods show similar contrasts. Note that the Multilevel method has the highest CNR in the axial direction along with QGDT in the lateral direction. CSDE shows the lowest CNR for both axial and lateral strain tensor images. To demonstrate the need for filtering on displacement estimates, a comparison of CNR obtained with and without median filtering of displacement estimates are shown in Figure 3.8.

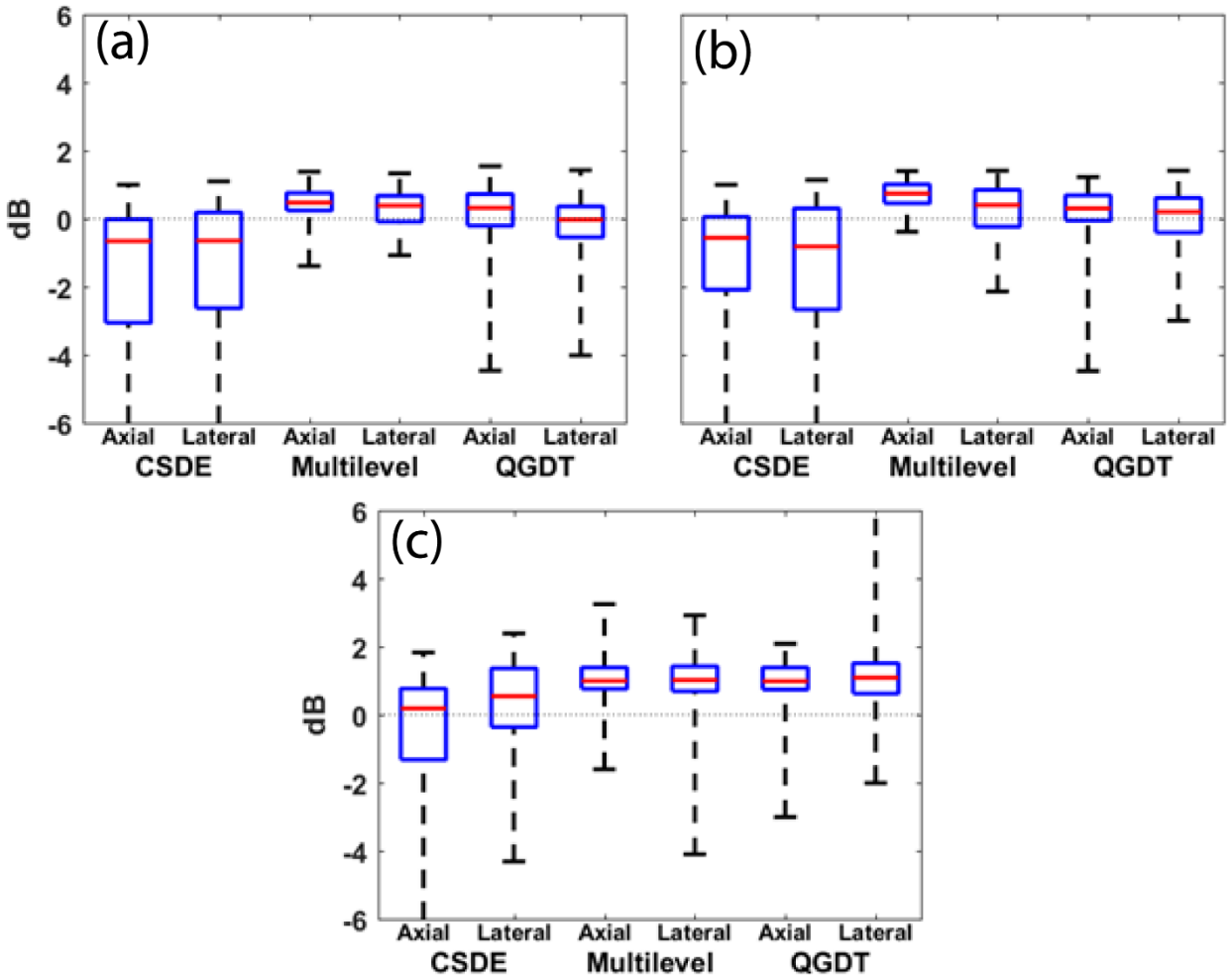

Figure 3.8 - Comparison of CNR distributions after filtering stages for all masses. Distributions are shown for (a) no filtering, (b) median filtering, and (c) median filtering with spline smoothing of displacements before strain estimation.

Observe that with median filtering and spline smoothing, the CNR increases for all displacement tracking strategies, except for axial strain tensors estimated with Multilevel processing where quartile ranges remain similar when compared to median filtered results, but with a larger range after spline filtering. The increase in CNR can be attributed to the reduction of noise artifacts with both filtering approaches. Another example of axial and lateral strain tensor images obtained from the same frame pair for the three different strategies are shown in Figure 3.9. Note that additional filtering within the ablation region after strain tensor estimation was performed to improve visualization of the ablation region. Analogous to results

presented in Figure 3.2, CSDE seems to trend toward larger ablation region dimensions when compared to either Multilevel or QGDT. Although the size differentiation among the methods is not quantified in this study, it is an interesting trend to note and is an important factor for validating tumor ablation margins.

Axial strain tensor images obtained with CSDE show the sharpest delineation with the cleanest looking interiors, but often fail to show delineation at the distal part of the mass. Lateral strain estimated with CSDE does not provide a sharp delineation with clean interiors seen with axial strain but provides better delineation of the distal mass. Axial strain images obtained using Multilevel processing typically provide good delineation for masses over the entire circumference of the mass, however it does not match the sharpness obtained with axial strain tensor images obtained with CSDE. Lateral strain tensor images computed using Multilevel analysis show similar results as the lateral CSDE with improved mass delineation and contrast. Axial strain tensor images estimated with QGDT show good delineation, but also contain the most noise artifacts visualized inside and outside the ablated regions. These increased artifacts are quantified by the standard deviation distributions shown in Figure 3.4. Lateral QGDT provides improved delineation of ablated regions among lateral strain tensor images. An interesting aspect seen in strain tensor images generated with Multilevel and QGDT is that ablated region dimensions are always smaller than ablated regions delineated by CSDE, which is clearly demonstrated in both Figure 3.2 and Figure 3.9.

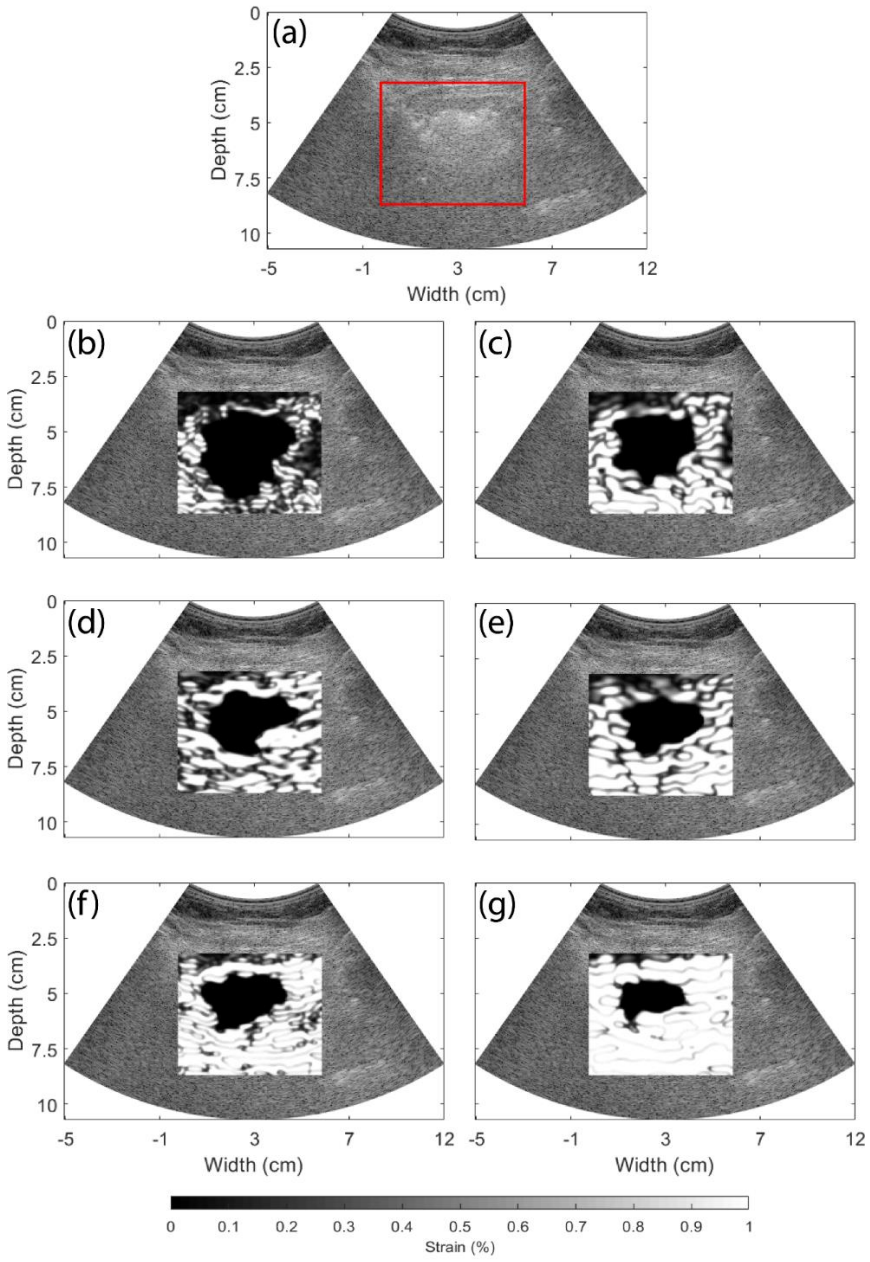

Figure 3.9 - Improved visualization of strain tensor images for a patient with HCC at a depth of 5 cm generated using CSDE, Multilevel, and QGDT, respectively. Additional noise reduction is performed within the ablated region using morphological operators to improve visualization of the ablated region. (a) B-mode image with ROI, (b) CSDE axial strain tensor image, (c) CSDE lateral strain tensor image, (d) Multilevel axial strain tensor image, (e) Multilevel lateral strain tensor image, (f) QGDT axial strain tensor image, and (g) QGDT lateral strain tensor image.

The success rates shown in Table 3.2 show that CSDE provides the lowest image success rate of the three methods, while Multilevel presents the highest success rate for both axial and lateral strain tensors. Interestingly, lateral strain tensor imaging with CSDE has a higher success rate than that obtained with axial strain tensor imaging. Table 3.3 displays the mean and standard deviation for contrast and CNR of CSDE, Multilevel and QGDT. Like the results shown in Figure 3.5, axial strain tensor images obtained with CSDE shows the highest contrast with values approximately 6 dB lower than the other methods. It is also seen that Multilevel and QGDT strain tensor images offer higher CNR than depicted with CSDE.

There are two important points regarding the results presented in this study. First, we present a brief discussion on the need for comparison between mass sizes estimated on strain tensor images and CECT imaging. Unfortunately, obtaining 'true' mass size and areas *in-vivo* in human subjects is difficult, as the ablations are not excised for histopathological analysis. CECT imaging, as the current "gold standard" for post-ablation assessments, offers a means of comparison of ablated lesion dimensions, areas, and volumes. Since current B-mode imaging and RF data collection utilize a curvilinear array, with a single 2D imaging plane, we are limited to displacement tracking and strain estimation along this imaging plane. Therefore, registration of the 2D ultrasound B-mode and strain images to the 3D CECT data sets is essential for accurate comparison of lesion dimensions and areas. A second aspect to be discussed is regularization of strain tensor images, if any, that is incorporated in these methods. CSDE integrates a Viterbi based regularization scheme, while Multilevel and QGDT do not incorporate regularization. Regularization in CSDE may explain the more consistent mean and lower standard deviations of strain estimates within ablated regions due to the additional smoothening that regularization offers. This regularization-based smoothening may also contribute to the differences of visualized lesion size produced by CSDE when compared to the other methods presented.

3.5 Selection of a Displacement Estimation Approach for EDE

CSDE provides the most consistent mean and standard deviation for strain magnitudes within ablation regions as compared to Multilevel and QGDT. Axial strain tensors using CSDE also provide the highest contrast between ablation zones and surrounding liver tissue. However, CSDE only has a 63% success rate when compared to the other methods with higher success rates as shown in Table 3. These results indicate that axial strain tensor images with CSDE may provide better delineation of ablated regions from surrounding tissue than the other methods. Note that the CNR, lies in a similar range (with higher CNR values) for both Multilevel and QGDT, when compared to CSDE. The CNR metric quantifies both the contrast and noise properties of the strain tensor image and is a measure of the detectability of the ablated region in the strain tensor images. Since the emphasis in this chapter is on the depiction and delineation of the ablated region, we utilize the CNR metric. In addition, since the Multilevel method has the highest success of 89% and 79% for axial and lateral strain tensor images, respectively, along with the highest axial CNR and the tightest CNR distributions for axial and lateral strain tensors; it may be the best approach in a clinical setting as it enables more consistent delineation of ablated regions in the clinic. Future work will correlate strain tensor mass sizes with registered CECT mass sizes and will explore regularization methods to improve means and standard deviations of ablated regions estimated with the Multilevel method.

3.6 References

[1] R. M. Pohlman, T. Varghese, J. Jiang, T. J. Ziemlewicz, M. L. Alexander, K. L. Wergin, J. L. Hinshaw, M. G. Lubner, S. A. Wells, and F. T. Lee, Jr., "Comparison of Displacement Tracking Algorithms for *in Vivo* Electrode Displacement Elastography," *Ultrasound in Medicine and Biology*, vol. 45, no. 1, pp. 218-232, 2019, doi: 10.1016/j.ultrasmedbio.2018.09.001.

[2] F. Viola and W. F. Walker, "A comparison of the performance of time-delay estimators in medical ultrasound," *IEEE Transactions on Ultrasonics, Ferroelectronics, and Frequency Control*, vol. 50, no. 4, pp. 392-401, Apr 2003. [Online]. Available: https://www.ncbi.nlm.nih.gov/pubmed/12744395.

[3] R. Zahiri-Azar and S. E. Salcudean, "Motion estimation in ultrasound images using time domain cross correlation with prior estimates," *IEEE Transactions on Biomedical Engineering*, vol. 53, no. 10, pp. 1990-2000, Oct 2006, doi: 10.1109/TBME.2006.881780.

[4] S. Langeland, J. D'Hooge, H. Torp, B. Bijnens, and P. Suetens, "Comparison of time-domain displacement estimators for two-dimensional RF tracking," *Ultrasound in Medicine and Biology*, vol. 29, no. 8, pp. 1177-86, Aug 2003. [Online]. Available: https://www.ncbi.nlm.nih.gov/pubmed/12946520.

[5] M. McCormick, T. Varghese, X. Wang, C. Mitchell, M. A. Kliewer, and R. J. Dempsey, "Methods for robust in vivo strain estimation in the carotid artery," (in eng), *Phys Med Biol*, vol. 57, no. 22, pp. 7329-53, Nov 21 2012, doi: 10.1088/0031-9155/57/22/7329.

[6] Z. Liu, C. Huang, and J. Luo, "A Systematic Investigation of Lateral Estimation Using Various Interpolation Approaches in Conventional Ultrasound Imaging," *IEEE Transactions on Ultrasonics, Ferroelectronics, and Frequency Control*, vol. 64, no. 8, pp. 1149-1160, Aug 2017, doi: 10.1109/TUFFC.2017.2705186.

[7] R. Z. Azar, O. Goksel, and S. E. Salcudean, "Sub-sample displacement estimation from digitized ultrasound RF signals using multi-dimensional polynomial fitting of the cross-correlation function," *IEEE transactions on ultrasonics, ferroelectrics, and frequency control*, vol. 57, no. 11, pp. 2403-2420, 2010.

[8] E. Brusseau, J. Kybic, J. F. Deprez, and O. Basset, "2-D locally regularized tissue strain estimation from radio-frequency ultrasound images: theoretical developments and results on experimental data," *IEEE Transactions on Medical Imaging*, vol. 27, no. 2, pp. 145-60, Feb 2008, doi: 10.1109/TMI.2007.897408.

[9] J. Luo and E. E. Konofagou, "Effects of various parameters on lateral displacement estimation in ultrasound elastography," *Ultrasound Med Biol*, vol. 35, no. 8, pp. 1352-66, 2009, doi: 10.1016/j.ultrasmedbio.2009.03.001.

[10] X. Chen, M. J. Zohdy, S. Y. Emelianov, and M. O'Donell, "Lateral speckle tracking using synthetic lateral phase," *IEEE Transactions on Ultrasonics, Ferroelectronics, and Frequency Control,* vol. 51, no. 5, pp. 540-50, May 2004. [Online]. Available: https://www.ncbi.nlm.nih.gov/pubmed/15217232.

[11] E. S. Ebbini, "Phase-coupled two-dimensional speckle tracking algorithm," *IEEE Transactions on Ultrasonics, Ferroelectronics, and Frequency Control,* vol. 53, no. 5, pp. 972-90, May 2006. [Online]. Available: https://www.ncbi.nlm.nih.gov/pubmed/16764451.

[12] H. Rivaz, E. M. Boctor, M. A. Choti, and G. D. Hager, "Real-time regularized ultrasound elastography," *IEEE Trans Med Imaging,* vol. 30, no. 4, pp. 928-45, 2011, doi: 10.1109/TMI.2010.2091966.

[13] U. Techavipoo, Q. Chen, T. Varghese, and J. Zagzebski, "Estimation of displacement vectors and strain tensors in elastography using angular insonifications," *IEEE Trans Med Imaging,* vol. 23, no. 12, pp. 1479-1489, 2004.

[14] Q. He, L. Tong, L. Huang, J. Liu, Y. Chen, and J. Luo, "Performance optimization of lateral displacement estimation with spatial angular compounding," *Ultrasonics,* vol. 73, pp. 9-21, 2017, doi: 10.1016/j.ultras.2016.08.011.

[15] M. Rao, Q. Chen, H. Shi, T. Varghese, E. L. Madsen, J. A. Zagzebski, and T. Wilson, "Normal and Shear Strain Estimation Using Beam Steering on Linear-Array Transducers," *Ultrasound Med Biol.,* vol. 33, no. 1, pp. 57-66, 2007.

[16] L. Chen, G. M. Treece, J. E. Lindop, A. H. Gee, and R. W. Prager, "A quality-guided displacement tracking algorithm for ultrasonic elasticity imaging," *Medical Image Analysis,* vol. 13, no. 2, pp. 286-96, Apr 2009, doi: 10.1016/j.media.2008.10.007.

[17] J. Jiang and T. J. Hall, "A coupled subsample displacement estimation method for ultrasound-based strain elastography," *Physics in Medicine & Biology,* vol. 60, no. 21, pp. 8347-64, Nov 07 2015, doi: 10.1088/0031-9155/60/21/8347.

[18] H. Shi and T. Varghese, "Two-dimensional multi-level strain estimation for discontinuous tissue," *Physics in Medicine & Biology,* vol. 52, no. 2, pp. 389-401, Jan 21 2007, doi: 10.1088/0031-9155/52/2/006.

[19] L. Chen, G. M. Treece, J. E. Lindop, A. H. Gee, and R. W. Prager, "A quality-guided displacement tracking algorithm for ultrasonic elasticity imaging," *Med Image Anal,* vol. 13, no. 2, pp. 286-96, Apr 2009, doi: 10.1016/j.media.2008.10.007.

[20] W. Yang, T. J. Ziemlewicz, T. Varghese, M. L. Alexander, N. Rubert, A. N. Ingle, M. G. Lubner, J. L. Hinshaw, S. A. Wells, F. T. Lee, Jr., and J. A. Zagzebski, "Post-Procedure Evaluation of Microwave Ablations of Hepatocellular Carcinomas Using Electrode Displacement Elastography," *Ultrasound Med Biol,* vol. 42, no. 12, pp. 2893-2902, Dec 2016, doi: 10.1016/j.ultrasmedbio.2016.07.015.

[21] W. Yang, T. Varghese, T. Ziemlewicz, M. Alexander, M. Lubner, J. L. Hinshaw, S. Wells, and F. T. Lee, Jr., "Delineation of Post-procedure Ablation Regions with Electrode Displacement Elastography with a Comparison to Acoustic Radiation Force Impulse Imaging," *Ultrasound Med Biol,* Jun 05 2017, doi: 10.1016/j.ultrasmedbio.2017.04.021.

[22] J. Jiang and T. J. Hall, "A fast hybrid algorithm combining regularized motion tracking and predictive search for reducing the occurrence of large displacement errors," *IEEE Trans Ultrason Ferroelectr Freq Control,* vol. 58, no. 4, pp. 730-6, Apr 2011, doi: 10.1109/TUFFC.2011.1865.

[23] J. Jiang and T. J. Hall, "A coupled subsample displacement estimation method for ultrasound-based strain elastography," *Phys Med Biol,* vol. 60, no. 21, pp. 8347-64, Nov 07 2015, doi: 10.1088/0031-9155/60/21/8347.

[24] B. Peng, Y. Wang, W. Yang, T. Varghese, and J. Jiang, "Relative Elastic Modulus Imaging Using Sector Ultrasound Data for Abdominal Applications: An Evaluation of Strategies and Feasibility," *IEEE Trans Ultrason Ferroelectr Freq Control,* vol. 63, no. 9, pp. 1432-40, Sep 2016, doi: 10.1109/TUFFC.2016.2589270.

[25] R. M. Pohlman, J. Jiang, W. Yang, T. J. Ziemlewicz, M. L. Alexander, K. L. Wergin, M. G. Lubner, J. L. Hinshaw, F. T. Lee, and T. Varghese, "Comparison study of displacement estimation methods for microwave ablation procedures using electrode displacement elastography," in *Ultrasonics Symposium (IUS), 2017 IEEE International*, 2017: IEEE, pp. 1-4.

[26] H. Shi and T. Varghese, "Two-dimensional multi-level strain estimation for discontinuous tissue," (in eng), *Phys Med Biol,* vol. 52, no. 2, pp. 389-401, Jan 21 2007, doi: 10.1088/0031-9155/52/2/006.

[27] B. Peng, Y. Wang, W. Yang, T. Varghese, and J. Jiang, "Relative Elastic Modulus Imaging Using Sector Ultrasound Data for Abdominal Applications: An Evaluation of Strategies and Feasibility," *IEEE Transactions on Ultrasonics, Ferroelectrics, and Frequency Control,* vol. 63, no. 9, pp. 1432-40, Sep 2016, doi: 10.1109/TUFFC.2016.2589270.

[28] F. Kallel and J. Ophir, "A least-squares strain estimator for elastography," *Ultrasonic Imaging,* vol. 19, no. 3, pp. 195-208, Jul 1997, doi: 10.1177/016173469701900303.

[29] S. Bharat, T. G. Fisher, T. Varghese, T. J. Hall, J. Jiang, E. L. Madsen, J. A. Zagzebski, and F. T. Lee, Jr., "Three-dimensional electrode displacement elastography using the Siemens C7F2 fourSight four-dimensional ultrasound transducer," *Ultrasound in Medicine and Biology,* vol. 34, no. 8, pp. 1307-16, Aug 2008, doi: 10.1016/j.ultrasmedbio.2008.01.007.

[30] J. Jiang, T. Varghese, C. L. Brace, E. L. Madsen, T. J. Hall, S. Bharat, M. A. Hobson, J. A. Zagzebski, and F. T. Lee, "Young's modulus reconstruction for radio-frequency ablation electrode-induced displacement fields: a feasibility study," *IEEE Transactions on Medical Imaging,* vol. 28, no. 8, pp. 1325-34, Aug 2009, doi: 10.1109/TMI.2009.2015355.

[31] M. Z. Kiss, M. J. Daniels, and T. Varghese, "Investigation of temperature-dependent viscoelastic properties of thermal lesions in ex vivo animal liver tissue," (in eng), *J Biomech,* vol. 42, no. 8, pp. 959-66, May 29 2009, doi: 10.1016/j.jbiomech.2009.03.002.

[32] S. Bharat, U. Techavipoo, M. Z. Kiss, W. Liu, and T. Varghese, "Monitoring stiffness changes in lesions after radiofrequency ablation at different temperatures and durations of ablation,"

Ultrasound Med Biol, vol. 31, no. 3, pp. 415-22, Mar 2005, doi: 10.1016/j.ultrasmedbio.2004.12.020.

Chapter 4: Dictionary Learning and Representation for Denoising Displacement Estimates

Ultrasound based electrode displacement elastography (EDE) has demonstrated the potential to monitor ablated regions in human patients after minimally invasive microwave ablation (MWA) procedures. Displacement estimation for EDE is commonly plagued by decorrelation noise artifacts degrading displacement estimates. In this chapter, a global dictionary learning approach is proposed for denoising displacement estimates with an adaptively learned dictionary from EDE phantom displacement maps. The resulting algorithm represents displacement patches sparsely if they contain low noise and averages remaining patches thereby denoising displacement maps while retaining important edge information. Results of dictionary represented displacements presented with higher signal-to-noise ratio (SNR), contrast-to-noise ratio (CNR) with improved contrast, as well as improved phantom inclusion delineation when compared to initial displacement, median filtered displacement, and spline smoothened displacement, respectively. In addition to visualized noise reduction, dictionary represented displacement maps presented with the highest SNR, CNR and improved contrast with values of 1.77 dB, 4.56 dB, and 4.35 dB when compared to axial strain tensor images estimated using the initial displacement map. Following EDE phantom imaging, dictionary representations were validated using *in-vivo* patient data. With dictionary representations utilized for single vector displacements, dictionary learning was then extended to incorporate both displacement vectors to show improved denoising capability.

4.1 Motivation for Use in Elastography

Many algorithms exist for performing displacement estimation, some of which vary in accuracy, sensitivity, spatial and temporal resolution, and complexity, respectively [1-8]. In this chapter we utilize a 2-D Multilevel method previously proposed by Shi and Varghese [9]. This approach uses block matching on a hierarchical pyramid structure, first obtaining coarse estimates followed by finer displacement

R. M. Pohlman and T. Varghese, "Dictionary Representations for Electrode Displacement Elastography," *IEEE Transactions on Ultrasonics, Ferroelectrics, and Frequency Control*, vol. 65, no. 12, pp. 2381-2389, 2018, doi: 10.1109/TUFFC.2018.2874181.

R. M. Pohlman and T. Varghese, "Adaptation of Dictionary Learning for Electrode Displacement Elastography," in *2020 42nd Annual International Conference of the IEEE Engineering in Medicine & Biology Society (EMBC)*, 20-24 July 2020, pp. 2023-2026, doi: 10.1109/EMBC44109.2020.9175319.

estimates. Block matching techniques estimate motion by matching patterns of radiofrequency (RF) or envelope signals between pre- and post-deformation echo signals [10]. Unfortunately, these displacement estimates are commonly plagued by decorrelation noise from non-rigid motion [11]. Some approaches attempt to alleviate this problem via companding [12] or temporal stretching before block-matching [13-15], while many recent approaches utilize regularization during the motion estimation process [16-21].

Regularization during block matching attempts to reduce decorrelation noise and increase local displacement estimate accuracy. A good example of this is shown by Jiang and Hall where the displacement estimation is reframed as an optimization problem to incorporate regularization of the estimated displacement [1]. With this optimization approach, their algorithm can simultaneously estimate a sequence of displacement vectors which maximize correlation and ensure local motion continuity [1]. Another proposed approach [3] applies Bayesian regularization [16] by redefining displacement estimation as a probabilistic function of similarity metrics between neighboring displacement estimates. This is incorporated by treating the similarity metric matrix as a probability density image and assuming neighboring estimates are independent. This follows with modelling probability as the maximum of neighboring probability density image values modulated via a Gaussian function. Rivaz *et al.* reported on a regularization approach utilizing analytic minimization to incorporate constraints on displacement intensity and continuity [17]. Simulation and phantom results present with improved signal-to-noise ratio (SNR) and CNR [5]. Following phantom results, *in-vivo* axial strain images were shown to correlate well with CT and pathology, yet these images lack strong thermal ablation boundary delineation. Despite the reduction in decorrelation artifacts improved boundary visualization of the ablated region is essential for MWA procedure success.

4.2 Background of Dictionary Learning

A more recent regularization approach utilizes the sparseness provided by dictionary learning for cardiac displacement estimation [22], where sparseness is defined as an array or matrix where most of the elements are zero. The idea of using dictionary learning to patch together sparse image patches was first

shown in [23], and has been utilized in several imaging applications [24-28] including denoising [29]. The regularization approach proposed by Ouzir *et al.* frames the displacement estimates as the minimum sum of a data fidelity term based on the Rayleigh noise model and a regularization term based on spatial smoothness and sparsity [22]. The spatial smoothness term enforces small gradients, while the sparsity term reinforces the displacement estimate that is best approximated using a small set of atoms, or sparse set of atoms, from a dictionary. Although implementation of dictionary learning within the displacement estimation process was novel, their approach was limited to using a pre-constructed or offline dictionary.

Other approaches have incorporated machine learning algorithms for liver imaging mainly focusing on classification or image generation. Classification using machine learning is utilized for diagnosing and staging liver fibrosis [30-32]. Liver fibrosis is a pathological process as results in chronic liver diseases. If fibrosis is detected, clinical intervention at early stages can slow the development of liver cirrhosis which often results in liver cancer. Outside of classifying liver fibrosis staging, machine learning shows utility for classifying breast mass as normal, benign, or malignant masses [33]. Machine learning has also been used for reconstructing elastography images in the form elastography directly from radiofrequency (RF) data [34-36] and B-mode images [37] as well as utility with shear wave elasticity images [38]. However, these methods depend on obtaining accurate training models.

In this chapter, we utilize conventional displacement tracking methods but incorporate machine learning utilizing dictionary learning to improve image denoising while retaining boundary information. An adaptively learned global dictionary is utilized for denoising displacement estimates. Initial displacement estimates were calculated using a 2-D Multilevel algorithm [9]. Once displacement estimates are obtained, a sparse and redundant representation of “ideal”, non-synthetic, displacement maps were implemented to reduce the decorrelation noise seen in the displacement maps. Corresponding strain tensor images obtained with dictionary learning were then compared to current approaches used to reduce decorrelation noise in strain imaging. Results are presented utilizing an EDE phantom and reproducibility validated on *in-vivo* data sets acquired on human subjects.

RF data was collected using a Siemens S2000 (Siemens, Malvern, PA) system with a 6C1 HD curvilinear transducer on an EDE phantom with deformations introduced using an actuator (Physik Instrumente (PI) GmbH & Co. KG; Karlsruhe, DE). EDE phantom data collection incorporated 12 independent datasets from maximum distance to minimum distance from transducer with sinusoidal displacements of 100 μm peak magnitude. The transducer center beam line was affixed parallel to needle placed in the phantom.

Human *in-vivo* data sets acquired after minimally invasive MWA procedures with deformations introduced freehand at the University of Wisconsin-Madison Hospital and clinics were then utilized to demonstrate feasibility. *In-vivo* data collection followed a protocol approved by the health sciences institutional review board (HS-IRB) at UW-Madison with patients providing informed consent before procedure commencement. Once MWA antenna placement was verified via CT imaging, 80 frames of RF data were collected while the physician manually perturbed the antenna by approximately ±1mm. Signal processing for displacement estimation, dictionary learning, and strain tensor calculation was done off-line using corresponding software packages in MATLAB.

4.3 Single Displacement Vector Dictionary

Elad and Aharon [29], derived a minimization algorithm for image denoising utilizing dictionary learning. For consistency we will follow a similar notation as used in their paper. Let us assume that we have a known dictionary, $D \in \mathbb{R}^{n \times k}$, where k is the number of atoms (columns vectors $\mathbf{d} \in \mathbb{R}^n$) in the dictionary and $\sqrt{n}$ is the patch height and width, where $k > n$ provides that we have an overcomplete, redundant dictionary. Along with this known dictionary, let us assume we have a noisy displacement estimation map calculated using our Multilevel algorithm. This noisy displacement estimate is median filtered to remove extraneous, false peaks resulting in a median filtered noisy displacement map referred to as Y. The sparsity term from Elad and Aharon's approach utilized an $\ell 0$-norm, which is non-convex, thereby computationally intensive to compute and difficult to obtain an exact solution [39-41]. As a good approximation, the $\ell 1$-norm can be substituted [42-44] changing the minimization equation to (5)

$$\left\{\alpha_{ij}, X\right\} = \arg\min_{\alpha_{ij}, X} \lambda \left\| X - Y \right\|_2^2 + \sum_{ij} \mu_{ij,sparse} \left\| \alpha_{ij} \right\|_1 + \sum_{ij} \left\| D\alpha_{ij} - R_{ij} Y \right\|_2^2 \quad (5)$$

where (i, j) is the block location from the displacement estimate, X is the denoised displacement estimate, Y is the median filtered noisy displacement estimate, and R_{ij} is the matrix that extracts the (i, j) block from the displacement map. Following the same approach as shown in [45], the optimization problem of Eqn. (5) can be rewritten via proximal splitting and solved using the Douglas-Rachford (DR) algorithm [46]. This results in an algorithm that represents patches sparsely if a sparsely represented patch and corresponding noisy patch are similar, otherwise it simply averages a patch with overlapping neighbor patches thereby reducing noise. The algorithm in (5) assumes a known fixed dictionary. There are three different methods we can use for selecting the dictionary: predefining an overcomplete dictionary, adaptively learning a dictionary on every displacement map that will be denoised, or adaptively learning a global dictionary from a set of "good" examples that can be used globally over all the data for denoising [29].

One of the simplest methods for evaluation of sparse representations is utilizing a pre-constructed dictionary. Several examples of pre-constructed dictionaries are described in the literature [42, 47, 48]. Adaptively learned dictionaries on the other hand provide improved reconstruction performance [49]. Although an adaptively learned dictionary for each displacement map may provide the best reconstruction results as shown in [29], a globally learned dictionary may be sufficient for producing reproducible denoising performance. This will save computational time when compared to computing a dictionary for each displacement map. In addition, all displacement maps can be represented using a linear combination of these ideal displacement patches.

To adaptively learn a global dictionary, an additional iterative processing chain is added to the algorithm. Now assuming dictionary D is unknown, we create our initial dictionary directly from our noisy median filtered displacement Y estimated using a Multilevel method from an EDE phantom. This begins by selecting an arbitrary number m of $\sqrt{n} \times \sqrt{n}$ patches from Y with the largest root mean squared energy

providing m representative noisy patches $(y_j)_{j=1}^{m} \in \mathbb{R}^{n \times m}$. Of these y_j patches, k patches were randomly selected as the initial atoms $\mathbf{d}$ for the dictionary, D. An example of normalized initial atoms for a dictionary are shown in Figure 4.1 (a) where the atoms have dimensions of 10 pixels × 10 pixels (4 mm × 4 mm) chosen randomly from y_j. Each atom was normalized independently such that minimum to maximum values of each atom range from 0 to 1. The dictionary learning process then begins by minimizing the constrained optimization problem shown by (2)

$$\min_{\|\alpha\|_0 \leq \kappa} \frac{1}{2} \|y - D\alpha\|^2 \tag{6}$$

where $\kappa > 0$ is the upper bound sparsity of coefficients α. The iterative dictionary learning optimization alternates between updating dictionary atoms $\mathbf{d}$ and coefficients α, and is solved using a block-coordinate descent method [50]. Once this iterative process is completed, the global dictionary shown in Figure 4.1 (b) can be used for dictionary representations. Note the adjustments of atoms shown in Figure 4.1 (b) that occurs during the dictionary learning process to reduce noise and provide better sparse representations of the median filtered displacements.

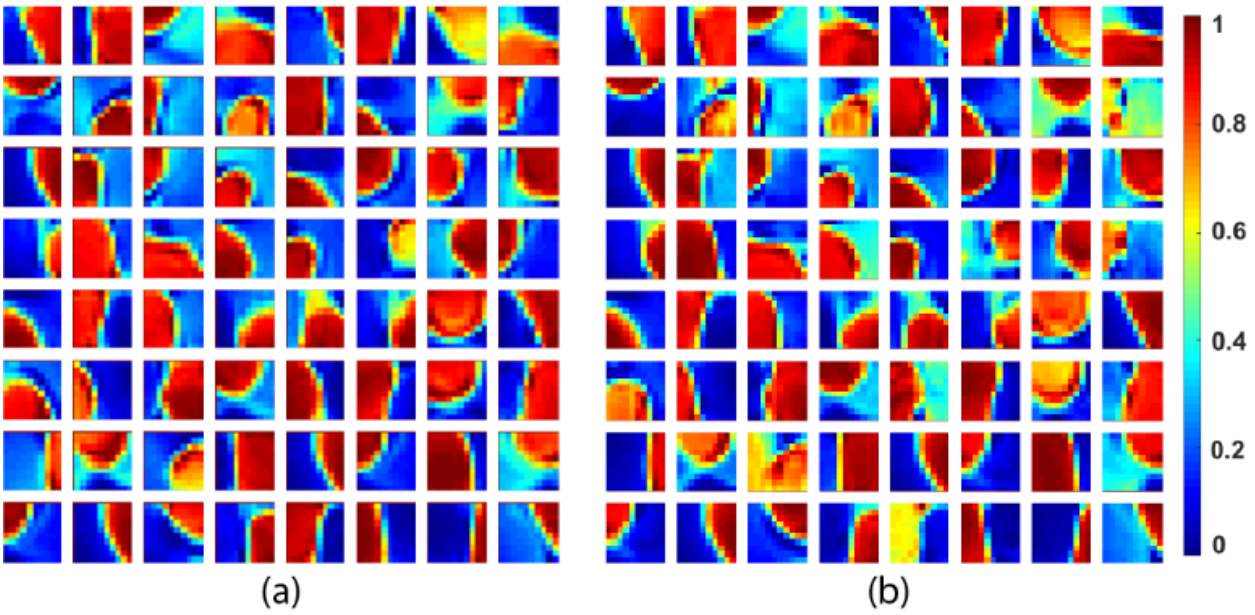

Figure 4.1 - Examples of dictionary atoms before and after training. (a) The initial dictionary atoms selected from the phantom median filtered displacement map and (b) the same dictionary atoms after iterative training.

Displacements between frames of maximum to minimum axial displacement were estimated utilizing a Multilevel approach demonstrated in [9] using a kernel sizes of [16, 12, 8, 4] wavelengths × [7, 5, 3, 3] A-lines. Median filtering with a window size of 1.9 mm × 1.9 mm was used to remove false peaks from displacement estimation. After median filtering, the displacement estimate was resampled to result in a pixel size of 0.4 mm × 0.4 mm and normalized. A globally learned dictionary was then trained from median filtered displacement frames demonstrating the largest inclusion displacement ($n=12$). A patch size of 10 × 10 pixels was chosen using a heuristic approach as a compromise between computational load and denoising performance, utilizing $k=200$ atoms for the dictionary, resulting in $D\in\mathbb{R}^{100\times200}$. The upper bound sparsity of $\kappa=4$ was used and (6) is iterated until $\left\|D_{\tau+1}-D_{\tau}\right\|<10^{-4}$ or 500 iterations have been reached. Utilizing this globally learned dictionary, median filtered displacements were denoised for all displacement maps estimated. During the denoising iterative process, the sum of squared errors (SSE) between estimated denoised patches and clean patches shown in (7) was computed. Denoising was iterated

until the root mean squared error (RMSE) between iterations fell below a convergence value chosen heuristically to be 5×10^{-6} as shown in (8).

$$Error_{\tau}(j)=\sqrt{\sum_{i=1}^{n}\left[\left(D\left(\alpha_{i,j}\right)_{\tau}-y_{i,j}\right)^{2}\right]}\quad 1\le j\le m \tag{7}$$

$$\left[\sqrt{\frac{1}{m}\sum_{j=1}^{m}\left(Error_{\tau}(j)-Error_{\tau-1}(j)\right)^{2}}\right]\le 5\times10^{-6} \tag{8}$$

Computational time required for the global dictionary training was approximately 5 minutes while the displacement dictionary representation convergence required approximately 2 minutes for a typical sector ultrasound image of width and depth 8 cm × 12 cm (200 pixels × 300 pixels). All processing was performed on a Windows 10 desktop PC with Intel Core i7-7700K CPU (4× 4.20 GHz) and 48 GB DDR4 RAM.

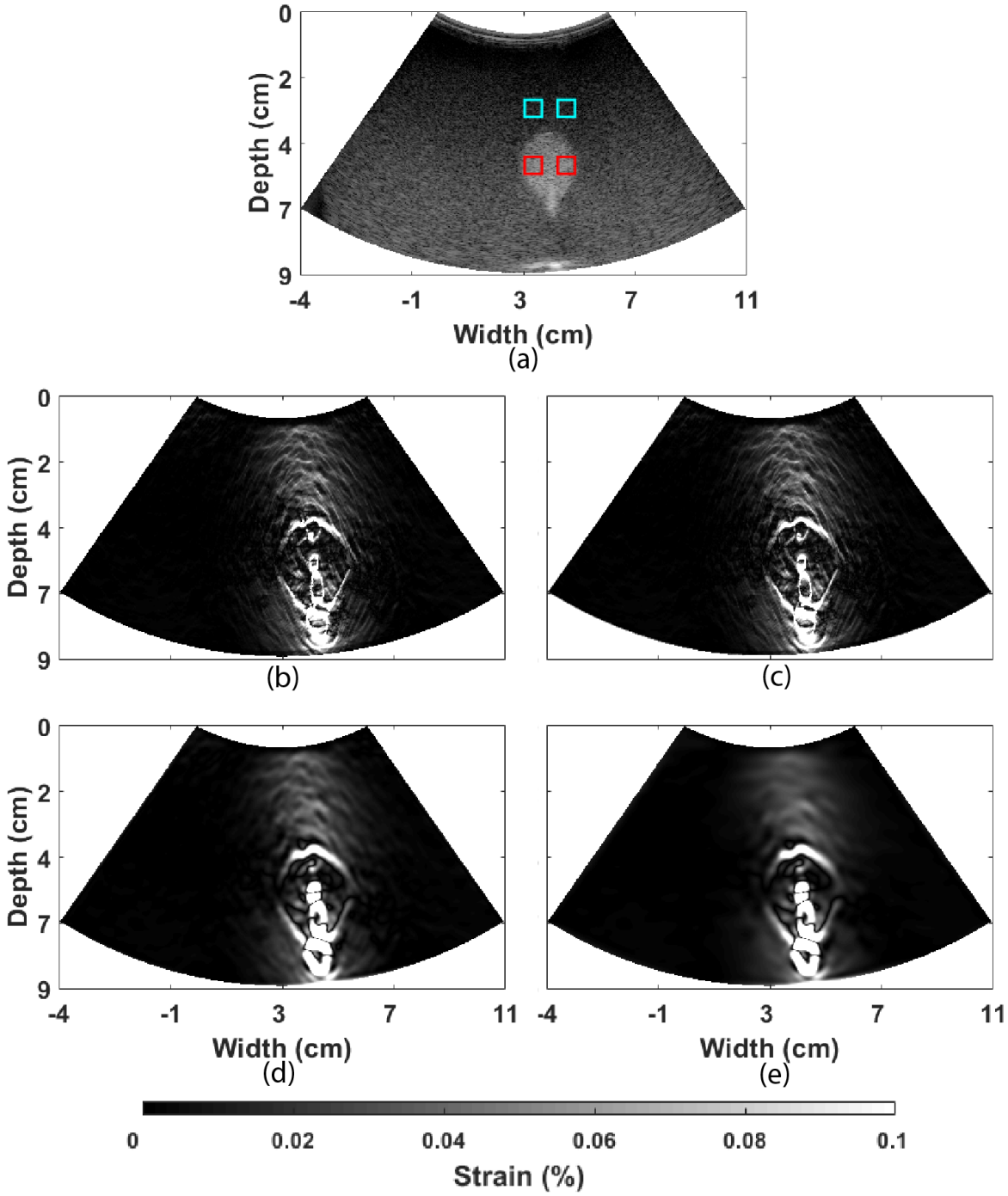

Figure 4.2 – Axial strain tensor images showing visualization differences with the filtering approaches on the EDE phantom. (a) B-mode image of EDE phantom pre-deformation with region-of-interest used for quantitative metrics, strain tensor images from (b) initial estimated displacement, (c) median filtered displacement, (d) spline smoothening of median filtered displacement, and (e) dictionary represented displacement.

4.3.1 Comparison with Conventional Filtering Approaches

After the displacement estimates were denoised via dictionary representation, the inclusion was visualized from strain tensor images calculated using a least-squares method after filtering and dictionary denoising [2]. Denoised strain tensor images were compared to strain tensor images after median filtering and spline smoothening [51, 52]. In the interest of quantifying strain tensors from initial displacement maps and displacement maps represented by a sparse set of dictionary patches, we utilized similar region-of-interest (ROI) as used in [53]. We then calculated the following three quantitative metrics shown in Eqn. (9), (10), and (11), namely the SNR, contrast, and CNR [51, 52]

$$SNR = \frac{\bar{s}_I}{\sigma_I} \tag{9}$$

$$Contrast = \frac{\bar{s}_I}{\bar{s}_B} \tag{10}$$

$$CNR = \frac{2(\bar{s}_I - \bar{s}_B)^2}{(\sigma_I^2 + \sigma_B^2)} \tag{11}$$

where I and B refer to the inside and background ROIs respectfully, $\bar{s}$ and σ are the mean and standard deviation of strain tensor magnitudes.

4.3.2 Comparison of Single Displacement Vector Dictionary to Conventional Filtering

For the purposes of providing deformations to the inclusion in the EDE phantom, cyclic motions using a linear actuator were used as previously discussed. Since cyclic motions were used, peak displacements occur during downward and upward motions generated by the actuator. Peak displacements were used because they provide the largest deformation applied to the inclusion. Over the 120 RF frames collected, this peak displacement occurs n = 12 times. Strain tensor images for an EDE phantom with sinusoidal displacements with a peak magnitude of 100 μm are shown in Figure 4.2.

Figure 4.2 shows the advantages of dictionary-represented displacements for strain tensor visualization. Figure 4.2 (a) displays the B-mode image of an EDE phantom with ROIs selected to avoid the needle artifacts near the bottom of the inclusion representative of the inside and outside of the inclusion

in red and blue, respectively. Figure 4.2 (b) shows the axial strain tensor image obtained from the initial displacement calculated with a Multilevel method, (c) median-filtered Multilevel displacement, (d) spline smoothened, median-filtered Multilevel displacement, and (e) dictionary represented Multilevel displacement.

Qualitatively in Figure 4.2 (e), improvements obtained utilizing dictionary denoising were observed in the increased homogeneity in strain tensor magnitudes above the inclusion as well as a slight reduction in the noise artifacts seen inside the inclusion, disregarding the needle artifacts. Additionally, we note no loss of inclusion delineation in the visualized strain tensor image, respectively. Note that with utilizing solely median filtering, very small changes in the strain tensor magnitudes are seen inside and outside the inclusion between the initial, nonfiltered displacement except for a slight smoothening seen above the inclusion and along the boundary. Using spline smoothening after median filtering reduces noise seen both inside and outside the inclusion while retaining the edge information, providing better visualization over median filtering alone. However, inspection of strain tensor image produced from dictionary represented displacements provides reduction in noise above the inclusion as well as in homogeneous regions of the phantom, lateral to the inclusion. A slight reduction of noise is also perceived within the inclusion without any loss of inclusion boundary sharpness. Note that a needle artifact exists in all strain tensor images near the bottom and below the inclusion.

Following visualization of the inclusion, a quantitative comparison of displacement estimation results was performed for strain tensor imaging. ROIs were selected to avoid the needle artifact near the bottom of the inclusion and strain tensor magnitudes were used since visualization only requires relative differences in strain. Quantitative distribution of the parameters over all displacement frames is shown in Figure 4.3 - Figure 4.5 showing that dictionary represented strain tensor images provided statistically significant improvements in SNR and CNR ($p < 0.001$) calculated using a one-way analysis of variance.

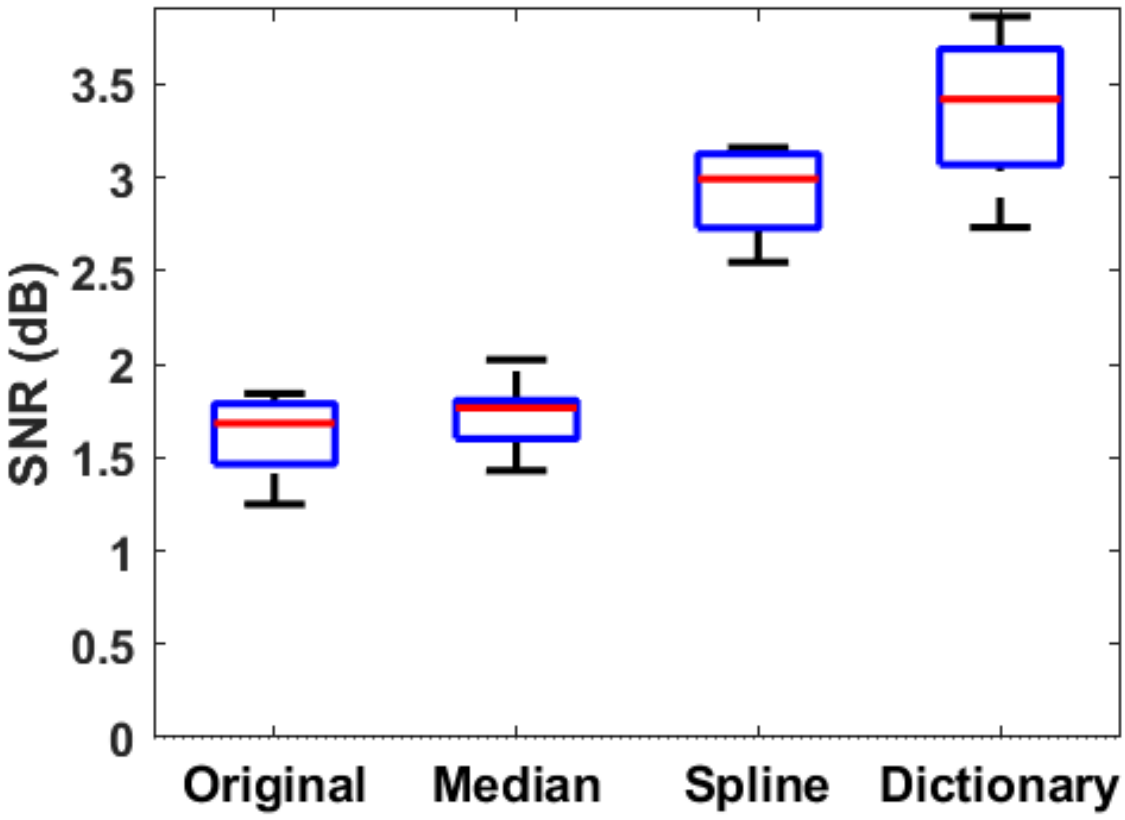

Figure 4.3 – Signal-to-noise ratio distributions of the axial strain tensor magnitude utilizing ROIs inside and above the EDE phantom inclusion and calculated over 12 independent realizations. Distributions are shown for initial displacement (1.61 dB), median filtered displacement (1.73 dB), median filtered displacement with spline smoothening (2.93 dB), and dictionary represented displacement (3.38 dB). Mean values are presented in parenthesis.

Figure 4.3 displays inclusion strain tensor SNR distributions over the 12 displacement frames estimated. All methods demonstrate a positive SNR above 1 dB. Median filtering increases the SNR seen from initial displacement estimate, which can be attributed to reducing large peaks inside of the phantom inclusion. Following median filtering, spline smoothening greatly increases strain tensor SNR, nearly doubling the median SNR with similar distribution width. Greater SNR values can be credited to noise reduction that spline smoothening offers. Now looking at distributions from the proposed, dictionary

represented approach, we see the largest SNR values with median and quartile values greater than the median SNR from any other method. Greater SNR values are likely from the denoising obtained with the sparseness dictionary representation offers.

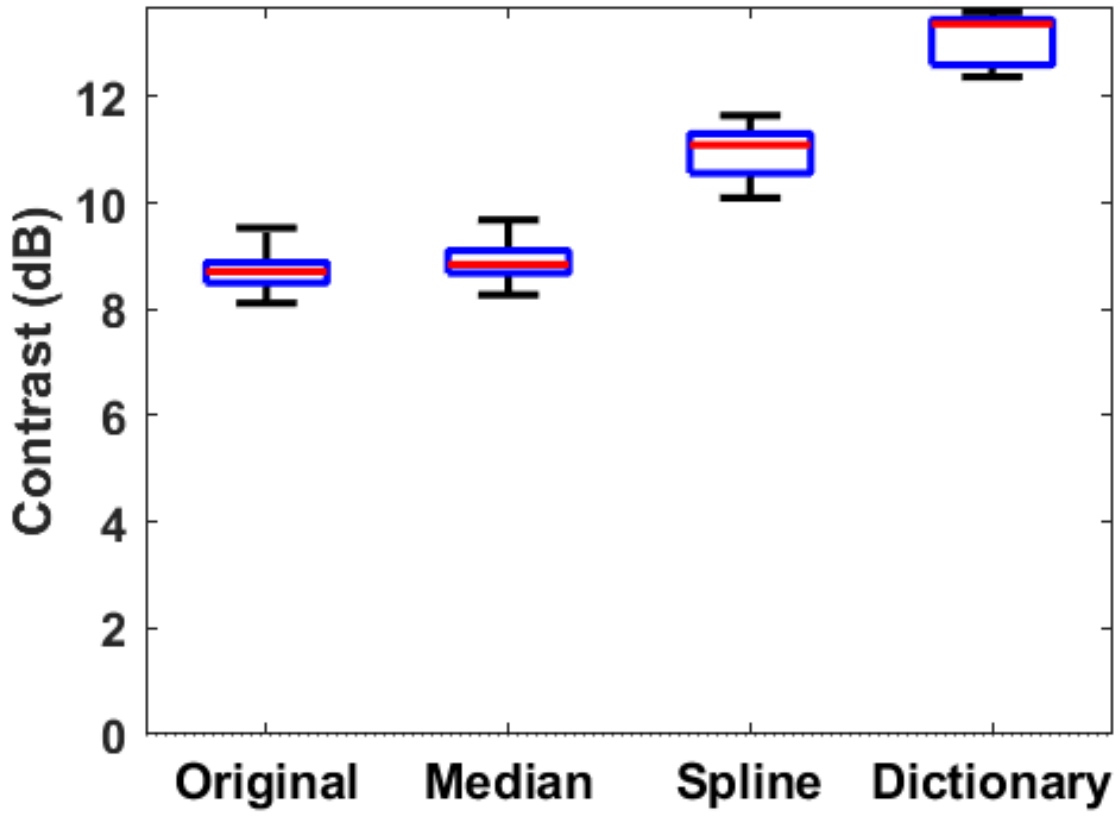

Figure 4.4 – Contrast distributions of the axial strain tensor magnitude utilizing ROIs inside and above the EDE phantom inclusion and calculated over 12 independent realizations. Distributions are shown for initial displacement (8.72 dB), median filtered displacement (8.90 dB), median filtered displacement with spline smoothening (10.92 dB), and dictionary represented displacement (13.07 dB). Mean values are presented in parenthesis.

Using Eqn. (10) contrast distributions were calculated and shown in Figure 4.4. Contrast values are positive since the stiffer phantom inclusion presents with lower strain values while the softer background regions outside of the inclusion provide higher strain values. Following this logic, larger values result in

higher contrast between the phantom inclusion and surrounding medium. Median filtering of displacements appears to provide little contrast improvement from initial displacement estimates. Spline smoothening shows significantly more improvement for median and quartile values increasing entire distribution by approximately 2 dB. Dictionary represented strain tensor images demonstrate the greatest distribution of contrast values with an additional increase of 2 dB over spline smoothening contrast. Distributions from all methods retain a similar width, while the spline smoothening and dictionary representation demonstrate wider quartile ranges.

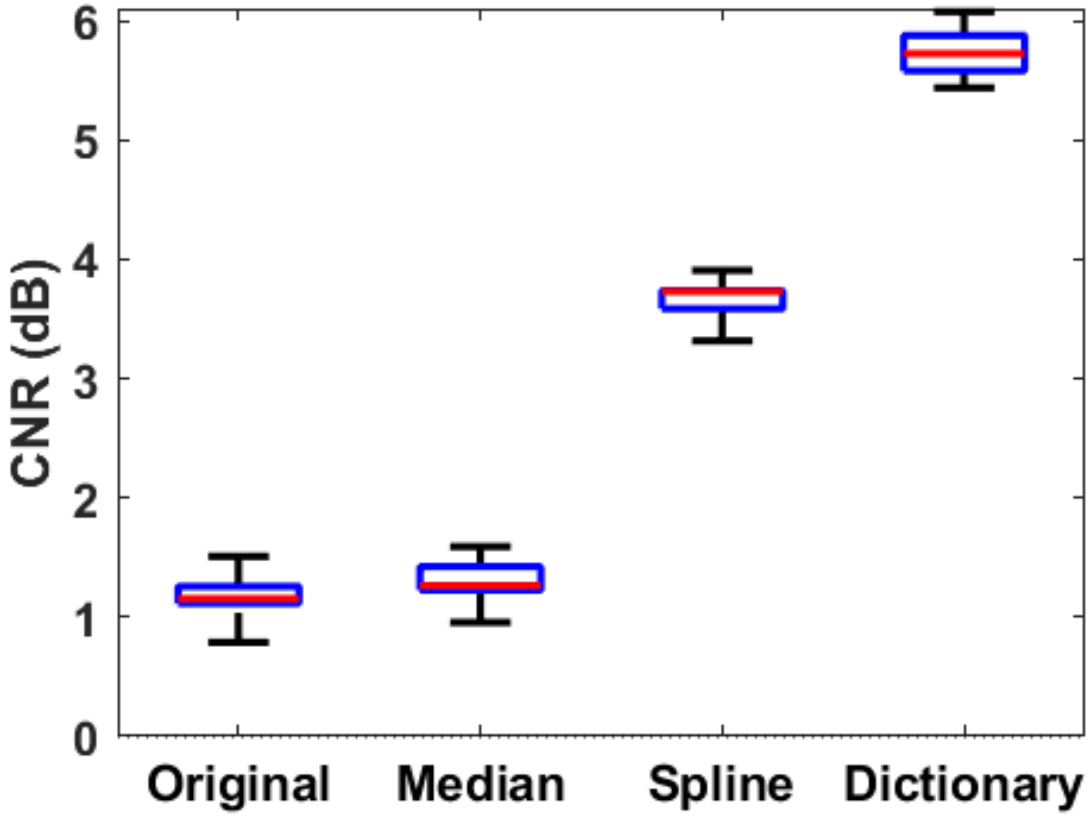

Figure 4.5 – Contrast-to-noise ratio distributions of the axial strain tensor magnitude utilizing ROIs inside and above the EDE phantom inclusion and calculated over 12 independent realizations. Distributions are shown for initial displacement (1.37 dB), median filtered displacement (1.30 dB), median filtered displacement with spline smoothening (3.66 dB), and dictionary represented displacement (5.73 dB). Mean values are presented in parenthesis.

In Figure 4.5, CNR distributions calculated using (11) are shown. Median filtered and initial displacement distributions show positive and similar results slightly above 1 dB. Although median filtering removes noise from displacement estimates, it does not affect contrast levels noticeably accounting for the similar CNR values after median filtering. Spline smoothening after median filtering increases CNR values, likely due to noise removal and some improvement in contrast. Utilizing a dictionary represented displacement provides the highest CNR values seen as compared to the other methods. These higher CNR values can be attributed to not only large noise removal of displacements but also improvement in contrast that dictionary representations provide.

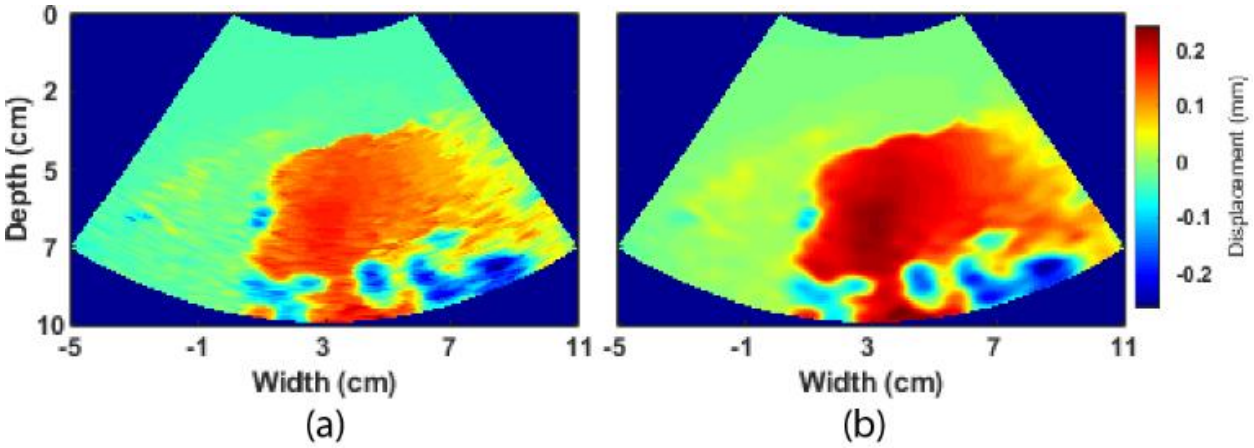

Figure 4.6 – Displacement maps from a patient with colon metastasis at a depth of 6 cm demonstrating improved displacements from dictionary representations. (a) The initial displacement map estimated after median filtering and (b) the same displacement map after dictionary representation.

Now with knowledge that dictionary representations increase detectability and visualization of the inclusion in the phantom, dictionary represented displacements were validated using *in-vivo* data. Dictionary used for representing *in-vivo* displacements was the same dictionary learned from EDE phantom median filtered displacement maps. Results on *in-vivo* data are shown in Fig. 4.6 – 4.8.

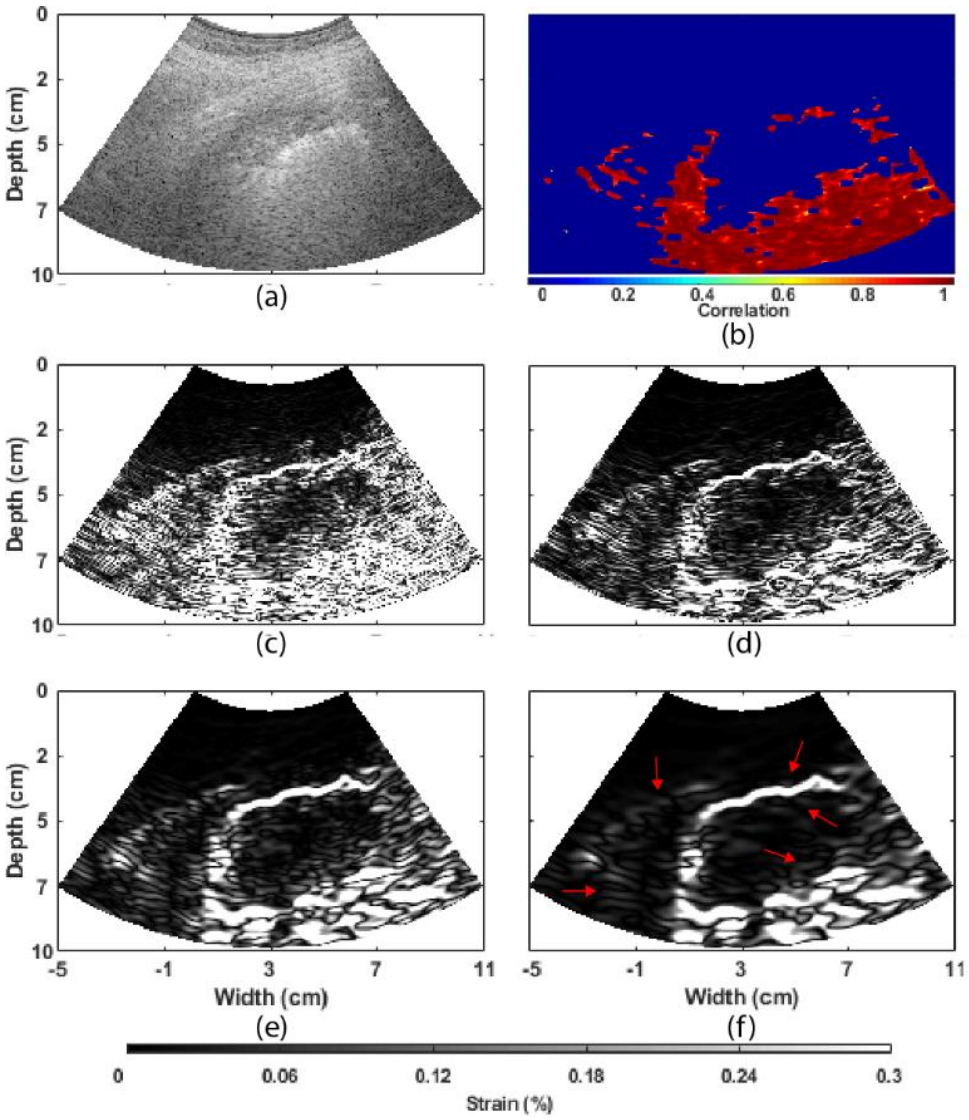

Figure 4.7 – EDE based axial strain tensor images for a patient with colon metastases at a depth of 6 cm showing visualization differences with the different filtering approaches. (a) B-mode image of the ablated colon metastases, (b) correlation map between dictionary and initial displacement patch. Strain tensor images using (c) estimated displacement with no filtering (SNR: 1.09 dB, contrast: 11.6 dB, CNR: -1.13 dB), (d) median filtered displacement (SNR: -1.89 dB, contrast: 13.7 dB, CNR: -1.40 dB), (e) spline smoothening median filtered displacement (SNR: 1.58 dB, contrast: 14.9 dB, CNR: 0.51 dB), and (f) dictionary represented displacement (SNR: 2.38 dB, contrast: 14.5 dB, CNR: 0.97 dB). Arrows indicate locations where dictionary representation provided noticeable noise reduction, yet ablated region edge information was maintained.

Although quantitative improvements in dictionary learning on axial strain tensor images are presented, these are also visualized on displacement maps as shown in Figure 4.6. Figure 4.6 (a) shows the initial displacement map where decorrelation noise artifacts are seen as the blurred boundaries on the right side of the ablated region. Alternatively, Figure 4.6 (b) presents the dictionary represented displacement map that is smoother with better-defined ablated region boundaries and a clearly delineated right side of the ablated region, retaining a similar displacement magnitude range to the median filtered displacement.

Figure 4.7 provides an example on the use of dictionary representation for EDE via axial strain tensor images from the same *in-vivo* human subject data as shown in Figure 4.6. Using median filtering shown in Fig. 4.7 (d) corresponding to the displacement map shown in Figure 4.6 (a), we see some denoising of the ablated region when compared to initial displacements in Fig. 4.7 (b), yet the boundary remains noisy and difficult to determine. Following median filtering, spline smoothening reduces ablated region noise and provides a slight increase in ablated region contrast. Although noise is reduced, rough and jagged edges linger along the ablated region boundary along with noise lateral to the ablated region. If instead of using spline smoothening, we utilize a dictionary representation, the highest reduction of noise is visualized as shown in Fig. 4.7 (f) corresponding to the displacement map in Figure 4.6 (b). This patch representation effectively reduced noise seen both inside and outside the ablated region as shown by the red arrows, while retaining a high contrast ablated region boundary. Figure 8 presents similar results for a patient with an ovarian metastasis at a depth of 9 cm. These axial strain tensor images display a similar trend as in Fig. 4.7.

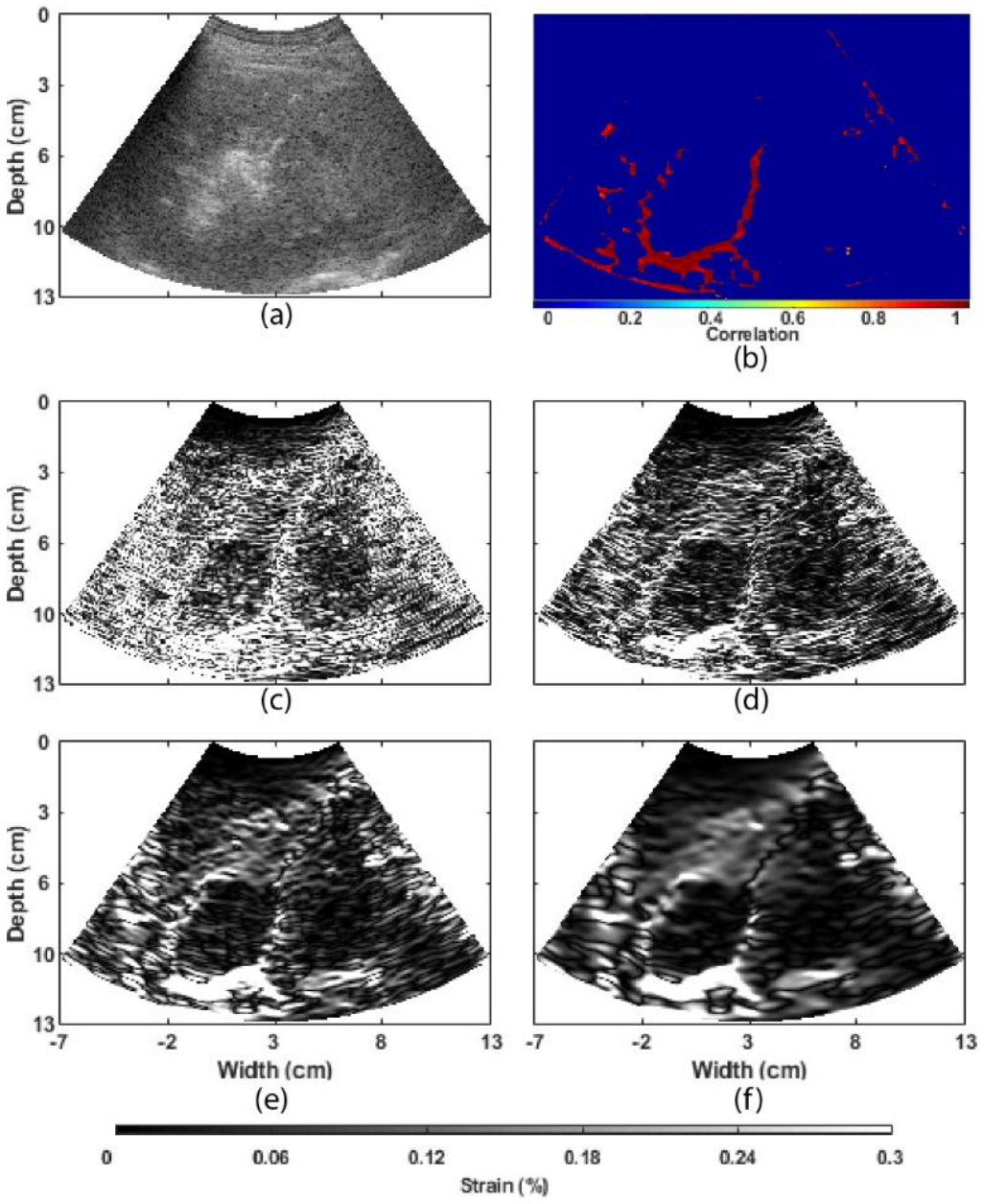

Figure 4.8 – EDE based axial strain tensor images for a patient with ovarian metastasis at a depth of 9 cm showing visualization differences with different filtering approaches. (a) B-mode image the ablated ovarian mass with the MWA antenna, (b) correlation map between dictionary patch and initial displacement patch, and strain tensor images from (c) estimated displacement with no filtering (SNR: 0.67 dB, contrast: 12.0 dB, CNR: -1.00 dB), (d) median filtered displacement (SNR: -0.47 dB, contrast: 14.5 dB, CNR: -1.73 dB), (e) spline smoothening median filtered displacement (SNR: 4.75 dB, contrast: 14.8 dB, CNR: 0.46 dB), and (f) dictionary represented displacement (SNR: 5.31 dB, contrast: 15.1 dB, CNR: 0.74 dB).

4.3.3 Benefits of Dictionary Learning for Electrode Displacement Elastography

Improvements using dictionary representation from the phantom experiments are shown in Table 4.1. These results demonstrate that dictionary representations provide the highest SNR, CNR and improved contrast. For all values compared, the trend is towards higher values with additional filtering performed.

Table 4.1 – Dictionary representation improvements for SNR, contrast, and CNR for displacement estimates where peak inclusion displacement occurs (n=12).

	DICTIONARY IMPROVEMENT		
	SNR	**Contrast**	**CNR**
INITIAL	23%	65%	185%
MEDIAN	21%	61%	177%
SPLINE	5%	28%	61%

For depicting success of utilizing sparse representations for the inclusion, we computed the normalized cross correlation between sparsely represented displacement patches and initial noisy image patches. Note the displacement patches that were represented via sparse representations and patches that were averaged to reduce noise are clearly visualized in Figure 4.9, where (a) shows the estimated displacement with median filtering, (b) the normalized cross correlation of patch representation, and (c) dictionary represented displacement.

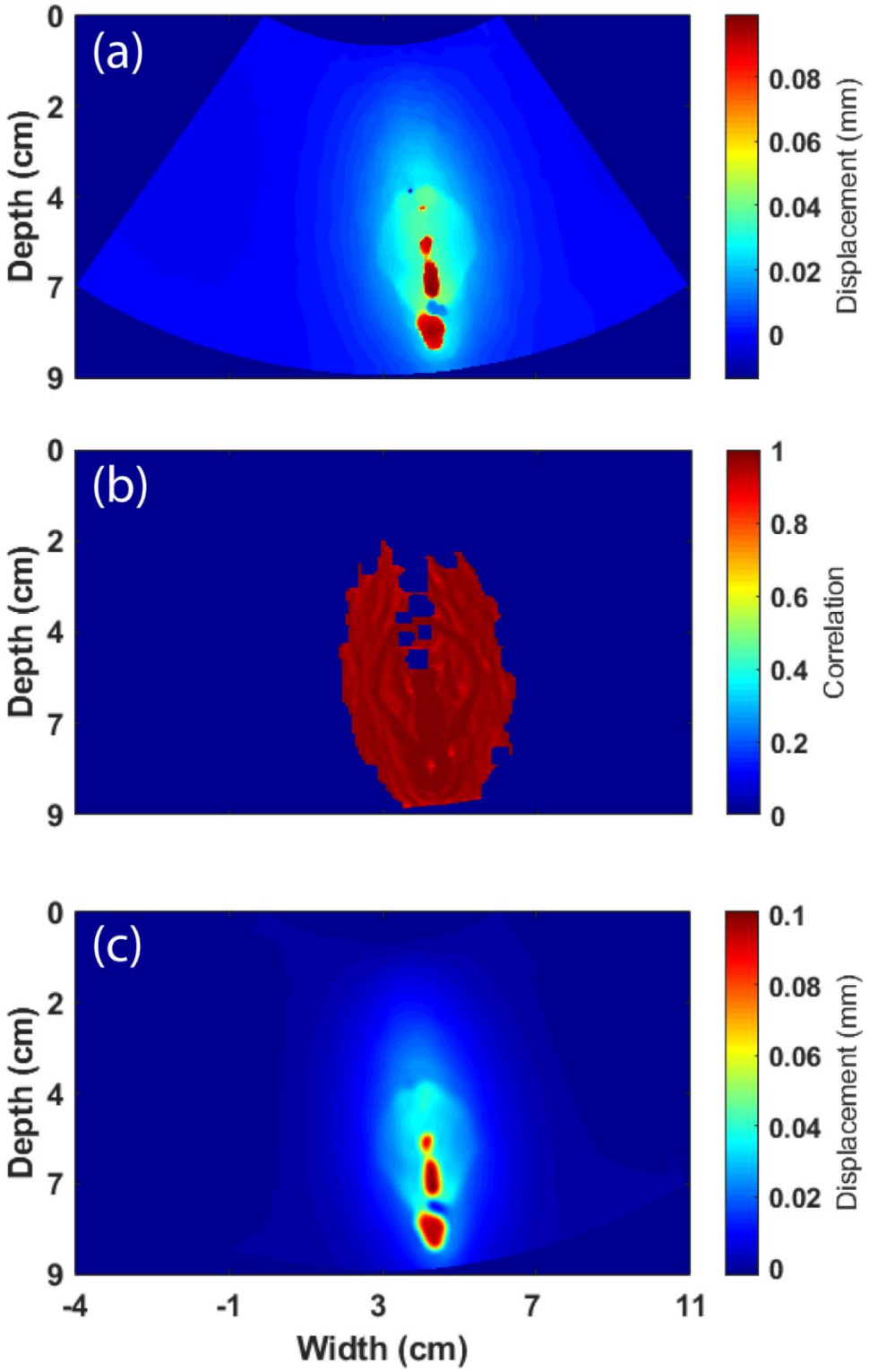

Figure 4.9 – Demonstration of dictionary patch matching for axial EDE phantom displacement. (a) Estimated displacement with median filtering, (b) correlation map between the dictionary patch and initial displacement patch, and (c) dictionary represented displacement

In Figure 4.9 (b), observe that patches in and around the inclusion were represented effectively by patches from the learned dictionary. Patches outside the inclusion were not represented by dictionary patches and therefore averaged. This provides us insight as to how the dictionary representation denoises displacements. First, let us look at locations where displacements were represented by dictionary patches. Here, dictionary patches sparsely represented noisy displacement patches. These sparse dictionary representative patches retain high correlation to noisy displacements because displacement information at these locations is more prominent as opposed to noise. In this manner, a sparse dictionary representation provides denoising by representing the prominent displacements without noise, since noise can often not be accurately represented sparsely. Following this logic, we see why patches outside of the inclusion were not represented by dictionary patches. Displacement patches outside of the inclusion do not contain prominent displacements over noise levels. These patches therefore cannot be represented sparsely by the dictionary; hence, patch values are simply averaged reducing noise. Figure 4.7 (b) and Figure 4.8 (b) present the dictionary patch representation used for denoising displacements for the *in-vivo* examples where we observe a similar trend of patch representation shown in Figure 4.9 (b). As shown by Figure 4.7 and Figure 4.8, dictionary representation reduced noise and provided a smooth delineated boundary for *in-vivo* data as opposed to the jagged boundary seen with spline smoothening, regardless of ablated region depth. Based on these examples, an important takeaway from dictionary representation is improved ablation delineation with no degradation in the ablated region boundary from denoising.

4.4 Combined and Magnitude Vector Displacement Dictionaries

After seeing the benefits of dictionary representation for single displacement vector estimates, the next step was to extend the dictionary learning algorithm to incorporate both displacement vector estimates for representation. These new developed algorithms are utilized on both phantom and *in-vivo* datasets. The protocol used for analysis in this section is shown in Figure 4.10, where the red box labeled filtering incorporates the adapted dictionary learning algorithms [52]. Flowchart steps in Figure 4.10 are further described in the following subsections. For comparing the different methods, n = 15 patients were utilized

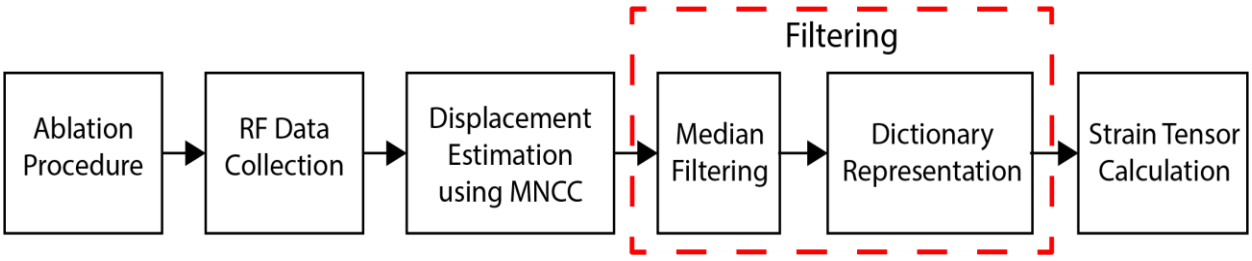

Figure 4.10 – The flowchart from ablation procedure to producing strain tensor images for electrode displacement elastography. Red box indicating filtering was the portion of flowchart that was varied based on Table 4.2.

Table 4.2 – Description of various filtering methods utilized in this work.

FILTERING METHOD			DESCRIPTION OF FILTERING METHOD
I	Unfiltered	–	No filtering of displacement estimates from MNCC algorithm.
II	Median Filtering	–	Median filtering only.
III	Individual Dictionary	–	After median filtering, dictionary representation of axial and lateral displacements separately.
IV	Combined Dictionary	–	After median filtering, dictionary representation of axial and lateral displacements together using Eq. (1).
V	Magnitude Vector Dictionary	–	After median filtering, dictionary representation of vector $\vec{d}$.
VI	Magnitude Component Dictionary	–	After median filtering, dictionary representation of $\vec{d}$ then converting displacements back to axial and lateral displacement vectors.

4.4.1 Filtering Displacement Estimates

Various approaches to filtering displacement estimates were used to assess visual and quantitative differences. Description of each filtering method are shown in

FILTERING METHOD	DESCRIPTION OF FILTERING METHOD

I	Unfiltered	–	No filtering of displacement estimates from MNCC algorithm.
II	Median Filtering	–	Median filtering only.
III	Individual Dictionary	–	After median filtering, dictionary representation of axial and lateral displacements separately.
IV	Combined Dictionary	–	After median filtering, dictionary representation of axial and lateral displacements together using Eq. (1).
V	Magnitude Vector Dictionary	–	After median filtering, dictionary representation of vector $\vec{d}$.
VI	Magnitude Component Dictionary	–	After median filtering, dictionary representation of $\vec{d}$ then converting displacements back to axial and lateral displacement vectors.

. Median filtering utilized a kernel size of 1.9×1.9 mm and dictionary representation [52] utilized a patch size of 4.0×4.0 mm and 80% patch overlap with dictionaries learned directly from displacement estimates to be filtered. To maintain consistency, a single displacement frame showing largest cross-sectional area was manually selected for each patient by an untrained observer for comparison.

When filtering using the individual dictionary method, the algorithm used is identical to that described in [52] and performed individually on axial and lateral vectors. Conversely, for a combined representation, the dictionary learning process had to be linked, where coefficients and denoised displacement image for axial and lateral vectors were obtained using the combined dictionary representation in (12). After minimizing (12), the coefficient vector, α_{Comb} , was updated using (13). Here $\phi = 0.5$ was used to dictate the weight of the axial and lateral coefficient vector onto the combined coefficient vector, where a $\phi = 0$ used only the axial updated coefficient vector and $\phi = 1$ used lateral. Similarly to learning the individual dictionary, the axial and lateral combined dictionaries, D_{Ax} and D_{Lat}, were found using a common coefficient vector as shown in (14).

$$\begin{aligned}\{\alpha_{Ax}, X_{Ax}\} &= \arg\min_{\alpha_{Ax}, X_{Ax}} \lambda \left\| X_{Ax} - Y_{Ax} \right\|_2^2 + \sum_{ij} \mu_{sparse} \left\| \alpha_{Comb} \right\|_1 + \sum_{ij} \left\| D_{Ax} \alpha_{Comb} - R_{ij} Y_{Ax} \right\|_2^2 \\ \{\alpha_{Lat}, X_{Lat}\} &= \arg\min_{\alpha_{Lat}, X_{Lat}} \lambda \left\| X_{Lat} - Y_{Lat} \right\|_2^2 + \sum_{ij} \mu_{sparse} \left\| \alpha_{Comb} \right\|_1 + \sum_{ij} \left\| D_{Lat} \alpha_{Comb} - R_{ij} Y_{Lat} \right\|_2^2 \end{aligned} \quad (12)$$

$$\alpha_{Comb} = \phi(\alpha_{Lat} - \alpha_{Ax}) + \alpha_{Ax} \quad (13)$$

$$\min_{\|\alpha\|_0 \le \kappa} \left[\left\| y_{Axial} - D_{Axial}\alpha \right\| + \left\| y_{Lateral} - D_{Lateral}\alpha \right\| \right] \tag{14}$$

The magnitude of the dictionary representation was also utilized by noting that all displacement estimates contain an axial (dy) and lateral (dx) component which can also be represented as a magnitude vector ($\vec{d}$) and phase angle (θ) shown in Figure 4.11. This allows a single individual dictionary to be learned by using $\vec{d}$ as displacements in the individual dictionary representation algorithm. Strain tensors can be directly estimated from magnitude displacement map or decomposed into axial and lateral components before strain tensor calculation. All strain tensors were estimated using a 2D Savitzky-Golay digital differentiator of size 0.2 × 5.0 mm using 0^{th} × 2^{nd} order polynomials for x and y directions respectively [54].

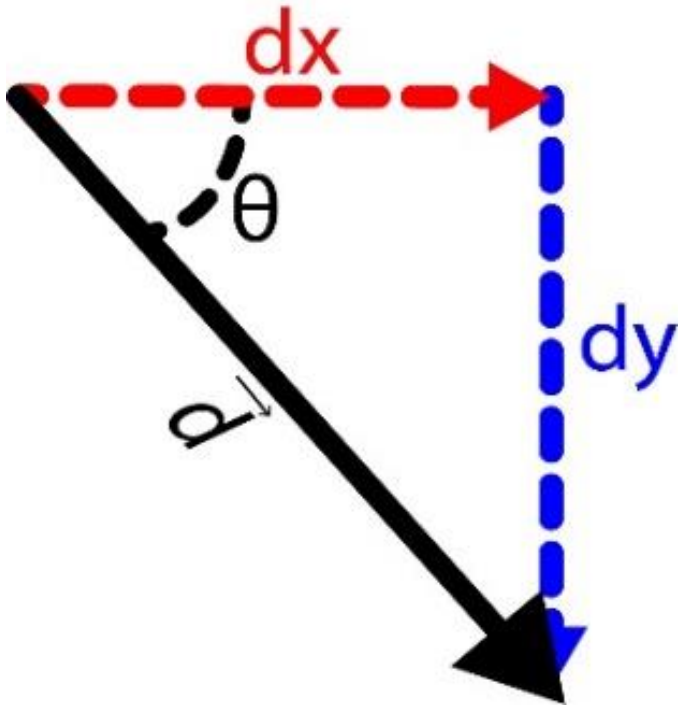

Figure 4.11 – Displacement estimation variations of axial (dy) and lateral (dx) or magnitude ($\vec{d}$) and phase (θ).

4.5 Performance Comparison of Dictionary Learning Methods

After performing displacement estimation using MNCC, all filtering methods described in

FILTERING METHOD			DESCRIPTION OF FILTERING METHOD
I	Unfiltered	–	No filtering of displacement estimates from MNCC algorithm.
II	Median Filtering	–	Median filtering only.
III	Individual Dictionary	–	After median filtering, dictionary representation of axial and lateral displacements separately.
IV	Combined Dictionary	–	After median filtering, dictionary representation of axial and lateral displacements together using Eq. (1).
V	Magnitude Vector Dictionary	–	After median filtering, dictionary representation of vector $\vec{d}$.
VI	Magnitude Component Dictionary	–	After median filtering, dictionary representation of $\vec{d}$ then converting displacements back to axial and lateral displacement vectors.

were performed, each followed by strain tensor calculation for an EDE phantom and 15 *in-vivo* patients. First, quantitative metrics were obtained for each filtering method. Target and background ROIs were placed to calculate SNR, contrast, and CNR for all methods and patients using the procedure defined in [55]. EDE phantom metrics are shown in Table 4.3. The combined dictionary presents with the highest SNR and CNR, while also showing a slight reduction in contrast. On the other hand, magnitude dictionaries show higher SNR, contrast, and CNR than original and median filtered results, yet lower than other dictionary methods.

Table 4.3 – Mean (μ) and standard deviation (σ) of various filtering methods on 15 axial strain tensor images from EDE phantom data.

	SNR (dB)			CONTRAST (dB)			CNR (dB)		
METHOD	**μ**		**σ**	**μ**		**σ**	**μ**		**σ**
I	3.57	±	2.18	8.14	±	7.40	-0.48	±	5.18
II	3.27	±	3.11	8.83	±	7.77	0.74	±	2.82
III	5.93	±	5.47	17.44	±	2.79	5.43	±	1.09
IV	7.47	±	6.14	15.26	±	3.70	6.10	±	1.57

V	5.01	±	2.18	13.85	±	5.57	3.84	±	2.66
VI	4.25	±	0.88	9.43	±	8.12	0.17	±	3.01

4.5.1 Quantitative Distribution Metrics with Filtering Methods

Following the same processing described for phantom data, *in-vivo* strain tensor metrics are shown in the boxplots in Figure 4.12, where (a) shows SNR, (b) shows contrast, and (c) shows CNR with axial results in blue and lateral results in red.

SNR distributions in Figure 4.12 (a) show very little difference between original and median filtered filtering approaches except that the median value of median filtered slightly decreased when compared to the original. Moving to dictionary representations, the individual and combined dictionaries both show very similar results to each other, where axial SNR shows the highest values with the combined dictionary representation. Axial SNR shows the tightest and highest distribution with mean and standard deviation of 4.38 ± 0.69 dB. Magnitude vector dictionary provides the lowest values with mean of 1.31 dB, while magnitude components provide higher median values of 2.39 dB and 2.86 dB for axial and lateral, respectively. Magnitude components also had the widest distribution with standard deviations of 1.4 dB axially and 1.98 dB laterally inferring inconsistent SNR obtained across patients.

Contrast distributions shown in Figure 4.12 (b) again show very similar results for the original with means of 26.0 dB and 15.0 dB and median filtered filtering with means of 26.6 dB and 15.6 dB. On the other hand, lateral individual, lateral combined, and magnitude vector dictionaries show similar distributions with mean values of 21.7 dB, 20.6 dB, and 20.8 dB, respectively. Axial individual and combined dictionaries provide similar tight distribution widths with standard deviations of 2.2 dB and 1.5 dB while the individual dictionary representation has the highest and tightest contrast distribution with mean of 26.7 dB.

CNR distributions are shown in Figure 4.12 (c), where again original and median filtered distributions look very similar with mean and standard deviations of 1.92 ± 1.09 dB and 2.15 ± 1.02 dB

axially and 2.34 ± 0.70 dB and 2.60 ± 0.64 dB laterally. However, CNR distributions of individual and combined dictionaries are much higher than other distributions with combined dictionary with the highest in axial and lateral directions with means of 3.90 ± 0.45 dB and 4.08 ± 0.84 dB. The magnitude vector distribution was the lowest of all methods with mean of 1.86 ± 0.63 dB.

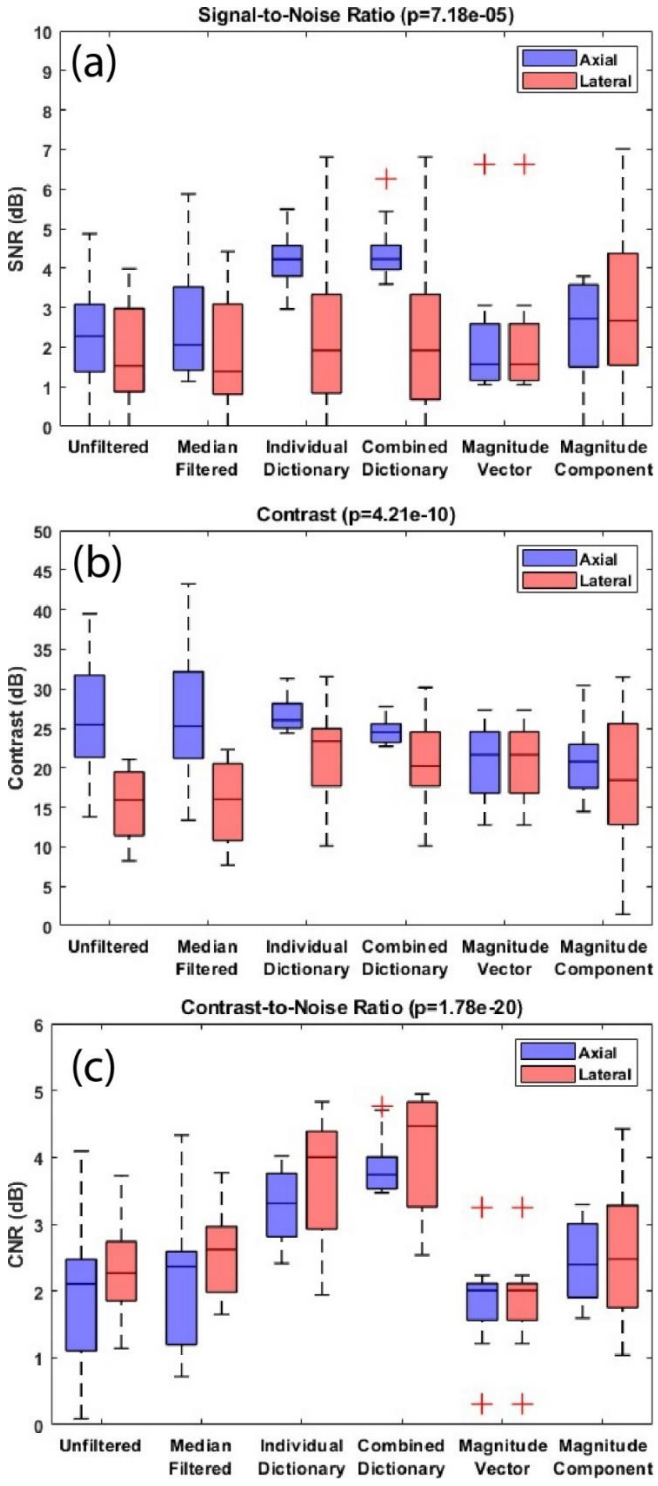

Figure 4.12 – Distributions (n=15) of signal-to-ratio (a), contrast (b), and contrast-to-noise ratio (c) for all filtering variations used where I is unfiltered, II is median filtered, III is individual dictionary, IV is combined dictionary, V is magnitude dictionary vector, and VI is magnitude dictionary component.

Overall, the combined dictionary learning algorithm improved SNR and CNR by 1.54 dB (26%) and 0.67 dB (12%) when compared to individual dictionary learning, while also showing a decrease in contrast by 2.18 dB (13%) for EDE phantom data. Similarly, the combined dictionary improved SNR and CNR by approximately 0.17 dB (4.0%) and 0.63 dB (19%), while also showing a decrease in contrast by 2.2 dB (8.2%) for *in-vivo* patients.

4.5.2 Visualization with Different Filtering Approaches

Finally, visualization using each of the filtering methods from Table 4.1 are shown in Figure 4.13 for a patient with colon cancer metastasized to the liver. Figure 4.13 (a) shows the B-mode and strain tensor images with the following filtering applied (b) magnitude vector dictionary, (c) unfiltered axial, (d) unfiltered lateral, (e) median filtered axial, (f) median filtered lateral, (g) individual dictionary axial, (h) individual dictionary lateral, (i) combined dictionary axial, (j) combined dictionary lateral, (k) magnitude dictionary component axial, and (l) magnitude dictionary component lateral. The approximate location of the ablation zone shown in Figure 4.13 (a) were matched by size and location in strain tensor images in Figure 4.13 (b-l). Looking at images Figure 4.13 (c,e,g,i) we observe a gradual increase in lesion boundary contrast and lowered noise within the ablated region as well as lower noise outside the ablated region. Conversely, although when lateral images Figure 4.13 (d,f,h,j) depict an ablated zone, this zone is smaller and of reduced boundary smoothness than axial strain tensor images. Despite this fact, lateral strain tensor images similarly reduce in noise as additional filtering is performed with the lowest noise and best boundary delineation obtained with the combined dictionary representation. When looking at the magnitude component images in Figure 4.13 (k) and (l), an increase in pixel resolution can be seen however, the noise increases within the lesion. Similarly, the magnitude image in Figure 4.13 (b) shows lower boundary smoothness and high noise levels. Despite varying levels of contrast and noise, all filtering methods maintain lesion visualization in a similar location as seen on the B-mode image, i.e., Figure 4.13 (a).

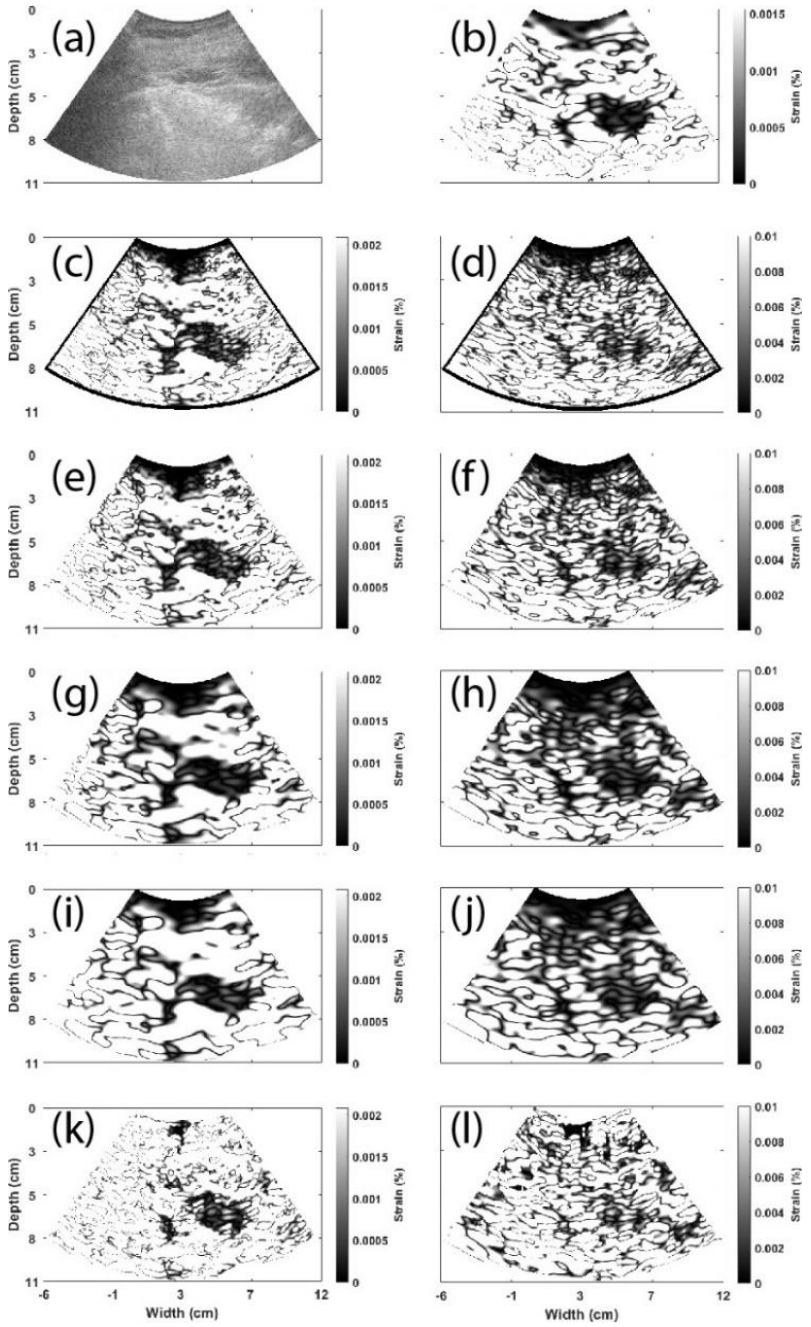

Figure 4.13 – Ultrasound B-mode and strain tensor images from a post-microwave ablation patient with colon cancer metastasized to the liver. (a) shows the ultrasound B-mode, and strain tensor images from (b) magnitude vector dictionary, (c) unfiltered axial, (d) unfiltered lateral, (e) median-filtered axial, (f) median-filtered lateral, (g) individual dictionary axial, (h) individual dictionary lateral, (i) combined dictionary axial, (j) combined dictionary lateral, (k) magnitude dictionary axial component, and (l) magnitude dictionary lateral component.

4.6 Expanding Results to Larger Number of Patient Datasets

The results previously shown were published in a peer-reviewed conference paper [55]. However, to better evaluate the proposed dictionary representations a larger sample of images were utilized. We performed dictionary analysis on n = 94 pre-ablation and n = 92 post-ablation strain tensor image pairs (axial and lateral strain tensors) or independent *in vivo* patient data sets. A total of n = 372 images was analyzed for these patients. For analysis, regions of interest (ROIs) were selected manually as discussed in Section 4.3.1. Instead of showing a distribution of computed quantitative metric values as shown in Figure 4.3, Figure 4.4, Figure 4.5, and Figure 4.12, in this section, the filtering method which provided the highest SNR, contrast, and CNR for each patient were tallied and a histogram used to portray the methods that provided improved performance.

4.6.1 Dictionary Results on Pre-Ablation Tumor Visualization

Results from n = 94 pre-ablation *in vivo* datasets is shown in Figure 4.14. These results show a cumulated count for each patient index tumor where a tally was given for the method producing the highest of each quantitative metric, i.e., SNR, contrast, and CNR. The results in Figure 4.14 depicts a histogram of the method that outperformed all others over each of the n = 94 pre-ablation index tumors. Figure 4.14 shows that strain tensor images computed from the original displacement estimates provided the lowest quantitative metric values. Median filtering provided improved quantitative metrics for axial strain, with the highest contrast, second highest SNR, and third highest CNR, while for lateral strain median filtering did not provide any significant improvement in the results. When reviewing the results obtained with the individual component dictionary, axial strain tensor metrics did not outperform the other filtering approaches, while for lateral strain images the individual dictionary representation presented with the highest SNR and contrast, while the second highest for CNR. The combined dictionary representation demonstrated the highest SNR and the second highest CNR for axial strain images, while showing the lowest contrast. For lateral strain images the combined dictionary representation provided the second highest SNR and highest CNR, while having the lowest contrast. The low contrast obtained with the

combined dictionary method was likely from the extra smoothening and denoising that the combined representation performed on the displacement estimates. The magnitude dictionary representation improved the contrast when compared to the combined dictionary representation, yet the increased noise levels reduced the SNR and CNR for both axial and lateral strain tensor images.

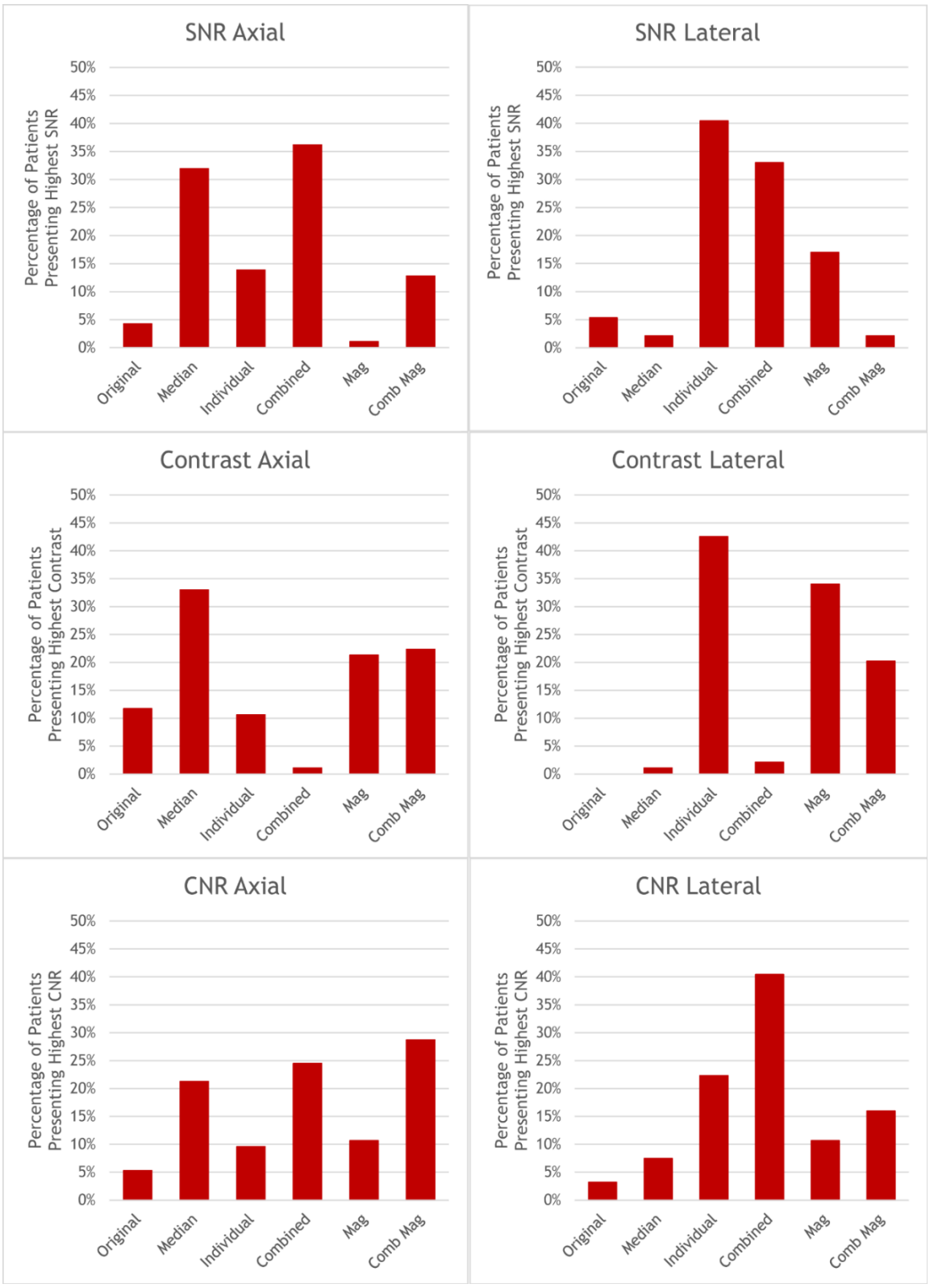

Figure 4.14 – Histograms for the SNR, contrast, and CNR for pre-ablation strain tensor images for the filtering approaches described in this chapter.

4.6.2 Dictionary Results on Post-Ablation Strain Images

Results from n = 92 post-ablation *in vivo* datasets are shown in Figure 4.15. Like the results reported in Figure 4.14, these results show a cumulated tally for each patient ablation zone strain tensor where a tally was given for the method producing the highest of each quantitative metric, i.e., SNR, contrast, and CNR. This results in a histogram indicating which method outperformed others over each of the n = 92 post-ablation zones. Figure 4.15 shows that when filtering was not applied it results in low SNR, contrast, and CNR. Median filtering shows similar results when compared to no filtering except for axial contrast where median filtering provides the highest results and CNR in the axial direction shows the third highest tally among all the methods. Individual vector dictionary representation shows the second highest SNR tally for axial strain, third highest SNR for lateral strain, and the highest contrast for lateral strain. The combined dictionary representation presents with the largest number of patients with high SNR for all the filtering methods for axial strain and similar results as individual and magnitude dictionary representations for lateral strain. The combined dictionary indicates the lowest contrast tallies, while CNR for axial strain is second highest and CNR for lateral strain shows very high values over other methods. The magnitude dictionary representation provided low tally values for axial strain while for lateral strain it provided the highest SNR and second highest contrast with poor CNR. The decomposed magnitude dictionary representation method showed poor SNR results, the second and third highest contrast for axial and lateral strain images respectively, and the highest results for axial CNR.

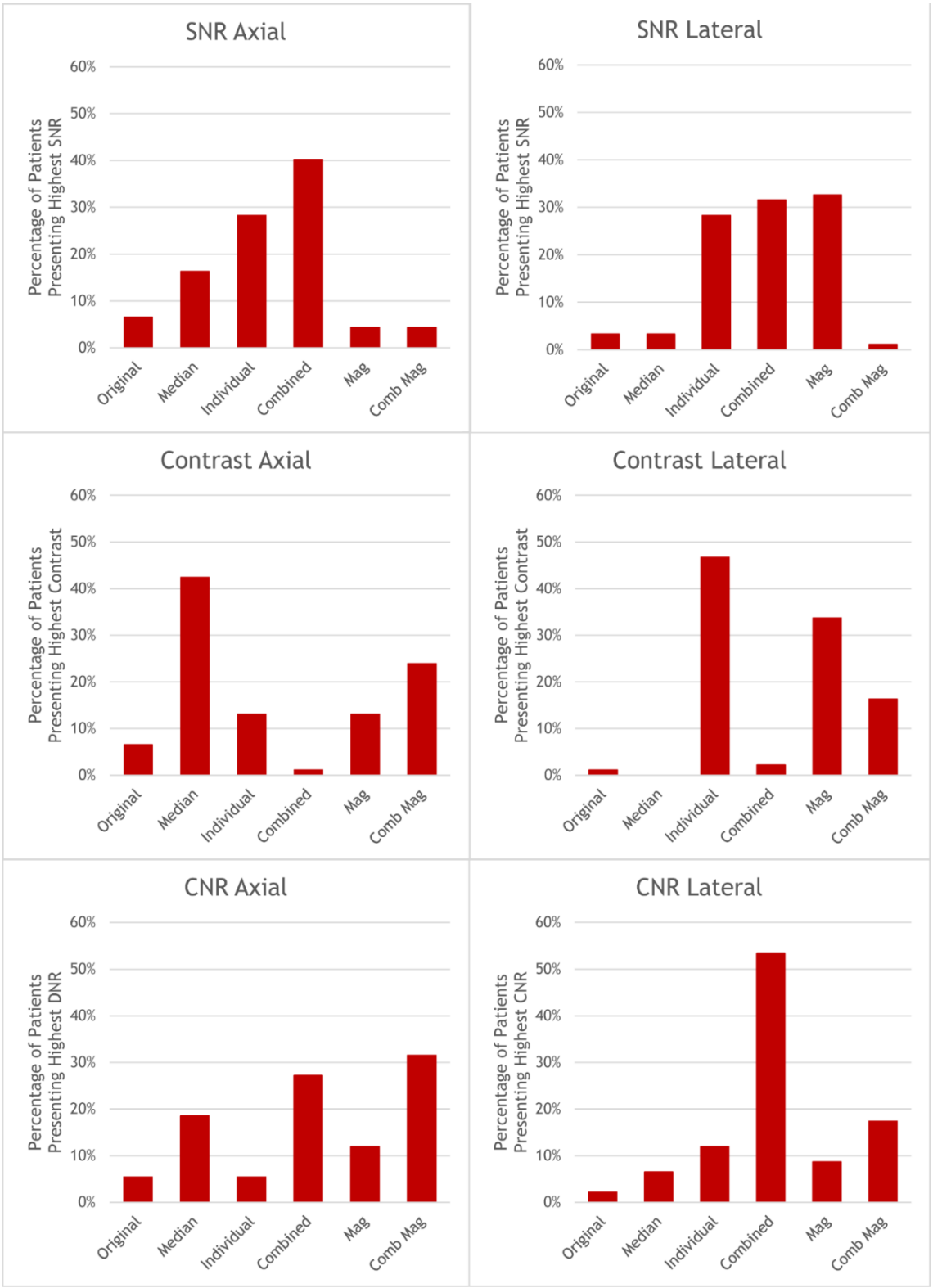

Figure 4.15 – Histogram of SNR, contrast, and CNR for post-ablation strain tensor images for the filtering approaches described in this chapter.

4.7 Choice of Dictionary for EDE

In conclusion, quantitative metrics obtained were compared from an EDE phantom and 15 *in vivo* patient strain tensor images initially using dictionary learning as well as its adaptations to unfiltered and median filtered displacement estimates. EDE phantom data shows that combined axial and lateral dictionary-learning algorithms produced the highest SNR and CNR with improvements of 3.90 dB and 6.58 dB in the axial strain tensors when compared to unfiltered strain tensor images. In contrast, magnitude dictionaries did not reduce visualized strain tensor noise and decreased SNR, contrast, and CNR as compared to original displacement estimates. As a result, the combined axial and lateral dictionary-learning algorithms are best for filtering displacements seen in EDE.

When comparing across a large set of axial and lateral strain tensor images on patients, the combined vector representation method performed consistently and provided better results when compared to other methods for SNR and CNR metrics for both axial and lateral strain images. Median filtering provided the best performance for axial strain images, while the individual dictionary representation provided the best results for strain contrast in lateral strain images. As a result, the combined axial and lateral dictionary-learning algorithms provided the best performance for filtering displacement estimates obtained with EDE based on SNR and CNR metrics.

4.8 References

[1] J. Jiang and T. J. Hall, "A coupled subsample displacement estimation method for ultrasound-based strain elastography," *Physics in Medicine and Biology*, vol. 60, no. 21, pp. 8347-8364, 2015/10/12 2015, doi: 10.1088/0031-9155/60/21/8347.

[2] F. Kallel and J. Ophir, "A least-squares strain estimator for elastography," *Ultrasonic Imaging*, vol. 19, no. 3, pp. 195-208, Jul 1997, doi: 10.1177/016173469701900303.

[3] M. McCormick, N. Rubert, and T. Varghese, "Bayesian Regularization Applied to Ultrasound Strain Imaging," *IEEE Transactions on Biomedical Engineering*, vol. 58, no. 6, pp. 1612-1620, 2011, doi: 10.1109/TBME.2011.2106500.

[4] L. Chen, R. J. Housden, G. M. Treece, A. H. Gee, and R. W. Prager, "A hybrid displacement estimation method for ultrasonic elasticity imaging," *IEEE Transactions on Ultrasonics, Ferroelectrics, and Frequency Control*, vol. 57, no. 4, pp. 866-882, 2010, doi: 10.1109/TUFFC.2010.1491.

[5] H. Rivaz, E. M. Boctor, M. A. Choti, and G. D. Hager, "Real-Time Regularized Ultrasound Elastography," *IEEE Transactions on Medical Imaging*, vol. 30, no. 4, pp. 928-945, 2011, doi: 10.1109/TMI.2010.2091966.

[6] J. Luo and E. E. Konofagou, "A fast normalized cross-correlation calculation method for motion estimation," *IEEE Transactions on Ultrasonics, Ferroelectrics, and Frequency Control*, vol. 57, no. 6, pp. 1347-1357, 2010, doi: 10.1109/TUFFC.2010.1554.

[7] H. Chen and T. Varghese, "Multilevel hybrid 2D strain imaging algorithm for ultrasound sector/phased arrays," *Medical Physics*, vol. 36, no. 6Part1, pp. 2098-2106, 2009, doi: 10.1118/1.3121426.

[8] G. Treece, J. Lindop, L. Chen, J. Housden, R. Prager, and A. Gee, "Real-time quasi-static ultrasound elastography," *Interface Focus*, 10.1098/rsfs.2011.0011 vol. 1, no. 4, p. 540, 2011. [Online]. Available: http://rsfs.royalsocietypublishing.org/content/1/4/540.abstract.

[9] H. Shi and T. Varghese, "Two-dimensional multi-level strain estimation for discontinuous tissue," *Physics in Medicine & Biology*, vol. 52, no. 2, pp. 389-401, Jan 21 2007, doi: 10.1088/0031-9155/52/2/006.

[10] J. Ophir, I. Cespedes, H. Ponnekanti, Y. Yazdi, and X. Li, "Elastography: A Quantitative Method for Imaging the Elasticity of Biological Tissues," *Ultrasonic Imaging*, vol. 13, no. 2, pp. 111-134, 1991, doi: 10.1177/016173469101300201.

[11] I. Cespedes and J. Ophir, "Reduction of Image Noise in Elastography," *Ultrasonic Imaging*, vol. 15, no. 2, pp. 89-102, 1993, doi: https://doi.org/10.1006/uimg.1993.1008.

[12] P. Chaturvedi, M. F. Insana, and T. J. Hall, "2-D companding for noise reduction in strain imaging," *IEEE Transactions on Ultrasonics, Ferroelectrics, and Frequency Control,* vol. 45, no. 1, pp. 179-191, 1998, doi: 10.1109/58.646923.

[13] T. Varghese and J. Ophir, "Enhancement of echo-signal correlation in elastography using temporal stretching," *IEEE Transactions on Ultrasonics, Ferroelectrics, and Frequency Control,* vol. 44, no. 1, pp. 173-180, 1997, doi: 10.1109/58.585213.

[14] B. Jing, D. Chuxiong, L. Jianwen, and H. Ping, "Estimation and reduction of decorrelation effect due to tissue lateral displacement in elastography," *IEEE Transactions on Ultrasonics, Ferroelectrics, and Frequency Control,* vol. 49, no. 5, pp. 541-549, 2002, doi: 10.1109/TUFFC.2002.1002452.

[15] S. K. Alam, J. Ophir, and E. E. Konofagou, "An adaptive strain estimator for elastography," *IEEE Transactions on Ultrasonics, Ferroelectrics, and Frequency Control,* vol. 45, no. 2, pp. 461-472, 1998, doi: 10.1109/58.660156.

[16] P. M. Hayton, M. Brady, S. M. Smith, and N. Moore, "A non-rigid registration algorithm for dynamic breast MR images," *Artificial Intelligence,* vol. 114, no. 1-2, pp. 125-156, 1999.

[17] H. Rivaz, E. Boctor, P. Foroughi, R. Zellars, G. Fichtinger, and G. Hager, "Ultrasound elastography: a dynamic programming approach," *IEEE transactions on medical imaging,* vol. 27, no. 10, pp. 1373-1377, 2008.

[18] C. Pellot-Barakat, F. Frouin, M. F. Insana, and A. Herment, "Ultrasound elastography based on multiscale estimations of regularized displacement fields," *IEEE transactions on medical imaging,* vol. 23, no. 2, pp. 153-163, 2004.

[19] E. Brusseau, J. Kybic, J.-F. Déprez, and O. Basset, "2-D locally regularized tissue strain estimation from radio-frequency ultrasound images: Theoretical developments and results on experimental data," *IEEE Transactions on Medical Imaging,* vol. 27, no. 2, pp. 145-160, 2008.

[20] N. H. Meshram and T. Varghese, "Fast multilevel Lagrangian carotid strain imaging with GPU computing," *Ultrasonics Symposium (IUS), 2017 IEEE International,* pp. 1-4, 2017.

[21] J. Jiang, T. Varghese, C. L. Brace, E. L. Madsen, T. J. Hall, S. Bharat, M. A. Hobson, J. A. Zagzebski, and F. T. Lee, "Young's modulus reconstruction for radio-frequency ablation electrode-induced displacement fields: a feasibility study," *IEEE Transactions on Medical Imaging,* vol. 28, no. 8, pp. 1325-34, Aug 2009, doi: 10.1109/TMI.2009.2015355.

[22] N. Ouzir, A. Basarab, H. Liebgott, B. Harbaoui, and J.-Y. Tourneret, "Motion estimation in echocardiography using sparse representation and dictionary learning," *IEEE Transactions on Image Processing,* vol. 27, no. 1, pp. 64-77, 2018.

[23] B. A. Olshausen and D. J. Field, "Emergence of simple-cell receptive field properties by learning a sparse code for natural images," *Nature,* vol. 381, no. 6583, p. 607, 1996.

[24] Y. Xu, Z. Li, J. Yang, and D. Zhang, "A Survey of Dictionary Learning Algorithms for Face Recognition," *IEEE Access,* vol. 5, pp. 8502-8514, 2017, doi: 10.1109/ACCESS.2017.2695239.

[25] S. P. Kasiviswanathan, H. Wang, A. Banerjee, and P. Melville, "Online l1-dictionary learning with application to novel document detection," *Advances in Neural Information Processing Systems,* pp. 2258-2266, 2012.

[26] L. Ma, L. Moisan, J. Yu, and T. Zeng, "A dictionary learning approach for Poisson image deblurring," *IEEE Transactions on medical imaging,* vol. 32, no. 7, pp. 1277-1289, 2013.

[27] L.-K. Liu, S. H. Chan, and T. Q. Nguyen, "Depth reconstruction from sparse samples: Representation, algorithm, and sampling," *IEEE Transactions on Image Processing,* vol. 24, no. 6, pp. 1983-1996, 2015.

[28] J. Yang, Z. Wang, Z. Lin, S. Cohen, and T. Huang, "Coupled dictionary training for image super-resolution," *IEEE transactions on image processing,* vol. 21, no. 8, pp. 3467-3478, 2012.

[29] M. Elad and M. Aharon, "Image denoising via sparse and redundant representations over learned dictionaries," *IEEE Transactions on Image processing,* vol. 15, no. 12, pp. 3736-3745, 2006.

[30] I. Gatos, S. Tsantis, S. Spiliopoulos, D. Karnabatidis, I. Theotokas, P. Zoumpoulis, T. Loupas, J. D. Hazle, and G. C. Kagadis, "A machine-learning algorithm toward color analysis for chronic liver

disease classification, employing ultrasound shear wave elastography," *Ultrasound in medicine & biology*, vol. 43, no. 9, pp. 1797-1810, 2017.

[31] K. Wang, X. Lu, H. Zhou, Y. Gao, J. Zheng, M. Tong, C. Wu, C. Liu, L. Huang, and F. Meng, "Deep learning Radiomics of shear wave elastography significantly improved diagnostic performance for assessing liver fibrosis in chronic hepatitis B: a prospective multicentre study," *Gut*, pp. gutjnl-2018-316204, 2018.

[32] Y. Chen, Y. Luo, W. Huang, D. Hu, R.-q. Zheng, S.-z. Cong, F.-k. Meng, H. Yang, H.-j. Lin, and Y. Sun, "Machine-learning-based classification of real-time tissue elastography for hepatic fibrosis in patients with chronic hepatitis B," *Computers in biology and medicine*, vol. 89, pp. 18-23, 2017.

[33] P. C. Ngo, A. A. Winarto, C. K. L. Kou, S. Park, F. Akram, and H. K. Lee, "Fence GAN: Towards Better Anomaly Detection," in *2019 IEEE 31st International Conference on Tools with Artificial Intelligence (ICTAI)*, 4-6 Nov. 2019 2019, pp. 141-148, doi: 10.1109/ICTAI.2019.00028.

[34] S. Wu, Z. Gao, J. Luo, Z. Liu, H. Zhang, and S. Li, "Direct Reconstruction of Ultrasound Elastography Using an End-to-End Deep Neural Network," in *International Conference on Medical Image Computing and Computer-Assisted Intervention*, 2018: Springer, pp. 374-382.

[35] M. Kibria and H. Rivaz, "Global Ultrasound Elastography Using Convolutional Neural Network," *arXiv preprint arXiv:1805.07493*, 2018.

[36] C. Hoerig, J. Ghaboussi, and M. F. Insana, "An information-based machine learning approach to elasticity imaging," *Biomechanics and modeling in mechanobiology*, vol. 16, no. 3, pp. 805-822, 2017.

[37] R. R. Wildeboer, R. J. Van Sloun, C. K. Mannaerts, P. Moraes, G. Salomon, M. Chammas, H. Wijkstra, and M. Mischi, "Synthetic Elastography using B-mode Ultrasound through a Deep Fully-Convolutional Neural Network," *IEEE Transactions on Ultrasonics, Ferroelectrics, and Frequency Control*, 2020.

[38] T. Ahmed and M. Hasan, "SHEAR-net: An End-to-End Deep Learning Approach for Single Push Ultrasound Shear Wave Elasticity Imaging," *arXiv preprint arXiv:1902.04845*, 2019.

[39] E. J. Candes and T. Tao, "Decoding by linear programming," *IEEE transactions on information theory*, vol. 51, no. 12, pp. 4203-4215, 2005.

[40] E. J. Candes, J. K. Romberg, and T. Tao, "Stable signal recovery from incomplete and inaccurate measurements," *Communications on pure and applied mathematics*, vol. 59, no. 8, pp. 1207-1223, 2006.

[41] D. L. Donoho, "Compressed sensing," *IEEE Transactions on information theory*, vol. 52, no. 4, pp. 1289-1306, 2006.

[42] M. Elad, *Sparse and Redundant Representations: From Theory to Applications in Signal and Image Processing*. Springer, New York, 2010, p. 376.

[43] C. Ramirez, V. Kreinovich, and M. Argaez, "Why l1 is a good approximation to l0: A geometric explanation," *Journal of Uncertain Systems*, vol. 7, no. 3, pp. 203-207, 2013.

[44] D. L. Donoho, "For most large underdetermined systems of linear equations the minimal l1-norm Near-Solution Approximates the Sparsest Near-Solution," *Communications on Pure and Applied Mathematics*, vol. 59, no. 6, pp. 797-829, 2006 2006, doi: 10.1002/cpa.20132.

[45] G. Peyré, "The Numerical Tours of Signal Processing," *Computing in Science & Engineering*, vol. 13, no. 4, pp. 94-97, 2011, doi: 10.1109/MCSE.2011.71.

[46] P. L. Combettes and J.-C. Pesquet, "Proximal splitting methods in signal processing," in *Fixed-point algorithms for inverse problems in science and engineering*: Springer, 2011, pp. 185-212.

[47] R. R. Coifman and D. L. Donoho, "Translation-invariant de-noising," in *Wavelets and statistics*: Springer, 1995, pp. 125-150.

[48] E. Le Pennec and S. Mallat, "Sparse geometric image representations with bandelets," *IEEE transactions on image processing*, vol. 14, no. 4, pp. 423-438, 2005.

[49] M. Aharon, M. Elad, and A. Bruckstein, "K-SVD: An algorithm for designing overcomplete dictionaries for sparse representation," *IEEE Transactions on signal processing*, vol. 54, no. 11, pp. 4311-4322, 2006.

[50] P. Tseng, "Convergence of a block coordinate descent method for nondifferentiable minimization," *Journal of optimization theory and applications,* vol. 109, no. 3, pp. 475-494, 2001.

[51] R. M. Pohlman, J. Jiang, W. Yang, T. J. Ziemlewicz, M. L. Alexander, K. L. Wergin, M. G. Lubner, J. L. Hinshaw, F. T. Lee, and T. Varghese, "Comparison study of displacement estimation methods for microwave ablation procedures using electrode displacement elastography," in *2017 IEEE International Ultrasonics Symposium (IUS)*, 2017: IEEE, pp. 1-4.

[52] R. M. Pohlman and T. Varghese, "Dictionary Representations for Electrode Displacement Elastography," *IEEE Transactions on Ultrasonics, Ferroelectrics, and Frequency Control,* vol. 65, no. 12, pp. 2381-2389, 2018, doi: 10.1109/TUFFC.2018.2874181.

[53] S. Bharat, T. Varghese, E. L. Madsen, and J. A. Zagzebski, "Radio-frequency ablation electrode displacement elastography: a phantom study," *Medical Physics,* vol. 35, no. 6, pp. 2432-42, Jun 2008, doi: 10.1118/1.2919763.

[54] J. Luo, K. Ying, P. He, and J. Bai, "Properties of Savitzky–Golay digital differentiators," *Digital Signal Processing,* vol. 15, no. 2, pp. 122-136, 2005.

[55] R. M. Pohlman, T. Varghese, J. Jiang, T. J. Ziemlewicz, M. L. Alexander, K. L. Wergin, J. L. Hinshaw, M. G. Lubner, S. A. Wells, and F. T. Lee, Jr., "Comparison of Displacement Tracking Algorithms for *in Vivo* Electrode Displacement Elastography," *Ultrasound in Medicine and Biology,* vol. 45, no. 1, pp. 218-232, 2019, doi: 10.1016/j.ultrasmedbio.2018.09.001.

Chapter 5: Physiological Motion Reduction using Lagrangian Tracking for Electrode Displacement Elastography

Minimally invasive treatments such as microwave ablation (MWA), have been growing in popularity for extending liver cancer survival rates in patients, when surgery is not an option. As a nonionizing, real-time alternative to contrast-enhanced computed tomography (CECT), electrode displacement elastography (EDE) has shown promise as an imaging modality for MWA. Despite imaging efficacy, motion artifacts present due to physiological motion result in unintended speckle pattern variance thereby inhibiting consistent and accurate ablated region visualization. To combat these unavoidable motion artifacts, a Lagrangian deformation tracking (LDT) approach based on freehand EDE was developed to track tissue movement and better define tissue properties. For validating LDT efficacy, a spherical inclusion tissue-mimicking phantom as well as 7 in vivo data sets were processed, and strain tensor images compared to identical time sampled images estimated using a traditional Eulerian approach. In vivo results demonstrate greater consistency among visualized LDT strain tensor images, with segmented ablated regions showing standard deviation reductions of up to 98% when compared to Eulerian strain tensor images. Additionally, Lagrangian strain tensor images provided Dice coefficient improvements up to 25% and success rates improved from approximately 50% to nearly 100% for ablated region visualization.

5.1 Background Literature on Lagrangian Deformation Tracking (LDT)

According to the National Cancer Institute (NCI) Surveillance, Epidemiology, and End Results Program (SEER), 1 in every 100 persons will be diagnosed with some type of primary liver cancer. Of those diagnosed, less than 18% will survive 5 or more years after diagnosis [1]. Additionally, as of 2018, liver and intrahepatic bile duct cancers are the fifth leading cause of cancer related deaths in the United States with the number of cases more than tripling since 1980 [2]. Unfortunately these statistics do not take

R. M. Pohlman and T. Varghese, "Physiological Motion Reduction Using Lagrangian Tracking for Electrode Displacement Elastography," Ultrasound in Medicine and Biology, vol. 46, no. 3, pp. 766-781, March 01, 2020, doi: 10.1016/j.ultrasmedbio.2019.11.001.

into account the vast numbers of metastatic liver cancers originating from a variety of primary cancer locations, such as colorectal, lung, breast, and melanoma [3]. As an example, over 50% of colorectal primary cancers (CRC) will result in liver metastasis leading to the high mortality of CRC patients due to hepatic failure [4]. To address these diseases, several liver cancer treatments have been adopted, namely liver transplantation [5, 6], resection [7, 8], chemotherapies [7, 9], and recently minimally invasive percutaneous treatments [10-14].

As a means of combating the growing trend of liver cancer diagnosis and low survival rates, minimally invasive approaches such as microwave ablation (MWA) have shown promise in extending patient's survival for up to 10 or more years [5, 7, 15]. Yet a main contingency, as for any minimally invasive method of treatment, is accurate and consistent imaging to ensure proper procedure execution [12, 16, 17]. In the case of MWA, this is specifically aimed towards proper placement of ablation antennae as well as verification of 0.5 – 1.0 cm margin of normal tissue necrosis surrounding tumor cells to minimize any residual tumor progression [8, 16, 18]. Most often visualization takes the form of contrast enhanced computed tomography (CECT). Although this provides an accurate depiction of liver cancers and ablated regions, CECT is ionizing, time-consuming, and expensive for clinical use. Consequently, there is significant interest in developing other comparable imaging modalities**.**

As an alternative to CECT imaging, ultrasound is showing progress as a future comparable imaging modality for visualizing MWA. Ablated regions are depicted in B-mode ultrasound via a hyperechoic region surrounding ablated regions due to the high scatterer density of bubbles arising in tissue at high temperatures. Unfortunately, B-mode ultrasound visualization lacks the specificity necessary to delineate ablated regions accurately. The lack in accuracy is due to hyperechoic regions often overestimating areas of tissue necrosis and bubbles migrating during and after procedures leaving echogenicity as an unreliable predictor of MWA effectiveness [19]. Therefore B-mode ultrasound can only be considered as a rough estimate of induced tissue necrosis [20]. Contrast enhanced US (CEUS), has shown improved effectiveness in the assessment of ablation when compared to conventional B-mode US. In comparison to CECT, CEUS provides faster image acquisition, lower cost, and reduced nephrotoxicity [21, 22]. Additionally, CEUS and

CECT have presented with similar sensitivity and specificity, however CEUS still fails to detect some liver masses detected with CECT [23].

Although CEUS may provide higher specificity than conventional B-mode US, elastography [24] has shown similar or improved diagnostic accuracy of hepatic masses as compared to CEUS. [25, 26]. Fortunately, an elastography method, namely electrode displacement elastography (EDE), has overcome B-mode ultrasound's limitations for this application [27]. EDE uses the MWA electrode to induce localized, quasi-static deformations directly to the liver mass and ablated region [28]. The tissue's response to these localized deformations is measured using ultrasound radiofrequency (RF) signals. RF echo signals are processed to estimate and present the tissue's elastic properties [29-31]. Additionally, gas bubble echogenicity that degrades thermal ablated region boundaries in B-mode ultrasound does not inhibit strain tensor estimation [32]. Many sequential publications have shown successes of EDE in simulation, tissue mimicking (TM) phantom, *ex vivo*, and *in vivo* data [28, 33-40] as well as high correlation between elastography strain tensor images and histopathology [37]. Further improvements to displacement estimation used for estimating tissue properties in EDE have greatly improved visualization of liver masses and ablated regions presented in [41] and with the addition of machine learning in [42], yet low success rates and varying ablated region sizes hinder clinical utilization.

Despite improved visualization, a remaining constraint of EDE is low successful ablated region visualization rates and varying ablation sizes previously shown in [40, 41]. A likely culprit of low success rates and ablation size variability are the various motion artifacts present within the 2D imaging plane. More specifically, as focused deformations are induced to the ablated region via electrode perturbations other physiological motion still occur, such as essential physiological motion, out-of-plane motion, freehand transducer movement, and electrode perturbation inconsistency. As a result, ideal cyclic electrode movements are corrupted with motion artifacts likely resulting in unintended speckle pattern changes. These speckle pattern changes may manifest as additional displacement estimation variance [43] and strain tensor visualization inconsistencies, thereby inhibiting accurate visualization of the ablated region and degrading delineation of ablated margins. This may have been perceived similarly in [41] as low success

rates and varying ablation sizes. Hence further improvements to EDE visualization require a reduction in these motion artifacts.

Several approaches have been pursued to alleviate the impact of motion artifacts. One common approach is to utilize increasingly robust displacement estimation approaches to reduce signal decorrelation. Displacement estimation algorithms have reduced decorrelation by regularization [44-49], and recently machine learning [50-53]. Although these methods improve displacement estimation, they do not necessarily account for large motion artifacts, likely seen *in vivo* during EDE. Alternatively, a possible solution may be to apply a known displacement or force to the electrode using a mechanical device such as linear actuators [54]. With a known force acting on the liver mass, other motion artifacts can be accounted for, thereby reducing effects of motion artifacts. Although this may offer good results, this approach would add additional equipment, cost, and time; undesirable for MWA. Therefore, other elastographic approaches, which encountered similar large motion artifacts, were examined.

5.2 Motivation for Use in Elastography

Upon investigating elastographic approaches for other organs, a similar paradigm was observed with carotid and cardiac elastography [49, 55-58]. During cardiac elastography, translational motion and variability in the deformation present over the cardiac cycle impose large motion artifacts greatly impeding accurate description of tissue elastic properties over time. A traditional Eulerian description of motion was insufficient to describe tissue properties as it was limited to descriptions at specific time instances over a cardiac cycle. Cardiac elastography overcame this hurdle by utilizing a Lagrangian description of deformation for strain estimation. With a Lagrangian description, tissue deformation was tracked so that tissue properties may be accurately described locally. Following a similar logic to carotid and cardiac elastography, a Lagrangian description of tissue motion may be helpful in reducing the various motion artifacts seen during EDE. In this work, we show that Lagrangian deformation tracking (LDT) accounts for some of these motion artifacts. When properly tracked, accumulated displacements following a Lagrangian

description present consistent, improved strain tensor image visualization and reduced ablation size variance.

5.3 Algorithm Development for Lagrangian Deformation Tracking

5.3.1 Data Collection for Lagrangian Deformation Tracking

Ultrasound radiofrequency (RF) data was collected from two different sources for the study reported in this chapter using a Siemens S2000 system with a 6C1 HD curvilinear transducer (Siemens, Malvern, PA). First, RF data was collected from a CIRS ultrasound QA 049 phantom with a 4.3 cm^3 spherical 85 kPa inclusion embedded in 28 kPa background (Computerized Imaging Reference Systems, Inc., Norfolk, VA) during manual cyclic compressions. The second preliminary data set was collected from 7 patients shortly after a minimally invasive MWA procedure at the University of Wisconsin-Madison Hospital and clinics. Finally, the third completed data set was collected from 30 patients as an extension of the initial 7 patients. *In vivo* data collections followed a protocol approved by the health sciences institutional review board at UW-Madison with all patients providing informed consent prior to the procedure. After verifying proper electrode placement, 80 frames of RF data were acquired during controlled ≈1 mm electrode perturbation by the operating clinician. Signal and image processing were performed offline using corresponding software packages in MATLAB.

5.3.2 Lagrangian Description of Motion

A LDT model for EDE was implemented following an approach described by Maurice and Bertrand [43]. A Lagrangian description of tissue motion describes a feature's position as its initial position and motion trajectory as a function of time. As a result, conservation of motion can be represented through inverse trajectory functions using a given trajectory of material features (speckle tracking). Following this logic, motion reduction may be achieved by transforming coordinates through a forward trajectory function, which may take the form of an affine transformation [59].

5.3.3 LDT Algorithm Flowchart

The LDT algorithm derived for EDE is shown in Figure 5.1. First, features with higher echogenicity were automatically selected from B-mode images and then tracked over an EDE cycle. Following the trajectory of tracked features, affine transformations were estimated as a function of time and applied to a rectangular coordinate grid. With this transformed grid, displacements estimated for a Eulerian description of motion were interpolated onto the new coordinates of the transformed grid. The Lagrangian description of deformation, now spatially aligned, were accumulated over an EDE deformation cycle. The resulting LDT displacements were compared to the temporally aligned Eulerian displacements by segmenting thermally ablated regions from the strain tensor images.

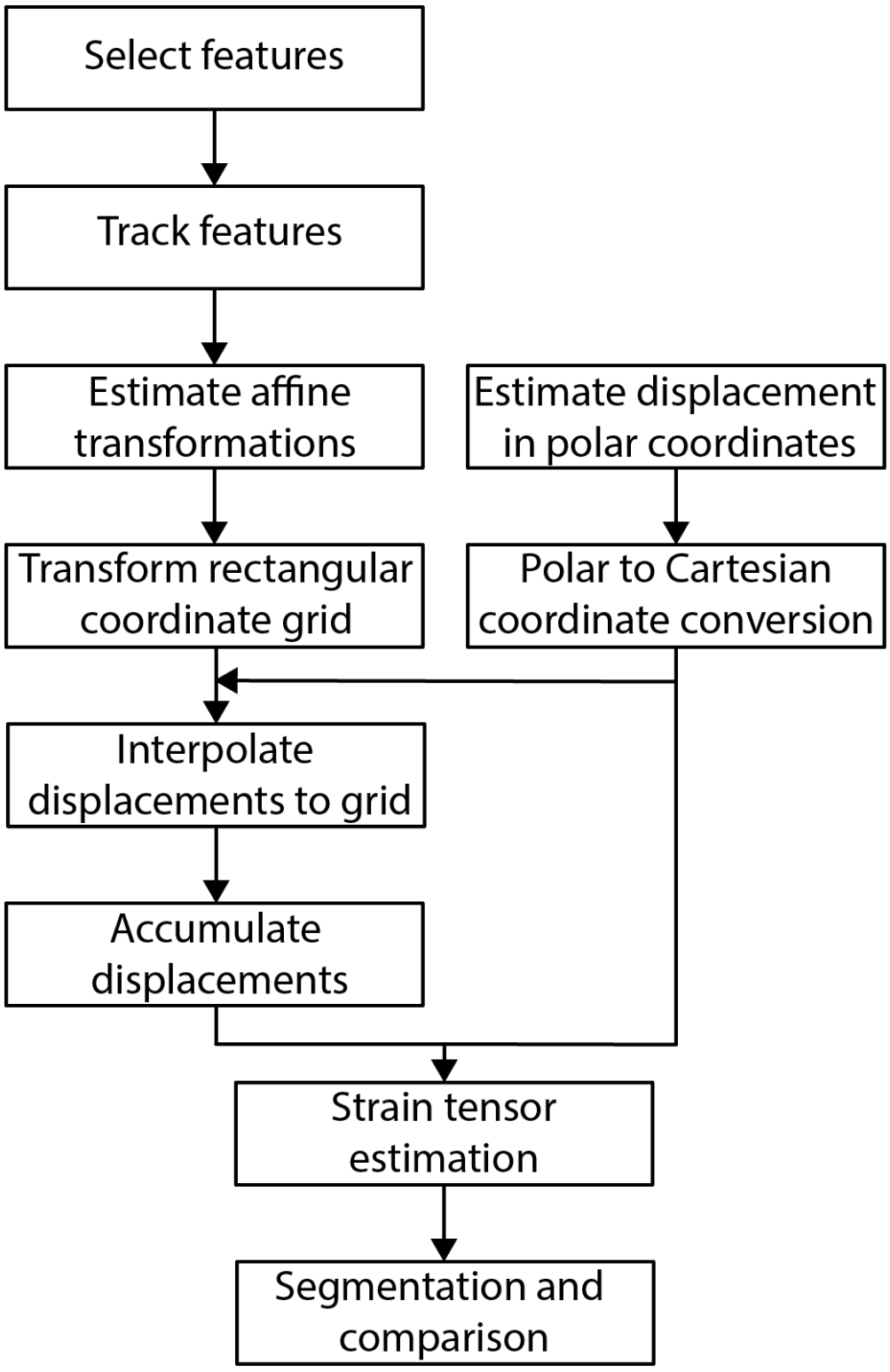

Figure 5.1 - Flowchart of the Lagrangian Deformation Tracking (LDT) algorithm.

5.3.4 LDT Feature Selection

The first step for LDT involved selecting B-mode features to be tracked over an EDE cycle. The initial B-mode frame was chosen for selecting these features, as it offers visualization of the MWA antenna and ablated region. An obvious approach to obtain these features would be manual selection, yet this process may be time-consuming depending on the desired number of features. An alternative approach used in this work enabled features to be automatically selected from this image following a prior probability distribution derived as a function of brightness (hyperechoic intensity) in the B-mode image. This means that features were randomly sampled from weighted probability distribution function with weights defined using the relative pixel brightness of the B-mode image. Hyperechoic regions were chosen as they indicate tumors and ablated regions in B-mode images. This process resulted in selection of 20 or more pixels with a relative gray-scale intensity greater than 0.95 after normalizing gray values to a 0-1 scale. After a feature was selected from the probability distribution, all pixels within a 2 mm window around the feature in the B-mode image were removed from the distribution before sampling for the next feature. This process was then repeated for the required number of samples. To demonstrate similarities in manual and automatic approaches, an example feature selection is shown in Figure 5.2. Note the similar locations of the automatic and manually selected features.

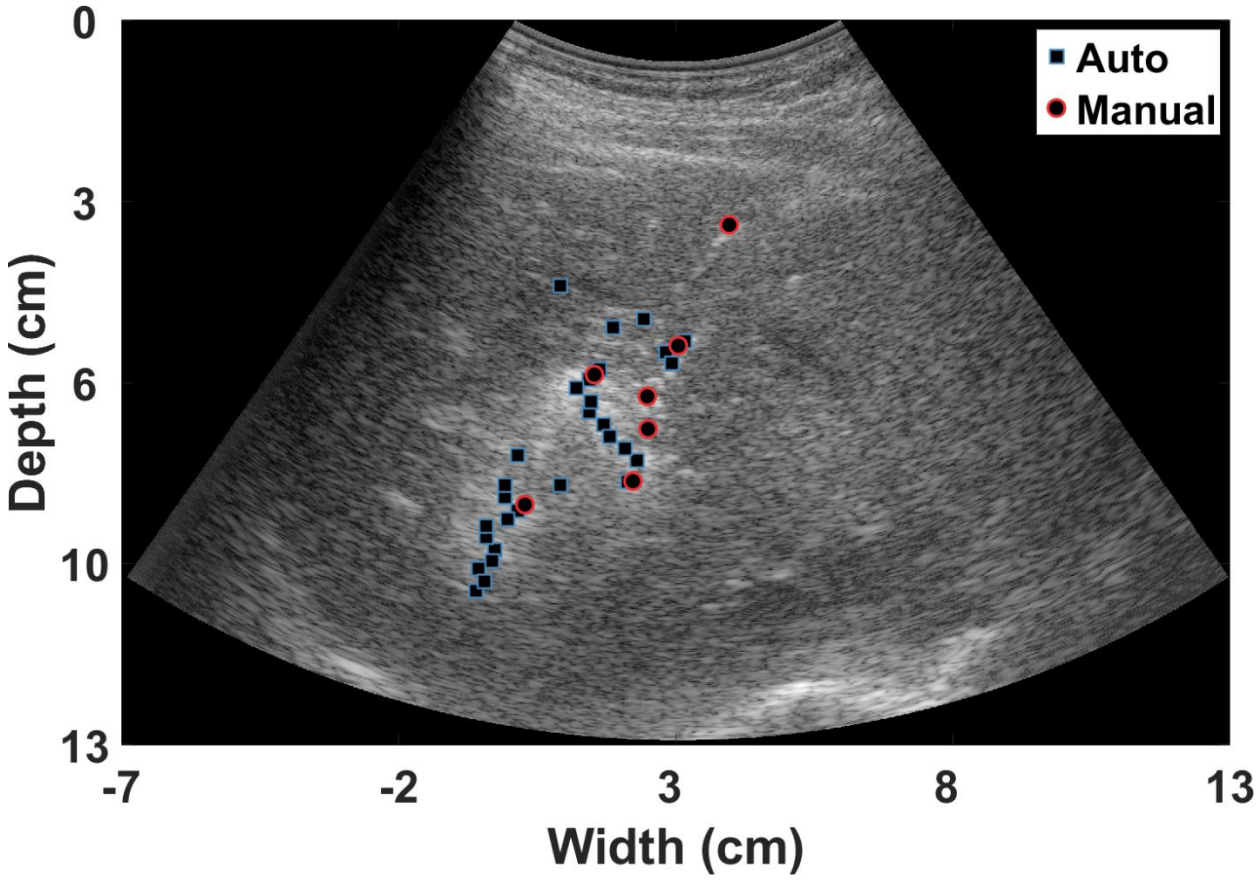

Figure 5.2 - Example of automatic feature selection (blue squares) vs. manual feature selection (red circles) in ultrasound B-mode image.

5.3.5 Feature Tracking using LDT

After feature selection, a kernel size of 6 wavelengths by 3 A-lines was centered about each feature in RF frame n where n is the RF frame sampled at time τ_n for $n = 1, \cdots, N-1$ and N is the total number of RF frames sampled during EDE perturbations. Fixing this kernel in frame n, the same kernel location in frame $n+1$ was shifted in a range of 1 wavelength by 3 A-lines. The normalized cross correlation (NCC) values were estimated, and the peak value defined the movement vector of that feature kernel. Since high resolution tracking was desired, RF data was then up-sampled after initial movement vector estimation using sinc interpolation. Data was up-sampled by a factor 2× and 10× for axial and lateral directions while the search range reduced by 2× and 10× respectively. The peak NCC and up-sampling process was repeated

6× similarly to [49]. After tracking, any features where the peak NCC value dropped below 0.9 were removed. The x and y coordinates of remaining features were arranged into row vectors, $\vec{u}_n$ and $\vec{v}_n$.

5.3.6 Affine Transformation Estimation

After tracking these selected features, the next step was to estimate the trajectory functions to be applied to the displacement vector. For EDE tracking, an affine transformation was used to allow linear transformations without introducing nonlinear distortions to negatively affect estimations. The affine transformation from τ_n to τ_{n+1} was calculated using (15).

$$\begin{bmatrix} \vec{u}_{n+1} \\ \vec{v}_{n+1} \end{bmatrix} = \begin{bmatrix} s_x(\tau)\cos\theta(\tau) & -h_x(\tau)\sin\theta(\tau) \\ h_y(\tau)\sin\theta(\tau) & s_y(\tau)\cos\theta(\tau) \end{bmatrix} \begin{bmatrix} \vec{u}_n \\ \vec{v}_n \end{bmatrix} + \begin{bmatrix} T_x(\tau) \\ T_y(\tau) \end{bmatrix} \tag{15}$$

Where s is shear, h is scale, θ is rotation, and T is translation for x and y vectors as function of time τ solved using homologous coordinates. Affine transformation calculation required a minimum of 3 pairs of feature coordinates. Using more features may enable more robust transformation estimation (an additional benefit of automatic feature selection). For this work, approximately 20 features were automatically selected for each patient and the least squares solution of Eqn. (15) was calculated resulting in a single universal affine transformation from τ_n to τ_{n+1}

An example of this affine transformation coordinate tracking is shown in Figure 5.3. Figure 5.3 (a) shows an example ablated region as an ellipse with inserted electrode with 5 selected features used for LDT. Additionally (a) shows the initialized rectangular coordinate grid encompassing the ablated region. Figure 5.3 (b) - (d) show how the ablated region was deformed via electrode perturbations as time elapsed. Features located in the B-mode image track this movement locally, with the corresponding features' relative position and displacement shown in (e) and (f), respectively, at sample times (a) - (d). (Note the cyclic motion of coordinates, as this is similar to what is seen for *in vivo* perturbations.) As a result of tracking features over time, affine transformations were estimated and applied to the rectangular coordinate grid. As shown in (b) – (d), the grid deforms and follows the ablated region using the feature coordinates as guides.

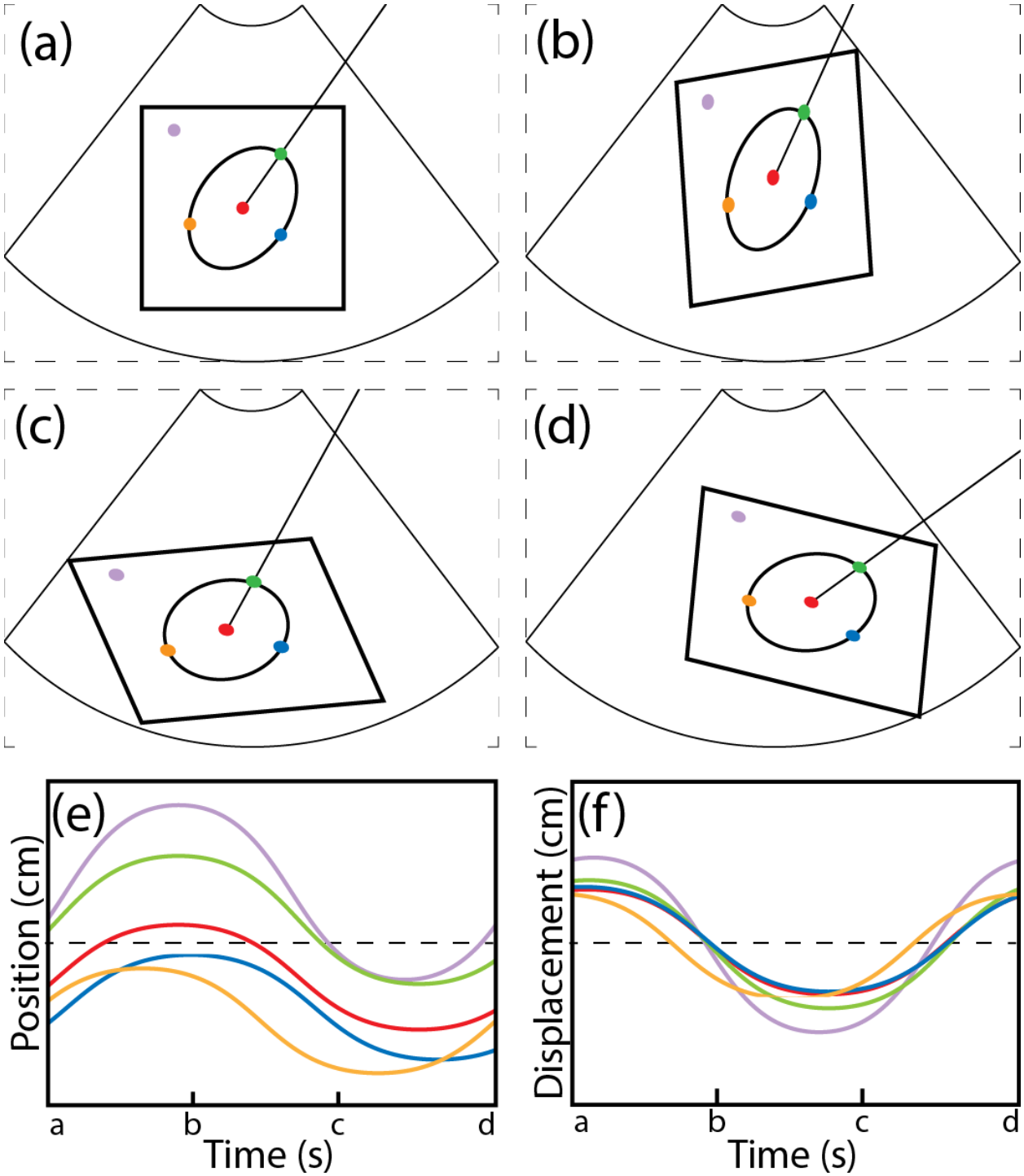

Figure 5.3 - An example of affine transformed coordinate tracking used in LDT. First frame (a), of image with ablated region as an ellipse, initialized coordinate grid as rectangle, and 5 sample tracking features. Panels (b-d) show transformation of coordinate grid over time as features follow antenna and ablated region. Relative position (e), and displacement (f), of the features at time steps a-d.

5.3.7 Coordinate Transformation

After calculating affine transformation variables of shear s, scale h, rotation θ, and translation T, the affine transformation matrix A can be formed shown in Eq. (16).

$$A(\tau)=\begin{bmatrix} s_x(\tau)\cos\theta(\tau) & -h_x(\tau)\sin\theta(\tau) & T_x(\tau) \\ h_y(\tau)\sin\theta(\tau) & s_y(\tau)\cos\theta(\tau) & T_y(\tau) \\ 0 & 0 & 1 \end{bmatrix} \tag{16}$$

Next, we need to define the coordinate grid that will be tracked over τ. This was initiated after manual selection of the initial region of interest (ROI) including the ablated region. The x and y coordinates of the entire ROI were then sampled at 0.1 mm increments and placed into vectors X and Y, respectively. These coordinates were transformed to remove tracked motion using Eq. (17).

$$\begin{bmatrix} X_n \\ Y_n \\ 1 \end{bmatrix} = A(\tau_n)\left(A(\tau_{n-1})\cdots A(\tau_2)\left(A(\tau_1)\begin{bmatrix} X \\ Y \\ 1 \end{bmatrix}\right)\right) \tag{17}$$

where X_n and Y_n are new sample coordinates for the displacement estimate n. To obtain spatially aligned displacement ROI, the Eulerian displacement, I_{Eul}, estimated from τ_n to τ_{n+1} and sampled at coordinates X_n and Y_n using bilinear interpolation were used to create the transformed displacement estimate, I^*_{Eul}. For future calculations, these transformed displacement estimates of the ROI were stacked into a 3D matrix I^*_{Eul}, where the first two dimensions are the size of the ROI and the third dimension is $N-1$.

5.3.8 Frame Selection and Interpolation

However, using an affine transformation as the trajectory function does not consider the possibility of out-of-plane motion. Assuming tissue continuity, features neighboring each other should generally move together, thus low variation in feature movement was expected especially due to high NCC constraints on feature tracking (NCC > 0.9). Despite these considerations, some features presented with high variation in

local movement, and thus a possible indicator of out-of-plane motion. Using this logic, a strategy was determined for reducing the effects of out-of-plane motion.

Movement of feature coordinates can be defined in terms of vectors $\vec{u}_n$ and $\vec{v}_n$ as $\vec{\mu}_n = \frac{\partial \vec{u}_n}{\partial \tau} = \frac{\vec{u}_{n+1} - \vec{u}_n}{\partial \tau}$ and similarly $\vec{v}_n = \frac{\partial \vec{v}_n}{\partial \tau}$.The variance in feature trajectories at each sample frame n was then calculated using Eq. (18).

$$\begin{aligned} \vec{\boldsymbol{\mu}}_n &= \mathrm{E}\left[\left(\vec{\mu}_n - \mathrm{E}\left[\vec{\mu}_n\right]\right)^2\right] \\ \vec{\mathbf{v}}_n &= \mathrm{E}\left[\left(\vec{v}_n - \mathrm{E}\left[\vec{v}_n\right]\right)^2\right] \end{aligned} \tag{18}$$

With trajectory variation estimated at each sampled time, mean, λ, and variance, Λ, were calculated for each sample frame over the entire EDE data collection as shown in Eq. (19) and (20), respectively. The feature trajectory variation was then standardized so that values could be compared using z-scores [60] as shown by Eq. (21).

$$\lambda = \frac{1}{N-1}\sum_{n=1}^{N-1}\sqrt{\left(\vec{\boldsymbol{\mu}}_n\right)^2 + \left(\vec{\mathbf{v}}_n\right)^2} \tag{19}$$

$$\Lambda = \frac{1}{\left(N-1\right)^2}\sum_{n=1}^{N-1}\left[\left(\sqrt{\left(\vec{\boldsymbol{\mu}}_n\right)^2 + \left(\vec{\mathbf{v}}_n\right)^2} - \lambda\right)^2\right] \tag{20}$$

$$z_n = \frac{\sqrt{\left(\vec{\boldsymbol{\mu}}_n\right)^2 + \left(\vec{\mathbf{v}}_n\right)^2} - \lambda}{\sqrt{\Lambda}} \tag{21}$$

The vector $\vec{z}$ now contains the standardized feature trajectory variance at each sample n, and out-of-plane motion was defined as outliers of this standardized set determined using a z-score threshold, ζ. Using this terminology, good frames ℓ were chosen as frames where $\left|z_i\right| \le \zeta$. The z-score threshold, ζ, was chosen heuristically as the $\min \zeta \ge 1$ such that $0.8 \times \left(N-1\right) \le \sum_{i=1}^{N-1} \mathbb{I}_{\{|z_i| \le \zeta\}}$, where $\mathbb{I}$ is the indicator function that is 1 where $\left|z_i\right| \le \zeta$. Plainly stated, ζ was chosen as the minimum value greater than 1 so that

at most 20% of frames are deemed outliers. The choice for a maximum number of outlier frames was heuristically chosen as some *in vivo* cases may present with large deformations or out of plane motion resulting in many frames to be deemed as outliers, thereby reducing the accuracy of the later interpolation stage. As a compromise between removing outlier frames and retaining valid information for interpolation, outlier frames were limited to a maximum of 20% of the frames in a tracked cycle. The displacement matrix was then resampled at outlier frames using a spline interpolation estimated from good frames.

Finally the accumulated displacement matrix under a Lagrangian description of the deformation, I_{Lag}, was obtained by accumulating displacements over discrete sample frames of an EDE cycle, namely $\{\eta,\ldots,\eta+\kappa-1\}$ in the set n, where η is the starting sampled frame and κ is the number of sampled frames in the tracked EDE cycle shown by Eq. (22). The first two dimensions of the resulting LDT deformation matrix are the size of the ROI and the third dimension as the number of frames in the tracked EDE cycle.

$$I_{Lag,k} = \sum_{\alpha=0}^{k-1} I^{*}_{Eul,\eta+\alpha} \quad \forall k \in \{1,\ldots,\kappa\} \tag{22}$$

5.3.9 Displacement and Strain Tensor Estimation

Initial Eulerian displacements were estimated using a Multilevel 2-D Normalized Cross-Correlation (MNCC) method developed by Shi and Varghese [61]. This method operates in a pyramidal hierarchy first estimating local displacements using large 2D kernels to provide high SNR and following with smaller kernels to improve spatial resolution while maintaining high SNR by utilizing higher level estimations as initial displacements for the lower levels. To further improve displacement estimation, 2D sinc-interpolation in the discrete cosine transform (DCT) domain [62] was utilized to estimate subsample displacements after each displacement estimation level. Displacement estimates with correlation coefficients less than 0.75 were interpolated using its nearest neighbors. For this work, four levels were used with kernel sizes of (8, 4, 2, 1) wavelengths by (8, 5, 3, 3) A-lines with the first, largest level using envelope data and the remaining levels utilizing RF data. Since a curvilinear transducer was used for RF

data collection, estimated displacements were converted from a polar to Cartesian coordinate system using trigonometric functions. Following coordinate conversion, displacement maps were then median filtered with a 1.9 mm $\times$ 1.9 mm kernel and then smoothed using dictionary representation with a patch size of 4.0 mm $\times$ 4.0 mm and 80% patch overlap. These estimated displacements were defined as the Eulerian displacements, I_{Eul}, and Lagrangian model for deformations, I_{Lag}, were estimated using Eq. (22). Finally, Eulerian and Lagrangian strain tensors were calculated using a 2D Savitzky-Golay digital differentiator of size 0.2 mm × 5.0 mm using 0^{th} × 2^{nd} order polynomials for x and y directions respectively [63, 64]. The operation time for LDT algorithm, namely automatic feature selection, tracking of 20 points, affine transformation estimation, coordinate transformation, and frame selection/interpolation, is approximately 3-5 min for each patient largely dependent on number of points tracked and size of ROI.

5.3.10 Segmentation and Comparison of Strain Tensor Images

Eulerian and Lagrangian strain tensors images were used to segment ablated regions using active contours in the form of snakes. Snakes can conform to unique shapes and edges making them well suited for segmenting ablation regions due to the high-contrast boundary delineation obtained with strain tensor images [65-67]. Snakes were initialized by a single manually segmented image for each patient. That single segmentation was used as an initial contour for axial and lateral strain tensor images of both Eulerian and Lagrangian descriptions of motion. By using the same initialization for all tracked frames axially and laterally, snake segmentation reduces the effects of observer bias. Following segmentation, areas were calculated by summing segmented pixels and normalizing based on pixel size. The mean and standard deviation of segmented regions over an EDE cycle were then compared.

In addition to segmented region areas, further comparisons were performed using center of mass differences and Sørensen-Dice coefficients, also known as the Dice similarity coefficient (DSC) [68]. Changes in center of mass (CoM) provided insight if subsequent segmented regions obtained over the strain tensor loop were centered similarly to each other, while DSC provides a measure of segmented area overlap throughout an EDE cycle. The center of mass for each image was determined by summing pixels within

segmented region and normalized based on pixel size and CoM values were calculated using the 2-norm between centers of mass measured using Eq. (24). DSC was calculated using Eqn. (25) and values were averaged over the EDE cycle to obtain a single value for each patient.

$$C = \left(c_i, c_j\right) = \left(\frac{\sum_{i=1}^{N}\sum_{j=1}^{M} i \times \mathbb{I}_{\{B_{i,j}=1\}}}{\sum_{i=1}^{N}\sum_{j=1}^{M} \mathbb{I}_{\{B_{i,j}=1\}}}, \frac{\sum_{i=1}^{N}\sum_{j=1}^{M} j \times \mathbb{I}_{\{B_{i,j}=1\}}}{\sum_{i=1}^{N}\sum_{j=1}^{M} \mathbb{I}_{\{B_{i,j}=1\}}} \right) \tag{23}$$

$$CoM = \left\langle C_n, C_{n'} \right\rangle \tag{24}$$

$$DSC = \frac{2\left|B_n \cap B_{n'}\right|}{\left|B_n\right| + \left|B_{n'}\right|} \tag{25}$$

where i, j are the x, y coordinates of the segmented image B, $\mathbb{I}_{\{B_{i,j}=1\}}$ is the indicator function that is 1 if the i, j lies within the segmented region and 0 otherwise, n is sample frame number, and $\langle \bullet \rangle$ is defined as the ℓ_2-norm. DSC is defined as twice the number of elements common to both segmented images divided by the sum of elements in each image [68]. To compare the difference in segmented values, percent difference was calculated from traditional Eulerian to Lagrangian description shown by Eq. (26).

$$\frac{Lagr - Eul}{Eul} \times 100\% \tag{26}$$

5.3.11 Success Rates for Ablation Visualization

Since qualitative visualization is also vital to EDE, a qualitative assessment of ablated region visualization was done using strain tensor success rates [41]. Success rates were calculated by a single blinded observer visualizing Eulerian and Lagrangian axial and lateral strain tensor images for a strain dynamic range of 0-1%.

5.4 Tracking Results for Elastography Data

5.4.1 Tissue-Mimicking Phantom Tracking Results

Figure 5.4 and Figure 5.5 show a visual comparison between axial strain tensor images of a TM spherical inclusion phantom with a stiffness of 85 kPa embedded within a 28 kPa background over a cycle of manual external compression. Lateral strain tensors were not considered for phantom data as manual compressions were performed axially. The B-mode image of the stiffest inclusion is shown in Figure 5.4 (a). Additionally, the set of chosen tracking features are shown in Figure 5.4 (a) along with the rectangular tracking grid in green. The axial position and displacement of the tracked features are shown in Figure 5.4 (b) and (c), respectively over the manual compression cycle for 0.58 seconds. The feature position and corresponding displacement are tracked very accurately as illustrated by the alignment of the curve alignment in Figure 5.4 (b) and (c). Figure 5.5 (a) and (b) show the strain tensor images for Eulerian and Lagrangian axial at 4 different time instants. Since Lagrangian tracked displacements are accumulated, note the difference in strain tensor magnitudes between the methods. All strain tensor images provide a very consistent inclusion size and location, but the Eulerian approach fails to visualize at time 0.332 seconds. This is a reasonable outcome due to the small displacement vectors at that time verified in Figure 5.4 (b) and (c). On the contrary, since LDT accumulates displacements, the strain tensor image at 0.332 provides the maximum strain on the inclusion in Figure 5.5 (b).

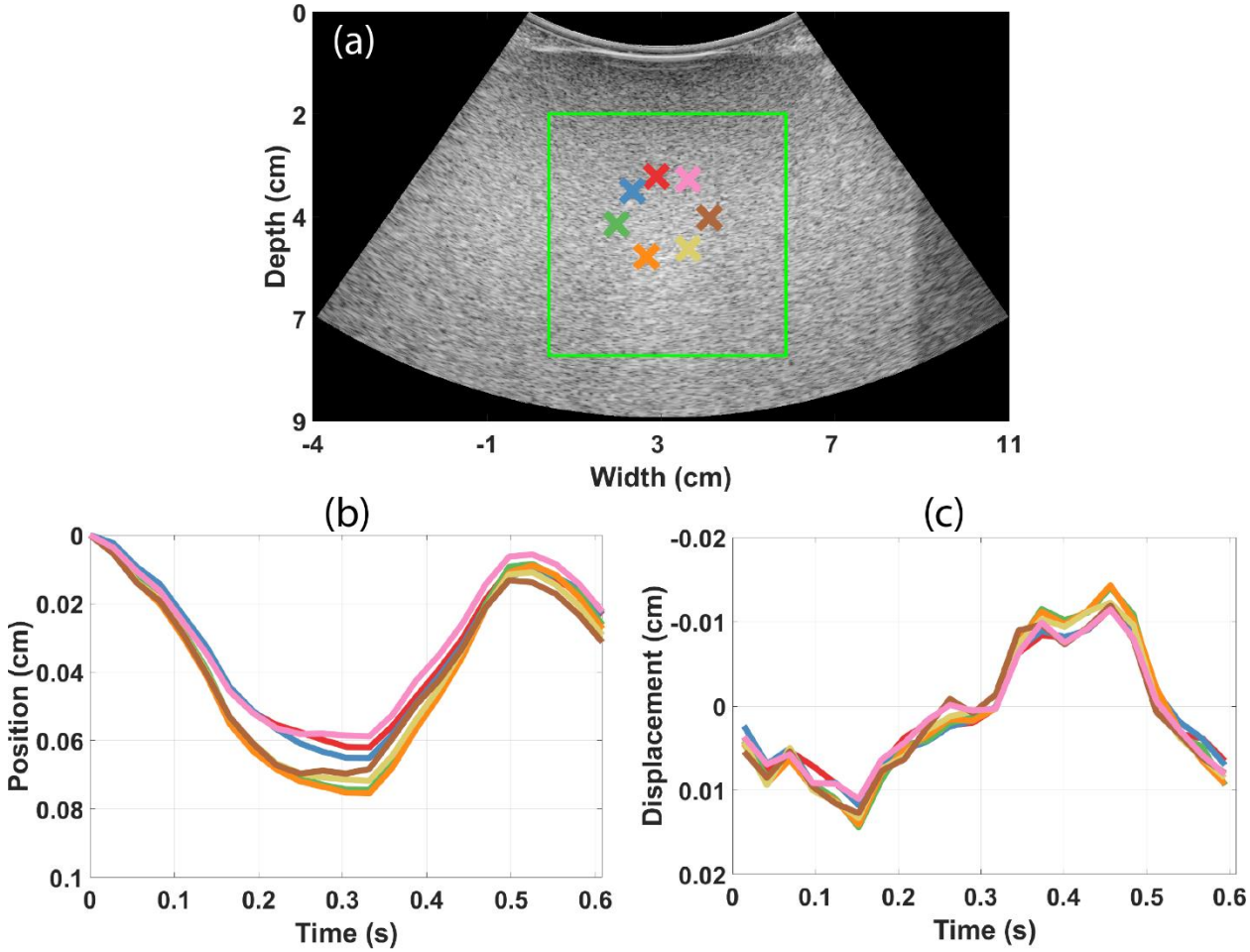

Figure 5.4 - Visual comparison between Eulerian and Lagrangian descriptions of motion in a TM phantom undergoing manual compression. Ultrasound B-mode image (a), showing the rectangular coordinate grid in green and sample of tracking features. Position (b), and displacement (c), of the tracked features over an EDE cycle.

The inclusion strain tensor image segmentation results of area mean, and standard deviation, dice coefficient, and center of mass are shown in Table 5.1. The segmented area means were found to be nearly identical between the tracking methods, while there was a standard deviation reduction of 74%. The average Dice coefficient of LDT increased by 10% to almost 1 and all center of mass differences fell to below 1 mm. These results demonstrate the improved consistency of LDT, hence tracking results of *in vivo* data were investigated.

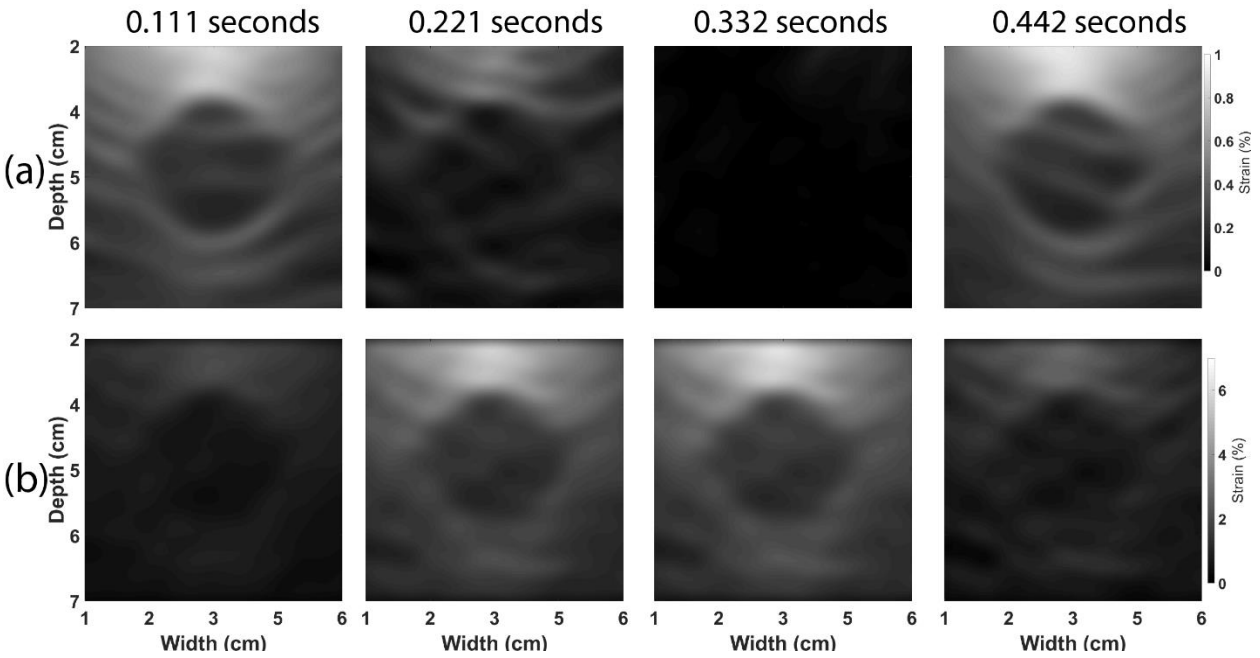

Figure 5.5 - Visual comparison between Eulerian and Lagrangian descriptions of motion in a phantom undergoing manual compression. Axial strain tensor images at 4 sample times during a single compression cycle utilizing Eulerian (a), and Lagrangian (b), descriptions of motion, respectively.

Table 5.1 - Comparison between the segmented areas from Eulerian and Lagrangian descriptions of strain tensors over manual compression cycle for the TM phantom.

			SEGMENTED AREA (CM^2)		**DICE COEFFICIENT**		**CENTER OF MASS DIFFERENCE (MM)**		
SAMPLE SIZE (N)	Track Time (s)	Method	Mean	Standard Deviation	Mean	Standard Deviation	Min	Mean	Max
21	0.58	Eulerian	4.9	1.1	0.88	0.09	0.004	0.13	0.37
		Lagrangian	4.9	0.29	0.96	0.02	0.002	0.024	0.049
		Percent Difference	-0.2%	-74%	10.%	-73%	-64%	-81%	-87%

5.4.2 *In vivo* Ablated Region Tracking Results

Ablated regions were successfully tracked for 7 *in vivo* data sets for approximately one cycle of electrode perturbation. Examples of strain tensor images from both descriptions of motion can be seen in

Figure 5.6-Figure 5.9. Quantitative results of comparing segmented regions are shown in Table 5.2 and CoM and DSC in Table 5.3. Figure 5.6 and Figure 5.7 shows visualization of an ablated region over an EDE cycle for Patient ID 2. A small subset of chosen tracking features can be seen in Figure 5.6 (a) along with the rectangular grid used for tracking shown in green. Figure 5.6 (b) and (c) represent the axial position and displacement, respectively, of this subset of tracked features over the EDE cycle with color corresponding to feature colors in Figure 5.6 (a). Figure 5.7 (a) – (d) show the strain tensor images for Eulerian axial, Eulerian lateral, Lagrangian axial, and Lagrangian lateral, respectively, at 4 different sample times over the EDE cycle. It is important to note that the Eulerian descriptions shown in Figure 5.7 (a) and (b) failed to provide ablated region depiction at tracked sample times 0.649 seconds. On the other hand, the Eulerian description at sample times 0.081, 0.24, and 0.487 seconds successfully provided ablated region depiction, but the size, shape, and contrast of the ablated region delineation varied. In contrast the Lagrangian descriptions shown in Figure 5.7 (c) and (d) show very consistent ablated region depiction, size, and shape at all sample times. A similar visual example is shown in Figure 5.8 and Figure 5.9 where lesion is shown tracked over two consecutive EDE cycles.

Table 5.2 – Comparison between the segmented areas from Eulerian and Lagrangian descriptions of strain tensors over a single EDE cycle.

				EULERIAN SEGMENTED AREA (CM^2)		**LAGRANGIAN SEGMENTED AREA (CM^2)**		**PERCENT DIFFERENCE**	
ID #	Sample Size (n)	Track Time (s)	Direction	Mean	Standard Deviation	Mean	Standard Deviation	Mean	Standard Deviation
1	9	0.61	Axial	23	11	10	0.89	-55%	-92%
			Lateral	24	7.0	9.8	0.40	-59%	-94%
2	8	0.65	Axial	22	11	11	0.37	-51%	-97%
			Lateral	20	6.5	9.6	1.7	-53%	-73%
3	13	0.83	Axial	32	4.1	24	2.9	-26%	-28%
			Lateral	28	5.3	16	2.7	-42%	-50%
4	15	0.87	Axial	30	6.6	14	5.0	-53%	-24%
			Lateral	28	6.0	21	2.8	-26%	-53%
5	8	0.43	Axial	25	7.6	5.7	0.18	-78%	-98%
			Lateral	25	7.9	6.3	0.19	-75%	-98%

6	9	0.73	Axial	40	1.2	6.0	0.35	-85%	-72%
			Lateral	38	3.0	3.4	0.39	-91%	-87%
7	7	0.47	Axial	18	9.7	3.5	0.74	-81%	-92%
			Lateral	26	8.0	3.4	0.30	-87%	-96%

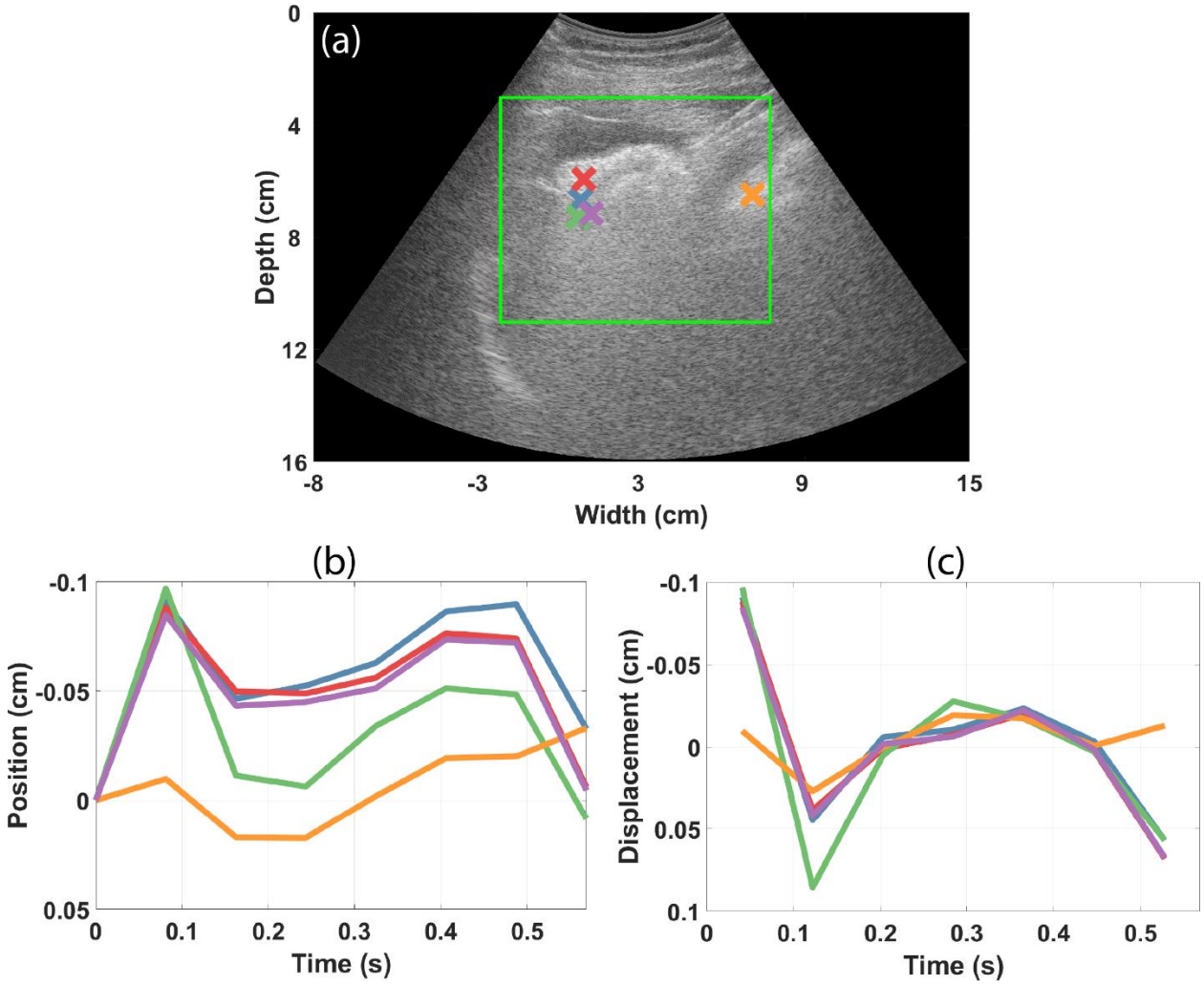

Figure 5.6 - Visual comparison between Eulerian and Lagrangian descriptions of motion in EDE for patient ID 2. (a) Ultrasound B-mode image showing the rectangular coordinate grid in green and subsample of tracking features. (b) and (c) show the position and displacement, respectively, of the tracked features over an EDE cycle.

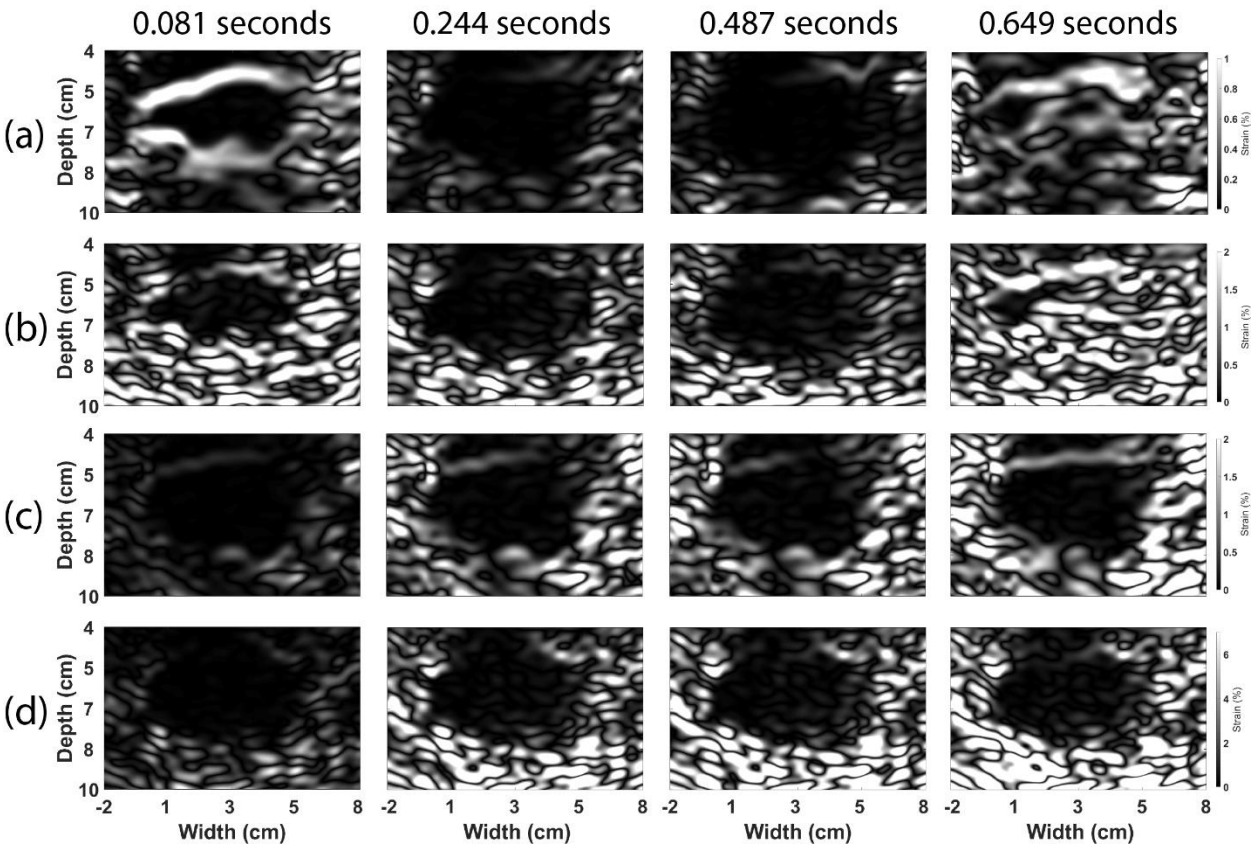

Figure 5.7 - Visual comparison between Eulerian and Lagrangian descriptions of motion in EDE for patient ID 2. Axial (a) and lateral (b) strain tensor images at 4 sample times during an EDE cycle utilizing an Eulerian description of motion. Axial (c), and lateral (d), strain tensor images at the same 4 sample times during the EDE cycle utilizing a Lagrangian description of motion.

Table 5.2 provides a comparison of the mean and standard deviation of segmented ablated region sizes using Eulerian and Lagrangian description of motion. Note that the perturbation frequency of the applied deformation varied with clinicians and depth of the liver mass varied with the patient. Therefore, a single cycle of electrode perturbation varied in the number of frames (n) and total tracked time in seconds ranging from 0.43 to 0.87 seconds as shown in Table 5.2. For all the patients within each description of the deformation, the mean segmented area for axial and lateral directions showed similar sizes meaning little discrepancy between directions. On the contrary, Eulerian and Lagrangian description differed with a

segmented area mean and standard deviation reduction of 61.5% and 75%, obtained with the Lagrangian description, respectively.

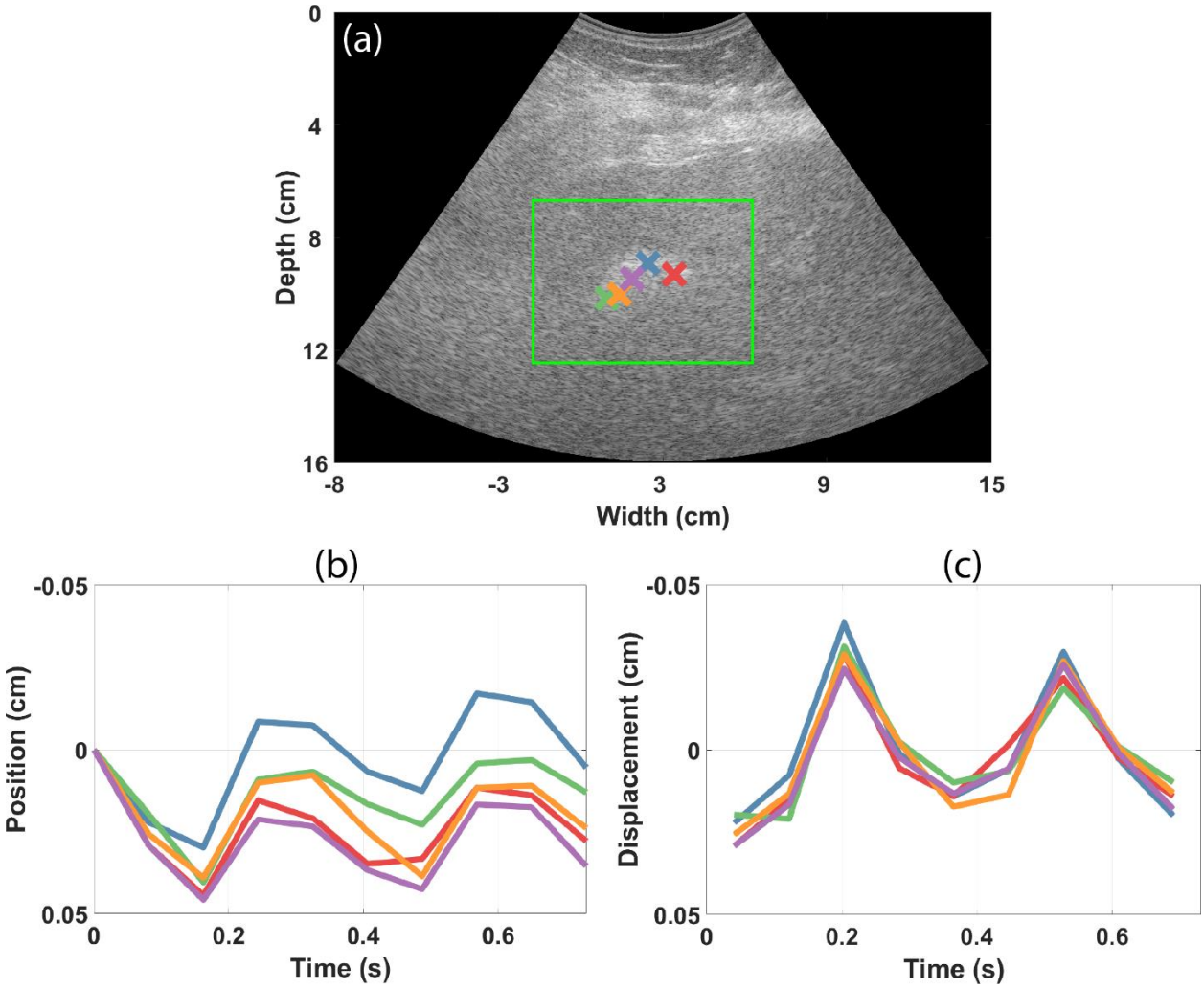

Figure 5.8 - Visual comparison between Eulerian and Lagrangian description of motion in EDE for patient ID 6. (a) Ultrasound B-mode image showing the rectangular coordinate grid in green and subsample of tracking features. Position (b), and displacement (c) of the tracked features over two EDE cycles.

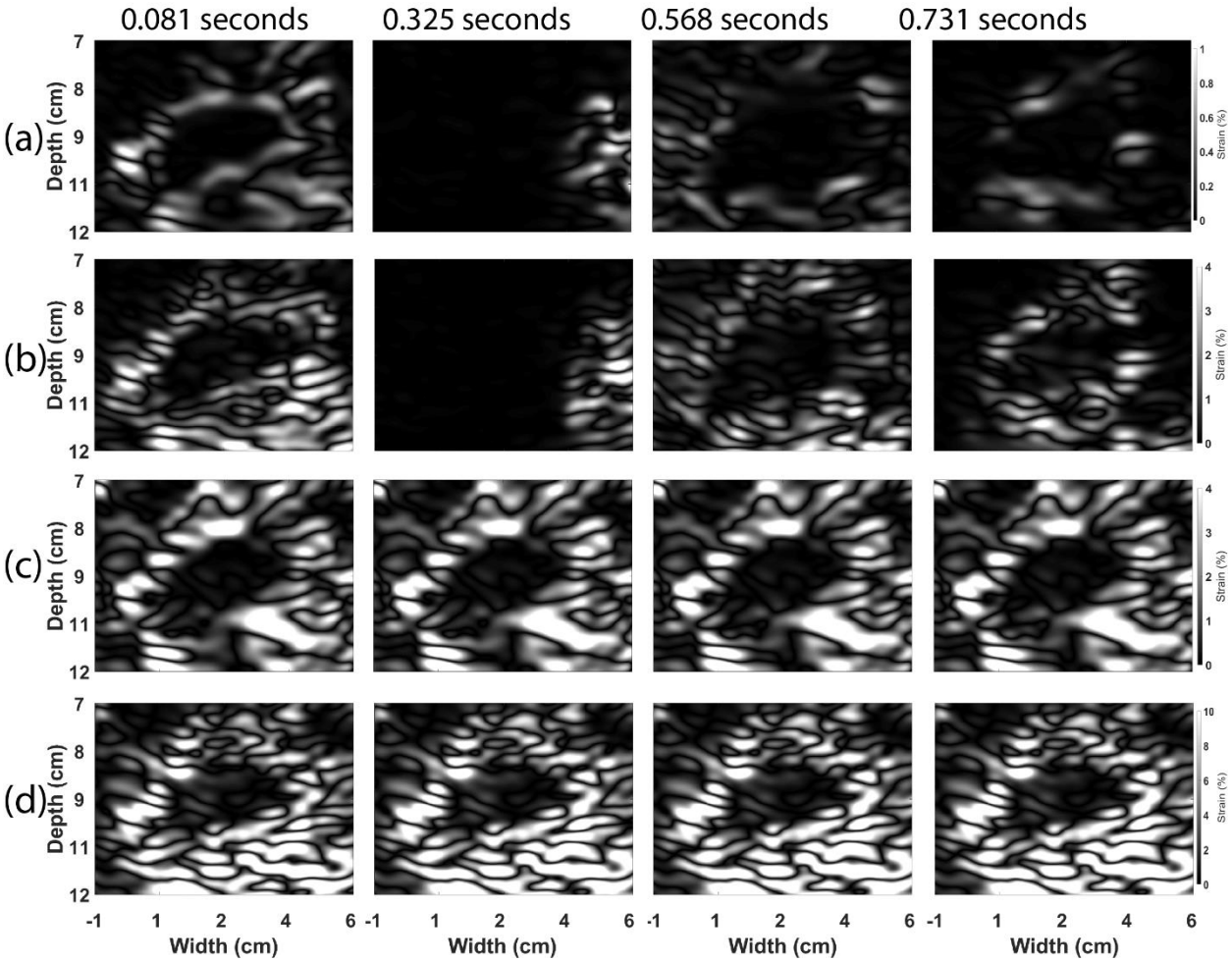

Figure 5.9 - Visual comparison between Eulerian and Lagrangian descriptions of motion in EDE for patient ID 6. Axial (a), and lateral (b), strain tensor images at 4 sample times during the tracked EDE cycles utilizing an Eulerian description of motion. Axial (c), and lateral (d), strain tensor images at the same 4 sample times during the tracked EDE cycles utilizing a Lagrangian description of motion.

The Dice similarity coefficient and center of mass differences also provided insight into the consistency of ablated region location and size. Table 5.3 shows results of the DSC and CoM for all 7 patients in this study. All patients provided the same or higher DSC values using a Lagrangian description of motion when compared to that of a traditional Eulerian description of up to 25%. Minimum, mean, and maximum CoM differences over the EDE cycle are shown in Table 5.3. In all datasets, lower values of

minimum, mean, and maximum are seen with LDT as opposed to Eulerian description, except for axial strain tensor image for patient 4.

Table 5.3 - Segmented area comparisons for ablated regions with Eulerian and Lagrangian description of motion.

		DICE COEFFICIENT			CENTER OF MASS DIFFERENCE (CM)					
					Eulerian			Lagrangian		
ID #	Direction	Eul	Lag	% Increase	Min	Mean	Max	Min	Mean	Max
1	Axial	0.74	0.94	20%	0.048	0.39	1.0	0.004	0.15	0.27
	Lateral	0.83	0.96	13%	0.015	0.33	0.73	0.004	0.088	0.18
2	Axial	0.73	0.98	26%	0.11	0.43	1.1	0.001	0.016	0.050
	Lateral	0.81	0.94	13%	0.016	0.31	0.52	0.004	0.054	0.17
3	Axial	0.89	0.94	4.9%	0.056	0.43	1.0	0.004	0.22	0.74
	Lateral	0.86	0.91	5.2%	0.060	0.40	0.98	0.005	0.25	0.60
4	Axial	0.83	0.84	0.8%	0.026	0.57	1.2	0.008	0.51	1.3
	Lateral	0.84	0.89	5.1%	0.052	0.58	1.2	0.009	0.37	0.83
5	Axial	0.82	0.98	16%	0.025	0.42	0.77	0.004	0.021	0.046
	Lateral	0.78	0.97	19%	0.080	0.64	1.2	0.004	0.088	0.22
6	Axial	0.98	0.97	-1.3%	0.021	0.10	0.19	0.013	0.049	0.089
	Lateral	0.95	0.94	-0.5%	0.047	0.24	0.61	0.007	0.047	0.084
7	Axial	0.71	0.88	17%	0.11	0.67	1.5	0.011	0.21	0.42
	Lateral	0.81	0.95	15%	0.14	0.53	1.1	0.009	0.075	0.20

5.4.3 Success Rates for Ablation Visualization

Success rates offer valuable insight to visualization performance of the two descriptions of motion. Success rates are defined as an ablated region visualization by a single observer over the tracked EDE cycle. It is calculated as a percentage of sample frames that an ablated region can be seen over the number of sample frames in an EDE cycle. Examples of positive visualization can be seen in Figure 5.9 (a) and (b) at sample times 0.08 and 0.57 seconds and all sample times for Figure 5.9 (c) and (d), while Figure 5.9 (a) and (b) at sample times 0.33 and 0.49 seconds provide examples of failed ablated region visualization.

The success rates for each of the patients is shown in Table 5.4. It is shown that none of the patients using a Eulerian description show ablated region visualization for the entire EDE cycle, and the average of

all patients only resulted 55% and 49% of frames in the EDE cycle be seen for axial and lateral strain tensors using Eulerian description. In contrast, LDT shows 100% success for axial and 91% success for lateral.

Table 5.4 – Success rates over an EDE cycle of Eulerian and Lagrangian description of motion for 7 patients

	EULERIAN		**LAGRANGIAN**	
ID #	Axial	Lateral	Axial	Lateral
1	89%	78%	100%	100%
2	63%	63%	100%	100%
3	31%	54%	100%	92%
4	67%	20%	100%	67%
5	38%	50%	100%	100%
6	44%	44%	100%	100%
7	57%	57%	100%	100%
ALL	55%	49%	100%	91%

5.5 Extension to Larger Number of MWA Patients

5.5.1 Data Selection and Methods for Extended Lagrangian Study

With feasibility shown initially with 7 patients, the next step was to apply LDT to a larger set of patient datasets to statistically evaluate performance. For this larger study, we utilized n = 30 patient data sets.

Automatic segmentation that will be discussed in Chapter 6 was utilized for segmenting strain tensor images for both Lagrangian and Eulerian tracked cycles in this larger study. Although automated segmentation results may not be ideal, this was beneficial for several reasons as described below. Automatic segmentation was much faster to perform without the requirement to manually segment each strain tensor image, i.e., approximately 10 frames per patient $\times$ 2 images: Eulerian and Lagrangian image $\times$ 30 patients = 600 images requiring manual segmentation and allowed for unbiased segmentation of strain tensor images.

5.5.2 Results of the Extended Lagrangian Study

Analysis of LDT was performed like the initial study of 7 patients with results for n = 30 patients shown in Figure 5.10 - Figure 5.12. Figure 5.10 presents a scatter plot of the Dice coefficients (DSC) between Lagrangian and Eulerian tracked EDE cycles for the 30 patients in the extended study. Although some DSC values are low, DSC obtained with LDT provides consistently greater DSC values than the corresponding Eulerian DSC by an average of 27.7%.

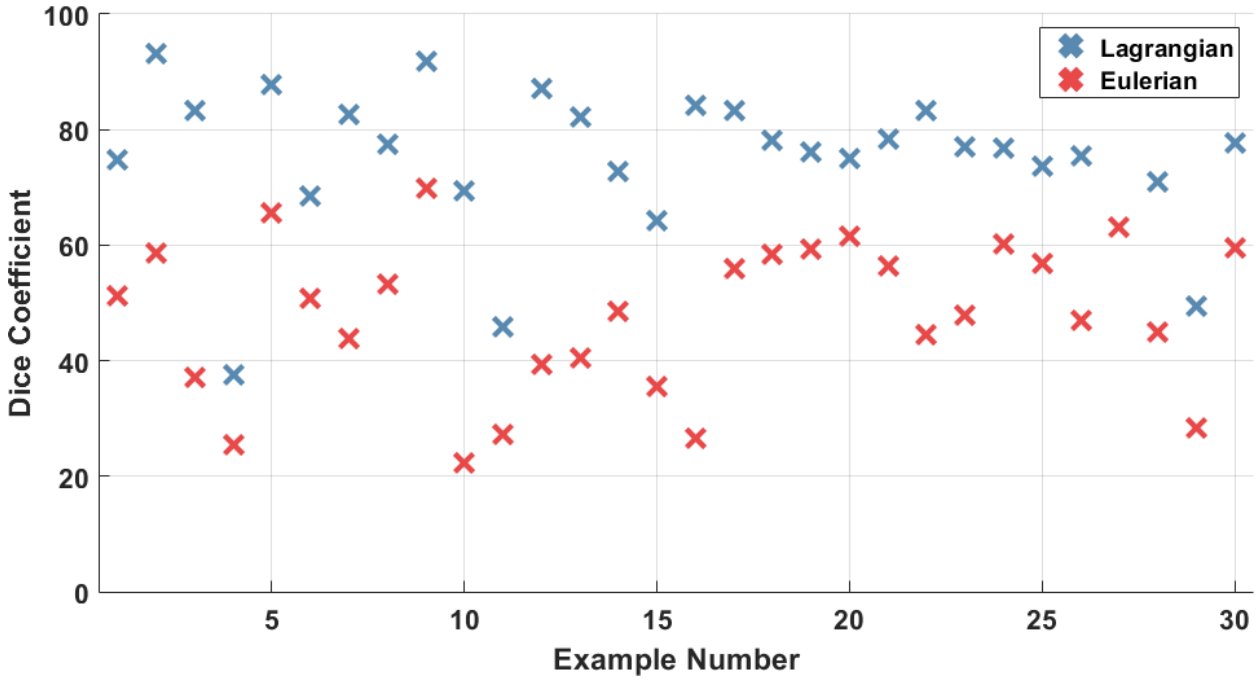

Figure 5.10 – Dice Coefficient values for n=30 patients with LDT denoted in blue and Eulerian tracking in red.

The extended results for cross-sectional ablation areas are shown in Figure 5.11. In Figure 5.11, the ‘x’s represent the average cross-sectional ablation area for each patient obtained using LDT in blue and Eulerian tracking in red. The standard deviation of cross-sectional areas over each cycle is represented by the associated bar for each patient example. The cross-sectional area from the Lagrangian deformation approach showed on average 45% lower cross-sectional area over the perturbation cycle than the Eulerian approach and similarly standard deviations of segmented area over each cycle reduced by approximately 153%.

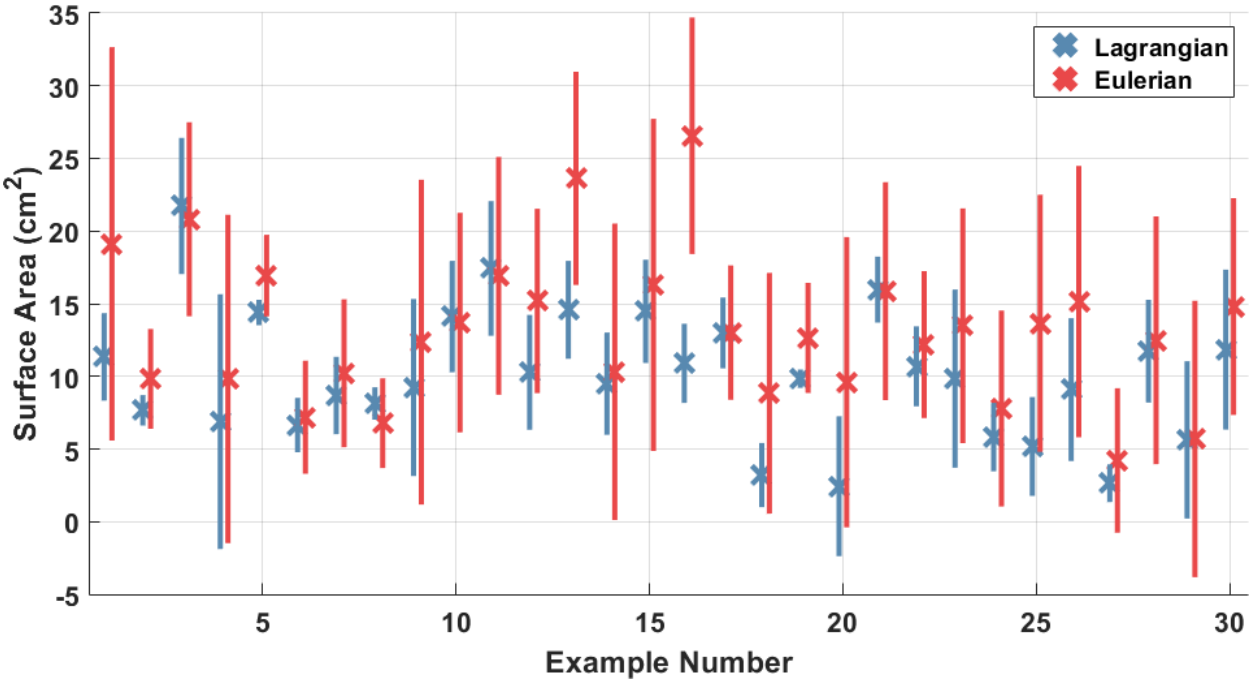

Figure 5.11 – Cross-sectional ablation area comparison of n=30 patients from LDT in blue and Eulerian tracking in red. The ‘x’s represent the average cross-sectional area over the tracked cycle, while the line represents the standard deviation from the mean over the tracked cycle.

The extended results for centroid difference are shown in Figure 5.12. In Figure 5.12, the ‘x’s represent the mean centroid difference for each patient for LDT in blue and Eulerian tracking in red. The range of differences over each cycle is shown by the associated bar for each patient example. The average mean centroid difference is 0.7 cm less for the LDT than Eulerian tracking across all patients. Similarly, the average minimum and maximum centroid differences were 0.17 cm less and 1.4 cm less, respectively, for LDT.

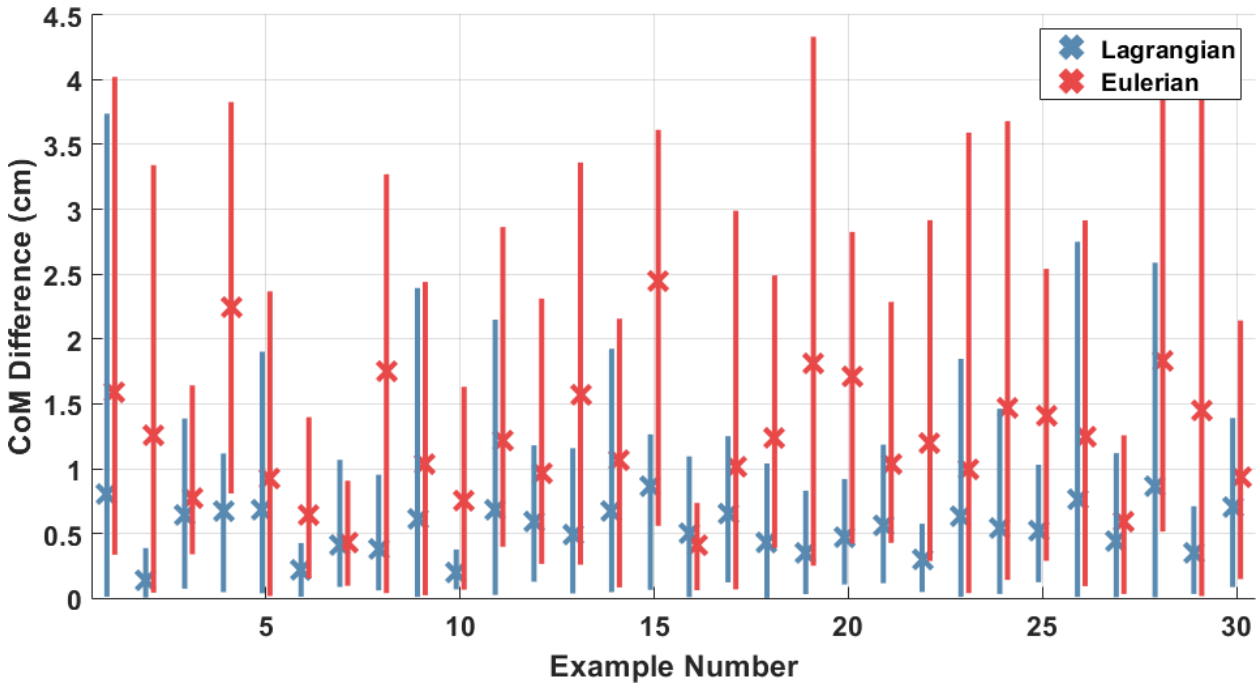

Figure 5.12 – Centroid or center of mass difference comparison for n=30 patients with results from LDT in blue and Eulerian tracking in red over a tracked EDE cycle. The 'x's represent the average centroid difference over the tracked cycle, while the line represents the centroid difference range over the tracked cycle.

In addition to centroid differences, success rates which were shown for the smaller data set were repeated for the larger *in-vivo* dataset which is shown in Figure 5.13. The LDT approach showed an average success rate of 89% which was 57% higher than the average Eulerian success rate of 32%.

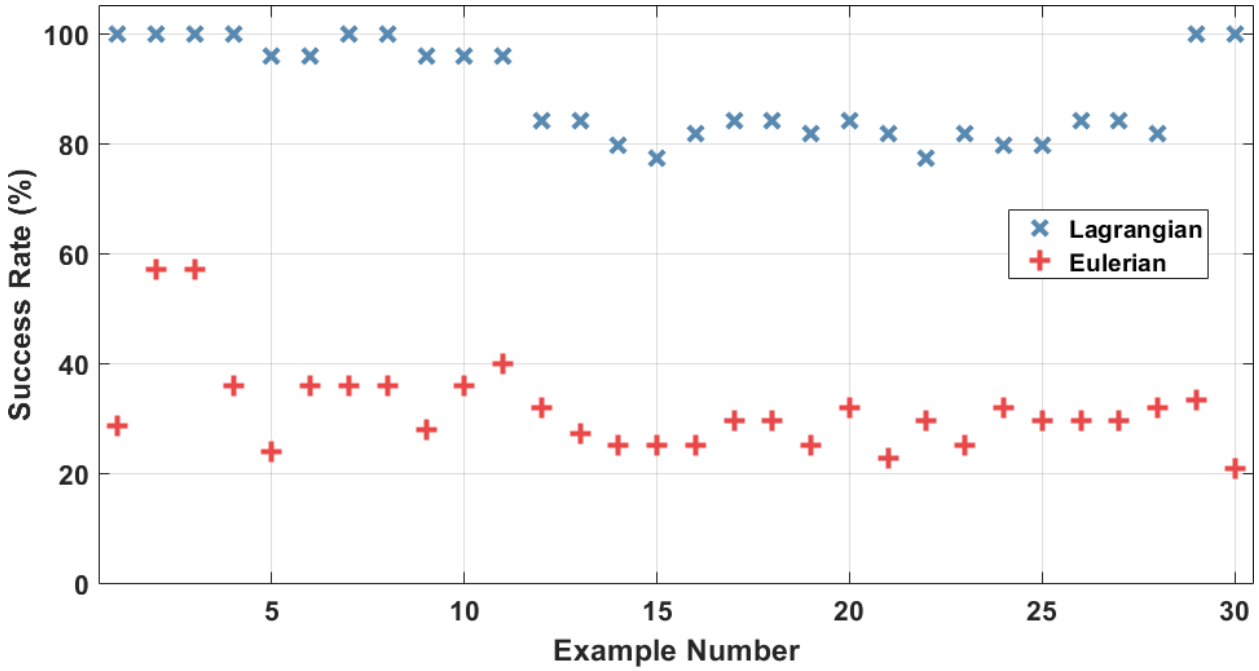

Figure 5.13 – Success rate over a tracked EDE cycle comparison for n=30 patients with results from LDT in blue 'x's and Eulerian tracking in red '+'s.

5.5.3 LDT Comparison to CECT

In addition to comparing metrics between Lagrangian and Eulerian deformation tracking approaches, it is important to verify cross sectional areas obtain on the corresponding strain images to segmented areas of current clinical standard of care CECT imaging. The mean cross-sectional segmented area from both Eulerian and Lagrangian tracking approaches was compared to manually segmented clinical standard of care image which was completed using RadiAnt [69]. Results of this comparison are shown in Figure 5.14 where red asterisks denote the Lagrangian obtained cross-sectional areas while the blue triangles denote that obtained with Eulerian tracking. Results showed that Lagrangian tracking provided cross-sectional areas that more closely correspond to the clinical standard of care 2D CECT virtual slice with a $R^2 = 0.91$, while the Eulerian approaches resulted in $R^2 = 0.68$. These results also indicate that Eulerian tracking provided significantly larger cross-section areas with EDE when compared to the clinical standard while the Lagrangian results aligned closely with clinical standard of care.

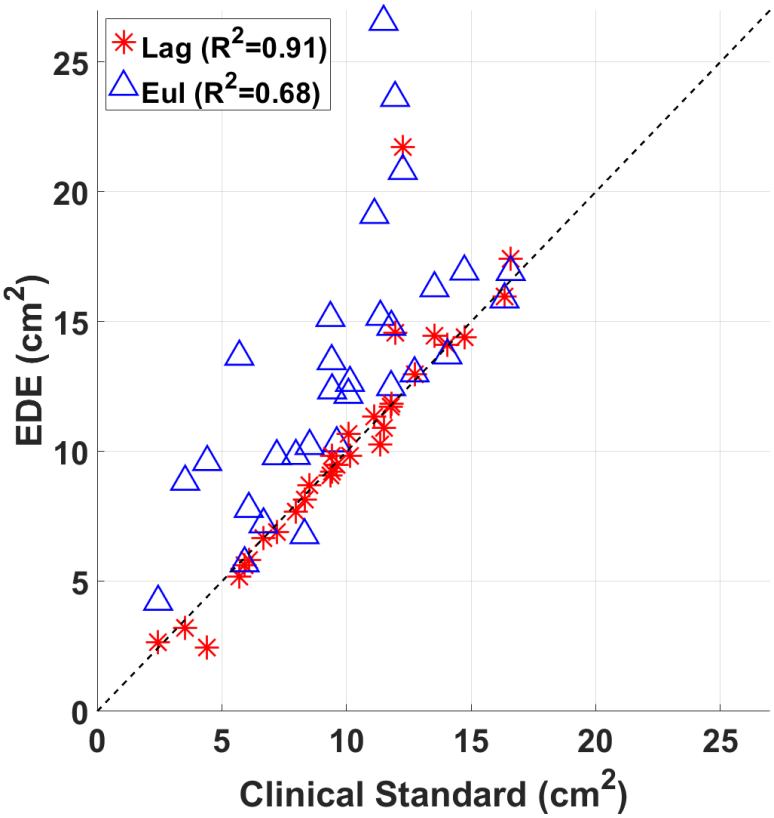

Figure 5.14 – Cross-sectional areas from EDE segmentations for Lagrangian and Eulerian deformation tracking approaches against the clinical standard of care manually segmented cross-sectional areas.

As shown in Figure 5.14, there are some examples where Lagrangian and/or Eulerian segmentations differ from the clinical standard of care CECT images. To visualize these changes, Figure 5.15 and Figure 5.16 are presented that show two different *in-vivo* cases where the image panel depicts (a) clinical B-mode ultrasound, (b) virtual slice from CECT, (c) s Eulerian tracked strain tensor image, and (d) the Lagrangian tracked strain tensor image. Figure 5.15 shows an *in-vivo* example of patient post-ablation images for MWA of a liver adenoma. Both Figure 5.15 (c) and (d) show very similar ablation regions both in size and location as well as similar alignment with Figure 5.15 (a) and (b). The example from Figure 5.15 presents with cross-sectional areas of 0.99 cm^2 from CECT, 0.95 cm^2 for Eulerian axial strain tensor image with a percent difference of 3.0% with CECT, and 1.01 cm^2 for Lagrangian strain tensor image with a percent difference of 2.0% when compared to CECT. Note that both Eulerian and Lagrangian strain tensor images provide cross-sectional areas like that obtained with CECT.

On the other hand, Figure 5.16 presents an *in-vivo* example of post-ablation images for a patient with a rectal metastasis where the different tracking methods provided cross-sectional areas that did not align with each other or the clinical standard of care. Figure 5.16 (c) from the Eulerian tracking presents with a cross-sectional area of 26.5 cm^2, while the LDT strain tensor image in (d) results in 16.5 cm^2. These both differ from the cross-sectional area found from the virtual slice CECT with a cross-sectional area of 15.5 cm^2, differing from Eulerian by 71% and Lagrangian by 6.5%. This example reinforces how LDT provides more consistent lesion visualization versus conventional Eulerian tracking.

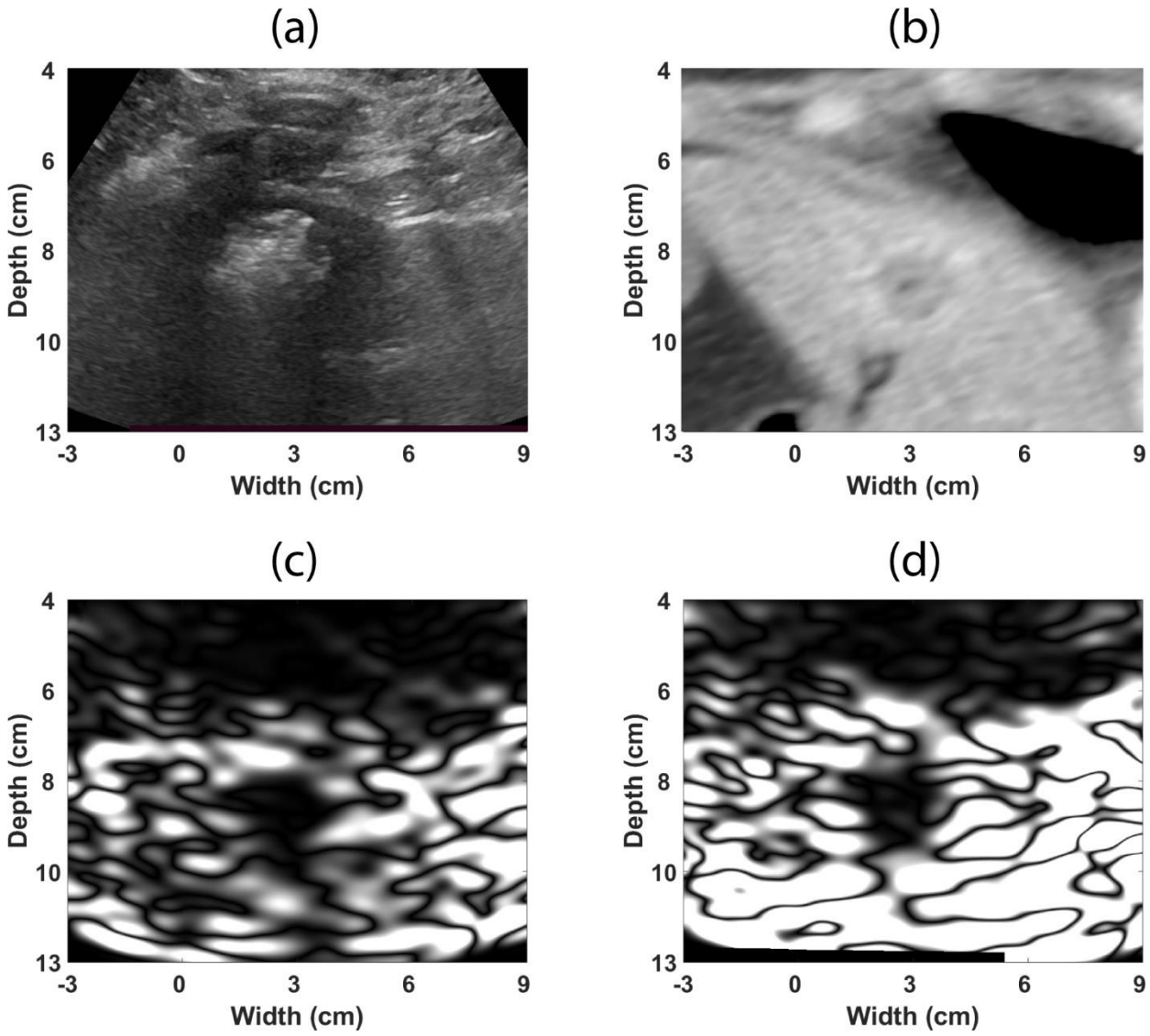

Figure 5.15 – A post-ablation example of a patient presenting with a liver adenoma at an approximate depth of 9 cm where Eulerian and Lagrangian strain tensor images aligned well with CECT. (a) shows the clinical B-mode image, (b) shows the virtual slice from CECT, (c) shows the Eulerian tracked strain tensor image, and (d) shows the Lagrangian strain tensor image.

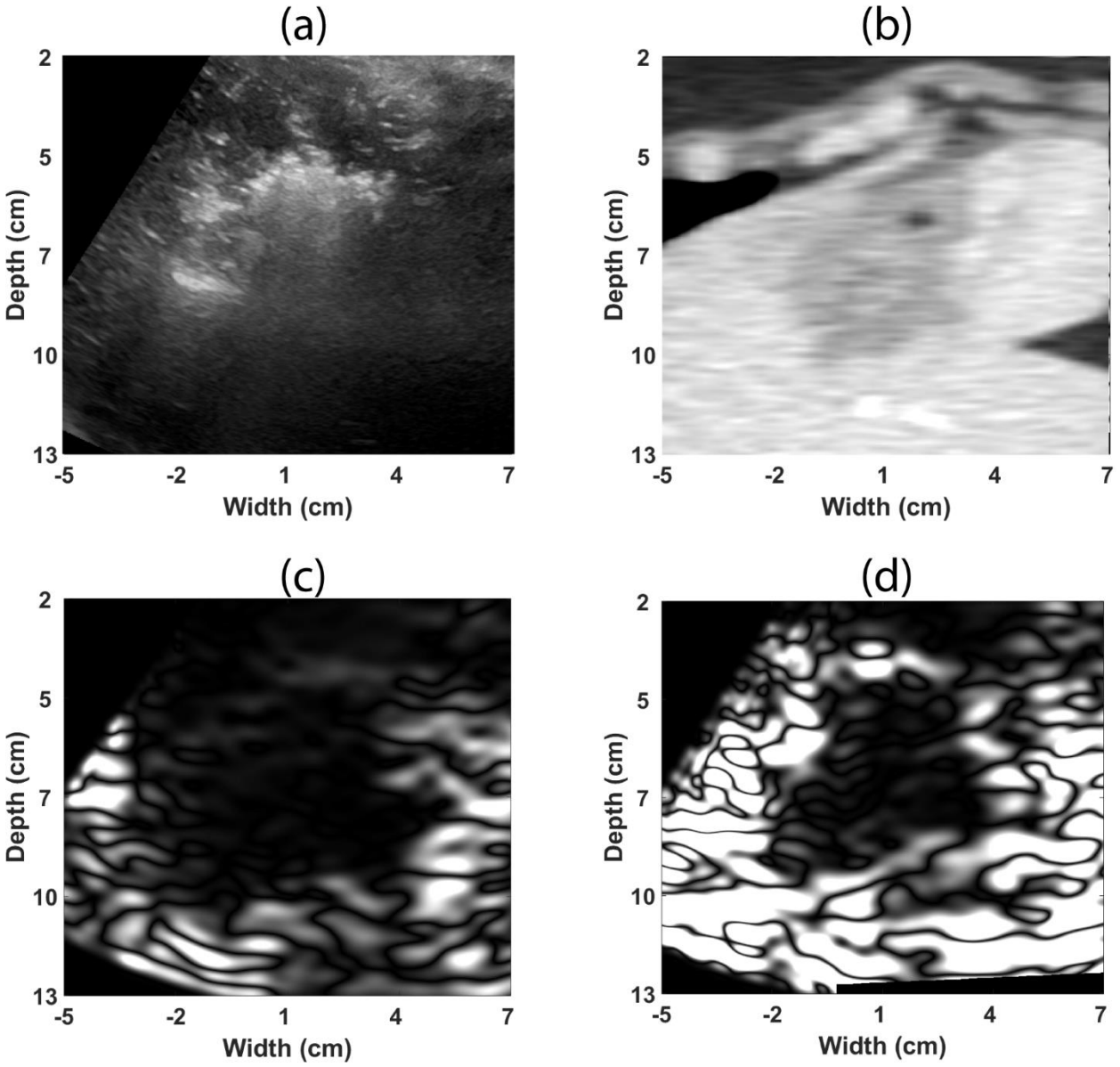

Figure 5.16 – A post-ablation example from a patient presenting with rectal metastasis at an approximate depth of 7.5 cm where Eulerian tracked strain tensor does not align well with CECT, while the Lagrangian strain tensor image aligned well with CECT. (a) shows the clinical B-mode image, (b) shows the virtual slice from CECT, (c) shows the Eulerian tracked strain tensor image, and (d) shows the Lagrangian strain tensor image.

5.6 LDT Discussion of Results

In this chapter, we describe the use of Lagrangian deformation tracking for microwave ablation elastography in the liver. In our approach, clinician introduced ablation antenna perturbations are the primary deformation of interest, which may be corrupted by various physiological deformations due to respiratory, cardiac, and patient movements, sonographer movement of the transducer. These extraneous deformation factors can differ greatly from patient to patient, and even within the same patient based on the liver lobe that is imaged.

Since the true ablated region size is not known, we are unable to draw any conclusions regarding the size or dimensions of the ablated region. For the phantom tracked cycle, the mean segmented area from the Lagrangian description did not differ from the traditional Eulerian description but showed improved consistency over time. For this reason, phantom results validated the consistency and accuracy of Lagrangian description of deformation as compared to the traditional Eulerian description. Although the true ablated region size is not known, we obtain a reduction in the segmented area standard deviations for the ablated regions, of at least 25% with the LDT approach when compared to the Eulerian approach for *in vivo* assessments. More importantly, we attain a large average reduction in the standard deviation by 75% demonstrating that LDT successfully provides more consistent segmented areas as opposed to the Eulerian approach. Additionally, LDT ablated regions resulted in much higher Dice coefficients and lower center of mass differences. This showed that segmented areas were similarly positioned and segmented overtime verifying the consistency of LDT and reduction in motion artifacts that plague the Eulerian description of motion. As a result of accurate tracking of ablated regions, success rates were greatly benefited with a nearly 100% successful visualization for axial and lateral directions using LDT.

Results of the extended study showed similar results as the initial study, a small reduction of mean segmented areas and a large reduction in standard deviation of areas over EDE cycles. It was also shown in Figure 5.10 that the Dice coefficient values for the Lagrangian tracking were 27% higher on average than the Eulerian tracking results. Also, important to note that the Dice coefficient values for the extended study are much lower than those in the initial study of 7 patients, this is likely due to the fully automatic

segmentation approach utilized in the extended study. Comparison of cross-sectional areas estimates obtained using both Lagrangian and Eulerian deformation tracking, demonstrating the close correspondence of cross-sectional areas obtained using LDT to the current clinical standard of care 2D CECT 'virtual slice'. We obtain Pearson's correlation coefficient values of $R^2 = 0.91$ with Lagrangian tracking, while the Eulerian approach resulted in a Pearson's coefficient values of $R^2 = 0.68$ on 30 independent patient data sets. Further shown by Figure 5.15 and Figure 5.16, there are a few examples of Eulerian tracking where cross-sectional areas align with those of CECT, while more examples of LDT align with CECT. Finally, success rates of LDT outperformed Eulerian tracking by 57% as shown in Figure 5.13.

5.6.1 Limitations of the work

A major limitation of this work is that we do not know the true size or location of ablated regions for patients, therefore we are unable to make any claims directly on the accuracy of the Eulerian or Lagrangian description of the deformation. We however demonstrate a comparison of size and locations of ablation zones using virtual slicing of the "gold-standard" CECT imaging for comparison to Eulerian and Lagrangian strain tensor images [70]. Although claims cannot be made on the accuracy of Eulerian or Lagrangian descriptions of deformation for *in vivo* cases, we are able to gain insight from phantom data and CECT comparisons.

5.7 Lagrangian Deformation Tracking Conclusion

Success rates and consistency of ablated region visualization using EDE have been previously limited by physiological and non-ideal motions present during *in vivo* data collection. To combat this issue, we proposed a Lagrangian deformation tracking approach (LDT) that tracks an ablated region temporally using affine transformations, significantly reducing the impact of these motions for ablated region visualization. Results of LDT showed a large decrease in segmented area standard deviation of nearly 100% on average and, using an ellipsoidal model, with low expected uncertainty of visualized ablative margins. Additionally, LDT showed higher consistency in ablated regions through an increase of Sørensen-Dice

coefficients of up to 25% from the traditional Eulerian approach as well as lower differences in center of mass between segmented regions. The results of this work show that LDT will be a vital addition to EDE for providing increased consistency and success in visualizing ablated regions. Utilizing LDT reduces the negative effects present during EDE visualization. Physiological motion artifacts are an inevitable consequence during *in vivo* MWA procedures, yet LDT shows reduction of these motion artifacts resulting in more consistent visualization of ablation regions. Incorporation of LDT further closes the gap between ultrasound and contrast enhanced computed tomography for imaging MWA procedures in a clinical setting.

5.8 Appendix A: Segmented Area and Ablated Margin

The main goal of MWA is to induce thermal necrosis of cancerous tissue of the liver and a margin of normal tissue necrosis of 0.5-1.0 cm. It is beneficial to relate segmented areas to size and error of desired ablated margins. If we assume that microwave energy radiated from the electrode created an ellipsoidal shape of necrosis [37], we can relate segmented area to ablated size and margin error by looking at Eq. (27)

.

$$Area \pm \Delta = \pi \left(\rho_1 \pm \delta \right) \left(\rho_2 \pm \delta \right) \tag{27}$$

Equation (27) is a modified equation for the area of an ellipse including the relationship of standard deviation on the area and radii of an ellipse, where ρ_1 and ρ_2 are the major and minor radii of the ablated ellipse, δ is the uniform radii standard deviation (ablated margin of error), and Δ is the segmented area standard deviation. Figure 5.17 visualizes this relationship between segmented area standard deviation and ablated margin error. Table 5.5 provides examples of expected area and deviation from an area given an ablative margin of error, δ. In addition to Table 5.5, Figure 5.18 shows the results against the $\delta = 0.1$ cm and $\delta = 0.25$ cm curves.

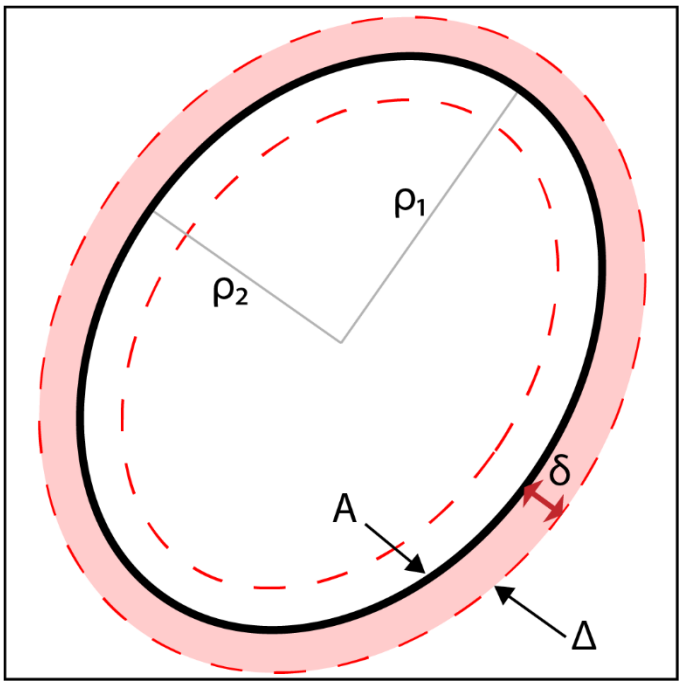

Figure 5.17 - Example of the relationship between the standard deviation in the segmented area versus the standard deviation of ablative margins.

Table 5.5 – Reference to ellipse area and standard deviation given ellipse radii and uncertainty in radius.

Ellipse Radii (cm)		*Area (cm^2)*	*Δ (cm^2) given δ= 0.1 cm*	*Δ (cm^2) given δ= 0.25 cm*
ρ_1	*ρ_2*			
1	*1*	3.1	0.66	1.8
1.5	*1*	4.7	0.82	2.2
2	*1*	6.3	1.0	2.6
2	*1.5*	9.4	1.1	3.0
2	*2*	13	1.3	3.3
2.5	*2*	16	1.5	3.7
3	*2*	19	1.6	4.1
3	*2.5*	24	1.8	4.5

3	*3*	28	1.9	4.9

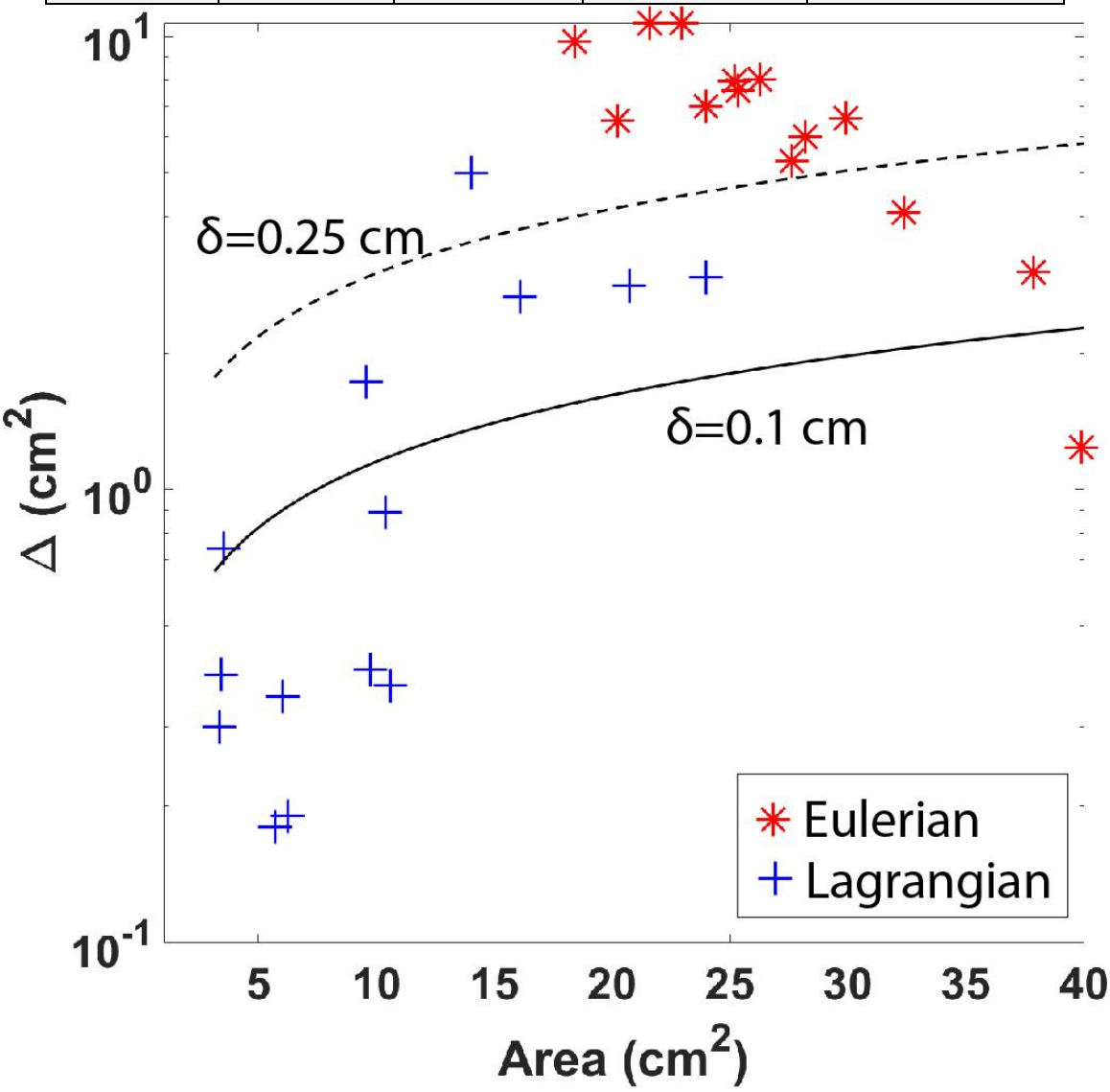

Figure 5.18 - The delta values for given segmented areas of the 7 *in vivo* examples for both Eulerian and Lagrangian tracking schemes with associated delta 0.1 cm and 0.25 cm.

As an example, if a clinician deems that the ideal ablation size for a patient is 2 cm -3 cm, referring to Table 5.5, this results in an ideal segmented area of 18.9 cm^2. If a segmented area showed a standard deviation of $\Delta < 1.60\ cm^2$, then we may assume that given an ellipsoidal ablation region the ablated margin should be within 0.1 cm of the ideal ablated margin. This of course only gives us a rough idea of the type

of consistency required for a method to be deemed reliable in detecting the true ablative margin. We cannot make any claims as to the accuracy of location or true shape of ablated regions.

We can estimate that the segmented area of the phantom inclusion provides a circular radius of 1.25 cm, while the radius of a 4.3 cm^3 inclusion is 1.01 cm. Although segmented inclusions from Eulerian and Lagrangian descriptions are slightly larger, area standard deviation of the Lagrangian description are well below a $\delta = 0.1$ cm using Table 5.5 as a guide. The Eulerian description on the other hand is greater than $\delta = 0.1$ cm. Additionally for *in vivo* cases, we can see that only one example, namely ID #6, of Eulerian segmented areas provided a standard deviation in the range of $\delta = 0.1$ cm for axial and $\delta = 0.25$ cm for lateral. This means that a high uncertainty of ablated margins was present using a Eulerian description of motion. On the contrary, standard deviations of Lagrangian segmented areas for ID #s 1, 2, 5, 6, and 7 demonstrated values representing close to $\delta = 0.1$ cm, or 10% of the ideal 1 cm margin and ID #3 of $\delta < 0.25$ cm. This result validates the importance of LDT's consistent segmented regions and resulting certainty that visualized ablated regions were relatively close ($\delta < 0.1$ cm) to the mean imaged ablated margin.

5.9 References

[1] A. M. Noone *et al.*, "SEER Cancer Statistics Review, 1975-2015," National Cancer Institute, Bethesda, MD, September 10, 2018 2018. [Online]. Available: https://seer.cancer.gov/csr/1975_2015/

[2] A. C. Society, "Facts & Figures 2018," 2018. [Online]. Available: https://www.cancer.org/cancer/liver-cancer/about/what-is-key-statistics.html.

[3] J. de Ridder, J. H. W. de Wilt, F. Simmer, L. Overbeek, V. Lemmens, and I. Nagtegaal, "Incidence and origin of histologically confirmed liver metastases: an explorative case-study of 23,154 patients," *Oncotarget*, vol. 7, no. 34, pp. 55368-55376, 2016, doi: 10.18632/oncotarget.10552.

[4] O. b. o. t. E. G. W. Group, E. Van Cutsem, B. Nordlinger, and A. Cervantes, "Advanced colorectal cancer: ESMO Clinical Practice Guidelines for treatment," *Annals of Oncology*, vol. 21, no. suppl_5, pp. v93-v97, 2010, doi: 10.1093/annonc/mdq222.

[5] D. Palmer and P. Johnson, "The clinical management of hepatic neoplasms," *Interventional radiological treatment of liver tumors*, A. Adam and P. R. Mueller, Eds., Cambridge ; New York: Cambridge University Press,, 2009, pp. 1-24.

[6] M. Maluccio and A. Covey, "Recent progress in understanding, diagnosing, and treating hepatocellular carcinoma," *A Cancer Journal for Clinicians,* vol. 62, no. 6, pp. 394-9, Nov-Dec 2012, doi: 10.3322/caac.21161.

[7] J. Bruix, G. J. Gores, and V. Mazzaferro, "Hepatocellular carcinoma: clinical frontiers and perspectives," *Gut,* vol. 63, no. 5, pp. 844-55, May 2014, doi: 10.1136/gutjnl-2013-306627.

[8] C. H. Liu, K. R. Avinssh, D. A. Gervais, and D. V. Sahan, "Diagnostic imaging pre- and post-ablation," *Interventional radiological treatment of liver tumors,* A. Adam and P. R. Mueller, Eds., Cambridge ; New York: Cambridge University Press, 2009, pp. 44, 73.

[9] R. Lencioni and L. Crocetti, "Local-regional treatment of hepatocellular carcinoma," *Radiology,* vol. 262, no. 1, pp. 43-58, Jan 2012, doi: 10.1148/radiol.11110144.

[10] K. T. Tan and C. S. Ho, "Percutaneous ethanol injection of hepatocellular carcinoma," *Interventional radiological treatment of liver tumors*, A. Adam and P. R. Mueller, Eds., Cambridge ; New York: Cambridge University Press,, 2009, pp. 108, 126 p.

[11] S. Ganguli and S. N. Goldberg, "Radiofrequency equipment and scientific basis for radiofrequency ablation," *Interventional radiological treatment of liver tumors*Cambridge ; New York: Cambridge University Press, 2009, pp. 167-180.

[12] G. D. Dodd, 3rd, M. S. Frank, M. Aribandi, S. Chopra, and K. N. Chintapalli, "Radiofrequency thermal ablation: computer analysis of the size of the thermal injury created by overlapping ablations," *Americal Journal of Roentgenology,* vol. 177, no. 4, pp. 777-82, Oct 2001, doi: 10.2214/ajr.177.4.1770777.

[13] S. N. Goldberg, G. S. Gazelle, and P. R. Mueller, "Thermal ablation therapy for focal malignancy: a unified approach to underlying principles, techniques, and diagnostic imaging guidance,"

Americal Journal of Roentgenology, vol. 174, no. 2, pp. 323-31, Feb 2000, doi: 10.2214/ajr.174.2.1740323.

[14] R. Murakami, S. Yoshimatsu, Y. Yamashita, T. Matsukawa, M. Takahashi, and K. Sagara, "Treatment of hepatocellular carcinoma: value of percutaneous microwave coagulation," *American Journal of Roentgenology,* vol. 164, no. 5, pp. 1159-64, May 1995, doi: 10.2214/ajr.164.5.7717224.

[15] S. Shiina *et al.*, "Radiofrequency ablation for hepatocellular carcinoma: 10-year outcome and prognostic factors," *Americal Journal of Gastroenterology,* vol. 107, no. 4, pp. 569-77; quiz 578, Apr 2012, doi: 10.1038/ajg.2011.425.

[16] C. M. Harari *et al.*, "Microwave Ablation: Comparison of Simultaneous and Sequential Activation of Multiple Antennas in Liver Model Systems," *Radiology,* vol. 278, no. 1, pp. 95-103, Jan 2016, doi: 10.1148/radiol.2015142151.

[17] M. J. Ryan *et al.*, "Ablation techniques for primary and metastatic liver tumors," *World journal of hepatology,* vol. 8, no. 3, pp. 191-199, 2016, doi: 10.4254/wjh.v8.i3.191.

[18] R. Lencioni and L. Crocetti, "Radiofrequency Ablation of Liver Cancer," *Techniques in Vascular and Interventional Radiology,* vol. 10, no. 1, pp. 38-46, 2007, doi: 10.1053/j.tvir.2007.08.006.

[19] A. Kelekis and D. Filippiadis, "Computed Tomography and Ultrasounds for the Follow-up of Hepatocellular Carcinoma Ablation: What You Need to Know," *Diagnostics,* vol. 6, no. 1, p. 9, 2016.

[20] J. R. Leyendecker *et al.*, "Sonographically Observed Echogenic Response During Intraoperative Radiofrequency Ablation of Cirrhotic Livers," *American Journal of Roentgenology,* vol. 178, no. 5, pp. 1147-1151, 2002/05/01 2002, doi: 10.2214/ajr.178.5.1781147.

[21] G. Mauri *et al.*, "Intraprocedural contrast-enhanced ultrasound (CEUS) in liver percutaneous radiofrequency ablation: clinical impact and health technology assessment," *Insights into imaging,* vol. 5, no. 2, pp. 209-216, 2014.

[22] C. P. Nolsøe *et al.*, "Use of ultrasound contrast agents in relation to percutaneous interventional procedures: A systematic review and pictorial essay," *Journal of Ultrasound in Medicine,* vol. 37, no. 6, pp. 1305-1324, 2018.

[23] W. K. Chong, V. Papadopoulou, and P. A. Dayton, "Imaging with ultrasound contrast agents: current status and future," *Abdominal Radiology,* vol. 43, no. 4, pp. 762-772, 2018.

[24] T. Varghese and J. Ophir, "Enhancement of echo-signal correlation in elastography using temporal stretching," *IEEE Transactions on Ultrasonics, Ferroelectrics, and Frequency Control,* vol. 44, no. 1, pp. 173-180, 1997, doi: 10.1109/58.585213.

[25] R. Huang *et al.*, "Comparative Diagnostic Accuracy of Contrast-Enhanced Ultrasound and Shear Wave Elastography in Differentiating Benign and Malignant Lesions: A Network Meta-analysis," *Frontiers in oncology,* vol. 9, p. 102, 2019.

[26] A. Wege, K. Schardt, S. Schaefer, A. Kroemer, G. Brockhoff, and E. Jung, "High resolution ultrasound including elastography and contrast-enhanced ultrasound (CEUS) for early detection and characterization of liver lesions in the humanized tumor mouse model," *Clinical hemorheology and microcirculation,* vol. 52, no. 2-4, pp. 93-106, 2012.

[27] T. Varghese, J. A. Zagzebski, and F. T. Lee, "Elastographic imaging of thermal lesions in the liver in vivo following radiofrequency ablation: preliminary results," *Ultrasound in Medicine & Biology,* vol. 28, no. 11-12, pp. 1467-1473, 2002/11 2002, doi: 10.1016/s0301-5629(02)00656-7.

[28] T. Varghese, "Quasi-Static Ultrasound Elastography," *Ultrasound Clin,* vol. 4, no. 3, pp. 323-338, Jul 2009, doi: 10.1016/j.cult.2009.10.009.

[29] J. Ophir, I. Cespedes, H. Ponnekanti, Y. Yazdi, and X. Li, "Elastography: a quantitative method for imaging the elasticity of biological tissues," *Ultrasonic Imaging,* vol. 13, no. 2, pp. 111-34, 1991.

[30] J. Ophir *et al.*, "Elastography: Imaging the elastic properties of soft tissues with ultrasound," *Journal of Medical Ultrasonics,* vol. 29, no. 4, pp. 155-171, 2002/12 2002, doi: 10.1007/bf02480847.

[31] G. Pareek *et al.*, "Elastographic measurements of in-vivo radiofrequency ablation lesions of the kidney," *J Endourol,* vol. 20, no. 11, pp. 959-64, Nov 2006, doi: 10.1089/end.2006.20.959.

[32] T. Varghese, U. Techavipoo, J. A. Zagzebski, and F. T. Lee Jr, "Impact of Gas Bubbles Generated During Interstitial Ablation on Elastographic Depiction of In Vitro Thermal Lesions," *Journal of Ultrasound in Medicine,* vol. 23, no. 4, pp. 535-544, 2004, doi: doi:10.7863/jum.2004.23.4.535.

[33] S. Bharat and T. Varghese, "Contrast-transfer improvement for electrode displacement elastography," *Physics in Medicine & Biology,* vol. 51, no. 24, pp. 6403-18, Dec 21 2006, doi: 10.1088/0031-9155/51/24/008.

[34] S. Bharat, T. Varghese, E. L. Madsen, and J. A. Zagzebski, "Radio-frequency ablation electrode displacement elastography: a phantom study," *Medical Physics,* vol. 35, no. 6, pp. 2432-42, Jun 2008, doi: 10.1118/1.2919763.

[35] J. Jiang *et al.*, "Young's modulus reconstruction for radio-frequency ablation electrode-induced displacement fields: a feasibility study," *IEEE Transactions on Medical Imaging,* vol. 28, no. 8, pp. 1325-34, Aug 2009, doi: 10.1109/TMI.2009.2015355.

[36] J. Jiang *et al.*, "Ultrasound-based relative elastic modulus imaging for visualizing thermal ablation zones in a porcine model," *Phys Med Biol,* vol. 55, no. 8, pp. 2281-306, Apr 21 2010, doi: 10.1088/0031-9155/55/8/011.

[37] N. Rubert *et al.*, "Electrode displacement strain imaging of thermally-ablated liver tissue in an *in vivo* animal model," *Medical Physics,* vol. 37, no. 3, pp. 1075-1082, 2010, doi: 10.1118/1.3301603.

[38] R. J. Dewall, T. Varghese, and C. L. Brace, "Visualizing ex vivo radiofrequency and microwave ablation zones using electrode vibration elastography," *Med Phys,* vol. 39, no. 11, pp. 6692-700, Nov 2012, doi: 10.1118/1.4758061.

[39] B. Peng, Y. Wang, W. Yang, T. Varghese, and J. Jiang, "Relative Elastic Modulus Imaging Using Sector Ultrasound Data for Abdominal Applications: An Evaluation of Strategies and Feasibility," *IEEE Transactions on Ultrasonics, Ferroelectrics, and Frequency Control,* vol. 63, no. 9, pp. 1432-40, Sep 2016, doi: 10.1109/TUFFC.2016.2589270.

[40] W. Yang *et al.*, "Post-Procedure Evaluation of Microwave Ablations of Hepatocellular Carcinomas Using Electrode Displacement Elastography," *Ultrasound in medicine & biology*, vol. 42, no. 12, pp. 2893-2902, 2016, doi: 10.1016/j.ultrasmedbio.2016.07.015.

[41] R. M. Pohlman *et al.*, "Comparison of Displacement Tracking Algorithms for *in Vivo* Electrode Displacement Elastography," *Ultrasound in Medicine and Biology*, vol. 45, no. 1, pp. 218-232, 2019, doi: 10.1016/j.ultrasmedbio.2018.09.001.

[42] R. M. Pohlman and T. Varghese, "Dictionary Representations for Electrode Displacement Elastography," *IEEE Transactions on Ultrasonics, Ferroelectrics, and Frequency Control*, vol. 65, no. 12, pp. 2381-2389, 2018, doi: 10.1109/TUFFC.2018.2874181.

[43] R. L. Maurice and M. Bertrand, "Lagrangian speckle model and tissue-motion estimation-theory [ultrasonography]," *IEEE transactions on medical imaging*, vol. 18, no. 7, pp. 593-603, 1999.

[44] M. McCormick, N. Rubert, and T. Varghese, "Bayesian Regularization Applied to Ultrasound Strain Imaging," *IEEE Transactions on Biomedical Engineering*, vol. 58, no. 6, pp. 1612-1620, 2011, doi: 10.1109/TBME.2011.2106500.

[45] J. Jiang and T. J. Hall, "A generalized speckle tracking algorithm for ultrasonic strain imaging using dynamic programming," *Ultrasound in Medicine and Biology*, vol. 35, no. 11, pp. 1863-1879, 2009.

[46] R. Zahiri-Azar and S. E. Salcudean, "Motion estimation in ultrasound images using time domain cross correlation with prior estimates," *IEEE Transactions on Biomedical Engineering*, vol. 53, no. 10, pp. 1990-2000, Oct 2006, doi: 10.1109/TBME.2006.881780.

[47] H. Rivaz, E. M. Boctor, M. A. Choti, and G. D. Hager, "Real-Time Regularized Ultrasound Elastography," *IEEE Transactions on Medical Imaging*, vol. 30, no. 4, pp. 928-945, 2011, doi: 10.1109/TMI.2010.2091966.

[48] E. Brusseau, J. Kybic, J.-F. Déprez, and O. Basset, "2-D locally regularized tissue strain estimation from radio-frequency ultrasound images: Theoretical developments and results on experimental data," *IEEE Transactions on Medical Imaging*, vol. 27, no. 2, pp. 145-160, 2008.

[49] N. H. Meshram and T. Varghese, "GPU accelerated multilevel Lagrangian carotid strain imaging," *IEEE Transactions on Ultrasonics, Ferroelectrics, and Frequency Control,* vol. 65, no. 8, pp. 1370 - 1379, August 2018 2018, doi: 10.1109/TUFFC.2018.2841346.

[50] N. Ouzir, A. Basarab, H. Liebgott, B. Harbaoui, and J.-Y. Tourneret, "Motion estimation in echocardiography using sparse representation and dictionary learning," *IEEE Transactions on Image Processing,* vol. 27, no. 1, pp. 64-77, 2018.

[51] C. Hoerig, J. Ghaboussi, and M. F. Insana, "An information-based machine learning approach to elasticity imaging," *Biomechanics and modeling in mechanobiology,* vol. 16, no. 3, pp. 805-822, 2017.

[52] S. Wu, Z. Gao, J. Luo, Z. Liu, H. Zhang, and S. Li, "Direct Reconstruction of Ultrasound Elastography Using an End-to-End Deep Neural Network," in *International Conference on Medical Image Computing and Computer-Assisted Intervention*, 2018: Springer, pp. 374-382.

[53] K. Wang *et al.*, "Deep learning Radiomics of shear wave elastography significantly improved diagnostic performance for assessing liver fibrosis in chronic hepatitis B: a prospective multicentre study," *Gut,* 2018, doi: 10.1136/gutjnl-2018-316204.

[54] S. M. Meyer, "Linear Actuator Mechanism," United States Patent Appl. 800,300, 1998.

[55] C. Ma and T. Varghese, "Lagrangian displacement tracking using a polar grid between endocardial and epicardial contours for cardiac strain imaging," *Medical physics,* vol. 39, no. 4, pp. 1779-1792, 2012.

[56] N. R. Saber and H. Wen, "Construction of the global lagrangian strain field in the myocardium using DENSE MRI data," in *Engineering in Medicine and Biology Society, 2004. IEMBS'04. 26th Annual International Conference of the IEEE*, 2004, vol. 2: IEEE, pp. 3670-3673.

[57] R. L. Maurice, J. Ohayon, G. Finet, and G. Cloutier, "Adapting the Lagrangian speckle model estimator for endovascular elastography: Theory and validation with simulated radio-frequency data," *The Journal of the Acoustical Society of America,* vol. 116, no. 2, pp. 1276-1286, 2004.

[58] H. Geyer *et al.*, "Assessment of myocardial mechanics using speckle tracking echocardiography: fundamentals and clinical applications," *Journal of the American Society of Echocardiography,* vol. 23, no. 4, pp. 351-369, 2010.

[59] A. Macovski, *Medical Imaging Systems*. Englewood Cliffs, NJ: Prentice-Hall, Inc., 1983.

[60] G. W. Milligan and M. C. Cooper, "A study of standardization of variables in cluster analysis," *Journal of Classification,* vol. 5, no. 2, pp. 181-204, 1988/09/01 1988, doi: 10.1007/BF01897163.

[61] H. Shi and T. Varghese, "Two-dimensional multi-level strain estimation for discontinuous tissue," *Physics in Medicine & Biology,* vol. 52, no. 2, pp. 389-401, Jan 21 2007, doi: 10.1088/0031-9155/52/2/006.

[62] L. Yaroslavsky, A. Happonen, and Y. Katyi, "Signal discrete sinc-interpolation in DCT domain: fast algorithms," *SMMSP 2002*, pp. 07.09. 2002-08.09. 2002, 2002.

[63] J. Luo, K. Ying, P. He, and J. Bai, "Properties of Savitzky–Golay digital differentiators," *Digital Signal Processing,* vol. 15, no. 2, pp. 122-136, 2005.

[64] A. Savitzky and M. J. Golay, "Smoothing and differentiation of data by simplified least squares procedures," *Analytical chemistry,* vol. 36, no. 8, pp. 1627-1639, 1964.

[65] M. Kass, A. Witkin, and D. Terzopoulos, "Snakes: Active contour models," *International journal of computer vision,* vol. 1, no. 4, pp. 321-331, 1988.

[66] J. Ivins and J. Porrill, "Everything you always wanted to know about snakes (but were afraid to ask)," *Artificial Intelligence,* vol. 2000, 1995.

[67] C. Xu and J. L. Prince, "Gradient vector flow: A new external force for snakes," in *Computer Vision and Pattern Recognition, 1997. Proceedings., 1997 IEEE Computer Society Conference on*, 1997: IEEE, pp. 66-71.

[68] T. Sørensen, "A method of establishing groups of equal amplitude in plant sociology based on similarity of species and its application to analyses of the vegetation on Danish commons," *Biol. Skr.*, vol. 5, pp. 1-34, 1948.

[69] *RadiAnt DICOM Viewer*. (2020). Accessed: 2020-03-09. [Online]. Available: https://www.radiantviewer.com

[70] R. M. Pohlman, M. R. Turney, P. H. Wu, C. L. Brace, T. J. Ziemlewicz, and T. Varghese, "2D US-CT Image Registration for Monitoring Percutaneous Hepatic Intervention (under review)," *Medical Physics*, 2019.

Chapter 6: Automatic EDE Ablation Segmentation

Microwave ablation (MWA) is rapidly becoming a popular minimally invasive percutaneous ablation method for treating liver tumors. One of the main contributing factors for the success of microwave ablation treatments is the accurate assessment of ablative margins, i.e., the amount of normal ablated region encompassing the index tumor. Elastography has been shown to be a novel and effective imaging modality for visualizing liver tumors and associated ablation zones. Despite qualitative imaging with elastography, the entire boundary of the targeted region may not be delineated requiring clinicians to make assumptions on the target size and shape. An automatic segmentation approach to provide a means for consistent delineation is described in this chapter. We chose to utilize automatic segmentation with initialization using an ellipse finding algorithm. To find an ellipse automatically, adaptation of the Hough transform was utilized. To test this method, the algorithm was applied to 14 strain tensor images from an inclusion phantom and 27 *in vivo* datasets from liver cancer patients. Results showed that 83% of segmentations were within ±10% of the ground truth phantom segmentation and 91% of segmentations were within ±16% of the ground truth for *in vivo* strain tensor images with an R-squared value of 0.95. The proposed work provides a segmentation method that will aid in treatment and assessment of liver tumors using MWA.

6.1 Segmentation for Electrode Displacement Elastography

6.1.1 Need for Automated Segmentation of Ablated Regions

With imaging provided with EDE, the requirement of verifying ablative margins is still necessary to evaluate treatment efficacy. For this task, manual segmentation is conventionally performed to determine ablative margins. Although manual segmentation on strain tensor images from EDE is not difficult, it still is time consuming and requires the trained eye of a radiologist for consistent segmentation. Despite training, segmentations may also vary between different observers (interobserver) as well as incur intraobserver

variation for the same observer or rater. Therefore, to increase productivity and consistency for interventional radiologist, a semi or fully automatic segmentation approach would be beneficial.

6.1.2 Segmentation Methods Described in Literature

Robust segmentation is very important for medical image processing to properly visualize sensitive anatomical structures for microwave liver ablation and to ensure that the entire tumor is encompassed to ensure effectiveness of ablative treatments [1]. To accomplish automated segmentation many methods have been described in the literature, namely thresholding, watershed algorithm, fuzzy and neutrosophic domains, or active contour segmentation [2-5].

The watershed method has shown good results for segmenting medical images yet is limited by possible over-segmentation [6-8]. Fuzzy logic is a clustering method that allows data pixels to belong to multiple classes with a varying level of membership, as opposed to conventional classification methods where pixels are exclusive to a single group [9]. The fuzzy set and neutrosophic domain are also used for mapping segmentations as shown in lung segmentation in CT images [10], glomerular basement membrane [11], and breast segmentations [12]. When compared to CT segmentations, iterative neutrosophic lung segmentations showed percentage overlap area (POA) to the ground truth to 91.2% and reduced Hausdorff and average distance by 6.6 mm and 1 mm, respectively when compared to expectation-maximization analysis and morphological operations [10]. Neutrosophic segmentation for glomerular basement membranes, a normally challenging segmentation due to large variants in microscopic images, showed a POA of 68%, Hausdorff distance of 4.6 pixels and average distance of 2.0 pixels [11]. For breast segmentation, the neutrosophic were used as a fully automatic segmentation method for accuracy in determining breast cancer diagnosis resulting in a true positive rate of 92.4 % and false positive rate of 7.2% [12].

6.1.3 Active Contour Models for Segmentation

Active contour models segment based on a curvature or contour flow utilizing constraints and energy forces to segment image pixels. Active contours take many forms including geodesic contours [13],

snakes [14], explicit functions [15], gradient vector flow and balloon models [16, 17]. Unfortunately, active contour models remain largely dependent on relatively accurate contour initialization to avoid local minima convergence [18].

6.1.4 Deep Learning and Neural Network Segmentation

With the recent advancements in computational hardware processing capabilities, deep learning approaches have grown in popularity for medical image segmentation [16]. Many deep learning approaches, namely those utilizing convolutional neural networks [19] have been used for brain image segmentation [20], based on training sets with non-medical image sources [21], and performing segmentation using multiple planes from the orthogonal domain [22]. Additionally, one of the most popular network architectures, U-Net [23], which utilizes deconvolution in the network [24] has been extensively used for medical image segmentations [25, 26]. Finally Convolutional Residual Networks allow the use of deeper networks as they can learn more features than shallower networks and utilize skip connections to reduce the degradation commonly seen in deeper neural networks [27]. An unfortunate downside to segmentation using neural networks is the requirement for training with large datasets to improve performance.

6.1.5 Segmentation of Elastographic Images Using a Coarse-to-Fine Active Contour Model

A previously developed method for automatic segmentation of strain tensor images for the purpose of EDE utilized correlation matching with templates from different radius circles [28]. Although this method showed good results when compared to *ex vivo* volumes and *in vivo* slices, this method was limited to circular targets due to the templates used. Additionally, results mainly dealt with inclusions that are fully contained by a delineating boundary. However, many *in vivo* elastograms do not present with these high contrast boundaries needed for active contour segmentation.

The novelty of this work will be incorporating the ellipsoidal shape as a means for initializing an active contour. By modelling an ellipse from edge points of the strain map, random sample consensus (RANSAC) was used to find the best-initialized ellipsoidal contour for automatic ablation segmentation.

Additional outcome of segmentation will provide a means of comparing registered CECT virtual slices [29] to evaluate the effectiveness of EDE ablation size and location depiction.

6.2 Automated Segmentation Methods

In this chapter, we utilized active contour snakes [14] with the addition of balloon forces [30] and gradient vector flow [31], conforming to strain depiction of ablations including discontinuous boundaries. In addition, we utilized an ellipsoidal parametric model of ablated masses and random sample consensus (RANSAC) [32] for snake initialization providing autonomous segmentation.

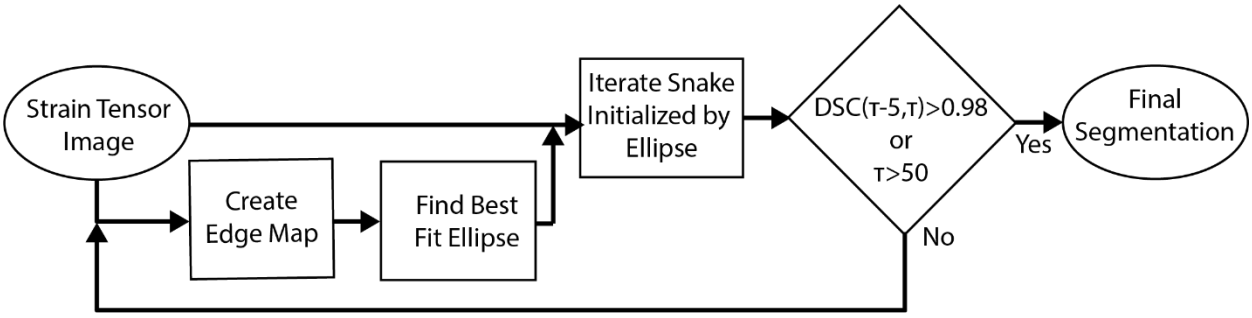

Figure 6.1 – Flowchart of proposed automatic segmentation algorithm.

6.2.1 Active Contours: Snakes

Active contours in the form of snakes can conform to unique shapes and edges making them well suited for segmenting ablations due to the excellent boundary delineation strain tensor images provide [14, 31, 33]. A traditional snake is a curve, $\mathbf{x}(s)$, and is demonstrated as Eq. (28).

$$\mathbf{x}(s) = [x(s), y(s)],\ s \in [0,1] \tag{28}$$

$$E = \int_0^1 \frac{1}{2}\left(\alpha\left|\mathbf{x}'(s)\right|^2 + \beta\left|\mathbf{x}''(s)\right|^2\right) + C \times E_{ext}\left(\mathbf{x}(s)\right) + D \times F_b\left(\mathbf{x}(s)\right) ds \tag{29}$$

$$E_{ext}(\mathbf{x}(s)) = -\left|\nabla I(\mathbf{x}(s))\right|^2 - \left|\nabla\left(G_\sigma(\mathbf{x}(s))\right) * \left(I(\mathbf{x}(s))\right)\right|^2 \tag{30}$$

$$F_b\left(\mathbf{x}(s)\right) = k_1 \mathbf{n}(s) - k\frac{\nabla P}{\left\|\nabla P\right\|} \tag{31}$$

Active contour snakes aim to minimize the energy E in Eq. (29) with additional energy terms derived from image intensities, namely Eq. (30) and balloon force Eq. (31). The image intensity energy allows the snake to be attracted or opposed to landmarks of an image (i.e., edges, lines, intersects, etc.), while the balloon force helps in avoiding issues when an active contour is initialized too far from an edge or does not have sufficient forces to keep the snake from shrinking on itself. Here α and β are weight parameters that control the 1st and 2nd derivatives, the snake's tension and rigidity, respectively, C is the weight of external energy, D is the weighting parameter of the balloon force, ∇ is the gradient operator, $G_\sigma(\mathbf{x}(s))$ is the 2-D Gaussian filter with standard deviation σ, P is the pressure force, $\mathbf{n}(s)$ is a normal unit vector to the curve at $\mathbf{x}(s)$, k is the amplitude of the balloon force, and the sign of k_1 dictates whether the force is inflation or deflation. The external energy E_{ext}, is found from the image itself such that smaller values occur at edges of interest. The term σ dictates the blur in image boundaries allowing the snake to detect the boundary from farther distances. The pressure force P dictates how strong of edges will inhibit the balloon force. Parameters used in this work are shown in Table 6.1.

Table 6.1– Parameters used in automatic segmentation algorithm.

Parameter		**Value**
α	=	2.4
β	=	2.7
C	=	20
σ	=	25
k	=	1.2
k_1	=	-1

6.2.2 Ellipse Finding Using Hough Transform

A limitation for consistent segmentation using active contours is the requirement for contour initialization relatively close to the target contour to ensure convergence to the true boundary. We utilized the ellipsoidal shape for initialization, which is often seen in tumors and ablated regions [34]. To find possible ellipses, the general quadratic form representing all conic sections [35], including ellipses, was used as shown by Eq. (32).

$$\omega(\mathbf{X}) = \mathbf{X}^T A\mathbf{X} + B^T\mathbf{X} + c = 0$$
$$\mathbf{X} = \begin{bmatrix} x \\ y \end{bmatrix}, \quad A = \begin{bmatrix} a_{11} & a_{12} \\ a_{12} & a_{22} \end{bmatrix}, \quad \text{and} \quad \mathrm{B} = \begin{bmatrix} b_1 \\ b_2 \end{bmatrix} \tag{32}$$

Using 5 point eigenvalues [35] or singular-value decomposition [36] the algebraic distance of Eq. (32) was minimized to find an ellipsoidal fit for a given 5 points. Points were selected using RANSAC [32] from an edge map created using a Canny edge detector [37] on a strain tensor image. To improve the computational efficiency of the ellipse finding algorithm, a generalized Hough transform was utilized to find ellipses largely based on [38]. This is repeated to find M possibilities for the best-fit ellipse. An added minimal roundness constraint of 0.3 (ratio of minor to major axis) was added to the ellipse calculations to eliminate unrealistic ellipse estimates leaving M_1 viable ellipses for the best-fit ellipse.

After finding M_1 ellipses, k-means was used to group similar ellipses. Each ellipse is then compared to the ellipse circumference that lies on the edge map, G, and range of strain tensor texture values, such as mean, $\mu_{BW,strain}$, and standard deviation, $\sigma_{BW,strain}$. To compare, the ellipses are scored using a value named normalized ellipse matching potential (NEMP) lying in the range of 0 – 1 shown in Eq. (33) . Here, the first term of Eq. (33) is the ratio of points along the ellipse circumference that lie on edges over the ellipse circumference while the second term is how low the mean strain inside the ellipse is over the max strain. An additional weighting term, γ, was utilized to adjust the weight of circumference and texture matching. A NEMP of 0 implies no overlap between the given ellipse and ideal ablation texture, while 1 means complete overlap.

$$NEMP_{ellipse} = \arg\max\left(\gamma\frac{\sum \mathbb{I}_{\{\omega(\mathbf{x})=\mathbf{G}\}}}{Circum_{\omega(\mathbf{x})}} + (1-\gamma)\left(1-\frac{\mu_{BW,strain}}{\max(strain)}\right)\right) \quad (33)$$

For this work, γ was set to 0.3 to put more weight on mean strain tensor magnitude inside the ellipse. Now that each ellipse has a rating score, the snake initialization curve was selected as the ellipse with the greatest NEMP as shown in Figure 6.2 (a) where the blue ellipse is selected as the initialization ellipse.

With the initial ellipse determined, the snake propagation is iterated until convergence. Figure 6.2 (b) shows the algorithm's converged segmentation in blue against the manual segmentation in red. Figure 6.2 (c) was created to show the repeatability and accuracy of the algorithm against the ground truth. The repeatability curve was produced by repeating the automatic segmentation algorithm 50 times for each frame from the TM Phantom. When the 50 repetitions of the algorithm were completed, the average segmentation cross-sectional area was calculated for each frame and the percentage error of each repetition from that average was found using Eqn (34).

$$\text{Repeatibility}_{F\times i} = \frac{\overline{A_F} - A_{F,i}}{\overline{A_F}} \quad (34)$$

where A is the area for frame, F, and repetition, i, and the $\overline{(\ )}$ denotes the average over all repetitions. This resulted in 50 repetitions $\times$ 14 frames $=$ 700 percentage error measurements which the probability density function (pdf) is shown by the red curve in Figure 6.2 (c). The ground truth curve in blue was found similarly by using Eqn. (35).

$$TruthError_{F\times i} = \frac{Truth_F - A_{F,i}}{Truth_F} \quad (35)$$

Where $Truth$ is the area for the manual segmentation at frame F. Like the repeatability measurement, this results in a distribution of 700 values which the pdf is shown as the blue curve in Figure 6.2 (c).

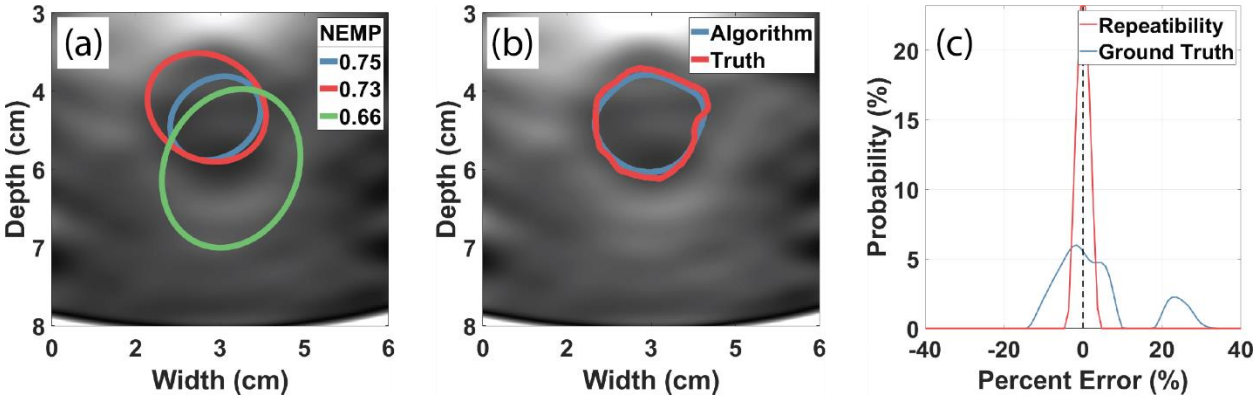

Figure 6.2 – TM Phantom strain image of a stiffer inclusion with the automatic segmentation algorithm applied. (a) shows the top 3 NEMP ellipses for possible snake initialization, (b) shows the automatic segmentation convergence in blue against the manual segmentation in red, and (c) shows the probability density function of the repeatability of the automatic segmentation algorithm in red and the accuracy of the automatic segmentation against the ground truth in blue.

6.2.3 Snake Banding Constraint for Segmentation

Unfortunately, snakes may have some limitations in this application as ablated regions may not be completely encompassed by high strain contrast due to low displacement estimates, attenuated ultrasound signal, or patient physiology. To combat this occurrence, a band constraint was established utilizing the initialization ellipse. The band constraint sets a small range or band inside and outside of the initialization ellipse that constrains snake propagation. For this work, the band was set as 0.5 cm to limit snakes from

propagating past discontinuous boundaries. Figure 6.3 shows segmentation on a patient example without using the snake banding constraint in Figure 6.3 (b) and with snake banding constraint in Figure 6.3 (c).

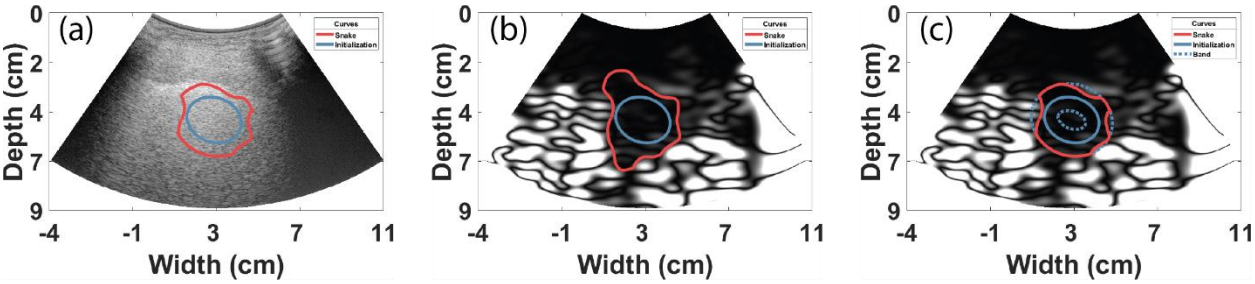

Figure 6.3 - Patient example with hepatocellular carcinoma demonstrating the banding constraint on snake propagation. (a) shows the B-mode image with the initialization curve in blue and banded snake convergence in red, (b) shows the strain tensor image with the initialization ellipse in blue and the unconstrained snake convergence, and (c) shows the strain tensor image with the initialization curve in the solid blue line, constraining band in the dashed blue line, and the constrained snake convergence in the solid red line.

6.2.4 Iterative Segmentation Algorithm

As the snake active contour iterates and is constrained by the band, the contour will converge quickly. Unfortunately, the initial chosen ellipse or snake iterations may result in a suboptimal convergence. To combat this possibility, the algorithm was iterated through the different stages of finding the optimal ellipse, contour initialization, and finally snake propagation to convergence. The next iteration begins by finding the ellipse that lies within the last iteration's contour convergence. These iterations are then repeated until the active contour segmentation retained a Dice-Sorensen coefficient of 0.98 for 5 consecutive iterations or after 100 iterations were completed.

6.2.5 Automated vs Manual Segmentation

To compare automatic segmentations, the *in vivo* ablated regions were manually segmented by a single blinded observer 5 times. The average contour obtained with manual segmentation was chosen as

the true segmentation that was then compared to results obtained with the proposed automatic segmentation algorithm.

We performed segmentation on data acquired using a CIRS phantom and *in vivo* data. All *in vivo* data used for analysis was tracked over a single antenna perturbation cycle with Lagrangian tracking to provide a more consistent strain tensor image. Visualized strain contrast was then set to maximize the contrast between strain estimated inside the target against the boundary. Strain tensor images were then normalized to this maximum contrast to maintain consistency for the segmentation algorithm.

To test efficacy of the automatic segmentation algorithm, the algorithm was executed 50 times for each sample image. This allowed for analysis of robustness of the algorithm against itself and its repeatability as well as independent realizations to compare against the ground truth segmentation shown by Eq. (36). The percent error versus the ground truth was found using Eq. (37).

$$\frac{\left(Area_{Algorithm} - \overline{Area}_{Algorithm}\right)}{\overline{Area}_{Algorithm}} \tag{36}$$

$$\frac{\left(Area_{Algorithm} - Area_{Truth}\right)}{Area_{Truth}} \times 100\% \tag{37}$$

6.3 Automated Segmentation Results

6.3.1 Segmentation Results from the CIRS Phantom

For this work, $n = 14$ strain tensor images were collected from a single inclusion phantom during manual quasi-static compression. For each strain tensor image, the algorithm was executed 50 times to assess segmentation repeatability. The percent error from all segmentations to the ground truth and from the average segmentation for each strain tensor image is shown in Figure 6.2 (c). Figure 6.2 (b) shows the comparison for a single frame to visually compare the algorithm converged segmentation in blue and the manually segmented ground truth shown in red. Results from Figure 6.2 (c) show two main peaks in algorithm's segmentations when compared to the ground truth. Of these peaks, the largest was centered at

-1.6% with 83% of segmentations lying in a range of -14% – 10% from the ground truth. The remaining 17% of segmentations are centered at 24%. The algorithm showed strong repeatability with a range of -5% - 5%.

6.3.2 Segmentation Results for Patient Data

For this work, $n = 27$ *in vivo* datasets were used. Figure 6.4 shows an example of the automatic segmentation algorithm from a patient with colon metastasis with the ground truth segmentation in red and algorithm segmentation in blue. Figure 6.4 (a) shows segmentations on a B-mode image where the segmentations do not necessarily align with the hyperechoic regions created during ablation. Contrary to Figure 6.4 (a), Figure 6.4 (b) shows the segmentations alignment with the strain tensor image with very similar segmentations between the algorithm and ground truth.

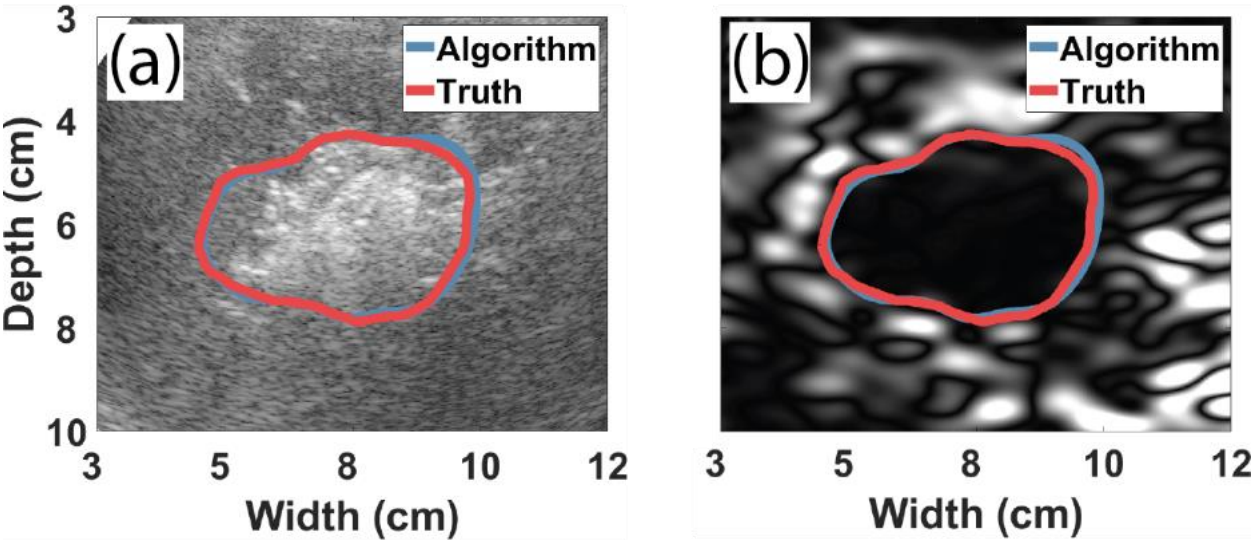

Figure 6.4 – Patient example with colon metastasis showing automatic segmentation in blue and ground truth segmentation in red with (a) B-mode and (b) axial strain tensor image.

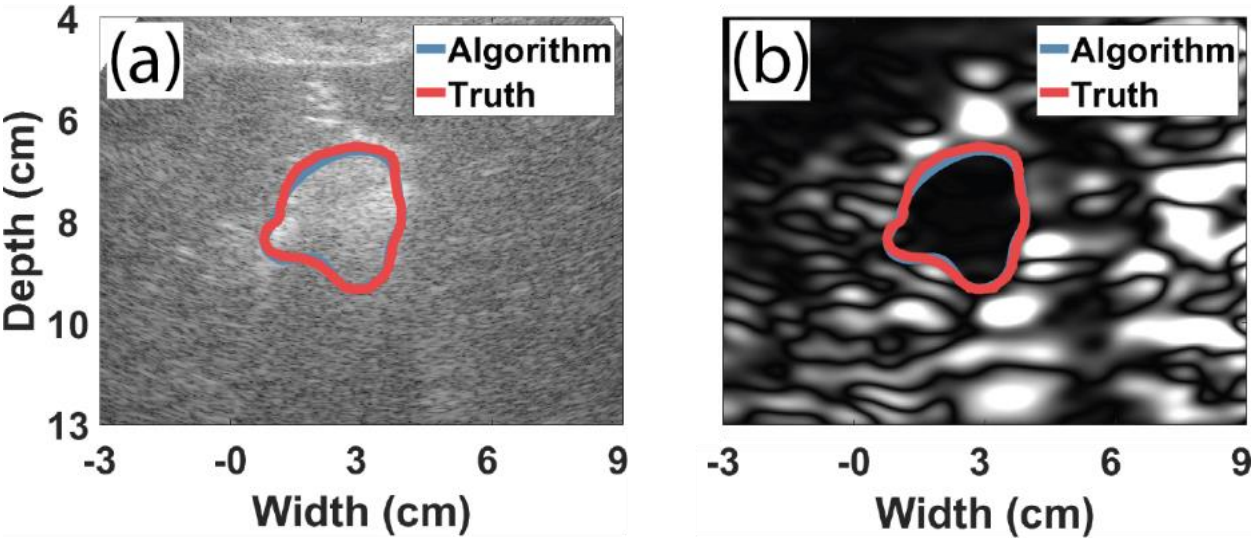

Figure 6.5 – Patient example with a carcinoid metastasis with automatic segmentation in blue and ground truth segmentation in red with (a) B-mode and (b) axial strain tensor image.

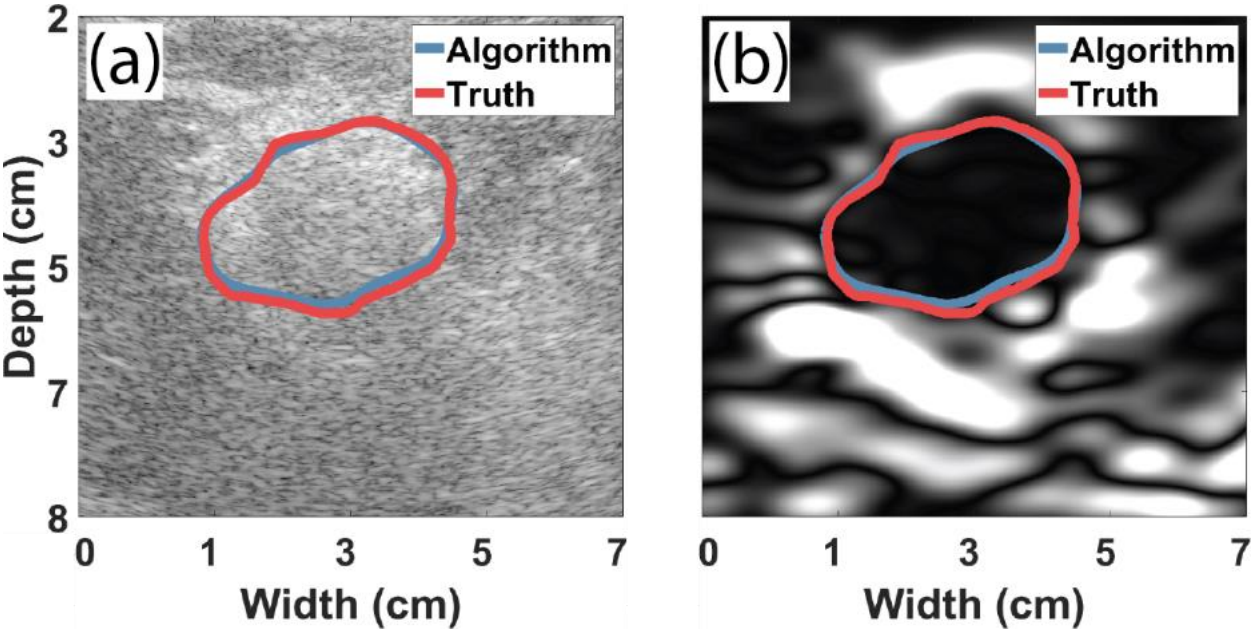

Figure 6.6 – Patient example with hepatocellular carcinoma with automatic segmentation in blue and ground truth segmentation in red with (a) B-mode and (b) axial strain tensor image.

Figure 6.5 shows an example of the proposed segmentation algorithm on a patient with carcinoid metastasis. Like Figure 6.4, the segmentations shown on the B-mode image in Figure 6.5 (a) do not align

with the hyperechoic regions from bubble formation. The automatic segmentation in blue shows good agreement with delineation of the strain tensor image as well as the ground truth in red in Figure 6.5 (b).

Figure 6.6 shows an example of the proposed segmentation algorithm on a patient with hepatocellular carcinoma. Like Figure 6.4, the segmentations shown on the B-mode image in Figure 6.6 (a) do not align with the hyperechoic regions from bubble formation. The automatic segmentation in blue shows good agreement with delineation of the strain tensor image as well as the ground truth in red in Figure 6.6 (b).

In addition to visualizing segmentation against the ground truth, quantitative measurements of R^2 value, percent error and repeatability are shown in Figure 6.7. Results using the median of repeated proposed segmentation algorithm surface area against the ground truth surface area showed an R^2 coefficient of 0.98 for the 27 patients in this study. The median algorithmic segmentation provided an average of 95% accuracy when compared to manual lesion segmentation with an average standard deviation of 0.2%. Algorithm segmentations also provided an average consistency of 98% over repeated segmentations on the same strain tensor image. Repeatability ranged from -25% – 28%. Against the ground truth, segmentation alignment showed main peak value at -1.2% error with a cumulative density of 91% between -16% - 16%. Finally, the segmentation algorithm provided a median Dice coefficient value of 0.91 ± 0.05.

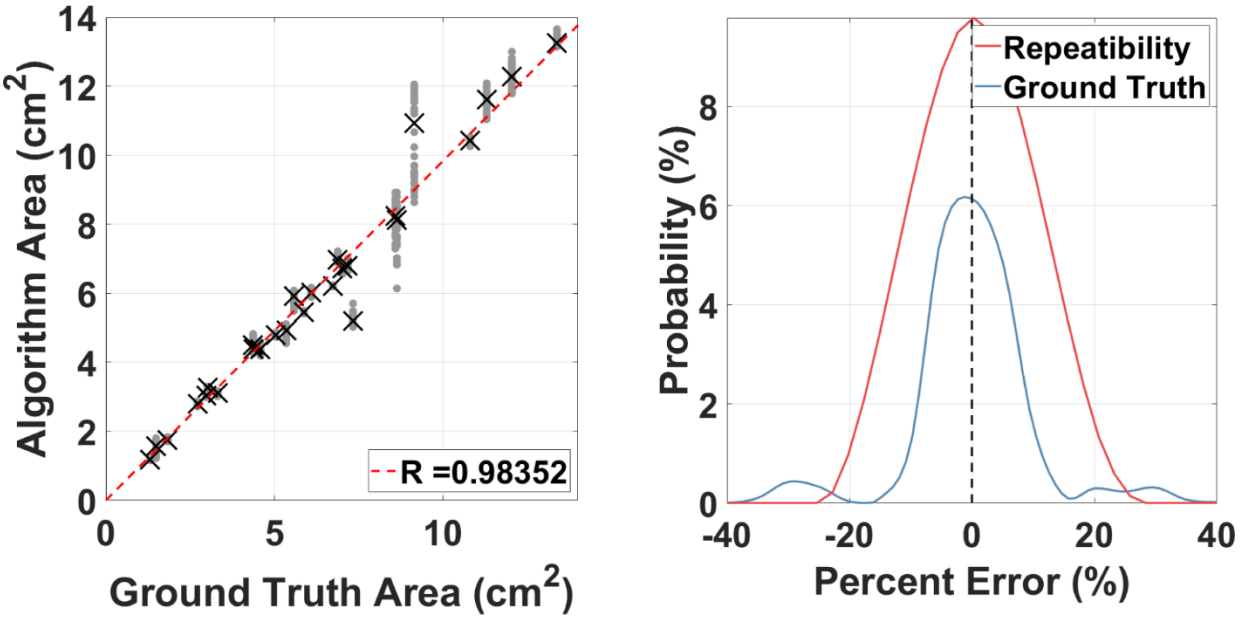

Figure 6.7 – Comparison of automatic and ground truth segmentations. (a) shows the correlation between median algorithm with and average standard deviation of 0.22 cm^2 and ground truth segmentation cross-sectional areas. Grey dots in (a) represent the algorithm segmentation values when repeated. (b) shows the probability density function of the repeatability of the automatic segmentation algorithm when repeated 50 times in red and the accuracy of the automatic segmentation against the ground truth in blue.

6.4 Discussion of Automated Segmentation for Ablation Monitoring

The proposed algorithm shows good alignment with manual ground truth segmentations. Since ablation zones are primarily represented as an ellipse from the manner energy is deposited as shown in Figure 6.8 [39]. Due to this ellipsoidal shape, the Hough transform ellipse initialization for snakes is very consistent and robust to noise seen in strain tensor images as well as initializing in proximity to the ground truth segmentations. Following similar logic, the snake banding constraint also allows for an ellipse approximation for segmentation where strong strain tensor delineation does not encapsulate the entire target circumference.

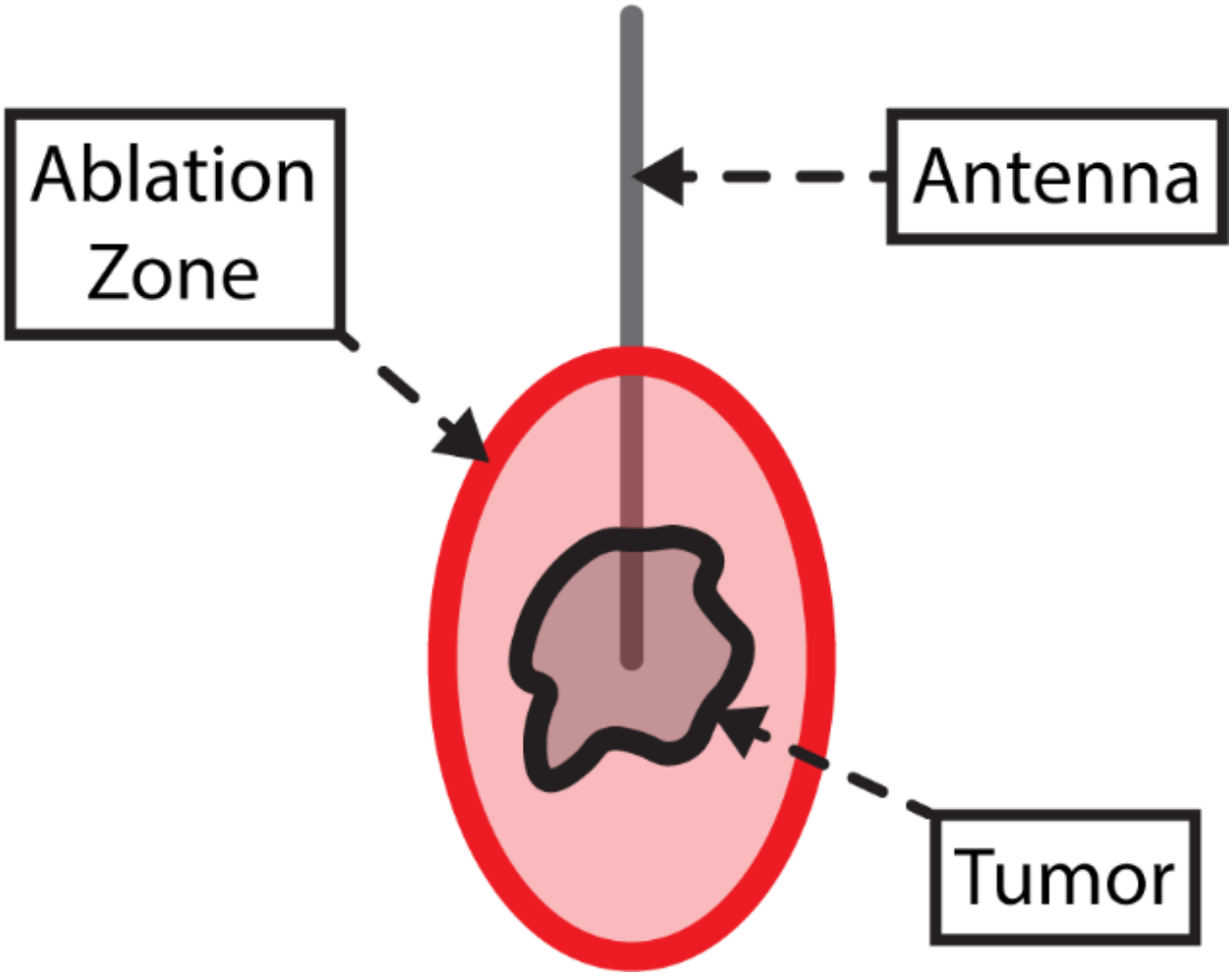

Figure 6.8 – Example of ellipsoid shape seen in microwave ablation procedures.

Although results of this algorithm are very promising, there is still room for improvement. If discontinuities are too large, this may introduce large approximation errors. To compensate for this, we will incorporate boundary information from both axial and lateral strain tensors and utilize ellipsoidal convexity to bridge larger discontinuities while retaining small discontinuities. Another potential problem may be presence of noise that may hinder texture matching to find the correct ellipse. If this problem occurs, we will implement a semi-automatic strategy for human intervention. Alternatively we will incorporate information from B-mode data to increase probability of segmenting ablations, as presented in [40]. This method utilizes bivariate distributions to include B-mode intensity information and elastography information which was derived using a Markov Random Field and maximum *a posteriori* framework [41].

Future work will incorporate additional means of verifying the robustness of this algorithm to delineate ablation boundaries. Corresponding CECT planes which are utilized as the clinical-gold standard of care for visualizing ablation effectiveness will be compared to strain segmentations. Additionally, the algorithm will also be assessed on pre-ablation index tumors for identifying the ablative margin which is a strong indicator of ablation efficacy. Finally, manual segmentations should be performed by multiple observers for robustness.

In this chapter, we presented an algorithm for automatically segmenting strain tensor images produced during electrode displacement elastography. This algorithm utilizes active contours in the form of snakes using initialization of an ellipsoidal boundary found automatically using RANSAC and Hough transforms. Results of the algorithm show high repeatability of 98% and an R^2-value of 0.95 when compared to the ground truth manual segmentation. This segmentation algorithm provides a means to verify efficacy of microwave ablation in real-time in the clinic.

6.5 References

[1] A. Mitiche and I. B. Ayed, *Variational and level set methods in image segmentation*. Springer Science & Business Media, 2010.

[2] O. Merveille, H. Talbot, L. Najman, and N. Passat, "Curvilinear structure analysis by ranking the orientation responses of path operators," *IEEE transactions on pattern analysis and machine intelligence,* vol. 40, no. 2, pp. 304-317, 2017.

[3] N. Passat *et al.*, "From Real MRA to Virtual MRA: Towards an Open-Source Framework," Springer International Publishing, 2016, pp. 335-343.

[4] D. A. Oliveira, R. Q. Feitosa, and M. M. Correia, "Segmentation of liver, its vessels and lesions from CT images for surgical planning," (in eng), *Biomed Eng Online,* vol. 10, pp. 30-30, 2011, doi: 10.1186/1475-925X-10-30.

[5] S. Lu, H. Huang, P. Liang, G. Chen, and L. Xiao, "Hepatic vessel segmentation using variational level set combined with non-local robust statistics," *Magnetic Resonance Imaging*, vol. 36, pp. 180-186, 2017/02/01/ 2017, doi: https://doi.org/10.1016/j.mri.2016.10.021.

[6] D. Mumford and J. Shah, "Optimal approximations by piecewise smooth functions and associated variational problems," *Communications on Pure and Applied Mathematics*, vol. 42, no. 5, pp. 577-685, 1989, doi: 10.1002/cpa.3160420503.

[7] G. Hamarneh and X. Li, "Watershed segmentation using prior shape and appearance knowledge," *Image and Vision Computing*, vol. 27, no. 1-2, pp. 59-68, 2009.

[8] L. Najman and M. Schmitt, "Watershed of a continuous function," *Signal Processing*, vol. 38, no. 1, pp. 99-112, 1994.

[9] X. Yang, W. Zhao, Y. Chen, and X. Fang, "Image segmentation with a fuzzy clustering algorithm based on Ant-Tree," *Signal Processing*, vol. 88, no. 10, pp. 2453-2462, 2008.

[10] Y. Guo *et al.*, "Automated iterative neutrosophic lung segmentation for image analysis in thoracic computed tomography," (in eng), *Med Phys*, vol. 40, no. 8, p. 081912, Aug 2013, doi: 10.1118/1.4812679.

[11] Y. Guo, A. S. Ashour, and B. Sun, "A novel glomerular basement membrane segmentation using neutrsophic set and shearlet transform on microscopic images," (in eng), *Health information science and systems*, vol. 5, no. 1, p. 15, Dec 2017, doi: 10.1007/s13755-017-0036-7.

[12] J. Shan, H. D. Cheng, and Y. Wang, "A novel segmentation method for breast ultrasound images based on neutrosophic l-means clustering," (in eng), *Med Phys*, vol. 39, no. 9, pp. 5669-82, Sep 2012, doi: 10.1118/1.4747271.

[13] V. Caselles, R. Kimmel, and G. Sapiro, "Geodesic active contours," *International journal of computer vision*, vol. 22, no. 1, pp. 61-79, 1997.

[14] M. Kass, A. Witkin, and D. Terzopoulos, "Snakes: Active contour models," *International journal of computer vision*, vol. 1, no. 4, pp. 321-331, 1988.

[15] D. Barbosa, T. Dietenbeck, J. Schaerer, J. D'hooge, D. Friboulet, and O. Bernard, "B-spline explicit active surfaces: an efficient framework for real-time 3-D region-based segmentation," *IEEE transactions on image processing*, vol. 21, no. 1, pp. 241-251, 2011.

[16] M. H. Hesamian, W. Jia, X. He, and P. Kennedy, "Deep Learning Techniques for Medical Image Segmentation: Achievements and Challenges," *Journal of Digital Imaging*, vol. 32, no. 4, pp. 582-596, 2019/08/01 2019, doi: 10.1007/s10278-019-00227-x.

[17] R. Hemalatha, T. Thamizhvani, A. J. A. Dhivya, J. E. Joseph, B. Babu, and R. Chandrasekaran, "Active contour based segmentation techniques for medical image analysis," *Med Biol. Image Anal*, vol. 17, 2018.

[18] L. Wang, Y. Chang, H. Wang, Z. Wu, J. Pu, and X. Yang, "An active contour model based on local fitted images for image segmentation," *Information Sciences*, vol. 418-419, pp. 61-73, 2017, doi: 10.1016/j.ins.2017.06.042.

[19] J. Long, E. Shelhamer, and T. Darrell, "Fully convolutional networks for semantic segmentation," in *Proceedings of the IEEE conference on computer vision and pattern recognition*, 2015, pp. 3431-3440.

[20] W. Zhang *et al.*, "Deep convolutional neural networks for multi-modality isointense infant brain image segmentation," *NeuroImage*, vol. 108, pp. 214-224, 2015.

[21] Y. Bar, I. Diamant, L. Wolf, and H. Greenspan, "Deep learning with non-medical training used for chest pathology identification," in *Medical Imaging 2015: Computer-Aided Diagnosis*, 2015, vol. 9414: International Society for Optics and Photonics, p. 94140V.

[22] A. Prasoon, K. Petersen, C. Igel, F. Lauze, E. Dam, and M. Nielsen, "Deep feature learning for knee cartilage segmentation using a triplanar convolutional neural network," in *International conference on medical image computing and computer-assisted intervention*, 2013: Springer, pp. 246-253.

[23] O. Ronneberger, P. Fischer, and T. Brox, "U-net: Convolutional networks for biomedical image segmentation," in *International Conference on Medical image computing and computer-assisted intervention*, 2015: Springer, pp. 234-241.

[24] M. D. Zeiler and R. Fergus, "Visualizing and understanding convolutional networks," in *European conference on computer vision*, 2014: Springer, pp. 818-833.

[25] Z. Zhang, C. Wu, S. Coleman, and D. Kerr, "DENSE-INception U-net for medical image segmentation," *Computer Methods and Programs in Biomedicine*, vol. 192, p. 105395, 2020/08/01/ 2020, doi: https://doi.org/10.1016/j.cmpb.2020.105395.

[26] Y. Gordienko *et al.*, "Deep learning with lung segmentation and bone shadow exclusion techniques for chest x-ray analysis of lung cancer," in *International Conference on Computer Science, Engineering and Education Applications*, 2018: Springer, pp. 638-647.

[27] K. He, X. Zhang, S. Ren, and J. Sun, "Deep residual learning for image recognition," in *Proceedings of the IEEE conference on computer vision and pattern recognition*, 2016, pp. 770-778.

[28] W. Liu, J. A. Zagzebski, T. Varghese, C. R. Dyer, U. Techavipoo, and T. J. Hall, "Segmentation of elastographic images using a coarse-to-fine active contour model," *Ultrasound in medicine & biology*, vol. 32, no. 3, pp. 397-408, 2006.

[29] R. M. Pohlman, M. R. Turney, P. H. Wu, C. L. Brace, T. J. Ziemlewicz, and T. Varghese, "2D US-CT Image Registration for Monitoring Percutaneous Hepatic Intervention (under review)," *Medical Physics*, 2019.

[30] L. D. Cohen, "On active contour models and balloons," *CVGIP: Image understanding*, vol. 53, no. 2, pp. 211-218, 1991.

[31] C. Xu and J. L. Prince, "Gradient vector flow: A new external force for snakes," in *Computer Vision and Pattern Recognition, 1997. Proceedings., 1997 IEEE Computer Society Conference on*, 1997: IEEE, pp. 66-71.

[32] M. A. Fischler and R. C. Bolles, "Random sample consensus: a paradigm for model fitting with applications to image analysis and automated cartography," *Communications of the ACM*, vol. 24, no. 6, pp. 381-395, 1981.

[33] J. Ivins and J. Porrill, "Everything you always wanted to know about snakes (but were afraid to ask)," *Artificial Intelligence*, vol. 2000, 1995.

[34] M. G. Lubner, C. L. Brace, T. J. Ziemlewicz, J. L. Hinshaw, and F. T. Lee, Jr., "Microwave ablation of hepatic malignancy," *Seminars in Interventional Radiology*, vol. 30, no. 1, pp. 56-66, Mar 2013, doi: 10.1055/s-0033-1333654.

[35] F. L. Bookstein, "Fitting conic sections to scattered data," *Computer Graphics and Image Processing*, vol. 9, no. 1, pp. 56-71, 1979.

[36] W. Gander, G. H. Golub, and R. Strebel, "Least-squares fitting of circles and ellipses," *BIT Numerical Mathematics*, vol. 34, no. 4, pp. 558-578, 1994.

[37] J. Canny, "A computational approach to edge detection," in *Readings in Computer Vision*: Elsevier, 1987, pp. 184-203.

[38] P. S. Nair and A. T. Saunders, "Hough transform based ellipse detection algorithm," *Pattern Recognition Letters*, vol. 17, no. 7, pp. 777-784, 1996/06/10/ 1996, doi: https://doi.org/10.1016/0167-8655(96)00014-1.

[39] C. L. Brace, "Microwave tissue ablation: biophysics, technology, and applications," *Critical Reviews™ in Biomedical Engineering*, vol. 38, no. 1, 2010, doi: 10.1615/CritRevBiomedEng.v38.i1.60.

[40] G. Pons, J. Martí, R. Martí, S. Ganau, and J. A. Noble, "Breast-lesion segmentation combining B-mode and elastography ultrasound," *Ultrasonic imaging*, vol. 38, no. 3, pp. 209-224, 2016.

[41] X. Guofang, M. Brady, J. A. Noble, and Z. Yongyue, "Segmentation of ultrasound B-mode images with intensity inhomogeneity correction," *IEEE Transactions on Medical Imaging*, vol. 21, no. 1, pp. 48-57, 2002, doi: 10.1109/42.981233.

Chapter 7: Computed Tomography to Ultrasound Image Registration

Deformable registration of ultrasound (US) and contrast enhanced computed tomography (CECT) images are essential for quantitative comparison of ablation boundaries and dimensions determined using these modalities. Stiffness-based imaging using ultrasound has become popular and offers nonionizing and cost-effective imaging modality for monitoring minimally invasive microwave ablation (MWA) procedures. A manual registration method is presented in this chapter. The two-dimensional (2D) virtual CT image plane that corresponds to the clinical US B-mode was obtained by "virtually slicing" the 3D CT volume along the plane containing the MWA antenna. The initial slice plane was generated using the vector acquired by rotating the normal vector of the transverse (i.e., xz) plane along the angle subtended by the antenna. This plane was then further rotated along the MWA antenna and shifted along with the direction of normal vector to obtain similar anatomical structures, such as the liver surface and vasculature that is visualized on both the CT virtual slice and US B-mode images. Finally, an affine transformation was estimated using anatomic and non-anatomic landmarks to account for distortion between the co-located CT virtual slice and US B-mode image resulting in a final registered CT virtual slice. Registration accuracy was measured by estimating the Euclidean distance between corresponding registered points on CT and US B-mode images. Mean and standard deviation of the affine transformed registration error was 1.85 ± 2.14 [mm] and 3.40 ± 3.79 mm for the target registration error, computed from 20 co-registered data sets. Results demonstrate the ability to obtain 2D virtual CT slices that are registered to clinical US B-mode images. The use of both anatomical and non-anatomical landmarks results in accurate registration useful for validating ablative margins and comparison to electrode displacement elastography (EDE) based images.

R. M. Pohlman, M. R. Turney, P. H. Wu, C. L. Brace, T. J. Ziemlewicz, and T. Varghese, "Two-dimensional ultrasound-computed tomography image registration for monitoring percutaneous hepatic intervention," *Medical physics*, vol. 46, no. 6, pp. 2600-2609, 2019, doi: 10.1002/mp.13554.

7.1 Background of CT and Ultrasound Registration

Although image fusion tools for CT-US registration have been under development for 20 years, the adoption of these tools has been delayed in the clinic due to the extra time required to achieve satisfactory alignment between the image modalities [1, 2]. Intrinsic registration and fusion of pre-operative CT/MR images to US [3-7] has been utilized in some centers [3-5], using common landmarks such as the liver surface and/or vasculature [3-6, 8-16], or electro-magnetic antenna tracking [5]. These approaches require appropriate and careful clinical setup [4]. Data acquisition during breath holds or respiratory gating is essential to improve the accuracy of image fusion [3, 6]. The registration/fusion of the images varies from real-time [3], 15~20 s [17], 29-74 s [8], to around 5-10 minutes [18]. Recent advancements in computing and automatic image analysis have significantly reduced the time required for the image registration so that image fusion becomes a feasible option in ablation procedures [19-23]. This initial rigid registration can be achieved by defining a minimum of three (3) non-collinear common fiducial points in both datasets, or by defining a common plane and single point [24]. Classical methods for implementing multi-modality image registration use mutual information to measure differences and a rigid transformation to warp the previously acquired data with the real time US B-mode image [25].

7.2 Motivation for Registering CT to Ultrasound Imaging Plane

Need for image fusion during percutaneous ablations arises when hepatic tumors cannot be clearly visualized with US because of their size or location [26, 27]. A growing alternative modality for visualizing liver masses and ablated regions utilizing US is electrode displacement elastography (EDE). EDE uses localized perturbations to detect differences in the tissue stiffness between normal liver and the ablated region to determine ablation zone dimensions. EDE has demonstrated high visualization and delineation in strain tensor images on phantoms [28-30], animal models [31 , 32], and human patients [33-36]. In addition, to ablated region visualization using EDE, an important metric to be evaluated is the area of the ablation region. The hyperechoic area on the B-mode image has been previously segmented and utilized for comparison to EDE [37]. However, the hyperechoic region on B-mode images does not provide an accurate

estimate of the ablation area, and can also shift due to outgassed bubble movement after ablation [38]. Comparison of EDE derived delineations of ablated regions with the current clinical gold-standard CECT are therefore necessary to verify EDE viability in clinical settings. Previous reports on area comparisons of ablated region obtained with EDE to pathology have demonstrated a close correspondence in animal models [39-41]. Comparisons of *ex vivo* ablation areas to CT without contrast have also demonstrated close correspondence of ablation areas between strain imaging, CT and pathological measurements [42]. However *in vivo* datasets require the proposed CT-US registration [37] for a direct comparison of EDE with CECT. In this chapter, a method for fusing intraoperative CT volumes with US B-mode is presented for potentially evaluating the efficacy of EDE for monitoring MWA [43].

In this chapter, an algorithm is derived for extracting, matching and co-locating a CT virtual slice [44] to clinical US B-mode images from 20 patients during ablation procedures under general anesthesia [18]. We utilize the non-anatomical microwave antenna to initiate and co-locate possible planes and finalize the virtual slice [44] with anatomical landmarks common between the CT and US B-mode image. Finally, an affine transformation is utilized to register the CT virtual slice to the US B-mode imaging plane.

7.3 Materials and Methods

7.3.1 Data Collection for Registration

This study was conducted under a protocol approved by the institutional review board at the University of Wisconsin-Madison. Informed consent was obtained from patients scheduled for a minimally invasive MWA procedure prior to data acquisition for EDE. We report on 20 patients with HCC or liver metastases with both US and CT data sets. All patients in this study were placed under general anesthesia prior to the procedure.

7.3.2 Microwave Ablation (MWA) Procedure

Microwave ablation procedures were conducted with a 2.45 GHz MWA system and 17-gauge antennas (Certus 140, Neuwave Medical Inc., Madison, Wisconsin). One or more antennas were used

depending on the number and size of tumors being treated. Antennas were generally guided using real-time US if the tumor could be visualized. Most ablations were performed using a power level of 65 Watts for 5 minutes.

In our facility, MWA procedures are performed on a CT imaging table, to ensure that the patient is in the same position for all treatment and imaging studies performed in the ablation suite. Patient position was determined during pre-ablation treatment planning based on the location of the tumor(s). All 20 patients used for this analysis from this cohort were placed in the supine position.

7.3.3 Imaging Before and After Microwave Ablation

US B-mode imaging with a C1-6 curvilinear array was utilized for ablation antenna placement (GE Logiq E9, GE Healthcare, Waukesha, Wisconsin). After the antenna was inserted into the tumor based on the treatment planning guidelines, it was locked into place using the cyro-lock feature of the system. CT scanning without contrast was then performed to verify antenna placement accuracy before initiating the ablation procedure (750HD, GE Healthcare).

The standard MWA procedure performed in our facility includes immediate post-ablation assessment using CECT while the patient is still under anesthesia. For the patients in this dataset, we also acquired radiofrequency (RF) data for EDE-based strain imaging induced through a manual perturbation of the antenna immediately before and after the ablation procedure. We anticipate tissue deformation due to respiratory and cardiac motion between the capture of both datasets would be present. Based on previous image fusion results, the expected accuracy of registration in this setting based on peer-reviewed literature results should fall between 1.90 and 6.55 mm [4, 10].

7.3.4 CT ‘Virtual Slice’ Selection[44] and Registration

In this section, we describe computation of the 2D CT virtual slice [44] that would correspond to the clinical B-mode image used for antenna placement. A flow-chart of the registration processing sequence is shown in Figure 7.1. The first registration stage performs a rigid registration to co-locate both US B-mode and ablation-suite CT virtual slice along the same imaging plane. The second stage estimates an affine

transformation for deformable registration of the CT virtual slice to the US B-mode imaging plane. Although manual selection process is time-consuming, it provided robust registration for initial transformation irrespective of B-mode ultrasound quality, where automatic registration schemes often fail.

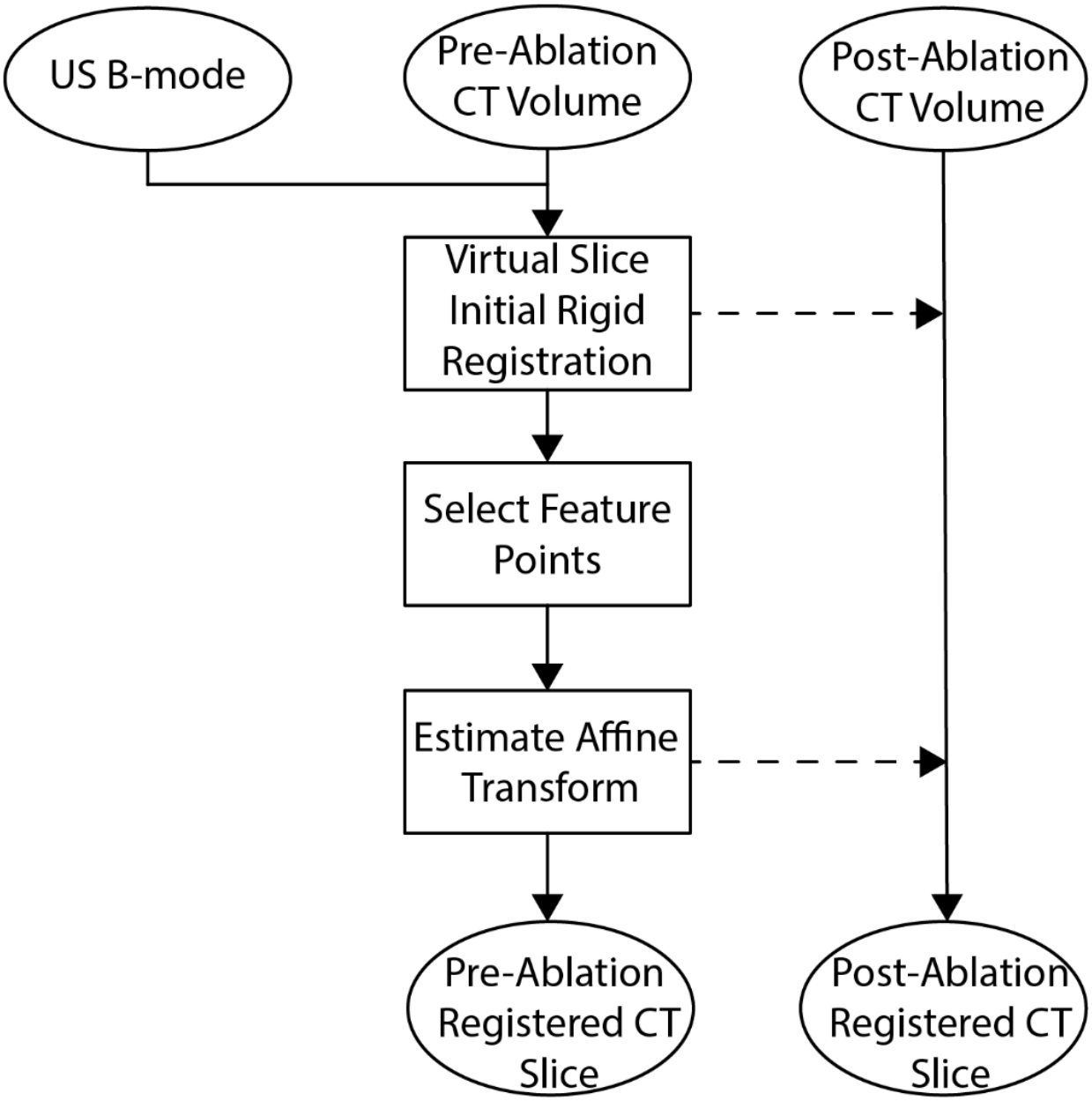

Figure 7.1 - Strategy for co-locating and registering a CT virtual slice from the 3D CT volume to the US B-mode imaging plane.

A plane in 3D space can be represented by the point-normal formula shown in (38)

$$\vec{n}_{VS} \cdot (r_1 - r_2) = 0 \tag{38}$$

where $\vec{n}_{VS}$ denotes the normal vector to the desired plane and r_1, r_2 are arbitrary points on that plane. $\vec{n}_{VS}$ can be calculated from the cross-product of any two vectors passing through a common reference point r_0 on the plane, as:

$$\vec{n}_{VS} = (r_1 - r_0) \times (r_2 - r_0) \tag{39}$$

To locate the imaging plane from the CT volume slices, we need to derive two vectors on the US B-mode image plane that encompasses the antenna as illustrated in Figure 7.2. An example of this approach on 3D CT volume data is shown in Figure 7.3 (a) and (b) with Figure 7.3 (c) showing an enlarged CT volume encompassing the antenna highlighted in green. For vector selection, the most intuitive choice was one vector along the orientation of the antenna and another vector along the direction of antenna to transducer. The vector denoting antenna orientation, $\vec{N}_1$, was derived based on the antenna tip-point and centroid of the antenna. The second vector, $\vec{N}_2$, was derived by the projection of $\vec{N}_1$ onto the normal vector of the xz-plane (see Figure 7.2) using the following vector reduction formula,

$$\vec{N}_2 = \vec{N}_1 - \left\langle \vec{N}_1, \vec{n}_{xz} \right\rangle \vec{n}_{xz} \tag{40}$$

The reasoning is that US transducer position will be parallel to the xz-plane under the assumption that the US transducer was positioned perpendicular to the patient surface [45] . This slice was obtained using the normal vector parallel to the xz plane, also representing the plane tangential to the patient surface where $\vec{N}_1$ and $\vec{N}_2$ are shown by green and blue arrows respectively as illustrated in Figure 7.2 and reproduced with actual data in Figure 7.3 (e). A vector selection example on patient data is shown in Figure

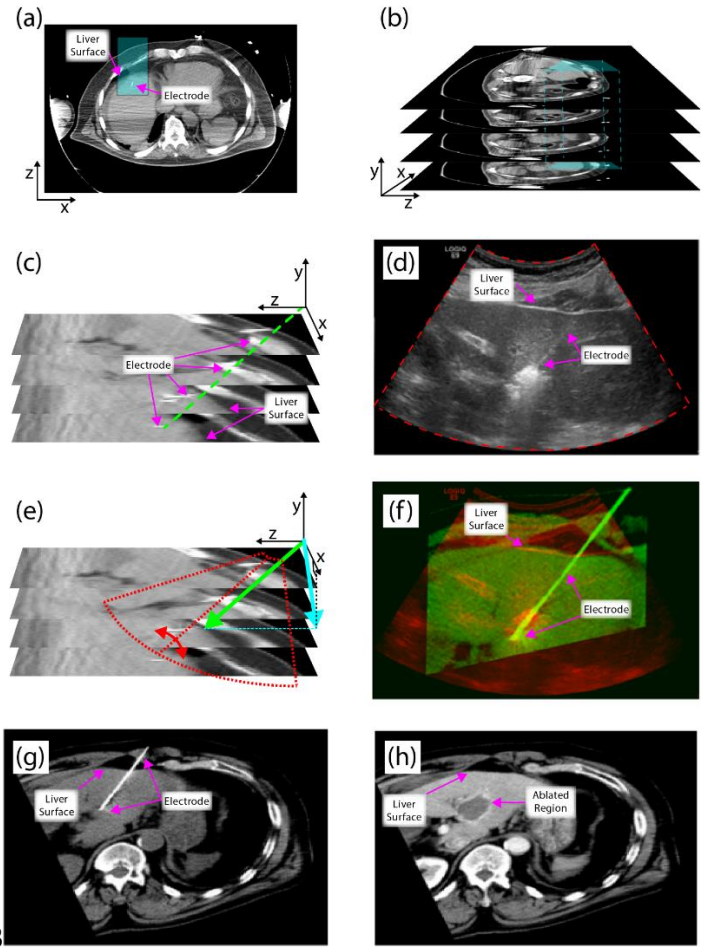

7.3 (e) where $\bar{N}_1$ and $\bar{N}_2$ are shown by green and blue arrows respectively. The virtual slice generated by these two vectors in the CT image space does not necessarily define the US B-mode image plane. The final virtual slice was identified by rotating the antenna plane until three clearly visible anatomic landmarks (e.g., un-deformed liver surface or vasculature points) match in both images. Landmarks are selected based on common visualization in both the US and CT slices. The virtual slice selected is primarily based on ablation antenna visualization over the 3D CT volume followed by rotation to align these common anatomical landmarks in both CT and US slices. This task does not require significant proficiency for the operator. For affine transformation, although the accuracy of selected points may vary based on operator's proficiency level in viewing these images, more than three set of non-collinear points can be selected so that the affine transformation can be found using

least squares formulations. Example images for landmark selection is illustrated in Figure 7.3 (d) and (e) indicated by the red sectors.

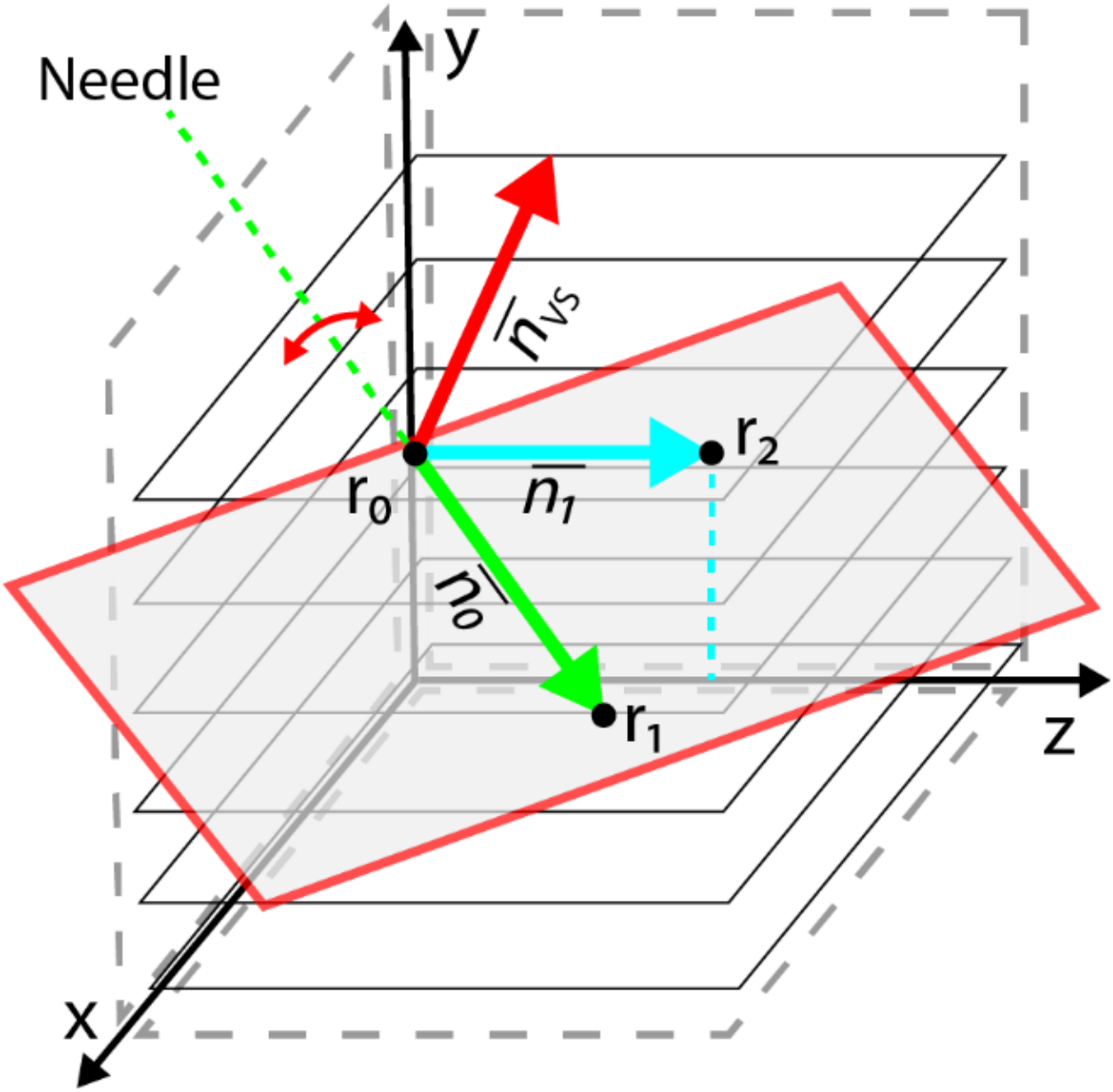

Figure 7.2 - Strategy for obtaining the CT virtual slice from the 3D CT volume. Potential slice planes were obtained by varying a normal vector around antenna to acquire the plane corresponding to the ultrasound B-mode image.

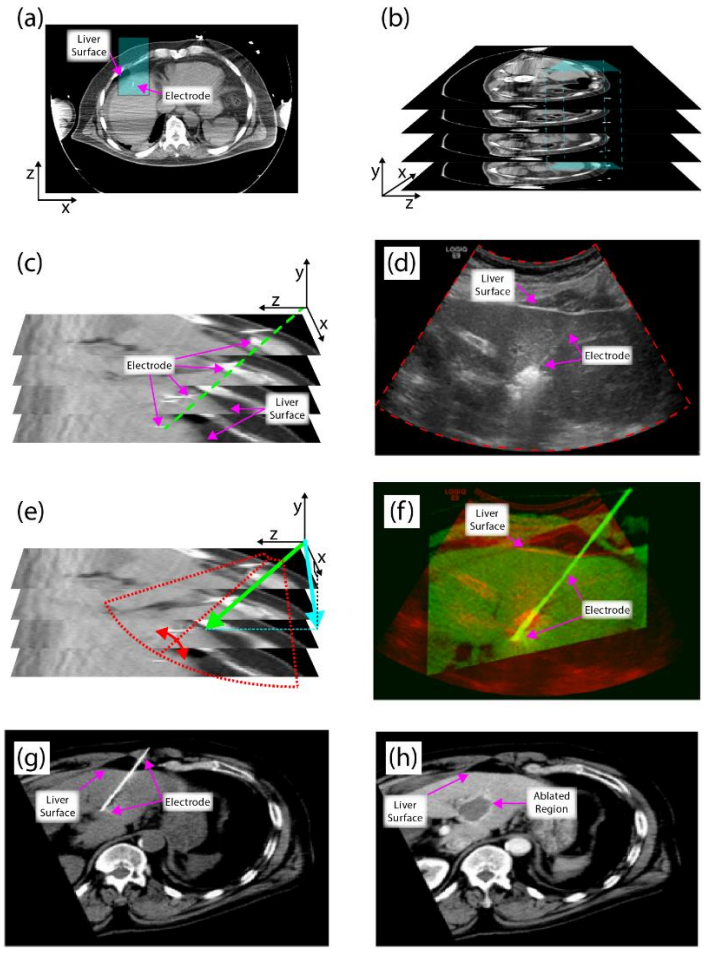

Figure 7.3 - An example workflow using patient image data illustrating the US B-mode – CT registration process. (a) Transverse slice with the antenna location highlighted in blue. (b) CT volume as a stack of transverse slices with the antenna location highlighted within the blue cube. (c) Zoomed in region of the antenna location in the CT volume with the antenna shown in green. (d) Comparable US B-mode image from patient after ablation with outline of sector image highlighted in red. (e) Zoomed in CT volume with the two vectors creating the virtual slice plane highlighted in green and blue for the vector along the direction of the antenna and the vector projected onto the xy-plane, respectively. An example sector US outline is transposed onto this plane which is rotated about the antenna to match three clearly visible

anatomic landmarks. (f) The resultant CT virtual slice after affine transformation in green transposed onto the red US B-mode image. (g) The entire CT virtual slice collected pre-ablation. (h) The CT virtual slice estimated post-ablation.

7.3.5 Affine Transformation for Virtual Slice Refinement

The final estimated virtual slice, shown in Figure 7.3 (g), may not co-register completely to the US B-mode image plane due to distortion from the US transducer placement (US imaging deforms the skin surface to make skin contact without an air interface) as well as respiratory and physiological motion. To correct for this distortion, an affine transformation was used in the second stage of the registration pipeline. Mathematically an affine transformation can be represented by (41).

$$\begin{bmatrix} x' \\ y' \\ 1 \end{bmatrix} = \begin{bmatrix} s_x \cos(\theta) & -h_x \sin(\theta) & t_x \\ h_y \sin(\theta) & s_y \cos(\theta) & t_y \\ 0 & 0 & 1 \end{bmatrix} \begin{bmatrix} x \\ y \\ 1 \end{bmatrix} \tag{41}$$

where s is scale, h is shear effects, and t is translation for the coordinates in CT images respectively, and θ allows for rotation correction. The parameters of the transformation matrix were estimated by registering the anatomical points on both CT and US images used in the virtual slice selection, and the transformation matrix was applied on the CT virtual slice to refine the registration to the US B-mode image plane. The resulting transformed CT virtual slice is shown overlaid in green on the underlying red US B-mode in Figure 7.3 (f). The ablated region shape and dimension on the registered CT images is considered as the gold standard for assessment of a successful ablation procedure and used for comparison to the US B-mode and EDE results. Assuming no gross patient movement, the estimated CT virtual slice and affine transformation parameters can be utilized on the post-ablation CECT to visualize the post-ablation region shown in Figure 7.3 (h).

7.3.6 Registration Error Analysis

Target registration error (TRE) is a measure used to validate the performance of point-based image registration accuracy [46, 47]. TRE was measured by comparing the Euclidean distance between corresponding identified points in both the image sets using (42).

$$TRE = \sqrt{\left(p_{xy} - T\left(q_{xy} \right) \right)^2} \tag{42}$$

where p_{xy} and q_{xy} are the x and y coordinates of a target registration point in the fixed image (US) and moving image (CT) respectively. T the estimated affine transform that attempts to register the CT image plane with US. Therefore, TRE quantifies how close features points in the transformed CT image are to the same features in the US B-mode image after registration. The points used for the registration error analysis include points near the antenna along with other anatomical landmarks visible in both the US and CT images. A minimum of three feature points were used for each pair of registered images.

7.4 Results and Discussion for Manual Registration

7.4.1 Registration Examples

Figure 7.3 (d), (f)-(h) illustrates the image fusion results for a patient starting with the B-mode image in Figure 7.3 (d) and the corresponding CT virtual slice in Figure 7.3 (g). Affine transformation to warp the virtual CT slice and merge it with the B-mode image is shown in Figure 7.3

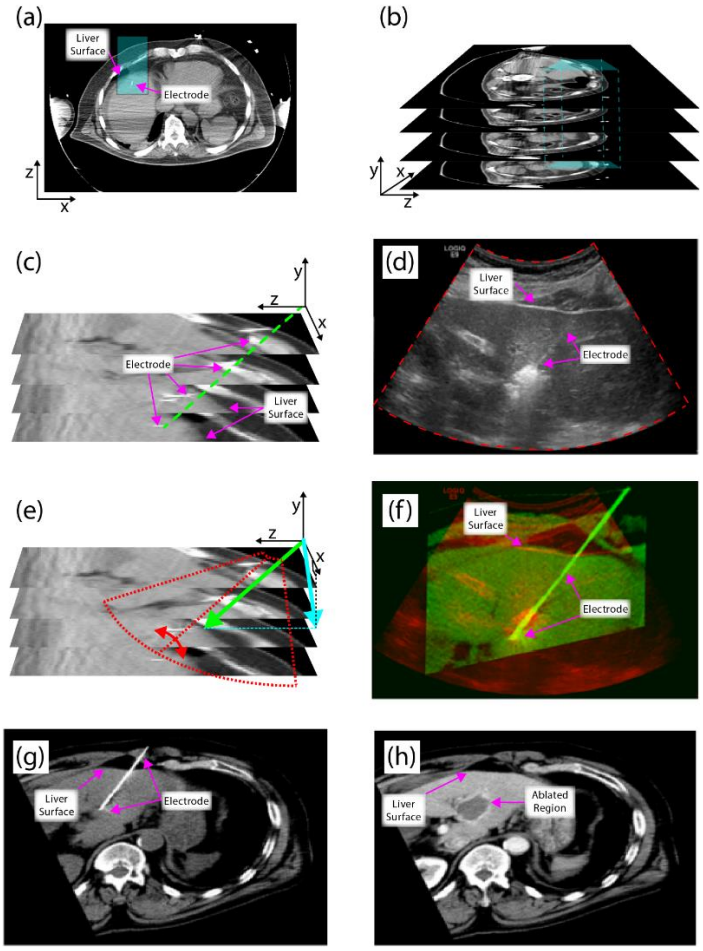

(f). Note the complete overlap of the ablation antenna in Figure 7.3 (f); the green map shows the CT virtual slice while the red image denotes the B-mode image. The final image in shows the corresponding post-ablation CECT virtual slice in Figure 7.3 (h), which is obtained using the same slicing parameters used for the CT-US registration and used to obtain Figure 7.3 (g), respectively.

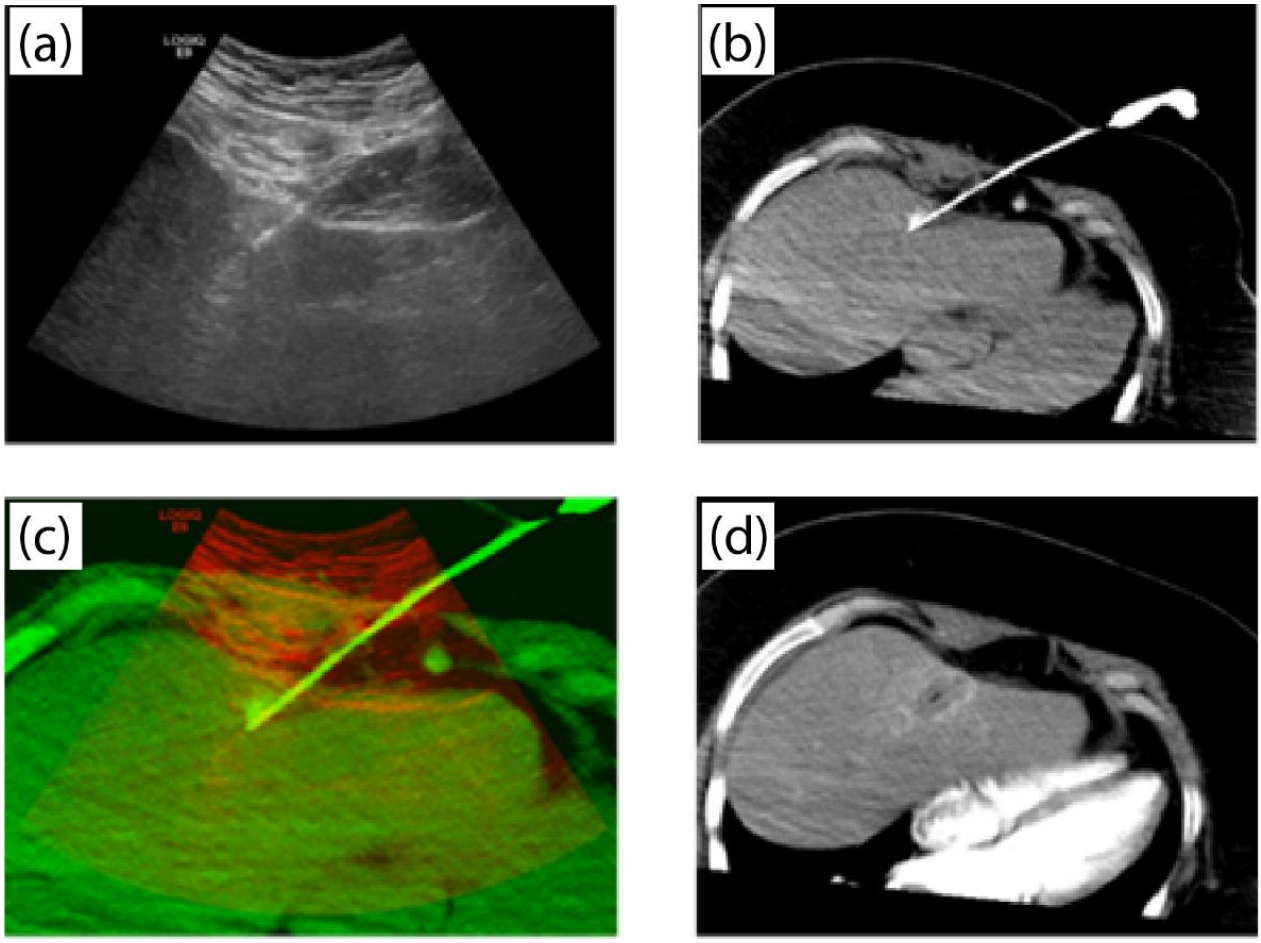

Figure 7.4 - An example of US B-mode – CT registration result for a second patient (a) US B-mode prior to ablation with antenna visible. (b) Co-located CT virtual slice. (c) The registered CT virtual slice after affine transformation in green transposed onto the red.

In a similar manner, Figure 7.4 presents image fusion results for a second patient, with the B-mode image in Figure 7.4 (a) and the corresponding CT virtual slice in Figure 7.4 (b). The affine transform used to align and fuse the virtual CT slice with the B-mode image is shown in Figure 7.4 (c). Note that the ablation antenna in Figure 7.4 (c) lies completely on the ablation antenna visualized in Figure 7.4 (a). The liver surface seen in Figure 7.4 (a) and Figure 7.4 (b) also coincide. The green image depicts the CT virtual slice while the red image depicts the US B-mode image. The corresponding post-ablation CECT virtual slice is shown in Figure 7.4 (d), which is obtained using the same slicing parameters used for the CT-US

registration to obtain Figure 7.4 (b), respectively. Both results demonstrate registration by the agreement of both anatomical and non-anatomical features.

The identified landmarks used for the registration error analysis in both image data sets include points near the antenna along with other anatomical landmarks visible in both the US B-mode and corresponding CT virtual slices. A minimum of three different (independent) manually selected feature points were used for each pair of registered images for both registration and validation. The fiducial mean ± standard deviation registration error was 1.85 ± 2.14 mm using both anatomical and non-anatomical landmarks.

7.4.2 Linear Regression Analysis of Registration

Linear regression analysis was performed for the feature points to determine correlation between the results for landmarks on US and CT. For each image set, the Euclidian distance from the origin was calculated for each feature point location in both the CT virtual slice and the US B-mode image as shown in Figure 7.5. The results show that points with the highest correlation come from non-anatomical landmarks (Figure 7.5 (a)) due to the rigid structure of the ablation antenna. Anatomical feature points also show good agreement on US and the transformed CT image but suffer from small differences due to minor tissue deformations in the US B-mode as displayed in Figure 7.5 (b). Figure 7.5 (c) shows the high correlation ($R^2 = 0.98$, $p<0.001$) between the complete set of feature points on corresponding CT and US B-mode images. These results are anticipated since the non-anatomical landmark (antenna) is clearly visualized in both modalities and does not deform with its dimensions remaining constant in both modalities. In addition to Figure 7.5, Figure 7.6 depicts the registration error reduction obtained using the affine transformation after the initial rigid registration (virtual slice) using 5 independent feature points for each registered data set. In addition, Figure 7.6 presents registration errors incurred after the rigid registration (virtual slice) stage, after the corresponding rigidly registered image pairs were appropriately scaled. Figure 7.6 also presents registration error results after rigid translation, rotation and the combination of scaling, rotation, and translation (SRT). Note that registration errors present after rigid registration are

significant when compared to registration errors after the affine registration stage. Utilizing the affine transformation allows for significantly lower registration errors.

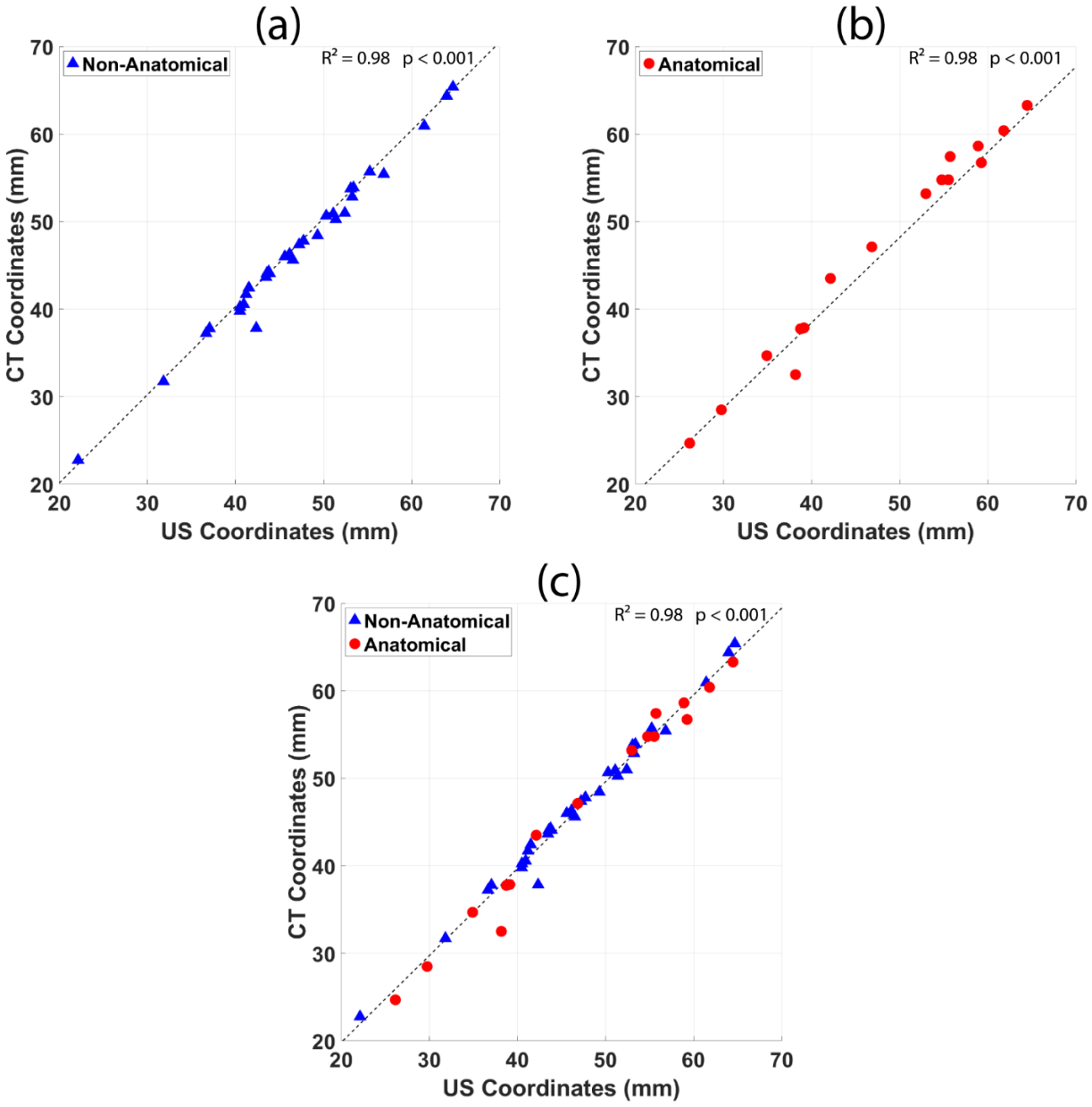

Figure 7.5 - CT virtual slice registration accuracy to US B-mode. (a) Plot of non-anatomical registration points (antenna) from US and CT. $R^2 = 0.98$, $p < 0.001$. (b) Plot of anatomical registration points on US and CT. $R^2 = 0.98$, $p < 0.001$. (c) Final plot of both anatomical and non-anatomical points on CT and US. $R^2 = 0.98$, $p < 0.001$.

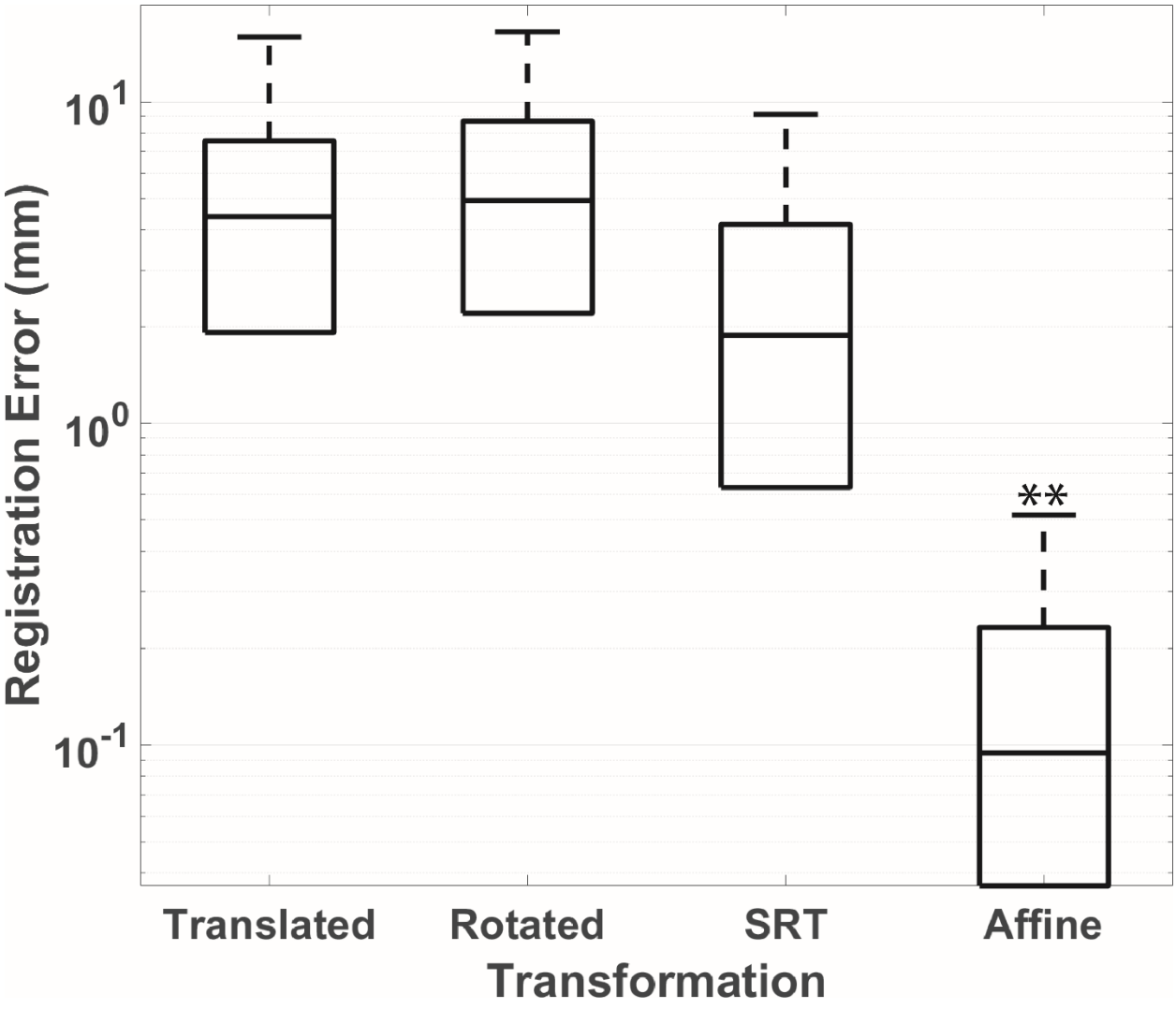

Figure 7.6 – Registration error distribution with translation, rotation, scaling rotation and translation (SRT) and affine transformation after the initial rigid registration (virtual slice) stage. Error is plotted on a log scale along the y-axis. The ** denotes statistically significant improvement with affine transformation.

7.4.3 Rationale for CT Registration

The results presented in this chapter describes utilization of the 'CT virtual slice' concept previously described by Wu et al. [44]. The CT virtual slice is obtained from a 3D CT volume by co-locating the imaging planes corresponding to a 2D clinical US B-mode image used to guide placement of the ablation antenna into the liver tumor to be ablated. Following computation of the co-located virtual slice from the 3D CT volume comprised of cross-sectional images or slices through the body, we account for local deformations present in these due to differences in the respiratory and cardiac phases and local deformation present with the US transducer. An affine transformation is used for deformable registration of the co-located CT virtual slice to the B-mode image.

Registration of US to CT images can be directly applied to ablation area delineation results obtained with electrode displacement elastography for comparative performance analysis in human subjects. Yang et al. [37] used the contrast and contrast-to-noise ratio to measure the feasibility of EDE for patients with HCC since no ground truth images were available. These metrics, by definition, require a defined region of interest (ROI) in and around the ablation region on the image. This variation in the calculation method for CNR makes it difficult to compare the performance of elastography algorithms across research studies and consequently imposes limitations on the reproducibility of this evaluation process. The method proposed in this chapter offers a solution to this problem by obtaining a ground-truth 'virtual' CT image, which can be compared with results from EDE. Comparison between ablation areas and dimensions between EDE and CECT images can therefore be performed, enabling a comparison to the current clinical gold standard.

7.4.4 Registration Processing Time

As the implementation in this chapter is a proof of concept, the computational requirement currently is not significant when compared to the time required for the manual selection of the virtual slice and feature points for registration. Most of the processing time is determined on operator's experience for selecting the virtual slice and feature points for registration. To improve registration accuracy, users can select more than the minimum three points to obtain a least squares solution to the affine transformation. Approximate

processing time for registration was primarily dictated by manual selection of features used for rigid registration of the virtual slice at 15 minutes, while the rigid registration and affine transformation steps take less than 1 minute combined.

7.4.5 Performance Against Other Algorithms

Schlaier et al. [48] on a phantom achieved an overall accuracy of 1.08 mm ± 0.61 mm (mean ± standard deviation) for the registration of reflective spheres between US and MR. However, these results were for a phantom with no motion errors. Wein et al. [10] across 25 patients showed a mean FRE and TRE of 9.5 mm and 8.1 mm respectively. Hakime et al. [4] using the GE Logiq E9 V-Nav system obtained their best accuracy of 1.9±1.4 mm with the patient under general anesthesia and both US and CT performed immediately (no motion artifacts). However, the registration accuracy reduced to 7.05 ± 6.95 mm when some time had elapsed (with motion artifacts) between the two modalities. In addition, the maximum absolute difference increased by 5.2 mm when no non-anatomical landmark was included in the registration process. Additionally, Banerjee et al. [15] reported an automated registration error of 3.6 mm using 300 matching points with a mean TRE of 3.9 mm for affine registration and 4.2 mm for rigid registration. For the patients studied in this chapter, post-ablation CT was performed under general anesthesia after the ablation procedure with US for antenna placement performed prior to the CT procedure used to verify antenna position. We obtained a fiducial mean registration error of 1.85 ± 2.14 mm (mean ± standard deviation) over 20 independent data sets using a minimum of three fiducials for each registered image pair (CT and US). This registration error lies between the errors reported in Hakime et al. [4] and compares favorably with the registration errors reported by Wein et al. [4, 10].

The low registration error was achieved by the two-stage registration process; first utilizing rigid, non-anatomic landmarks provided by the antenna to co-locate images from the two modalities, thereafter, incorporating visible anatomic landmarks for affine transformation and final registration. This is visualized in the merged images where the combined anatomic and non-anatomic landmarks depict the close

registration of the common image features such as the antenna and liver surface obtaining a target registration mean error of 3.40 ± 3.79 mm (mean ± standard deviation) over 20 independent data sets.

7.5 CT Registration Progress and Future Work

This chapter presents a registration method for fusing CT and US images from percutaneous liver ablation procedures. A virtual slicing technique was used to find and co-locate the slice corresponding to the US B-mode image plane, followed by affine registration using the antenna and anatomical markers. The resulting algorithm obtained fiducial and TRE of 1.85 ± 2.14 mm (mean ± standard deviation) and 3.40 ± 3.79 mm (mean ± standard deviation), respectively, over 20 independent data sets and using a minimum of three fiducials for each registered image pair (CT and US). This work is directly applicable to EDE performance analysis by providing the gold standard clinical CECT imaging plane for measuring the accuracy of EDE results.

7.5.1 Limitations of This Work

Manual selection of the anatomical landmarks is a limitation to this approach, and automated approaches will be pursued in future work. Future work will also, under the assumption that patient movement is minimal between the pre-ablation and post-ablation CT scans, apply the estimated registration and affine transformations from the pre-ablation CT volumes to post-ablation CT volumes to visualize the ablated tumor dimensions in the same plane as the US B-mode for further investigating accuracy of estimated registration and transformation parameters for post-ablation CECT volumes. Finally, registered CECT slices will be used as the gold-standard for validating electrode displacement elastography performance.

7.6 References

[1] J. Stoll, "Ultrasound fusion imaging," *Perspectives in Medicine*, vol. 1, no. 1, pp. 80-81, 2012/09/01/ 2012, doi: https://doi.org/10.1016/j.permed.2012.05.004.

[2] G. Srimathveeravalli, F. Cornelis, J. Mashni, H. Takaki, J. C. Durack, S. B. Solomon, and J. A. Coleman, "Comparison of ablation defect on MR imaging with computer simulation estimated treatment zone following irreversible electroporation of patient prostate," *Springerplus,* vol. 5, p. 219, 2016, doi: 10.1186/s40064-016-1879-0.

[3] J. Krücker, S. Xu, A. Venkatesan, J. K. Locklin, H. Amalou, N. Glossop, and B. J. Wood, "Clinical utility of real-time fusion guidance for biopsy and ablation," *J Vasc Interv Radiol,* vol. 22, no. 4, pp. 515-24, 2011, doi: 10.1016/j.jvir.2010.10.033.

[4] A. Hakime, F. Deschamps, E. G. De Carvalho, C. Teriitehau, A. Auperin, and T. De Baere, "Clinical evaluation of spatial accuracy of a fusion imaging technique combining previously acquired computed tomography and real-time ultrasound for imaging of liver metastases," *Cardiovasc Intervent Radiol,* vol. 34, no. 2, pp. 338-44, 2011, doi: 10.1007/s00270-010-9979-7.

[5] J. Krücker, S. Xu, N. Glossop, A. Viswanathan, J. Borgert, H. Schulz, and B. J. Wood, "Electromagnetic tracking for thermal ablation and biopsy guidance: clinical evaluation of spatial accuracy," *J Vasc Interv Radiol,* vol. 18, no. 9, pp. 1141-50, 2007.

[6] D. Spinczyk, "Towards the clinical integration of an image-guided navigation system for percutaneous liver tumor ablation using freehand 2D ultrasound images," *Comput Aided Surg,* vol. 20, no. 1, pp. 61-72, 2015, doi: 10.3109/10929088.2015.1076043.

[7] S. J. Ahn, J. M. Lee, D. H. Lee, S. M. Lee, J. H. Yoon, Y. J. Kim, J. H. Lee, S. J. Yu, and J. K. Han, "Real-time US-CT/MR fusion imaging for percutaneous radiofrequency ablation of hepatocellular carcinoma," *J Hepatol,* vol. 66, no. 2, pp. 347-354, 2017, doi: 10.1016/j.jhep.2016.09.003.

[8] A. Y. Kim, M. W. Lee, D. I. Cha, H. K. Lim, Y. T. Oh, J. Y. Jeong, J. W. Chang, J. Ryu, K. J. Lee, J. Kim, W. C. Bang, D. K. Shin, S. J. Choi, D. Koh, B. K. Seo, and K. Kim, "Automatic Registration between Real-Time Ultrasonography and Pre-procedural Magnetic Resonance Images: A Prospective Comparison between Two Registration Methods by Liver Surface and Vessel and by Liver Surface Only (Epub)," *Ultrasound Med Biol,* 2016, doi: 10.1016/j.ultrasmedbio.2016.02.008.

[9] D. H. Lee, W. H. Nam, J. Y. Lee, and J. B. Ra, "Non-rigid registration between 3D ultrasound and CT images of the liver based on intensity and gradient information," *Phys Med Biol,* vol. 56, no. 1, pp. 117-37, 2011, doi: 10.1088/0031-9155/56/1/008.

[10] W. Wein, S. Brunke, A. Khamene, M. R. Callstrom, and N. Navab, "Automatic CT-ultrasound registration for diagnostic imaging and image-guided intervention," *Med Image Anal,* vol. 12, no. 5, pp. 577-85, Oct 2008, doi: 10.1016/j.media.2008.06.006.

[11] T. Lange, N. Papenberg, S. Heldmann, J. Modersitzki, B. Fischer, H. Lamecker, and P. M. Schlag, "3D ultrasound-CT registration of the liver using combined landmark-intensity information," *International journal of computer assisted radiology and surgery,* vol. 4, no. 1, pp. 79-88, 2009.

[12] W. H. Nam, D.-G. Kang, D. Lee, J. Y. Lee, and J. B. Ra, "Automatic registration between 3D intra-operative ultrasound and pre-operative CT images of the liver based on robust edge matching," *Physics in Medicine & Biology,* vol. 57, no. 1, p. 69, 2011.

[13] C. Weon, W. H. Nam, D. Lee, J. Y. Lee, and J. B. Ra, "Position tracking of moving liver lesion based on real-time registration between 2D ultrasound and 3D preoperative images," *Medical physics,* vol. 42, no. 1, pp. 335-347, 2015.

[14] M. Keil, C. Oyarzun Laura, and S. Wesarg, "Ultrasound B-Mode Segmentation for Registration with CT in Percutaneous Hepatic Interventions," in *Clinical Image-Based Procedures. From Planning to Intervention*, Berlin, Heidelberg, K. Drechsler *et al.*, Eds., 2013// 2013: Springer Berlin Heidelberg, pp. 91-97.

[15] J. Banerjee, Y. Sun, C. Klink, R. Gahrmann, W. J. Niessen, A. Moelker, and T. van Walsum, "Multiple-correlation similarity for block-matching based fast CT to ultrasound registration in liver interventions," *Medical Image Analysis,* vol. 53, pp. 132-141, 2019/04/01/ 2019, doi: https://doi.org/10.1016/j.media.2019.02.003.

[16] M. W. Lee, "Fusion imaging of real-time ultrasonography with CT or MRI for hepatic intervention," *Ultrasonography,* vol. 33, no. 4, pp. 227-239, 10 2014, doi: 10.14366/usg.14021.

[17] Z. Su, K. Li, E. Xu, L. Wu, X. Wang, L. Li, J. Wang, P. Lin, Y. Chen, Y. Zhang, J. Li, C. Dufour, B. Mory, and R. Zheng, "A clinical validation study for the feasibility and reliability of three-dimensional ultrasound-ultrasound automatic image registration," *Int J Hyperthermia,* vol. 31, no. 8, pp. 875-82, 2015, doi: 10.3109/02656736.2015.1073370.

[18] D. A. Clevert, P. M. Paprottka, A. Helck, M. Reiser, and C. G. Trumm, "Image fusion in the management of thermal tumor ablation of the liver," *Clin Hemorheol Microcirc,* vol. 52, no. 2-4, pp. 205-16, 2012, doi: 10.3233/CH-2012-1598.

[19] E. F. Ferrante, Vivien; Paragios, Nikos, "Slice-to-Volume Deformable Registration: Efficient one shot consensus between plane selection and in-plane deformation," *International Journal of Computer Assisted Radiology and Surgery,* vol. 10, no. 6, pp. pp.791-800, 2015, doi: 10.1007/s11548-015-1205-2.

[20] E. Ferrante and N. Paragios, "Slice-to-volume medical image registration: A survey," *Medical Image Analysis,* vol. 39, pp. 101-123, 2017/07/01/ 2017, doi: https://doi.org/10.1016/j.media.2017.04.010.

[21] G. Balakrishnan, A. Zhao, M. R. Sabuncu, J. Guttag, and A. V. Dalca, "VoxelMorph: A Learning Framework for Deformable Medical Image Registration," *arXiv preprint arXiv:1809.05231,* 2018.

[22] A. Eklund, P. Dufort, D. Forsberg, and S. M. LaConte, "Medical image processing on the GPU – Past, present and future," *Medical Image Analysis,* vol. 17, no. 8, pp. 1073-1094, 2013/12/01/ 2013, doi: https://doi.org/10.1016/j.media.2013.05.008.

[23] E. Smistad, T. L. Falch, M. Bozorgi, A. C. Elster, and F. Lindseth, "Medical image segmentation on GPUs – A comprehensive review," *Medical Image Analysis,* vol. 20, no. 1, pp. 1-18, 2015/02/01/ 2015, doi: https://doi.org/10.1016/j.media.2014.10.012.

[24] E. M. Jung, C. Friedrich, P. Hoffstetter, L. M. Dendl, F. Klebl, A. Agha, P. Wiggermann, C. Stroszcynski, and A. G. Schreyer, "Volume navigation with contrast enhanced ultrasound and image fusion for percutaneous interventions: first results," *PLoS One,* vol. 7, no. 3, p. e33956, 2012, doi: 10.1371/journal.pone.0033956.

[25] S. R. Hertel and G. B. Avinash, "Method and apparatus of multi-modality image fusion," ed: Google Patents, 2010.

[26] H. Rhim, M. H. Lee, Y.-s. Kim, D. Choi, W. J. Lee, and H. K. Lim, "Planning Sonography to Assess the Feasibility of Percutaneous Radiofrequency Ablation of Hepatocellular Carcinomas," *American Journal of Roentgenology,* vol. 190, no. 5, pp. 1324-1330, 2008/05/01 2008, doi: 10.2214/AJR.07.2970.

[27] T. J. Ziemlewicz, J. L. Hinshaw, M. G. Lubner, C. L. Brace, M. L. Alexander, P. Agarwal, and F. T. Lee, "Percutaneous Microwave Ablation of Hepatocellular Carcinoma with a Gas-Cooled System: Initial Clinical Results with 107 Tumors," *Journal of Vascular and Interventional Radiology,* vol. 26, no. 1, pp. 62-68, 2015/01/01/ 2015, doi: https://doi.org/10.1016/j.jvir.2014.09.012.

[28] S. Bharat, T. Varghese, E. L. Madsen, and J. A. Zagzebski, "Radio-frequency ablation electrode displacement elastography: a phantom study," *Medical Physics,* vol. 35, no. 6, pp. 2432-42, Jun 2008, doi: 10.1118/1.2919763.

[29] S. Bharat and T. Varghese, "Radiofrequency electrode vibration-induced shear wave imaging for tissue modulus estimation: a simulation study," *Journal of the Acoustical Society of America,* vol. 128, no. 4, pp. 1582-5, Oct 2010, doi: 10.1121/1.3466880.

[30] J. Jiang, T. Varghese, Q. Chen, T. J. Hall, and J. A. Zagzebski, "Finite element analysis of tissue deformation with a radiofrequency ablation electrode for strain imaging," *IEEE Transactions on Ultrasonics, Ferroelectronics, and Frequency Control,* vol. 54, no. 2, pp. 281-9, Feb 2007. [Online]. Available: https://www.ncbi.nlm.nih.gov/pubmed/17328325.

[31] N. Rubert, S. Bharat, R. J. DeWall, A. Andreano, C. Brace, J. Jiang, L. Sampson, and T. Varghese, "Electrode displacement strain imaging of thermally-ablated liver tissue in an *in vivo* animal model," *Medical Physics,* vol. 37, no. 3, pp. 1075-1082, 2010, doi: 10.1118/1.3301603.

[32] A. T. Fernandez, O. Kolokythas, T. Gauthier, D. A. Herzka, A. V. Patil, and H. Xie, "Comparison of ultrasound strain images with multi-modality imaging techniques in liver RF ablation

assessment: Initial ex vivo and clinical results," *Ultrasonics Symposium, 2008.*, pp. 313-316, 2008, doi: 10.1109/ULTSYM.2008.0077.

[33] W. Yang, T. J. Ziemlewicz, T. Varghese, M. L. Alexander, N. Rubert, A. N. Ingle, M. G. Lubner, J. L. Hinshaw, S. A. Wells, F. T. Lee, and J. A. Zagzebski, "Post-Procedure Evaluation of Microwave Ablations of Hepatocellular Carcinomas Using Electrode Displacement Elastography," *Ultrasound in Medicine & Biology*, vol. 42, no. 12, pp. 2893-2902, 2016, doi: 10.1016/j.ultrasmedbio.2016.07.015.

[34] W. Yang, T. Varghese, T. Ziemlewicz, M. Alexander, M. Lubner, J. L. Hinshaw, S. Wells, and F. T. Lee, Jr., "Delineation of Post-Procedure Ablation Regions with Electrode Displacement Elastography with a Comparison to Acoustic Radiation Force Impulse Imaging," *Ultrasound in Medicine and Biology*, vol. 43, no. 9, pp. 1953-1962, Sep 2017, doi: 10.1016/j.ultrasmedbio.2017.04.021.

[35] R. M. Pohlman and T. Varghese, "Dictionary Representations for Electrode Displacement Elastography," *IEEE Transactions on Ultrasonics, Ferroelectrics, and Frequency Control*, 10/05/2018 2018, doi: 10.1109/TUFFC.2018.2874181.

[36] R. M. Pohlman, T. Varghese, J. Jiang, T. Ziemlewicz, M. Alexander, K. Wergin, J. L. Hinshaw, M. Lubner, S. A. Wells, and J. F.T. Lee, "Comparison of Displacement Tracking Algorithms for *in vivo* Electrode Displacement Elastography," *Ultrasound in Medicine and Biology*, (in press) 2018, doi: 10.1016/j.ultrasmedbio.2018.09.001.

[37] W. Yang, T. J. Ziemlewicz, T. Varghese, M. L. Alexander, N. Rubert, A. N. Ingle, M. G. Lubner, J. L. Hinshaw, S. A. Wells, F. T. Lee, Jr., and J. A. Zagzebski, "Post-Procedure Evaluation of Microwave Ablations of Hepatocellular Carcinomas Using Electrode Displacement Elastography," *Ultrasound Med Biol*, vol. 42, no. 12, pp. 2893-2902, Dec 2016, doi: 10.1016/j.ultrasmedbio.2016.07.015.

[38] L. Solbiati, T. Ierace, S. N. Goldberg, S. Sironi, T. Livraghi, R. Fiocca, G. Servadio, G. Rizzatto, P. R. Mueller, A. Del Maschio, and G. S. Gazelle, "Percutaneous US-guided radio-frequency tissue

ablation of liver metastases: treatment and follow-up in 16 patients," *Radiology,* vol. 202, no. 1, pp. 195-203, Jan 1997, doi: 10.1148/radiology.202.1.8988211.

[39] J. Jiang, T. Varghese, C. L. Brace, E. L. Madsen, T. J. Hall, S. Bharat, M. A. Hobson, J. A. Zagzebski, and F. T. Lee, "Young's modulus reconstruction for radio-frequency ablation electrode-induced displacement fields: a feasibility study," (in eng), *IEEE Trans Med Imaging,* vol. 28, no. 8, pp. 1325-34, Aug 2009, doi: 10.1109/tmi.2009.2015355.

[40] J. Jiang, C. Brace, A. Andreano, R. J. DeWall, N. Rubert, T. G. Fisher, T. Varghese, F. Lee, Jr., and T. J. Hall, "Ultrasound-based relative elastic modulus imaging for visualizing thermal ablation zones in a porcine model," *Phys Med Biol,* vol. 55, no. 8, pp. 2281-306, Apr 21 2010, doi: 10.1088/0031-9155/55/8/011.

[41] N. Rubert, S. Bharat, R. J. DeWall, A. Andreano, C. Brace, J. Jiang, L. Sampson, and T. Varghese, "Electrode displacement strain imaging of thermally-ablated liver tissue in an in vivo animal model," (in eng), *Med Phys,* vol. 37, no. 3, pp. 1075-82, Mar 2010.

[42] W. Liu, U. Techavipoo, T. Varghese, J. A. Zagzebski, Q. Chen, and F. T. Lee, Jr., "Elastographic versus x-ray CT imaging of radio frequency ablation coagulations: an in vitro study," (in eng), *Med Phys,* vol. 31, no. 6, pp. 1322-32, Jun 2004.

[43] S. Bharat, T. Varghese, E. L. Madsen, and J. A. Zagzebski, "Radio-frequency ablation electrode displacement elastography: a phantom study," (in eng), *Med Phys,* vol. 35, no. 6, pp. 2432-42, Jun 2008.

[44] P. H. Wu, Z. Borden, and C. L. Brace, "Ablation zone visualization enhancement by periodic contrast-enhancement computed tomography during microwave ablation," *Med Phys,* vol. 44, no. 6, pp. 2132-2140, 2017, doi: 10.1002/mp.12266.

[45] Z. Hu, "Extraction of Any Angle Virtual Slice on 3D CT Image," pp. 356-360, 2008, doi: 10.1109/iita.2008.399.

[46] J. M. Fitzpatrick, J. B. West, and C. R. Maurer, "Predicting error in rigid-body point-based registration," *IEEE Transactions on Medical Imaging,* vol. 17, no. 5, pp. 694-702, 1998, doi: 10.1109/42.736021.

[47] P. Jannin, J. M. Fitzpatrick, D. J. Hawkes, X. Pennec, R. Shahidl, and M. W. Vannier, "Validation of medical image processing in image-guided therapy," *IEEE Transactions on Medical Imaging,* vol. 21, no. 12, pp. 1445-1449, 2002, doi: 10.1109/TMI.2002.806568.

[48] J. R. Schlaier, J. Warnat, U. Dorenbeck, M. Proescholdt, K. M. Schebesch, and A. Brawanski, "Image fusion of MR images and real-time ultrasonography: evaluation of fusion accuracy combining two commercial instruments, a neuronavigation system and a ultrasound system," *Acta Neurochir (Wien),* vol. 146, no. 3, pp. 271-6; discussion 276-7, Mar 2004, doi: 10.1007/s00701-003-0155-6.

Chapter 8: Differential Imaging of Liver Tumors Before and After Microwave Ablation with Electrode Displacement Elastography

Liver cancer is a leading cause of cancer related deaths, however primary treatments such as surgical resection and liver transplants may not be viable options for many patients. Minimally invasive image-guided microwave ablation (MWA) provides a locally effective treatment option for these patients with an impact comparable to surgery for both cancer specific and overall survival. MWA efficacy is correlated with accurate image guidance, however conventional modalities such as B-mode ultrasound and computed tomography (CT) have limitations. Alternatively, ultrasound elastography has been utilized to demarcate post-ablation zones yet has limitations for pre-ablation visualization due to variability in strain contrast between cancer types. This study attempts to characterize both pre-ablation tumors and post-ablation zones using electrode displacement elastography (EDE) for 13 patients with hepatocellular carcinoma or liver metastasis. Typically, MWA ablation margins of 0.5 – 1.0 cm are desired, which are strongly correlated with treatment efficacy. Our results demonstrate an average estimated ablation margin inner quartile range of 0.54 – 1.21 cm with a median value of 0.84 cm. These treatment margins lie within or above the targeted ablative margin indicating the potential for using EDE for differentiating index tumors and ablated zones for use during clinical ablations. We also obtained a high correlation between corresponding segmented cross-sectional areas from contrast-enhanced computed tomography (CECT), the current clinical gold standard, when compared to EDE strain images with R^2 values of 0.97 and 0.98 for pre- and post-ablation regions.

8.1 Introduction to Differential Imaging

Minimally invasive tumor ablation modalities, including MWA, can be used for both curative and palliative patient treatments [1]. Based on the Barcelona Clinic Liver Cancer guidelines, a single HCC less than 5 cm in diameter or three HCCs less than 3 cm in diameter should be treated with curative intent using

R. M. Pohlman, J. L. Hinshaw, T. J. Ziemlewicz, M. G. Lubner, S. A. Wells, F. T. L. Jr., M. L. Alexander, K. L. Wergin, and T. Varghese, "Differential Imaging of Liver Tumors Before and After Microwave Ablation with Electrode Displacement Elastography (In Press)," Ultrasound in Medicine & Biology, 2021.

ablative techniques as long as there are no extra-hepatic metastasis or portal vein invasion and the patient does not qualify for surgery [2]. If the patient meets these guidelines, curative intent aims for complete tumor eradication which is defined as destruction of the tumor plus an ablative margin surrounding the tumor. While larger tumors can be effectively treated with image-guided ablation procedures, the efficacy decreases in the setting of larger tumors and in those cases, palliative treatments may be utilized to reduce tumor burden, control disease progression, reduce pain, or control hormonal symptoms related to metastatic neuroendocrine tumors [3, 4]. Similarly MWA of liver metastases is typically reserved for patients with low volume disease, namely those deemed not suitable for surgical resection and those who have failed other therapies [5]. In curative treatment of liver tumors using MWA, insufficient ablative margins have been shown as an independent and significant risk factor for local tumor progression [6]. Although various imaging modalities are available, CT and ultrasound are useful for monitoring the water vaporization, tissue contraction, coagulation, and desiccation arising from water and ion interactions immediately after the ablation and on follow-up imaging [2].

8.1.1 Computed Tomography for Ablation Monitoring

Diagnostic CECT or MRI are the primary imaging modalities used for initial diagnosis. Treatment planning for MWA then utilizes these CECT or MRI data sets similar to surgery for resection [7]. Intra-operative CT allows precise visualization of the position of MWA antenna and ablation monitoring for detection of possible complications as well as the vaporization process [1, 4]. More specifically water vapor on CT appears as a low attenuation area against the background liver parenchyma and can be used to define the potential ablation zone [8, 9], and also utilized for follow up [10].

8.1.2 Ultrasound for Antenna Placement

Free hand, real-time scanning with ultrasound is especially helpful as antennas often lie outside the axial plane of other imaging modalities, such as CT, enabling ultrasound to achieve full visualization of the antenna. Ultrasound contrast agents may also improve the visualization of tumors, their relationship to antenna placement, and any residual tumor post-ablation [11-13]. During the tissue heating phase of MWA,

water vaporization disperses from the center of the ablation zone where the backscatter from hyperechoic bubbles can be seen in B-mode ultrasound to approximate the developing ablation zone [3, 7, 14].

8.1.3 Fusion and Other Advanced Techniques

Image fusion, needle tracking, and robotic tracking are other techniques that may be used for more accurate visualization of tumors and adjacent structures that are not visible with ultrasound or CT alone [15-17]. Commonly, image registration and fusion are used for co-localization of an imaging modality with certain imaging strengths with another imaging modality that has different imaging strengths using anatomical or non-anatomical landmarks for alignment [18, 19]. Examples of registration include PET to CT, MRI to ultrasound, and CT to ultrasound [20-22]. However, co-localization requires accurate tracking and alignment to be useful requiring high computational capabilities [19].

Differential imaging to differentiate pre-ablation tumors and post-ablation ablation zones for use in verifying ablative margins along with a comparison to the current clinical standard of care is essential to evaluate the efficacy of microwave ablation procedures. Electrode displacement elastography (EDE), specifically has demonstrated promise via simulations where higher imaged contrast was obtained when compared to external compression elastography [23]. Phantom and *in-vivo* studies confirmed these simulation findings with contrast-to-noise ratio (CNR) and strain contrast obtained being significantly higher for EDE due to the local nature of the deformation applied [24-26]. In addition, *in vivo* animal models showed a high correlation between EDE strain and pathologic areas of ablated regions [27, 28]. EDE has recently been performed on human patients after the MWA procedure, verifying its ability to differentiate ablated regions with improved contrast, CNR, and boundary delineation when compared to B-mode or acoustic radiation force imaging [29-32]. The goal of this chapter is to demonstrate the ability of EDE for differential imaging by identifying and comparing pre-ablation tumor and post-ablation boundaries.

8.2 Methods and Materials

8.2.1 Patient Data Collection Protocol

Radiofrequency data was collected following the same procedure outlined in Chapter 3, subsection 3.2.1. Clinical B-mode images for this study were collected using a different ultrasound system (General Electric Medical Systems, Waukesha, WI) than the system used to collect RF data used to generate the B-mode and elastography images (Siemens Inc., Malvern, PA). Additionally, different transducers and image settings were used for the clinical images based on the operating clinician and sonographer's preferences. Segmentation curves shown on strain tensor images were estimated using the EDE strain tensor images and not obtained from the clinical images.

8.2.2 Electrode Displacement Elastography for Differential Imaging

After RF data collection, the data is imported into MATLAB for processing Within MATLAB, displacement estimates were calculated using a Multilevel 2-D Normalized Cross-Correlation (MNCC) method [33] from consecutive RF frames. Displacement estimation was improved with subsample estimation using 2D sinc-interpolation in the discrete cosine time domain after each displacement level [34]. Data was then filtered using median filtering of size 1.9×1.9 mm and then dictionary representation with a patch size of 4.0×4.0 mm and 80% patch overlap [35]. Physiological motion reduction using Lagrangian deformation tracking was utilized to ensure repeatability of strain tensor images across several frames [36]. Of these frames, with sufficient displacement to produce strain tensor images, an observer manually selected corresponding pre- and post-deformation frames that depict a mass with the largest cross-sectional area. After filtering displacements, strain tensors were calculated using a 2D Savitzky-Golay digital differentiator of size 0.2 × 5.0 mm using $0^{th} \times 2^{nd}$ order polynomials for lateral and axial directions respectively [37, 38]. As the estimated axial and lateral strain tensor images often present with large variance, histogram contrast equalization and bilateral filtering were performed for improved strain tensor visualization. Histogram equalization utilized Contrast-Limited Adaptive Histogram Equalization (CLAHE) [39] which creates a contrast transform function for image tiles such that each tile's histogram

roughly matches this specified distribution. Additionally, a clip limit can be implemented to reduce noise amplification in homogenous image locations. For this work, an exponential distribution was utilized with a rate of 0.5 and clip limit of 0.01. After CLAHE, bilateral filtering [40] (Tomasi and Manduchi 1998) was performed 5 times using spatial kernels of 0.5 mm and range kernels of twice the variance inside the ablation zone.

8.2.2.1 Contrast Optimization for Differential Imaging

Despite strain tensor estimation and filtering, visualization may still be limited due to varying stiffness contrast from patient to patient resulting in different relative strain tensor magnitudes seen from patient to patient. To achieve more consistent image contrast across patients, an algorithm was developed to optimize visualized contrast using (43).

$$\min_{s_{\max}} \left(e^{s_I^*} \right) \left(e^{1-s_B^*} \right) \tag{43}$$

$$s_I^* = \frac{1}{s_{\max} m_I n_I} \sum_{i,j=1}^{m_I, n_I} \min\left(s_{\max}, \left| s(i,j) \right| \right) \tag{44}$$

$$s_B^* = \frac{1}{s_{\max} m_B n_B} \sum_{i,j=1}^{m_B, n_B} \min\left(s_{\max}, \left| s(i,j) \right| \right) \tag{45}$$

where s_I^* is the mean normalized strain tensor within the user-defined region of interest (ROI) inside the inclusion where strain values are limited to $s_{\max}$, the maximum strain value. In Eq. (2) and (3), *i* and *j* are summation variables, and *m* and *n* denote the height and width of the target and background ROI, respectively. Similarly, s_B^* is the mean normalized strain tensor within a user-defined ROI in background tissue surrounding the inclusion. The ROIs were selected such that the target ROI was around the needle tip and background ROIs was at the same depth around the target boundary. When the target ROI was placed near the needle tip, the background ROIs locations were not sensitive to position as long they were outside of target and at the same depth as the target ROI. The maximum strain tensor value in the image is defined as the $s_{\max}$ which minimizes Eq. (43), to improve the strain tensor image contrast between the

inclusion and background tissue. By defining the strain maximum for each image, the perceived image contrast between tumor or ablation zone and background tissue can be maximized to improve visualization.

8.2.3 Tumor and Ablated Region Segmentation

After optimizing the strain tensor image contrast, segmentation was performed to differentiate pre-ablation tumors and post ablation zones. To avoid introducing operator bias, segmentation was done semi-automatically utilizing snakes. To begin, the mass (tumor or ablation) ROI from Eq. (44) was utilized to initialize the snake, which was iterated until convergence as previously discussed in [36]. Snake propagation was determined converged after the segmentation deviation between iterations dropped below 0.1 mm. After snake convergence or 300 iterations, pre and post-segmented regions were compared. Since depth, translational motion, and the 2D ultrasound imaging plane may differ between pre and post-ablation data collections, the pre and post image sets may not be co-localized since only 2D imaging planes were acquired in our study. Therefore, registration was required to accurately compare pre and post segmented regions.

8.2.4 Registration and Ablation Margin Estimation

Registration was initiated by aligning antenna axis found through manual delineation of the MWA antenna in B-mode frames as shown in Figure 8.1. After antenna alignment, the segmentation centroid, and other anatomical landmarks such as liver surface and vasculature were selected to align pre- and post-segmented regions along the antenna axis. However, regions may still be misaligned due to slightly different transducer placement between the pre- and post-ablation imaging sessions resulting in slightly misaligned 2D ultrasound imaging planes, speed of sound changes, or tissue contraction during heating [41-43]. To remedy for any remaining misalignment, post ablation segmented regions were translated along the axial and lateral directions by less than 0.5 mm to maximize overlap of the pre ablation segmentation. Although more advanced techniques for registration are essential to ensure treatment efficacy, these methods are beyond the scope of the 2D ultrasound and EDE data acquired for this study.

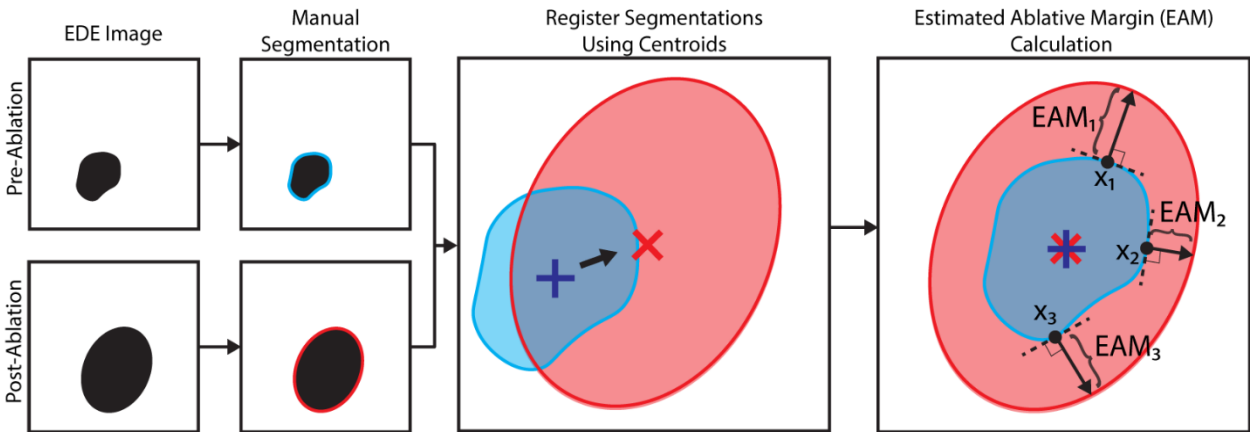

Figure 8.1 – Flowchart describing registration and estimated ablative margin calculation.

Now that pre-ablation tumors and post-ablation zones were segmented and registered, estimated ablative margins (EAMs) were computed. For EAM estimation, the pre-ablation tumor segmentation boundary was resampled uniformly with 500 points. EAM is defined as the distance between each uniformly sampled pre-ablation point to the point along the post-ablation segmentation boundary that was normal to the pre-ablation segmentation as shown in Figure 8.1. This results in a distribution of 500 EAM values for each patient.

8.2.5 Quantitative Metric Calculation

To quantitatively compare strain tensor images, SNR, contrast, and CNR were calculated using region-of-interest (ROI) similar to that described in [24]. Definitions for the quantitative metrics of SNR, contrast, and CNR are shown in Eqn. (4), (5), and (6),

$$SNR = \frac{\overline{s_T}}{\sigma_T} \tag{4}$$

$$Contrast = \frac{\overline{s_T}}{\overline{s_B}} \tag{5}$$

$$CNR = \frac{2\left(\overline{s_T} - \overline{s_B}\right)^2}{\left(\sigma_T^2 + \sigma_B^2\right)} \tag{6}$$

where T and B refer to the target and background ROIs respectively, $\bar{s}$ and σ are the mean and standard deviation of strain tensor magnitudes. In addition to quantitatively comparing images, it is important to compare Dice-Sorensen coefficient values (DSC) between EDE and clinical standard of care segmentations. DSC values were estimated using:

$$DSC = \frac{2\left|B_{EDE} \cap B_{SCI}\right|}{\left|B_{EDE}\right| + \left|B_{SCI}\right|} \tag{7}$$

where *B* is the binary mask of the EDE and SCI (standard of care image) segmentations, respectively.

8.2.6 EDE vs Clinical Standard CECT Segmentation

With segmentations of pre-ablation tumors and post-ablation zones from EDE images, an important consideration is validation against the current clinical gold standard. To accomplish this, diagnostic MRI or CECT images used for pre-procedure planning were used to locate and segment pre-ablation tumors and CECT images taken after the ablation procedure used for segmenting the post-ablation zone. Procedure planning images were used for pre-ablation tumors as during the procedure intra-operative images collected using CT typically have the antenna inserted making it difficult to segment the tumor accurately. MRI and CECT DICOM images were imported into RadiAnt DICOM Viewer (Radiant Version 2020.1, Mexidant, Poznań, Poland) and a multiplanar reconstruction was performed. Within the multiplanar format, the planes collected from initial antenna placement were adjusted so that the antenna lies along the intersection between two planes which are rotated around the antenna until anatomical markers, such as liver surface, surrounding organs, and vasculature points were aligned with clinical B-mode ultrasound images. Transformations performed for alignment were then utilized to transform the post-ablation CECT planes to locate the post-ablation volume and similarly for the pre-ablation tumor. Clinical segmentation was then performed by a trained medical physicist from the plane aligned with the clinical B-mode image.

8.3 Differential Imaging EDE Results

Demographic data for the 13 patients included in this study are shown in Table 8.1. Patients had an age range of 57 ± 16 (mean ± standard deviation) years and a body mass index (BMI) of 30.6 ± 6.6.

Representative *in vivo* patient images are shown in Figure 8.2 - Figure 8.6, depicting B-mode, CT slices, and EDE strain tensor images for patients with HCC in Figure 8.2, Figure 8.3, and Figure 8.6 and metastatic liver cancers in Figure 8.4 and Figure 8.5. The subfigures show the clinical B-mode images for (a) pre-ablation, (b) post-ablation, complementary CT or MRI planes for (c) pre-ablation, (d) post-ablation, B-mode images from the frames for which elastographic images were estimated for (e) pre-ablation, (f) post-ablation, and the axial strain tensor images (g) pre-ablation, and (h) post-ablation.

Table 8.1 – Demographics of the 13 patients included in this study.

Patient	Age at Procedure (years)	Sex	BMI	Race	Mass Type	Procedure Intent
1	59	Male	26.7	Caucasian	Metastasis	Curative
2	64	Female	21.1	Caucasian	Metastasis	Palliative
3	48	Male	28.7	Caucasian	HCC	Curative
4	55	Male	27.8	African American	HCC	Palliative
5	67	Male	24.5	Caucasian	HCC	Curative
6	51	Male	33.3	Caucasian	Metastasis	Palliative
7	28	Male	23.0	Caucasian	Metastasis	Palliative
8	54	Male	28.1	Caucasian	HCC	Curative
9	58	Male	40.5	Caucasian	HCC	Palliative
10	28	Female	38.0	Caucasian	HCC	Palliative
11	80	Male	26.4	Caucasian	Metastasis	Palliative
12	74	Female	40.0	Caucasian	HCC	Curative
13	79	Male	39.4	Caucasian	Metastasis	Palliative

Figure 8.2 represents patient ID 5 from Table 8.1. In Figure 8.2 (a), the ablation antenna can be seen clearly in the B-mode image, however, the tumor is not visible when compared to background tissue. Note that in Figure 8.2 (g) for the pre-ablation EDE axial strain tensor image, we obtained SNR, contrast, CNR and DSC values of 2.68 dB, 11.3 dB, 3.13 dB and 0.84. In addition observe that the axial strain tensor image shows a delineated tumor along a similar axis as the antenna shown in Figure 8.2 (a). Interestingly, this strain tensor image presents with two different stiffer regions along the antenna axis shown by the green arrows in Figure 8.2 (g). The distal region of these two regions was chosen as it enclosed the MWA antenna tip, which is the active ablation zone shown by the solid green arrow. This region also corresponds to the true tumor segmentation shown by the blue curve that occurs at a similar depth as the tip of antenna where

energy was deposited. In Figure 8.2 (b), in the B-mode image we visualize an approximate location of the ablation zone based on the hyperechogenic region located near the tip of the ablation antenna. Although the proximal region of the ablation zone provides adequate contrast for delineation, distal region delineation is difficult due to attenuation of ultrasound signals. On the other hand, Figure 8.2 (h) for the post-ablation EDE axial strain tensor image presents with SNR, contrast, CNR and DSC values of 4.50 dB, 13.9 dB, 5.08 dB and 0.87 and provides significant contrast around the entire circumference of the ablation zone, enabling complete ablation zone delineation. Note that the segmentation shown by the red curve fully encompases the pre-ablation segmentation of the targeted tumor.

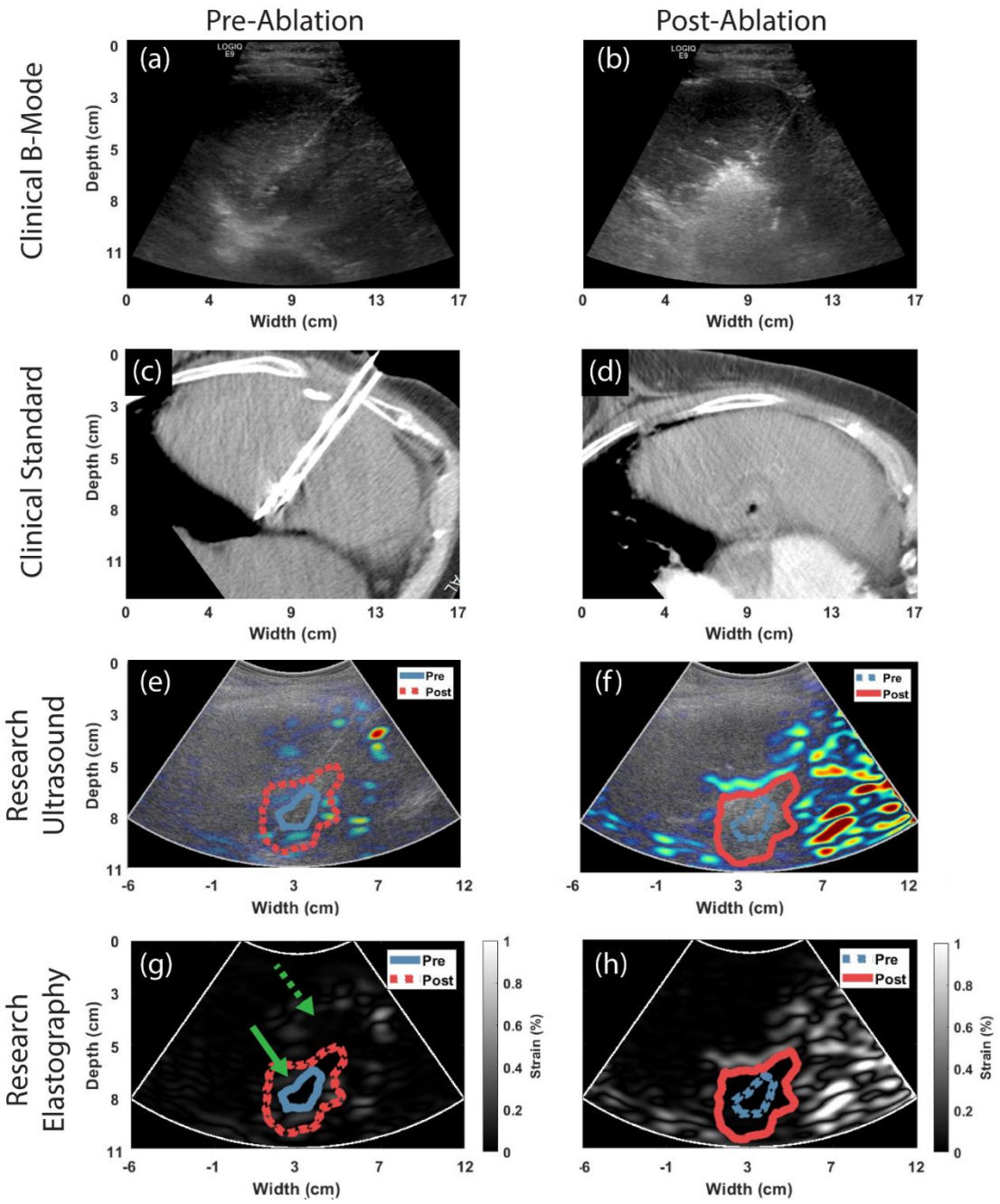

Figure 8.2 - An example of differentiating pre and post ablation regions from a patient with hepatocellular carcinoma (HCC). Subfigures (a) and (b) show the clinical B-mode images of pre and post ablation respectively, (c) and (d) show the CT slices complementing the planes shown in (a) and (b), (e) and (f) show the B-mode images from the frames which elastography images were estimated, while (g) and (h) show results of EDE with improved lesion visualization. Blue and red curves in (g) and (h) represent the pre-ablation tumor and post-ablation zone segmentations respectively from strain tensor images.

The second HCC example, patient ID 12, in Figure 8.3, provides a case where the B-mode contrast of pre-ablation tumor in Figure 8.3 (a) and post-ablation zone in (b) are low enough that delineation is very difficult and ablation antenna is not visible. This may be due to liver cirrhosis or the fat layer seen proximally in both images pointed out by the red arrows. When looking at pre-ablation tumor strain tensor images in Figure 8.3 (g) we obtain SNR, contrast, CNR and DSC values of 8.02 dB, 8.96 dB, 0.92 dB and 0.80. The distal location of the tumor in the EDE strain image shows higher contrast providing easier segmentation as shown by green arrows. However proximally, likely due to liver cirrhosis, the pre-ablation tumor has lower contrast pointed to by the yellow arrows, yet sufficient enough to provide tumor segmentation as shown by the blue curve. A similar phenomena is seen in Figure 8.3 (h), for the post-ablation EDE strain image where we obtain SNR, contrast, CNR and DSC values of 4.32 dB, 14.5 dB, 5.75 dB and 0.95. Note that post-ablation the ablation zone shows much higher contrast distally and slightly lower contrast proximally resulting in the segmentation shown by the red curve. The lower contrast seen proximally in both strain tensor images, Figure 8.3 (g) and (h), is likely caused by stiffer liver paranchyma due to cirrhosis thereby reducing the relative stiffness contrast between target tumor/ablation zone and background tissue. Despite lower proximal contrast, both pre and post ablation regions provided adequate contrast for segmentation with the post-ablation zone fully encompassing tumor segmentation.

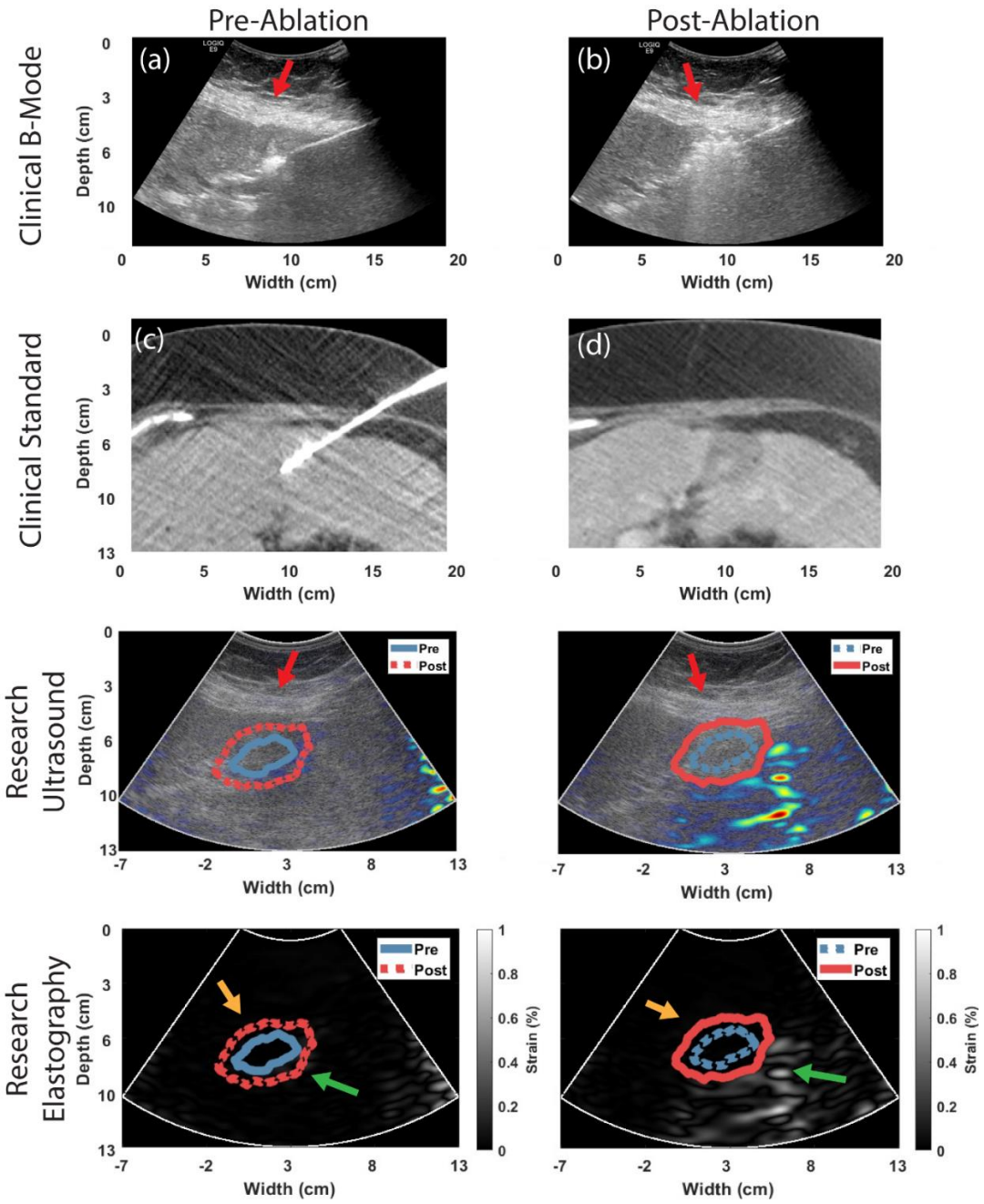

Figure 8.3 - An example of differentiating pre and post ablation regions from a patient with HCC. Subfigures (a) and (b) show the clinical B-mode images of pre and post ablation respectively, (c) and (d) show the CT slices complementing the planes shown in (a) and (b), (e) and (f) show the B-mode images from the frames which elastography images were estimated, while (g) and (h) show results of EDE with improved lesion visualization. Blue and red curves in (g) and (h) represent the pre-ablation tumor and post-ablation zone segmentations respectively from strain tensor images.

In a similar manner, Figure 8.4 and Figure 8.5 show results from patients presenting with metastasized tumors in the liver. Figure 8.4 shows patient ID 7 presenting with colon-adenocarcinoma. Here, the B-mode image in Figure 8.4 (a) clearly shows the MWA antenna along with an approximate location and size of tumor. Like previous examples signal attenuation reduces distal tumor contrast reducing accurate delineation of the tumor boundary. On the other hand, for the metastatic tumor in Figure 8.4 (g) we obtain SNR, contrast, CNR and DSC values of -1.03 dB, 11.06 dB, 3.77 dB and 0.83. We also observe high contrast delineation around the entire circumference of the tumor in the EDE strain tensor image providing clear tumor segmentation as shown by the blue curve. Post-ablation B-mode in Figure 8.4 (b), in a similar manner as Figure 8.4 (a) provides adequate contrast for antenna visualization as well as the ablated zone. Differing from previous examples, the target tumor seen in Figure 8.4 (g) has some jagged edges indicated by arrows in the figure. This results in a rough estimation of target tumor, as the jaggedness reduces ability to provide accurate segmented depiction of the target tumor. However, if the ablated region encompasses the target tumor, the ablation procedure would be considered a success. Conversely, post-ablation strain tensor image in Figure 8.4 (h) with SNR, contrast, CNR and DSC values of 5.42 dB, 10.4 dB, 4.28 dB and 0.91 shows a very smooth, high contrast ablation zone versus the surrounding tissue resulting in segmentation shown by red curve, which encompasses the entire pre-ablation tumor segmentation. One may note that Figure 8.4 (g) and (h) provide significantly higher contrast between targeted pre-ablation tumor and post-ablation zone against the surrounding liver parenchyma as opposed to axial strain tensor images shown in Figure 8.2 and Figure 8.3, (g) and (h). This is likely attributed to the patient in Figure 8.4not presenting with liver cirrhosis and a tumor metastasized from the colon embedded in normal liver parenchyma. As the colon metastasis provides higher stiffness than normal liver parenchyma, this results in higher strain tensor contrast seen in Figure 8.4.

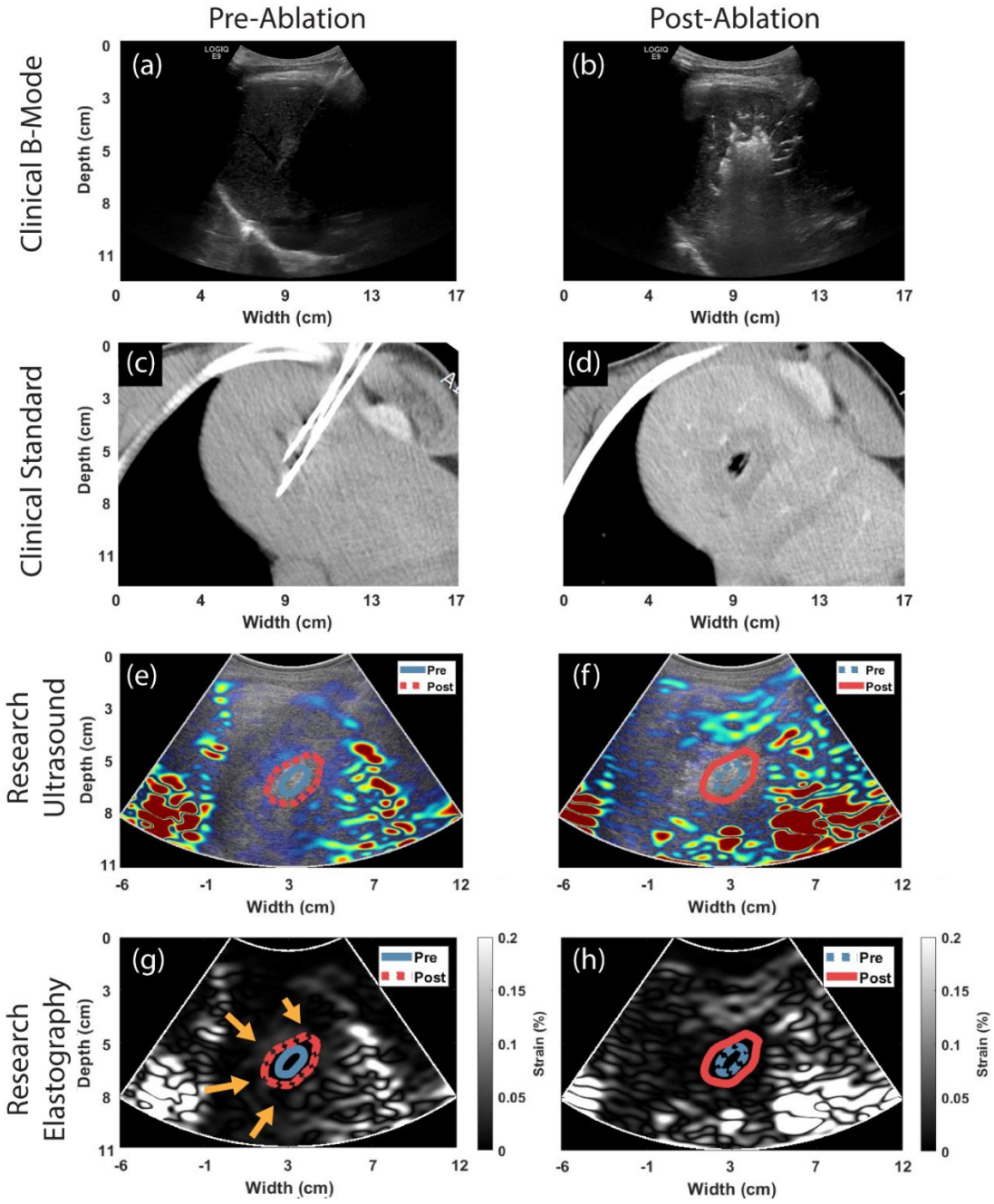

Figure 8.4 - An example of differentiating pre and post ablation regions from a patient with colon-adenocarcinoma. Subfigures (a) and (b) show clinical B-mode images of pre and post ablation respectively, (c) and (d) show the CT slices complementing the planes shown in (a) and (b), (e) and (f) show the B-mode images from the frames which elastography images were estimated, while (g) and (h) show results of EDE with improved lesion visualization. Blue and red curves in (g) and (h) represent the pre-ablation tumor and post-ablation zone segmentations respectively from strain tensor images.

Figure 8.5 shows patient ID 1, a metastasis patient presenting with a carcinoid tumor. Note that in the pre-ablation B-mode image in Figure 8.5 (a), it is difficult to visualize not only important features such as antenna or tumor, but also the proximal liver surface, hence segmenting the pre-ablation tumor from B-mode images would be extremely difficult. On the other hand, observe that in Figure 8.5 (g) with SNR, contrast, CNR and DSC values of 7.62 dB, 10.6 dB, 6.10 dB and 0.83, the pre-ablation strain tensor image provides high contrast at the boundary of tumor allowing for complete segmentation of the tumor shown by blue curve. Like the pre-ablation B-mode, observe that in Figure 8.5 (b), the post-ablation B-mode shows a visualized antenna with an approximate ablation zone represented proximally by gas bubble formation. As seen in previous images, these bubbles cause significant attenuation of the ultrasound signal causing distal portion of ablation zone to be lost in the noise floor of the B-mode image. The post-ablation axial strain tensor image in Figure 8.5 (h) with SNR, contrast, CNR and DSC values of 6.41 dB, 14.6 dB, 6.44 dB and 0.91 depicts an ablation zone with high contrast in a similar location seen from bubble formation in Figure 8.5 (b). Although located in similar location, Figure 8.5 (h) shows a slightly larger region than seen in (b) with the ablation zone segmented by the red curve. This post-ablation segmentation again fully encompasses pre-ablation segmented tumor.

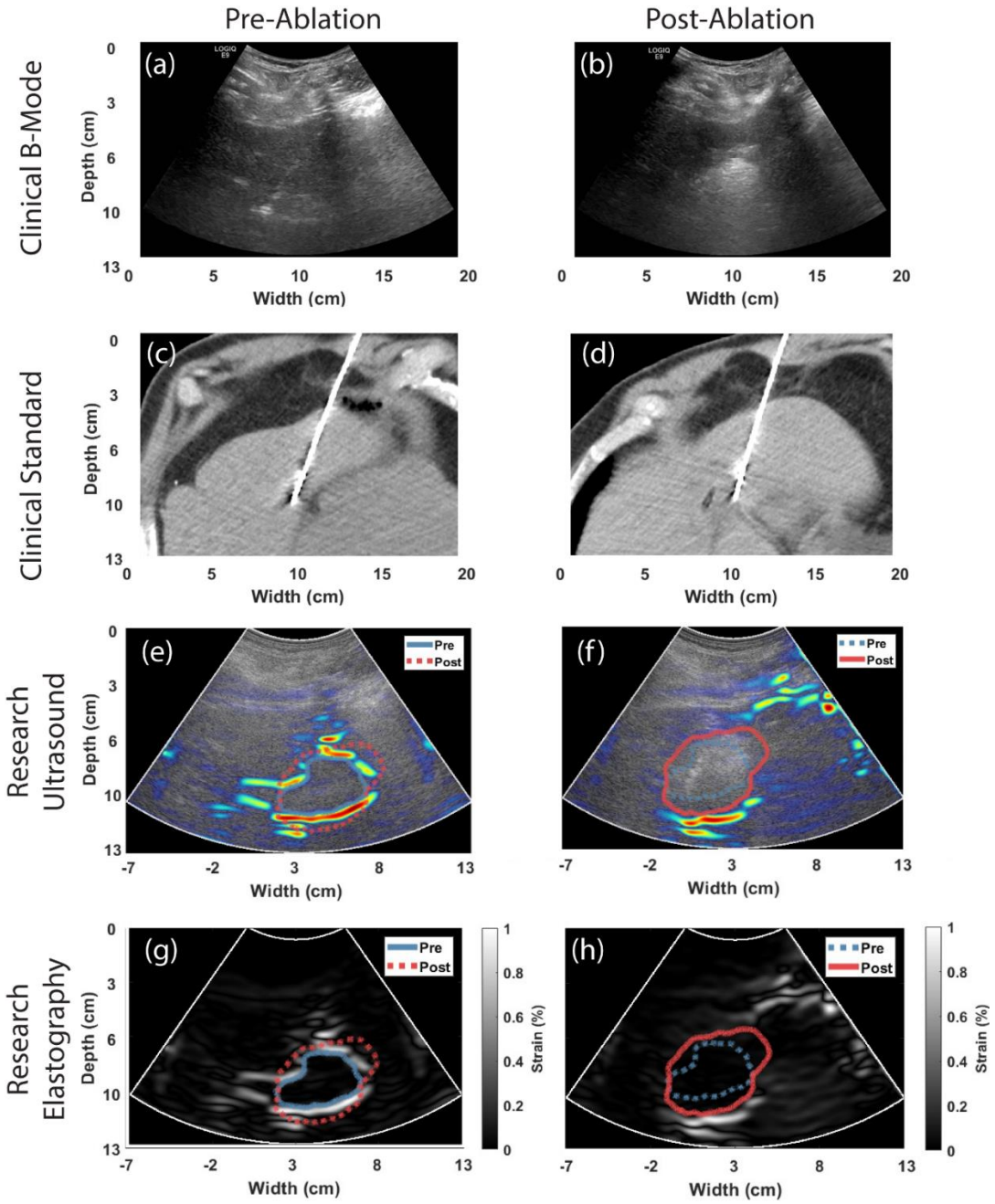

Figure 8.5 - An example of differentiating pre and post ablation regions from a patient with a carcinoid tumor. Subfigures (a) and (b) show the clinical B-mode images of pre and post ablation respectively, (c) and (d) show the CT slices complementing the planes shown in (a) and (b), (e) and (f) show the B-mode images from the frames which elastography images were estimated, while (g) and (h) show results of EDE with improved lesion visualization. Blue and red curves in (g) and (h) represent the pre-ablation tumor and post-ablation zone segmentations respectively from strain tensor images.

In addition to the use of CECT imaging for pre-procedural planning, MRI is also used. An example of using MRI for pre-procedural planning is shown for patient ID 8 with HCC in Figure 8.6, where (a) and (b) show the pre- and post- ablation clinical B-mode ultrasound, (c) shows the pre-procedural planning MRI images taken 2-3 months prior to the procedure, (d) shows the post-ablation CECT image, (e) and (f) show the B-mode from the frame that EDE strain was estimated with the strain tensors overlaid in color, and (g) and (h) show the pre- and post-ablation elastographic images. Figure 8.6 (g) presents with SNR, contrast, CNR and DSC values of 10.1 dB, 12.1 dB, 5.73 dB and 0.88 and Figure 8.6 (h) presents with SNR, contrast, CNR and DSC values of 7.70 dB, 9.76 dB, 4.70 dB and 0.87. It is important to note the difference in location of the tumor from the pre-procedural planning scan in (c) when compared to post-ablation image in (d) likely due to differing patient position during the scan and movement of organs over the duration between each of these scans.

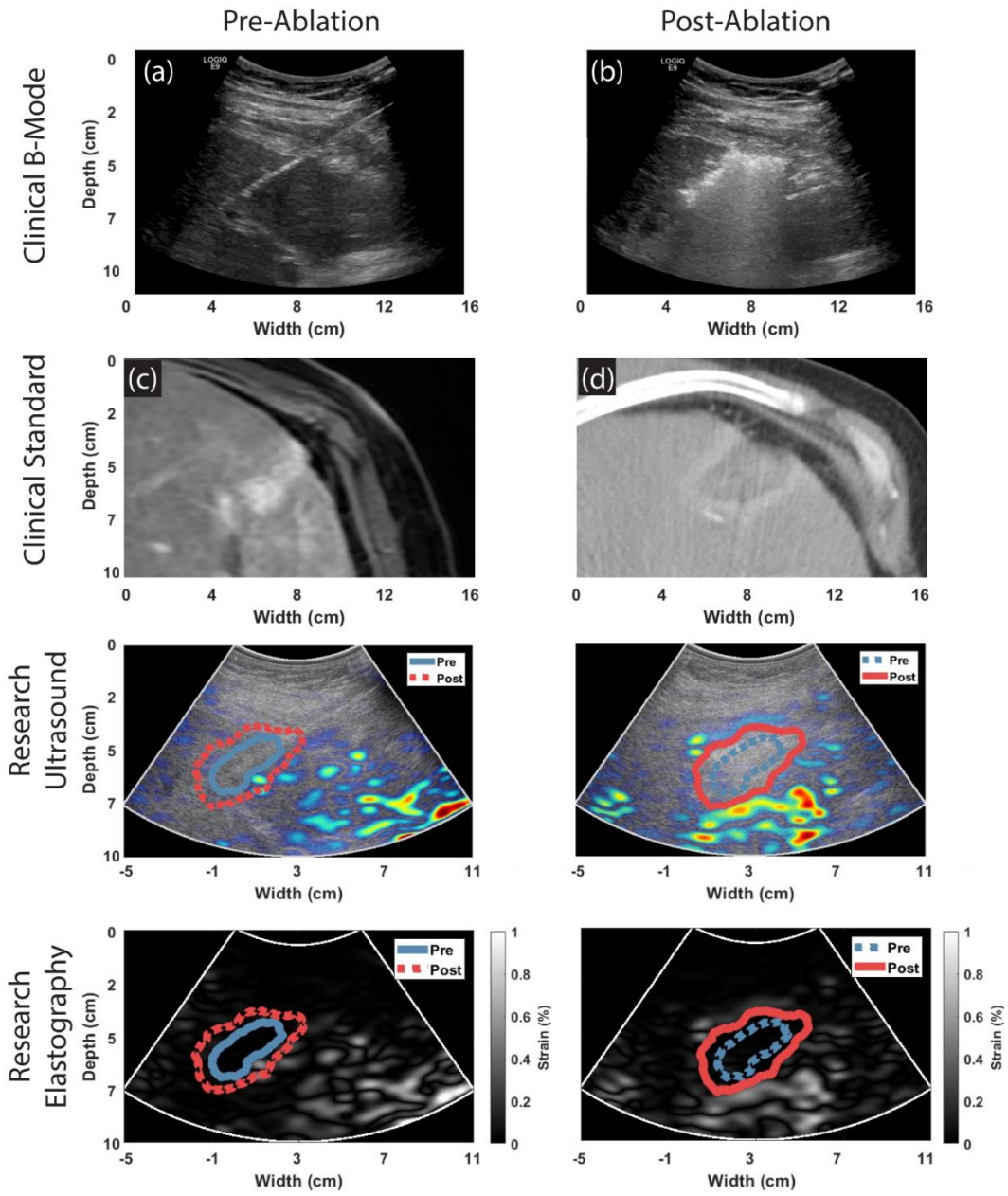

Figure 8.6 – An example of differentiating pre and post ablation regions from a patient with HCC. Subfigures (a) and (b) show the clinical B-mode images of pre and post ablation respectively, (c) shows the pre-procedural MR image of the target tumor and (d) shows the CT slice complementing the planes shown in (a) and (b), (e) and (f) show the B-mode images from the frames which elastography images were estimated, while (g) and (h) show results of EDE with improved lesion visualization. Blue and red curves in (g) and (h) represent the pre-ablation tumor and post-ablation zone segmentations respectively from strain tensor images.

Table 8.2 - Distribution of EAMs, Dice coefficients, and percentage of pre-ablation tumor segmentation inside of post-ablation zone segmentation for 13 patients with hepatocellular carcinoma or liver metastases. *Figures 8.2 – 8.5, 8.8, and 8.9 are represented in Table 8.1 as Patients 5, 12, 7, 1, 8 and 13, respectively.

Patient	Estimated Ablative Margin (cm)						Pre-Tumor Inside Post-Ablation
	Minimum	25th%	Median	Mean	75th%	Maximum	
1	0.61	0.82	1.08	1.20	1.45	2.20	100%
2	0.05	1.02	1.26	1.20	1.44	2.11	100%
3	0.04	0.42	0.83	0.88	1.13	2.25	100%
4	0.09	0.56	1.29	1.38	2.31	2.75	100%
5	0.35	0.79	1.07	1.01	1.19	1.67	100%
6	0.10	0.45	0.62	0.78	1.10	1.72	100%
7	0.23	0.55	0.63	0.59	0.67	0.84	100%
8	0.18	0.49	0.78	0.71	0.97	1.08	100%
9	0.06	0.26	0.50	0.55	0.83	1.20	100%
10	0.35	0.52	0.71	0.86	1.15	1.47	100%
11	0.13	0.43	0.76	0.91	1.44	1.90	100%
12	0.00	0.33	0.91	0.82	1.28	1.51	100%
13	0.01	0.33	0.49	0.52	0.71	1.09	100%
Average	0.17	0.54	0.84	0.88	1.21	1.68	100%

EAM distributions for each of the 13 patients are represented as boxplots as shown in Figure 8.7, with median value represented by central line and notch within each box, the box top and bottom edges representing data at the 25^{th} and 75^{th} percentile, while dashed lines represent outer quartiles of the distribution. In the EAM distributions, HCC data sets were colored blue while metastatic datasets are shown in red with target EAM region highlighted in green and statistical values from boxplot shown in Table 8.2. EAM values plotted in Figure 8.7 indicate that all patients had positive EAM values indicating that segmentations of the ablated regions were outside or encompassed pre-ablation tumor segmentations apart from patients 12 and 13 where tumor segmentations aligned with ablation zone segmentations at the extreme boundary of the distribution.

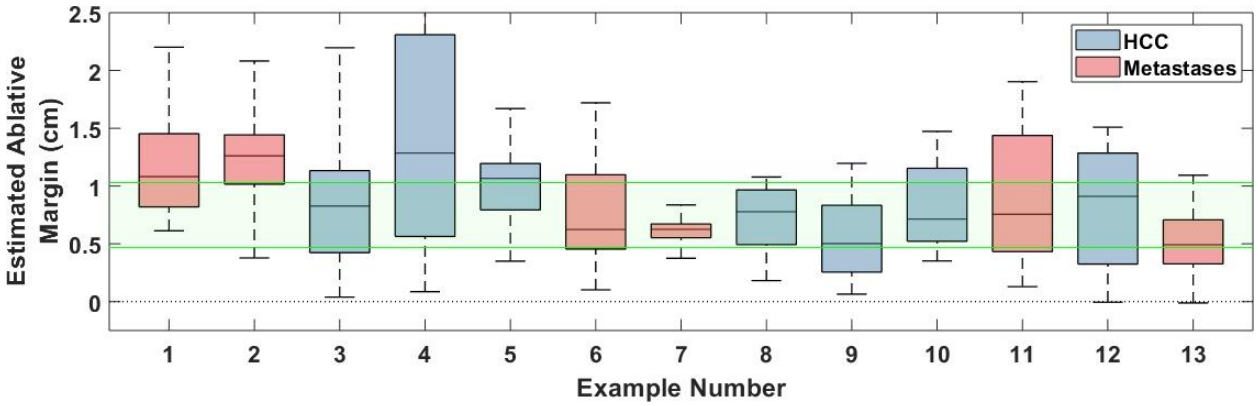

Figure 8.7 – Distributions of EAMs for 13 patients with hepatocellular carcinoma or liver metastases shown in blue or red, respectively.

Of the patients in this study, 12 of the 13 had CECT or MRI images that were utilized for comparison against EDE strain images with the results shown in Figure 8.8 where Figure 8.8 (a) represents pre-ablation tumor segmentations and Figure 8.8 (b) represents post-ablation zones. Results showed a high correlation between segmented sizes of the current clinical standard to EDE images with an R^2 values of 0.97 and 0.98 for pre- and post-ablation, respectively.

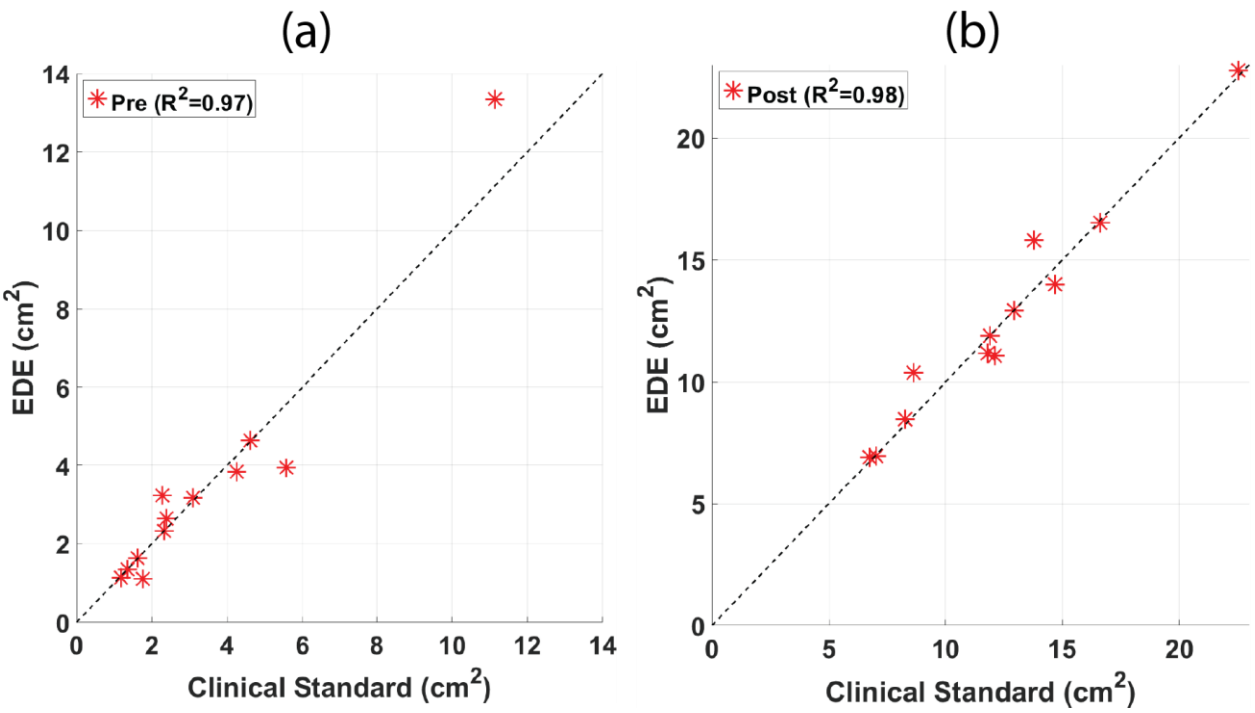

Figure 8.8 – Comparison of EDE segmented areas against the clinical segmented areas from respective MR or CT images. (a) represents pre-ablation tumors and (b) represents the post-ablation zones where the red asterisks show data points and dashed line represents the 45° correlation line.

Quantitative analysis to evaluate the overall quality of the strain images including the SNR, contrast, and CNR is shown in Table 8.2. Median values for SNR, Contrast, and CNR of 7.62 dB, 11.0 dB, and 3.84 dB for pre-ablation while post-ablation resulted in 5.42 dB, 12.2 dB, and 4.73 dB, respectively. Another important quantitative measure was the Dice-Sorensen coefficient (DSC) between the EDE and clinical standard of care segmentations shown in Table 3. DSC with a median value of 0.81 for pre-ablation tumor segmentations and 0.89 for post-ablation validate the correlation between EDE and clinical standard of care images.

Table 8.3 – Patient follow-up detailing local tumor progression, new tumor foci formation, and approximate time to recurrence in addition to current survival.

	Liver Tumor Recurrence			Survival After Procedure		
Patient	Local Tumor Progression	New Tumor Foci	Months Post Surgery	Deceased	Cause	Months Post Surgery

1	No	No	45	No	N/A	76
2	No	Yes	43	Yes	Metastasis	62
3	No	No	13	No	N/A	75
4	No	Yes	23	Yes	Metastasis	64
5	No	No	N/A*	Yes	Other Health Complications	29
6	No	Yes	24	Yes	Metastasis	35
7	No	Yes	27	Yes	Metastasis	40
8	No	No	51	No	N/A	60
9	No	No	9	No	N/A	58
10	No	No	11	No	N/A	41
11	No	No	N/A†	Yes	Other Health Complications	6
12	No	No	10	Yes	Other Health Complications	13
13	No	No	N/A‡	Yes	Other Health Complications	8

* Patient follow-up imaging was not performed at routine 1-3 month interval. No recurrence was seen 1 year after procedure.

† Patient follow-up imaging was not performed at routine 1-3 month interval as patient moved out of state and medical records were not available. Patient died from other medical complications not related to tumor treated.

‡ Patient follow-up imaging was not performed at routine 1-3 month interval to verify procedure efficacy due to patient comorbidities.

8.4 Discussion of EDE Differential Imaging

To completely assess elastographic imaging, patient follow-up is presented to correlate EAM values and technical success of the MWA procedure. Table 8.3 presents clinical follow-up information for the 13 patients included in this study. Of these patients, no local tumor progression was seen with follow-up imaging resulting in a 100% technique success and efficacy, which is also corroborated by the elastographic imaging results. Despite no local tumor progression, 31% of patients did present with new tumor foci in the liver at 26 ± 9 (median ± standard deviation) months after treatment arising from metastases from primary tumors. Following the procedure, patient survival rate was 39% with median survival of 41 ± 24 months, however, none of the patient's survival was negatively affected by the procedure. For the deceased patients, 50% were due to new liver tumor metastases and the other 50% was related to other co-morbidities. Surviving patients have remained liver tumor recurrence free for 60 ± 13 months.

8.4.1 Visualization Differences Between Pre- and Post-Ablation EDE

We present visualization of the target tumor pre ablation and ablated tumor post ablation in this chapter. Note that post ablation axial strain tensor images in Figure 8.2 - Figure 8.6 (f) demonstrate high contrast between the ablation zone and surrounding background liver tissue resulting in excellent visualization of the ablated region and boundary delineation regardless of malignancy type. This improved visualization is due to the high stiffness contrast between the ablation zone and surrounding liver tissue as tissue stiffness increases significantly in response to ablation or temperature elevation [44-46]. On the contrary, pre-ablation tumors do not always present with the high tissue stiffness contrast. This is particularly evident when comparing Figure 8.2 - Figure 8.6 (g), particularly Figure 8.2, Figure 8.4, and Figure 8.5 (g) where visualization contrast is significantly higher than that in Figure 8.3 (g). This is because most metastatic tumors are typically stiffer than normal liver providing sufficient stiffness contrast to visualize delineation via elastography. On the other hand, Figure 8.3 (g) shows lower visualized contrast likely seen as HCC is often present in liver with increased stiffness due to cirrhosis as compared to normal

liver stiffness [47-49] resulting in lower stiffness contrast between tumor and surrounding tissue. This finding shows that although differentiation is possible for all liver mass types, improved visualization success is more likely with metastatic tumors with an average median EAM of 0.81 cm as opposed to HCC patients with an average median EAM of 0.87 cm, especially those presenting with significant cirrhosis. Although improved visualization is more likely with metastatic patients, this work shows 100% success for visualizing all liver mass types. Despite significant filtering performed on patient data, all approaches used maintained boundary information while smoothing high variance regions. Preservation of EDE ablation dimensions were verified by comparison to the clinical standard of care image areas with R values of 0.97 and 0.98 for pre- and post-ablation, respectively.

Visualization of the ablation zone relative to pre-ablation tumor segmentation is important for clinical feedback, therefore EAMs are important as they correlate with successful ablation and reduced tumor recurrence. Box plots in Figure 8.7 show that all patients had a median EAM value within the target EAM, i.e., EAM values suggest accurate ablative margins. Additionally, all patients except patients 9, 12, and 13 also provided 25^{th} percentile EAM value within target EAM demonstrating the consistency of ablation around the entire tumor. However, we do note that all patients except patient 1 showed outliers with positive EAM values that did lie outside the targeted region. Although this may suggest inadequate ablation, more likely culprits are locations where registration of pre and post segmentation could be inaccurate. Despite this possibility, average EAM values of inner quantiles and median values shown in Table 8.2 represent a more general indication of successful ablation margins for patients in this study.

In addition to visualization, quantitative EAM results with lower values may be due to possible registration errors due to physiological motion, misalignment of the 2D B-mode imaging planes, and local speed of sound changes with temperature. Other factors that influence strain tensor imaging of post-ablation zones include tissue contraction and desiccation due to ablation. Most notably, increased speed of sound in ablated tissue results in faster echo signal arrival at a given depth thereby creating the illusion that the heated tissue is shallower than the corresponding CECT images. Other than speed of sound variations, water vapor formation and tissue contraction also occur due to the high ablation temperatures [40,50]. Due to this

contraction, post ablation imaging may underestimate the true volume of tissue destruction by up to 50%, additionally affecting differentiability with EDE [42,43].

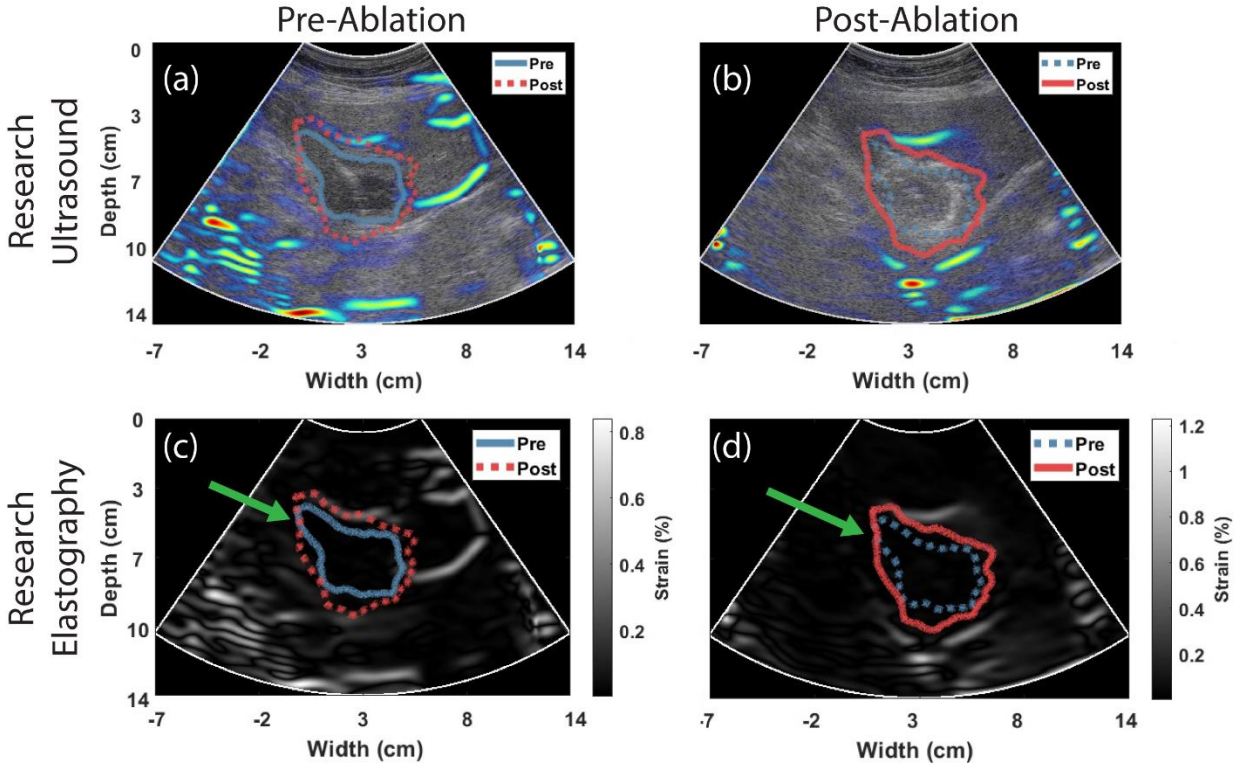

Figure 8.9 - An example of differentiating pre and post ablation regions from a patient with a squamous lung tumor metastasized in the liver. Subfigures (a) and (b) show the B-mode images for pre and post ablation respectively, while (c) and (d) show axial strain tensor imaging results of electrode displacement elastography with improved lesion visualization.

Additionally, low EAM values may also be due to segmentations including portions of background tissue that are not the target of the ablation procedure. This aspect is clearly exemplified by the patient images shown in Figure 8.9, where the patient presented with squamous lung cancer metastasized to the liver. This example is one of the cases where the ablation antenna can be seen clearly in both Figure 8.9 (a), pre-ablation B-mode, and (b), post-ablation B-mode. On top of clear antenna visualization, there is sufficient contrast enabling tumor delineation in the B-mode image itself, Figure 8.9 (a), and similarly the ablation zone can be delineated from the B-mode image in Figure 8.9 (b). Observe from the pre-ablation

strain tensor image in Figure 8.9 (c), the tumor is clearly delineated and segmented by the blue curve resembling the depiction seen in Figure 8.9 (a) on the B-mode image. Interestingly, the tumor alone does not appear in strain tensor image, but also a portion of tissue surrounding the antenna near the left proximal tumor boundary shown by the green arrow. This is possibly due to freezing the antenna to tissue with a nonlethal ice ball commonly used to reduce probe migration or compression of tissues adjacent to the antenna. This results in segmentation including a portion of tissue that may not necessarily represent the targeted tumor. A very similar phenomenon is seen post-ablation in Figure 8.9 (d) where the ablation zone can be delineated due to high boundary contrast, but a portion of the tissue surrounding antenna is also delineated. This results in a post-ablation segmentation shown in red curve that fully encompasses pre-ablation tumor segmentation but aligns where segmentation follows the antenna. Although low EAM values may suggest improper ablation, one may infer from B-mode and corresponding strain tensor images in this example that the portion of segmentation with low EAM values is in fact not part of targeted tumor, but instead tissue adjacent to the antenna. Despite this observation, comparison against current clinical standard of care images show that EDE segmented areas correlated well with these images. Future work will utilize registered CT 'virtual slices' to look more closely into locations with low EAM values [19] and compare our displacement tracking algorithms with other ablation monitoring techniques [51] and their fit for EDE for validating estimation efficacy. Additionally, three-dimensional (3D) ultrasound imaging may significantly mitigate the registration issues between pre- and post-ablation ultrasound and EDE data sets resulting in more consistent EAM values. This chapter demonstrates the differential imaging capability of EDE to differentiate pre-ablation tumors and post-ablation ablation zones for use in verifying ablative margins along with a comparison to the current clinical standard of care. Although important to compare against other liver cancer treatments, in this chapter *in-vivo* differential imaging was demonstrated on a small number of patients to validate EDE as a pilot study. For assessment of the efficacy of EDE as a diagnostic methodology for MWA efficacy, future work will perform a significantly larger number of patient studies.

8.5 EDE Conclusions on Differential Imaging

For the 13 patients in this study, electrode, or antenna displacement elastography was successful in delineating pre-ablation index tumors and post-ablation ablation zones for the purposes of differentiating tumors and respective ablation zones for validating ablative margins. Future work using 3D ultrasound and elastographic data sets are necessary along with accurate registration of the pre-ablation tumor with the ablation zone to verify that the margins obtained are consistent around the entire circumference of the malignant tumor. Registration with corresponding CECT images to verify size and location of images presented using EDE is also essential. Despite these remaining challenges, EDE not only successfully demarcates the ablation zone, but also pre-ablation tumor for clinical visualization in patients, thereby moving us closer to the application of this technology in the ablation suite.

8.6 References

[1] T. J. Vogl, N.-E. A. Nour-Eldin, R. M. Hammerstingl, B. Panahi, and N. N. Naguib, "Microwave ablation (MWA): basics, technique and results in primary and metastatic liver neoplasms–review article," in *RöFo-Fortschritte auf dem Gebiet der Röntgenstrahlen und der bildgebenden Verfahren*, 2017, vol. 189, no. 11: © Georg Thieme Verlag KG, pp. 1055-1066.

[2] M. F. Meloni, J. Chiang, P. F. Laeseke, C. F. Dietrich, A. Sannino, M. Solbiati, E. Nocerino, C. L. Brace, and F. T. Lee Jr, "Microwave ablation in primary and secondary liver tumours: technical and clinical approaches," *International Journal of Hyperthermia*, vol. 33, no. 1, pp. 15-24, 2017.

[3] M. Ahmed, L. Solbiati, C. L. Brace, D. J. Breen, M. R. Callstrom, J. W. Charboneau, M.-H. Chen, B. I. Choi, T. De Baère, and G. D. Dodd III, "Image-guided tumor ablation: standardization of terminology and reporting criteria—a 10-year update," *Radiology*, vol. 273, no. 1, pp. 241-260, 2014.

[4] P. Liang, J. Yu, M.-D. Lu, B.-W. Dong, X.-L. Yu, X.-D. Zhou, B. Hu, M.-X. Xie, W. Cheng, and W. He, "Practice guidelines for ultrasound-guided percutaneous microwave ablation for hepatic malignancy," *World journal of gastroenterology: WJG*, vol. 19, no. 33, p. 5430, 2013.

[5] A. Gillams, N. Goldberg, M. Ahmed, R. Bale, D. Breen, M. Callstrom, M. H. Chen, B. I. Choi, T. de Baere, and D. Dupuy, "Thermal ablation of colorectal liver metastases: a position paper by an international panel of ablation experts, The Interventional Oncology Sans Frontières meeting 2013," *European radiology,* vol. 25, no. 12, pp. 3438-3454, 2015.

[6] X. Wang, C. T. Sofocleous, J. P. Erinjeri, E. N. Petre, M. Gonen, K. G. Do, K. T. Brown, A. M. Covey, L. A. Brody, and W. Alago, "Margin size is an independent predictor of local tumor progression after ablation of colon cancer liver metastases," *Cardiovascular and interventional radiology,* vol. 36, no. 1, pp. 166-175, 2013.

[7] R. S. Puijk, A. H. Ruarus, H. J. Scheffer, L. G. Vroomen, A. A. van Tilborg, J. J. de Vries, F. H. Berger, P. M. van den Tol, and M. R. Meijerink, "Percutaneous liver tumour ablation: image guidance, endpoint assessment, and quality control," *Canadian Association of Radiologists Journal,* vol. 69, no. 1, pp. 51-62, 2018.

[8] J. Chiang, S. Birla, M. Bedoya, D. Jones, J. Subbiah, and C. L. Brace, "Modeling and validation of microwave ablations with internal vaporization," *IEEE Transactions on Biomedical Engineering,* vol. 62, no. 2, pp. 657-663, 2014.

[9] H. Ai, S. Wu, H. Gao, L. Zhao, C. Yang, and Y. Zeng, "Temperature distribution analysis of tissue water vaporization during microwave ablation: Experiments and simulations," *International Journal of Hyperthermia,* vol. 28, no. 7, pp. 674-685, 2012.

[10] V. Vilgrain, M. Esvan, M. Ronot, A. Caumont-Prim, C. Aubé, and G. Chatellier, "A meta-analysis of diffusion-weighted and gadoxetic acid-enhanced MR imaging for the detection of liver metastases," *European radiology,* vol. 26, no. 12, pp. 4595-4615, 2016.

[11] M. F. Meloni, A. Smolock, V. Cantisani, M. Bezzi, F. D'Ambrosio, M. Proiti, F. Lee, L. Aiani, F. Calliada, and G. Ferraioli, "Contrast enhanced ultrasound in the evaluation and percutaneous treatment of hepatic and renal tumors," *European journal of radiology,* vol. 84, no. 9, pp. 1666-1674, 2015.

[12] M. F. Meloni, A. Andreano, E. Franza, M. Passamonti, and S. Lazzaroni, "Contrast enhanced ultrasound: should it play a role in immediate evaluation of liver tumors following thermal ablation?," *European journal of Radiology,* vol. 81, no. 8, pp. 897-902, 2012.

[13] L. Crocetti, T. De Baere, and R. Lencioni, "Quality improvement guidelines for radiofrequency ablation of liver tumours," *Cardiovascular and interventional radiology,* vol. 33, no. 1, pp. 11-17, 2010.

[14] S. R. Wilson and P. N. Burns, "Microbubble-enhanced US in body imaging: what role?," *Radiology,* vol. 257, no. 1, pp. 24-39, 2010.

[15] G. Mauri, S. De Beni, L. Forzoni, S. D'Onofrio, V. Kolev, M. M. Laganà, and L. Solbiati, "Virtual navigator automatic registration technology in abdominal application," in *2014 36th annual international conference of the IEEE engineering in medicine and biology society*, 2014: IEEE, pp. 5570-5574.

[16] M. W. Lee, "Fusion imaging of real-time ultrasonography with CT or MRI for hepatic intervention," *Ultrasonography,* vol. 33, no. 4, p. 227, 2014.

[17] M. Rajagopal and A. M. Venkatesan, "Image fusion and navigation platforms for percutaneous image-guided interventions," *Abdominal Radiology,* vol. 41, no. 4, pp. 620-628, 2016.

[18] T. Fu, Q. Li, D. Liu, D. Ai, H. Song, P. Liang, Y. Wang, and J. Yang, "Local incompressible registration for liver ablation surgery assessment," *Medical physics,* vol. 44, no. 11, pp. 5873-5888, 2017.

[19] R. M. Pohlman, M. R. Turney, P. H. Wu, C. L. Brace, T. J. Ziemlewicz, and T. Varghese, "Two-dimensional ultrasound-computed tomography image registration for monitoring percutaneous hepatic intervention," *Medical physics,* vol. 46, no. 6, pp. 2600-2609, 2019, doi: 10.1002/mp.13554.

[20] G. Mauri, L. Cova, S. De Beni, T. Ierace, T. Tondolo, A. Cerri, S. N. Goldberg, and L. Solbiati, "Real-time US-CT/MRI image fusion for guidance of thermal ablation of liver tumors undetectable

with US: results in 295 cases," *Cardiovascular and interventional radiology,* vol. 38, no. 1, pp. 143-151, 2015.

[21] S. J. Ahn, J. M. Lee, D. H. Lee, S. M. Lee, J.-H. Yoon, Y. J. Kim, J.-H. Lee, S. J. Yu, and J. K. Han, "Real-time US-CT/MR fusion imaging for percutaneous radiofrequency ablation of hepatocellular carcinoma," *Journal of hepatology,* vol. 66, no. 2, pp. 347-354, 2017.

[22] M. W. Lee, H. Rhim, D. I. Cha, Y. J. Kim, and H. K. Lim, "Planning US for percutaneous radiofrequency ablation of small hepatocellular carcinomas (1–3 cm): value of fusion imaging with conventional US and CT/MR images," *Journal of Vascular and Interventional Radiology,* vol. 24, no. 7, pp. 958-965, 2013.

[23] S. Bharat and T. Varghese, "Contrast-transfer improvement for electrode displacement elastography," *Physics in Medicine & Biology,* vol. 51, no. 24, pp. 6403-18, Dec 21 2006, doi: 10.1088/0031-9155/51/24/008.

[24] S. Bharat, T. Varghese, E. L. Madsen, and J. A. Zagzebski, "Radio-frequency ablation electrode displacement elastography: a phantom study," *Medical Physics,* vol. 35, no. 6, pp. 2432-42, Jun 2008, doi: 10.1118/1.2919763.

[25] S. Bharat and T. Varghese, "Radiofrequency electrode vibration-induced shear wave imaging for tissue modulus estimation: a simulation study," *Journal of the Acoustical Society of America,* vol. 128, no. 4, pp. 1582-5, Oct 2010, doi: 10.1121/1.3466880.

[26] J. Jiang, T. Varghese, Q. Chen, T. J. Hall, and J. A. Zagzebski, "Finite element analysis of tissue deformation with a radiofrequency ablation electrode for strain imaging," *IEEE Transactions on Ultrasonics, Ferroelectrics, and Frequency Control,* vol. 54, no. 2, pp. 281-9, Feb 2007. [Online]. Available: https://www.ncbi.nlm.nih.gov/pubmed/17328325.

[27] N. Rubert, S. Bharat, R. J. DeWall, A. Andreano, C. Brace, J. Jiang, L. Sampson, and T. Varghese, "Electrode displacement strain imaging of thermally-ablated liver tissue in an in vivo animal model," *Medical Physics,* vol. 37, no. 3, pp. 1075-82, Mar 2010, doi: 10.1118/1.3301603.

[28] A. T. Fernandez, O. Kolokythas, T. Gauthier, D. A. Herzka, A. V. Patil, and H. Xie, "Comparison of ultrasound strain images with multi-modality imaging techniques in liver RF ablation assessment: Initial ex vivo and clinical results," in *Ultrasonics Symposium, 2008. IUS 2008. IEEE*, 2008: IEEE, pp. 313-316.

[29] W. Yang, T. Varghese, T. Ziemlewicz, M. Alexander, M. Lubner, J. L. Hinshaw, S. Wells, and F. T. Lee, Jr., "Delineation of Post-Procedure Ablation Regions with Electrode Displacement Elastography with a Comparison to Acoustic Radiation Force Impulse Imaging," *Ultrasound in Medicine and Biology*, vol. 43, no. 9, pp. 1953-1962, Sep 2017, doi: 10.1016/j.ultrasmedbio.2017.04.021.

[30] R. M. Pohlman, T. Varghese, J. Jiang, T. J. Ziemlewicz, M. L. Alexander, K. L. Wergin, J. L. Hinshaw, M. G. Lubner, S. A. Wells, and F. T. Lee, Jr., "Comparison of Displacement Tracking Algorithms for *in Vivo* Electrode Displacement Elastography," *Ultrasound in Medicine and Biology*, vol. 45, no. 1, pp. 218-232, 2019, doi: 10.1016/j.ultrasmedbio.2018.09.001.

[31] W. Yang, T. J. Ziemlewicz, T. Varghese, M. L. Alexander, N. Rubert, A. N. Ingle, M. G. Lubner, J. L. Hinshaw, S. A. Wells, F. T. Lee, Jr., and J. A. Zagzebski, "Post-Procedure Evaluation of Microwave Ablations of Hepatocellular Carcinomas Using Electrode Displacement Elastography," *Ultrasound Med Biol*, vol. 42, no. 12, pp. 2893-2902, Dec 2016, doi: 10.1016/j.ultrasmedbio.2016.07.015.

[32] W. Yang, T. Varghese, T. Ziemlewicz, M. Alexander, M. Lubner, J. L. Hinshaw, S. Wells, and F. T. Lee, Jr., "Delineation of Post-procedure Ablation Regions with Electrode Displacement Elastography with a Comparison to Acoustic Radiation Force Impulse Imaging," *Ultrasound in Medicine & Biology*, Jun 05 2017, doi: 10.1016/j.ultrasmedbio.2017.04.021.

[33] H. Shi and T. Varghese, "Two-dimensional multi-level strain estimation for discontinuous tissue," *Physics in Medicine & Biology*, vol. 52, no. 2, pp. 389-401, Jan 21 2007, doi: 10.1088/0031-9155/52/2/006.

[34] N. H. Meshram and T. Varghese, "GPU accelerated multilevel Lagrangian carotid strain imaging," *IEEE Transactions on Ultrasonics, Ferroelectrics, and Frequency Control,* vol. 65, no. 8, pp. 1370 - 1379, August 2018 2018, doi: 10.1109/TUFFC.2018.2841346.

[35] R. M. Pohlman and T. Varghese, "Dictionary Representations for Electrode Displacement Elastography," *IEEE Transactions on Ultrasonics, Ferroelectrics, and Frequency Control,* vol. 65, no. 12, pp. 2381-2389, 2018, doi: 10.1109/TUFFC.2018.2874181.

[36] R. M. Pohlman and T. Varghese, "Physiological Motion Reduction Using Lagrangian Tracking for Electrode Displacement Elastography," *Ultrasound in Medicine and Biology,* vol. 46, no. 3, pp. 766-781, March 01, 2020 2019, doi: 10.1016/j.ultrasmedbio.2019.11.001.

[37] J. Luo, K. Ying, P. He, and J. Bai, "Properties of Savitzky–Golay digital differentiators," *Digital Signal Processing,* vol. 15, no. 2, pp. 122-136, 2005.

[38] A. Savitzky and M. J. Golay, "Smoothing and differentiation of data by simplified least squares procedures," *Analytical chemistry,* vol. 36, no. 8, pp. 1627-1639, 1964.

[39] K. Zuiderveld, "Contrast limited adaptive histogram equalization," in *Graphics gems IV*, 1994: Academic Press Professional, Inc., pp. 474-485.

[40] C. Tomasi and R. Manduchi, "Bilateral filtering for gray and color images," in *Iccv*, 1998, vol. 98, no. 1, p. 2.

[41] C. L. Brace, "Radiofrequency and microwave ablation of the liver, lung, kidney, and bone: what are the differences?," *Current Problems in Diagnostic Radiology,* vol. 38, no. 3, pp. 135-143, 2009/05/01/ 2009, doi: https://doi.org/10.1067/j.cpradiol.2007.10.001.

[42] M. G. Lubner, T. J. Ziemlewicz, J. L. Hinshaw, F. T. Lee Jr, L. A. Sampson, and C. L. Brace, "Creation of short microwave ablation zones: in vivo characterization of single and paired modified triaxial antennas," *Journal of Vascular and Interventional Radiology,* vol. 25, no. 10, pp. 1633-1640, 2014.

[43] D. Liu and C. L. Brace, "CT imaging during microwave ablation: analysis of spatial and temporal tissue contraction," *Medical physics,* vol. 41, no. 11, p. 113303, 2014.

[44] Y.-J. Kim, P. D. Wolf, and T. D. Bahnson, "Shear wave elastography with intracardiac echocardiography characterizes atrial stiffness during catheter ablation for atrial fibrillation," *Circulation*, vol. 140, no. Suppl_1, pp. A17083-A17083, 2019.

[45] R. J. DeWall, T. Varghese, and C. L. Brace, "Quantifying local stiffness variations in radiofrequency ablations with dynamic indentation," *IEEE transactions on biomedical engineering*, vol. 59, no. 3, pp. 728-735, 2011.

[46] S. Bharat, U. Techavipoo, M. Z. Kiss, W. Liu, and T. Varghese, "Monitoring stiffness changes in lesions after radiofrequency ablation at different temperatures and durations of ablation," *Ultrasound Med Biol*, vol. 31, no. 3, pp. 415-22, Mar 2005, doi: 10.1016/j.ultrasmedbio.2004.12.020.

[47] M. Adler, L. Larocca, F. M. Trovato, H. Marcinkowski, Y. Pasha, and S. D. Taylor-Robinson, "Evaluating the risk of hepatocellular carcinoma in patients with prominently elevated liver stiffness measurements by FibroScan: a multicentre study," (in eng), *HPB (Oxford)*, vol. 18, no. 8, pp. 678-683, 2016, doi: 10.1016/j.hpb.2016.05.005.

[48] A. Tatsumi, S. Maekawa, M. Sato, N. Komatsu, M. Miura, F. Amemiya, Y. Nakayama, T. Inoue, M. Sakamoto, and N. Enomoto, "Liver stiffness measurement for risk assessment of hepatocellular carcinoma," *Hepatology Research*, vol. 45, no. 5, pp. 523-532, 2015, doi: 10.1111/hepr.12377.

[49] J. Fung, C.-k. Lee, M. Chan, W.-k. Seto, D. K.-h. Wong, C.-l. Lai, and M.-f. Yuen, "Defining normal liver stiffness range in a normal healthy Chinese population without liver disease," (in eng), *PloS one*, vol. 8, no. 12, pp. e85067-e85067, 2013, doi: 10.1371/journal.pone.0085067.

[50] A. Andreano, Y. Huang, M. F. Meloni, F. T. Lee Jr, and C. Brace, "Microwaves create larger ablations than radiofrequency when controlled for power in ex vivo tissue," *Medical physics*, vol. 37, no. 6Part1, pp. 2967-2973, 2010.

[51] M. Ashikuzzaman, C. J. Gauthier, and H. Rivaz, "Global Ultrasound Elastography in Spatial and Temporal Domains," (in eng), *IEEE Trans Ultrason Ferroelectr Freq Control*, vol. 66, no. 5, pp. 876-887, May 2019, doi: 10.1109/tuffc.2019.2903311.

Chapter 9: Research Contributions & Future Work

9.1 Contributions of this Research

We have previously demonstrated that using the microwave antennae for introducing quasi-static deformation required for elastography, subsequently named Electrode Displacement Elastography (EDE) [1], allows for imaging at all tumor depths when compared to either acoustic radiation force impulse (ARFI) [2] , shear wave elastography imaging (SWEI) [3, 4], or external compression [5]. EDE has also demonstrated high contrast and contrast-to-noise ratios (CNR) for strain imaging in phantoms [6-8], animal models [9 , 10], and human patients [2, 11]. The work in this dissertation improves the efficacy of EDE for depicting ablated regions by accomplishing the results discussed below.

The work performed in this dissertation takes the previously completed work with EDE and translates it for use in a clinical setting. This was completed in multiple stages illustrated by each Specific Aim. First, common methods for performing displacement estimation were compared in Chapter 3 to illustrate the benefits and pitfalls for EDE resulting in the Multilevel approach being chosen for EDE due to high success rates and improved CNR. Chapter 4 demonstrated the benefits of dictionary representation for denoising displacement estimates and comparing various dictionary representation approaches. Our results demonstrated that using a combined dictionary representation improves CNR for strain tensor visualization. Following dictionary denoising, Lagrangian tracking from Chapter 5 showed that tracking lesions over time allows for consistent strain tensor visualization as opposed to conventional Eulerian tracking. In addition, Lagrangian tracking provided cross-sectional areas closer to the CECT segmentations than the Eulerian approach. Chapter 6 next utilized strain tensor images and derived a fully automatic segmentation approach, which provides robust segmentation of ablated regions for feedback of ablation size and location. Chapter 7 takes a step away from ultrasound and develops a manual deformable registration model for showing the virtual CT slice corresponding to clinical ultrasound images which offers benefits to validating EDE performance. Finally, Chapter 8 combines contributions from the previous chapters demonstrating EDE's ability to determine pre- and post-ablation cross sectional areas for

estimating ablative margins, an essential measure of microwave ablation efficacy. EDE results were then compared to cross-sectional areas from clinical standard of care CECT images validating EDE's imaging performance as well as correlating local tumor progression with estimated ablative margins. As a result, the work in this dissertation will advance EDE to bridge the gap to possibly eventual clinical utilization.

9.2 Future Work

There are several avenues for future work in this research area that are listed below.

1. The results presented in this dissertation are primarily preliminary assessments of EDE feasibility in patients. Future work will correlate strain tensor mass dimensions with a larger set of registered CECT mass dimensions and positions. Regularization methods to improve the mean and standard deviations of ablated regions estimated with the Multilevel method need to be performed.
2. Dictionary learning using different size patches for reconstruction instead of singular 1 mm size patches used in this dissertation must be explored.
3. Lagrangian tracking would benefit from extension to three-dimensional ultrasound data sets when they become available. Three-dimensional tracking will enable more accurate lesion tracking over time and provide the ability to obtain volumetric information critical to ascertaining the success of the ablation procedure.
4. Automatic segmentation approaches utilizing machine learning is a topic with a lot of attention in the scientific community, hence comparing our approach to modern machine learning segmentation approaches may be beneficial. Like dictionary representation, improvements in computational efficiency will further improve utility for clinical application. Future work may also incorporate B-mode data as a means of improving accuracy.
5. Registration and fusion of CECT to EDE must be performed in an automated or semi-automated manner and on a larger number of data sets to demonstrate the accuracy and precision of EDE for use in a clinical setting.

6. As mentioned previously differential imaging must be performed on a larger group of patients to demonstrate the efficacy of EDE for evaluating both pre-ablation tumor imaging and post-ablation margin assessments. Utilization of automated and accurate registration and fusion will enable quantitative metric comparison between EDE and CECT segmentations, namely improved Dice coefficient calculation, centroid difference estimation, and boundary distance comparisons.

9.3 Published Work

9.3.1 Conference Poster Presentations

R. M. Pohlman, J. Jiang, W. Yang, T. J. Ziemlewicz, M. L. Alexander, K. Wergin, M. G. Lubner, J. L. Hinshaw, F. T. Lee Jr, and T. Varghese, "Comparison Study of Displacement Estimation Methods for Microwave Ablation Procedures Using Electrode Displacement Elastography," presented at the University of Wisconsin Carbone Cancer Center's Annual Research Retreat, Health Sciences Learning Center, March 4th, 2020.

R. M. Pohlman, J. L. Hinshaw, T. J. Ziemlewicz, M. G. Lubner, S. A. Wells, F. T. Lee Jr, M. L. Alexander, K. Wergin, and T. Varghese, "Electrode Displacement Elastography for Differentiating Metastatic Liver Cancer Microwave Ablation Procedures," presented at the University of Wisconsin Carbone Cancer Center's Annual Research Retreat, Health Sciences Learning Center, March 16th, 2021.

9.3.2 Conference Abstract Presentations

R. M. Pohlman, J. Jiang, T. J. Ziemlewicz, M. Alexander, K. Wergin, J. L. Hinshaw, M. G. Lubner, S. A. Wells, F. T. Lee Jr, T. Varghese, “Displacement Estimation Algorithms for Electrode Displacement Elastography in Liver Microwave Ablation Procedures,” in American Institute of Ultrasound in Medicine, Orlando, Florida, 2019.

R. M. Pohlman, & T. Varghese. (2019a). "Dictionary Learning and Sparse Representation for Imaging Liver Microwave Ablation Procedures". Paper presented at the American Institute of Ultrasound in Medicine, Orlando, Florida, 2019a.

R. M. Pohlman, & T. Varghese. (2019b). "Reduction of Physiological Motion Artifacts during Electrode Displacement Elastography". Paper presented at the American Institute of Ultrasound in Medicine, Orlando, Florida, 2019b.

G. Blitzer, C. Paz, J. Giri, A. Pennati, K. P. Nickel, C. A. Kelm-Nelson, V. L. Cannaday, **R. M. Pohlman**, T. Glazer, R. Mattison, T. Varghese, N. Pulia, J. Galipeau, and R. Kimple, "Salivary gland autotransplantation of marrow mesenchymal stromal cells for treatment of radiation-induced xerostomia - FDA IND enabling studies," in *American Society for Radiation Oncology 2020 Annual Meeting*, Miami Beach, Florida, 2020.

R. M. Pohlman and T. Varghese, "Electrode Displacement Elastography for Differentiating Metastatic Liver Cancer Microwave Ablation Procedures," in *Physics of Medical Imaging*, San Diego, California, 2021: SPIE, doi: 10.1117/12.2580741.

9.3.3 Conference Proceedings Papers

R. M. Pohlman, J. Jiang, W. Yang, T. J. Ziemlewicz, M. L. Alexander, K. L. Wergin, M. G. Lubner, J. L. Hinshaw, F. T. Lee, and T. Varghese, "Comparison study of displacement estimation methods for microwave ablation procedures using electrode displacement elastography," in *2017 IEEE International Ultrasonics Symposium (IUS)*, 2017: IEEE, pp. 1-4.

9.3.4 Peer Reviewed Conference Proceedings

R. M. Pohlman and T. Varghese, "Adaptation of Dictionary Learning for Electrode Displacement Elastography," in *2020 42nd Annual International Conference of the IEEE Engineering in Medicine & Biology Society (EMBC)*, 20-24 July 2020 2020, pp. 2023-2026, doi: 10.1109/EMBC44109.2020.9175319.

9.3.5 Peer Reviewed Journal Publications

R. M. Pohlman, & T. Varghese. (2018). "Dictionary Representations for Electrode Displacement Elastography". IEEE Transactions on Ultrasonics, Ferroelectrics, and Frequency Control, 65(12), 2381-2389. doi:10.1109/TUFFC.2018.2874181.

R. M. Pohlman, T. Varghese, J. Jiang, T. J. Ziemlewicz, M. L. Alexander, K. L. Wergin, J. L. Hinshaw, M. G. Lubner, S. A. Wells, & F. T. Lee, Jr. (2019). "Comparison of Displacement Tracking Algorithms for *in Vivo* Electrode Displacement Elastography". Ultrasound in Medicine and Biology, 45(1), 218-232. doi:10.1016/j.ultrasmedbio.2018.09.001.

R. M. Pohlman, M. R. Turney, P. H. Wu, C. L. Brace, T. J. Ziemlewicz, & T. Varghese. (2019). "Two-dimensional ultrasound-computed tomography image registration for monitoring percutaneous hepatic intervention". Medical Physics, 46(6), 2600-2609. doi:10.1002/mp.13554.

R. M. Pohlman, & T. Varghese. (2019). "Physiological Motion Reduction Using Lagrangian Tracking for Electrode Displacement Elastography". Ultrasound in Medicine and Biology. doi:10.1016/j.ultrasmedbio.2019.11.001.

R. M. Pohlman, J. L. Hinshaw, T. J. Ziemlewicz, M. G. Lubner, S. A. Wells, F. T. L. Jr., M. L. Alexander, K. L. Wergin, and T. Varghese, "Differential Imaging of Liver Tumors Before and After Microwave Ablation with Electrode Displacement Elastography (In Press)," *Ultrasound in Medicine & Biology*, 2021.

9.4 References

[1] S. Bharat and T. Varghese, "Contrast-transfer improvement for electrode displacement elastography," *Physics in Medicine & Biology,* vol. 51, no. 24, pp. 6403-18, Dec 21 2006, doi: 10.1088/0031-9155/51/24/008.

[2] W. Yang, T. Varghese, T. Ziemlewicz, M. Alexander, M. Lubner, J. L. Hinshaw, S. Wells, and F. T. Lee, Jr., "Delineation of Post-Procedure Ablation Regions with Electrode Displacement Elastography with a Comparison to Acoustic Radiation Force Impulse Imaging," *Ultrasound in*

Medicine and Biology, vol. 43, no. 9, pp. 1953-1962, Sep 2017, doi: 10.1016/j.ultrasmedbio.2017.04.021.

[3] M. Pernot, M. Couade, P. Mateo, B. Crozatier, R. Fischmeister, and M. Tanter, "Real-time assessment of myocardial contractility using shear wave imaging," *Journal of the American College of Cardiology,* vol. 58, no. 1, pp. 65-72, Jun 28 2011, doi: 10.1016/j.jacc.2011.02.042.

[4] P. J. Hollender, S. J. Rosenzweig, K. R. Nightingale, and G. E. Trahey, "Single- and multiple-track-location shear wave and acoustic radiation force impulse imaging: matched comparison of contrast, contrast-to-noise ratio and resolution," *Ultrasound Med Biol,* vol. 41, no. 4, pp. 1043-57, Apr 2015, doi: 10.1016/j.ultrasmedbio.2014.11.006.

[5] H. Rivaz, I. Fleming, L. Assumpcao, G. Fichtinger, U. M. Hamper, M. A. Choti, G. Hager, and E. Boctor, "Ablation monitoring with elastography: 2D in-vivo and 3D ex-vivo studies," *Med Image Comput Assist Interv,* vol. 11, no. 2, pp. 458-66, 2008.

[6] S. Bharat, T. Varghese, E. L. Madsen, and J. A. Zagzebski, "Radio-frequency ablation electrode displacement elastography: a phantom study," *Medical Physics,* vol. 35, no. 6, pp. 2432-42, Jun 2008, doi: 10.1118/1.2919763.

[7] S. Bharat and T. Varghese, "Radiofrequency electrode vibration-induced shear wave imaging for tissue modulus estimation: a simulation study," *Journal of the Acoustical Society of America,* vol. 128, no. 4, pp. 1582-5, Oct 2010, doi: 10.1121/1.3466880.

[8] J. Jiang, T. Varghese, Q. Chen, T. J. Hall, and J. A. Zagzebski, "Finite element analysis of tissue deformation with a radiofrequency ablation electrode for strain imaging," *IEEE Transactions on Ultrasonics, Ferroelectronics, and Frequency Control,* vol. 54, no. 2, pp. 281-9, Feb 2007. [Online]. Available: https://www.ncbi.nlm.nih.gov/pubmed/17328325.

[9] N. Rubert, S. Bharat, R. J. DeWall, A. Andreano, C. Brace, J. Jiang, L. Sampson, and T. Varghese, "Electrode displacement strain imaging of thermally-ablated liver tissue in anin vivoanimal model," *Medical Physics,* vol. 37, no. 3, pp. 1075-1082, 2010, doi: 10.1118/1.3301603.

[10] A. T. Fernandez, O. Kolokythas, T. Gauthier, D. A. Herzka, A. V. Patil, and H. Xie, "Comparison of ultrasound strain images with multi-modality imaging techniques in liver RF ablation assessment: Initial ex vivo and clinical results," *Ultrasonics Symposium, 2008.*, pp. 313-316, 2008, doi: 10.1109/ULTSYM.2008.0077.

[11] W. Yang, T. J. Ziemlewicz, T. Varghese, M. L. Alexander, N. Rubert, A. N. Ingle, M. G. Lubner, J. L. Hinshaw, S. A. Wells, F. T. Lee, and J. A. Zagzebski, "Post-Procedure Evaluation of Microwave Ablations of Hepatocellular Carcinomas Using Electrode Displacement Elastography," *Ultrasound in Medicine & Biology,* vol. 42, no. 12, pp. 2893-2902, 2016, doi: 10.1016/j.ultrasmedbio.2016.07.015.